DCU

Ollscoil Chathair
Bhaile Átha Cliath
Dublin City University

Metallated Triplex-Forming Oligonucleotides as Inducers of Sequence-Selective Chemical Modifications

Malou Coche MSc, Eng.

PhD Thesis

April 2025

Supervisor: Prof. Andrew Kellett

School of Chemical Sciences

Dublin City University

April 2026

1 Declaration

I hereby certify that this material, which I now submit for assessment on the programme of study leading to the award of Doctor of Philosophy (PhD) is entirely my own work, and that I have exercised reasonable care to ensure that the work is original and have conformed to the regulations on the use and declaration of Generative AI, and does not to the best of my knowledge breach any law of copyright, and has not been taken from the work of others save and to the extent that such work has been cited and acknowledged within the text of my work. I hereby certify that no Generative Artificial Intelligence (Gen AI) tools have been used in the creation of the thesis.

Signed: Malou Coche (Candidate) ID No.: 21268008 Date: 2 April 2026

2 Acknowledgements

I wish to thank my supervisor Prof. Andrew Kellett for his continuous knowledge-driven guidance and invaluable insights throughout this project. I am also deeply thankful to Dr. Bríonna McGorman for being such a helpful mentor, always willing to share her expertise and ideas. I would also like to thank Prof. Tom Brown and Dr. Afaf H. El-Sagheer for their kind and continued support, and for hosting me during a secondment in Oxford University. Thank you to Dr. Daniel Singleton for the great collaboration, for all the hard work that went into oligonucleotide synthesis and MS analysis, and for his continued help. I am grateful for all the assistance I received from colleagues from the Kellett Research Group and collaborators.

More specifically, I would like to thank Conor, whose friendship helped ease the challenges of the PhD every day. Thank you for always being willing to listen, I am grateful for the mutual support we have offered each other. My heartfelt thanks go to Simon who made Ireland feel like home. Words can not express how deeply thankful I am for your guidance, support and encouragement through every step of this journey.

I would also like to thank my friends back in France for their continued support and understanding. Whether through visiting me in Ireland or trips together, you have offered much-needed breaks and reminded me of the importance of balance and connection.

Finally, I am profoundly grateful to my family for the everlasting support and unwavering belief in me, making it possible for me to pursue this journey. To my Opa Jannes, whose curiosity and enthusiasm for science inspired my own love for the subject. You will always be my biggest fan, and me yours. And lastly, to my dearest Oma who only missed the last milestone, but whose love and support will forever remain with me.

3 Scientific Output

3.1 Presentations

- Participation at « Ma Thèse en 180 secondes » - 28th May 2022, UCD - national competition organised in partnership with the 'Association des études françaises et francophones d'Irlande', the French Embassy and the 'Agence universitaire de la Francophonie'.
- Poster presentation at the XVIIIth Symposium on Chemistry of Nucleic Acid Components. June 5th - 10th 2022, Czech Republic – 'A Click Chemistry Approach to *cis*-Platinum(II)-TFO Targeted DNA Crosslinking'. Joseph Hennessy, Malou Coche, Bríonna McGorman, Zara Molphy, Nicholas P. Farrell, Daniel Singleton, Tom Brown and Andrew Kellett.
- Poster presentation at the ETN-Symposium. November 9th - 10th 2023, France – 'Development of synthetic molecular scissors for artificial gene editing'. Malou Coche, Bríonna McGorman, Sean O'Halloran, Joseph Hennessy, Afaf H. El-Sagheer, Tom Brown and Andrew Kellett.
- Presentation at the 9th Annual DCU Chemical Research Symposium, May 10th 2024 – "Development of synthetic molecular scissors for artificial gene editing".
- Presentation at the RSC Nucleic Acid Forum, July 11th 2025 – "Prodigiosin Modified Triplex-Forming Oligonucleotide Hybrids Enable Autocatalytic DNA Cleavage".

3.2 Manuscripts

Published Manuscripts

- 'Thiazole Orange-Carboplatin Triplex-Forming Oligonucleotide (TFO) Combination Probes Enhance Targeted DNA Crosslinking'. Joseph Hennessy, Piotr Klimkowski, Daniel Singleton, Alex Gibney, Malou Coche, Afaf H. El-Sagheer, Tom Brown, Andrew Kellett. RSC Medicinal Chemistry, 2023, https://doi.org/10.1039/D3MD00548H.

Manuscripts in Preparation

- 'Prodigiosin Modified Triplex-Forming Oligonucleotide Hybrids Enable Self-Activated DNA Cleavage'. Malou Coche, Bríonna McGorman,

Daniel Singleton, Afaf H. El-Sagheer, Tom Brown and Andrew Kellett. Manuscript in preparation.

- ‘Development of Monofunctional Azide-modified Platinum(II) Complexes and SPAAC-labelling of TFO Probes for *EGFR*-specific Coordination Activity’. Malou Coche, Bríonna McGorman, Raphael E. F. De Paiva, Seán O’Halloran, Daniel Singleton, Diallo Traore, Afaf H. El-Sagheer, Tom Brown and Andrew Kellett. Manuscript in preparation.

4 Table of Contents

Metallated Triplex-Forming Oligonucleotides as Inducers of Sequence-Selective Chemical Modifications i

1 Declaration iii

2 Acknowledgements iv

3 Scientific Output v

3.1 Presentations ..... *v*

3.2 Manuscripts ..... *v*

4 Table of Contents vii

5 Table of Figures xi

6 Table of Tables xxv

7 List of Abbreviations xxvi

8 Abstract xxx

Chapter I 1

1 Introduction 2

1.1 Interaction of metal complexes with DNA *4*

1.1.1 Use of metals in medicine *4*

1.1.2 Platinum-based anticancer agents *5*

1.1.3 Copper-based artificial metallo-nucleases *9*

1.2 Targeted metal therapies using triplex-forming oligonucleotides *13*

1.2.1 Triplex-forming oligonucleotides *13*

1.2.2 Platinum(II)-TFO hybrids *18*

1.2.3 TFO-oxidative AMN hybrids: toward targeted DNA cleavage *21*

1.2.4 The epidermal growth factor receptor gene as a therapeutic target *24*

2 References 26

Chapter II 32

1 Project rationale 33

2 References 36

Chapter III 38

1 Introduction 39

2 Materials and Methods 41

2.1 General method *41*

2.2 Synthesis of NHS-ester TO_{B6} *42*

2.2.1 Synthesis of 3-(5-carboxypentyl)-2-methylbenzo[d]thiazol-3-ium bromide *42*

2.2.2 Synthesis of 4-chloro-1-methylquinolin-1-ium trifluoromethanesulfonate *42*

2.2.3 Synthesis of (E)-3-(5-carboxypentyl)-2-((1-methylquinolin-4(1H)-ylidene)methyl)benzo[d]thiazol-3-ium hexafluorophosphate (TO_{B6}) *43*

2.2.4 Synthesis of (E)-3-(6-((2,5-dioxopyrrolidin-1-yl)oxy)-6-oxohexyl)-2-((1-methylquinolin-4(1H)-ylidene)methyl)benzo[d]thiazol-3-ium hexafluorophosphate (NHS ester TO_{B6}) *44*

2.3 Synthesis of Pt-N_3-Oxali *45*

2.3.1 Synthesis of Di-tert-boc-2-hydroxy-1,3-diaminopropane *45*

2.3.2 Synthesis of Di-tert-boc-2-methanesulfonyl-1,3-diaminopropane *45*

2.3.3 Synthesis of Di-tert-boc-2-azido-1,3-diaminopropane *46*

2.3.4 Synthesis of 2-azidopropane-1,3-diamine dihydrochloride *46*

2.3.5 Synthesis of cis-[Pt(2-azidopropane-1,3-diamine)(Oxalate)] (Pt-N_3-Oxali) *47*

2.4 Post-synthetic labelling of TFOs *48*

2.4.1 One-pot TO_{B6} NHS ester (8) and CuAAC labelling of octadiynyl-modified TFOs. 48
2.4.2 SPAAC-labelling of 5'-DBCO TO-labelled TFOs 48
2.5 PAGE characterisation of the Pt(II)-TFO hybrids 48
2.5.1 Migration profile of the hybrids 48
2.5.2 Triplex formation activity of CuAAC- and SPAAC-generated Pt(II)-TFO hybrids 49

3 Results and discussion 50
3.1 Synthesis of NHS ester TO_{B6} and Pt-N_3-Oxali 50
3.1.1 Synthesis of NHS ester TO_{B6} 50
3.1.2 Synthesis of Pt-N_3-Oxali 50
3.2 Target selection and TFO design 52
3.2.1 Targeting the EGFR-gene 52
3.2.2 Optimisation of TFOs for triplex stabilisation 53
3.2.3 Strategies for labelling of TFOs 54
3.3 Comparative investigation of CuAAC and SPAAC for TFO conjugation with Oxaliplatin 55
3.3.1 Efficiency of the click labelling of TFOs 55
3.3.2 Apparent purity of the hybrids 56
3.3.3 Triplex formation 57

4 Conclusion 59

5 References 60

Chapter IV 62

1 Introduction 63

2 Materials and Methods 65
2.1 General method 65
2.2 Synthesis of Pt-N_3-Benzyl-DPA and Pt-N_3-Propyl-DPA 66
2.2.1 Synthesis of Pt-N_3-benzyl-DPA 66
2.2.2 Synthesis of N_3-propyl-DPA 66
2.2.2.1 Synthesis of 3-azidopropyl-1-amine 66
2.2.2.2 Synthesis of 3-azido-N,N-bis(pyridin-2-ylmethyl)propan-1-amine (N_3-propyl-DPA) 67
2.2.3 Synthesis of Pt-N_3-propyl-DPA 68
2.3 Interaction of the monofunctional Pt(II) complexes with plasmid DNA 68
2.4 Synthesis of oligonucleotides 69
2.4.1 NHS-ester labelling of duplex strands 69
2.4.2 SPAAC-labelling of TFOs 69
2.5 Triplex formation of Pt-TFO hybrids 69
2.5.1 Triplex formation analysis via PAGE 69
2.5.2 Melting temperature recording 69
2.6 Target-specific crosslinking of EGFR duplex by Pt-TFO hybrids determined by fluorescence denaturation 70
2.7 Inhibition of polymerase enzyme activity 70

3 Results and discussion 71
3.1 Synthesis of N_3-propyl-DPA and Pt-N_3-DPA complexes 71
3.2 Crosslinking of supercoiled plasmid DNA 72
3.3 Synthesis of oligonucleotides 73
3.3.1 SPAAC-labelling of the TFOs 73
3.3.2 Preparation of the target and off-target duplexes 74
3.4 Triplex recognition by monofunctional Pt-TFO hybrids 75
3.5 Target specific crosslinking of EGFR duplex by Pt-TFO hybrids (fluorescent denaturing experiment) 77
3.6 Primer extension inhibitory studies 80

4 Conclusion 83

5 References 85

Chapter V **87**

1 Introduction **88**

2 Materials and Methods **90**

2.1 General methods ***90***

2.2 Synthesis of an azide-functionalised prodigiosin analogue ***91***

2.2.1 Synthesis of 4-methoxy-3-pyrrolin-2-one *91*

2.2.2 Synthesis of N-((5-bromo-3-methoxy-2H-pyrrol-2-ylidene)methyl)-N-ethylethanamine *91*

2.2.3 Synthesis of 4-methoxy-1H,1'H-[2,2'-bipyrrole]-5-carbaldehyde *92*

2.2.4 Synthesis of 3-azidopropyl-1-amine *93*

2.2.5 Synthesis of N-(3-azidopropyl)-2,4-dimethyl-1H-pyrrole-3-carboxamide *93*

2.2.6 Synthesis of N-(3-azidopropyl)-5-((4'-methoxy-1H,5'H-[2,2'-bipyrrol]-5'-ylidene)methyl)-2,4-dimethyl-1H-pyrrole-3-carboxamide (N_3-PD) *94*

2.2.7 Synthesis of 5-azido-1,10-phenanthroline (N_3-Phen) *95*

2.3 Preliminary DNA cleavage activity assessment ***95***

2.3.1 Cleavage of pUC19 in the presence of Na-L-asc *95*

2.3.2 Self-activated pUC19 cleavage profile *95*

2.3.3 Mechanistic studies of pUC19 cleavage *96*

2.3.4 Groove-preference of [Cu(N_3-PD)(NO_3)$_2$] *96*

2.3.5 Sequence-specific cleavage preference of [Cu(N_3-PD)(NO_3)$_2$] *96*

2.4 SPAAC labelling of 5'-DBCO modified TFOs ***97***

2.4.1 Preparation of PD-TFO hybrids *97*

2.4.2 Preparation of phenanthroline-TFO hybrids *97*

2.4.3 SPAAC monitoring with denaturing PAGE *97*

2.5 Triplex formation of PD-TFO and Phen-TFO hybrids ***97***

2.5.1 PAGE visualisation of triplex formation *97*

2.5.2 Thermal melting studies *98*

2.6 Qualitative Cleavage Activity assessment of the PD-TFO Hybrids ***98***

2.6.1 Initial investigations of the cleavage activity of PD-TFO hybrids *98*

2.6.2 Comparison of PD-TFO and Phen-TFO hybrids using PAGE *98*

2.6.3 Amplicon expression *99*

2.6.4 qPCR quantification of damage *99*

3 Results and discussion **100**

3.1 Synthesis of N_3-PD ***100***

3.1.1 Synthesis of the bi-pyrrole moiety *100*

3.1.2 Optimising the synthesis of an azide-functionalised mono-pyrrole derivative *100*

3.1.3 Synthesis of N-(3-azidopropyl)-2,4-dimethyl-1H-pyrrole-3-carboxamide *103*

3.1.4 Coupling of the bi-pyrrole moiety and the azide-functionalised pyrrole *104*

3.2 Preliminary biophysical activity assessment ***104***

3.2.1 DNA cleavage assay *104*

3.2.2 Na-L-asc-mediated and self-activated cleavage activity of [Cu(N_3-PD)(NO_3)$_2$] *105*

3.2.3 Mechanistic studies *106*

3.3 SPAAC-labelling of the TFOs ***109***

3.4 Triplex formation experiments ***111***

3.5 Self-activated target specific cleavage of the EGFR duplex ***113***

3.5.1 Investigations on the cleavage activity of PD-2 in the presence of copper *113*

3.5.2 PAGE analysis of target specific cleavage activity *115*

3.5.3 qPCR quantification of the cleavage activity of the PD-TFO-2 hybrid. *116*

4 Conclusion **118**

5 References **120**

Chapter VI **122**

1 Introduction **123**

2 Materials and Methods **125**

2.1 General methods ***125***
2.2 Synthesis azide-functionalised ligands ***125***
2.2.1 Synthesis of 1,10-phenanthroline-5,6-dione *125*
2.2.2 Synthesis of N_3-DPPZ *126*
2.2.2.1 Synthesis of 11-nitrodipyrido[3,2-*a*:2',3'-*c*]phenazine (nitro-DPPZ) 126
2.2.2.2 Synthesis of 11-aminodipyrido[3,2-*a*:2',3'-*c*]phenazine (amino-DPPZ) 126
2.2.2.3 Synthesis of N_3-DPPZ 127
2.2.3 Synthesis of azido-ImPhen *128*
2.2.3.1 Synthesis of 2-(4-nitrophenyl)-1H-imidazo[4,5-*f*]-1,10-phenanthroline (nitro-ImPhen) 128
2.2.3.2 Synthesis of 2-(4-aminophenyl)-1H-imidazo[4,5-*f*]-1,10-phenanthroline (amino-ImPhen) 128
2.2.3.3 Synthesis of N_3-ImPhen 129
2.3 Screening of the cleavage activity of AMN-TFO hybrids ***129***
2.3.1 Cleavage activity of self-assembled PD-2 and PD-3 hybrids in the presence of copper *129*
2.3.2 Screening of ligands for AMN activity with TFO-2 *130*
2.3.3 Screening of metals for the cleavage activity of PD-2 *130*

3 Results and discussion **131**
3.1 Synthesis of N_3-ligands ***131***
3.2 Self-assembly of AMN-TFO hybrids via SPAAC ***132***
3.2.1 Experimental design *132*
3.2.2 Comparison of TFO-2 and TFO-3 for self-assembly application *134*
3.2.3 Screening of metal centre for the target-specific cleavage activity of self-assembled PD-TFO-2 *135*
3.2.4 Screening of different ligands for copper-mediated cleavage activity of self-assembled AMN-TFO hybrids *137*

4 Conclusion **140**

5 References **141**

Chapter VII **143**

Chapter VIII **1**

Appendix A **2**
A.1 Spectroscopic characterisation ***2***
A.2 HPLC trace and MS chromatogram of Pt-Oxali-TFO hybrids ***10***

Appendix B **14**
B.1 Spectroscopic characterisation ***14***
B.2 HPLC trace and MS chromatogram of Pt-TFO hybrids ***22***
B.3 PAGE gels ***28***

Appendix C **31**
C.1 Spectroscopic characterisation ***31***
C.2 HPLC trace and MS chromatogram of the PD- and Phen-TFO hybrids ***37***
C.3 Characterisation of the cleavage activity of [Cu(N_3-PD)(NO_3)$_2$]. ***41***

Appendix D **43**
D.1 Spectroscopic characterisation ***43***
D.2 PAGE analysis of the self-assembly assay ***47***

5 Table of Figures

Figure I.1: **a**. Structure of B DNA (1BNA). **b**. Structure of DNA duplets showing Watson-Crick hydrogen bonds between nucleobases.

Figure I.2: Common non-covalent B-DNA binding modes showing major and minor groove binding, intercalation, and electrostatic interaction.

Figure I.3: a. Structure of clinically approved *cis*-platinum(II) anticancer agents. b. Adducts generated by *cis*-platinum(II) crosslinking on two intrastrand guanines, intrastrand adenine and guanine, and interstrand guanines.

Figure I.4: **a**. Reduction of platinum(IV) with non-leaving group ligands (L), leaving group ligands (X) and axial ligands (R) to platinum(II), releasing axials ligands at tumour site. **b**. Structure of platinum(IV) drug candidates that entered clinical trials.

Figure I.5: Structure of a trinuclear platinum(II) complex, BBR3464 (triplatin) developed by Farrell and co-workers.[49]

Figure I.6: Schematic representation of the phosphate clamp binding mode of PPCs.

Figure I.7: **a**. Structure of pyriplatin and phenanthriplatin, two promising monofunctional platinum(II) anticancer agents. **b**. Inhibition of enzymatic activity by monofunctional platinum(II) assisted by steric repulsion by the ligand.

Figure I.8: Evolution of phenanthroline based Cu-AMNs from *bis*-phenanthroline complexes to caging ligands and binuclear Cu-AMNs.

Figure I.9: **a**. Structure of prodigiosin with the bipyrrole motif (blue), the methoxy group (orange) and the methylene bridge (green). **b**. Cleavage of supercoiled DNA by prodigiosin in the presence of copper generating single and double strand breaks. (Figure adapted from Melvin et al.).[78]

Figure I.10: Structure of triplexes (1BWG) and of base triplets in the case of parallel and antiparallel triplex formation, displaying Watson-Crick hydrogen bindings (·) between complementary (green) and target strand (purple) and hydrogen bonding (x) of the TFO strand (grey) on the Hoogsteen face of DNA duplets.

Figure I.11: **a**. Structure of triplets formed by cytosine and its analogues with increased triplex stabilisation, 5mC and Z. **b**. Use of thiazole orange (TO) for triplex stabilisation and triplex formation provbe **c**. Comparison of DNA phosphodiester backbone, phosphorodiamidate morpholino oligomer (PMO) and peptide nucleic acid (PNA) backbones.

Figure I.12: Cycle of solid phase synthesis (SPS) of oligonucleotide.

Figure I.13: Schematic representation of the incorporation of a DPA clicked monomer into a TFO sequence *via* SNI-PEX enzymatic oligonucleotide synthesis.

Figure I.14: Early strategies for the platination of oligonucleotides for target-specific DNA crosslinking.

Figure I.15: Use of click chemistry for labelling alkyne-modified TFOs with azide-functionalised metal centres.

Figure I.16: Structure of azide functionalised cisplatin, carboplatin and oxaliplatin that have been clicked onto *GFP*-targeting TFOs for target-specific DNA crosslinking.

Figure I.17: Reported EDTA- and Phen-functionalised oligonucleotides for targeted oxidative DNA cleavage.

Figure I.18: Structure of azide-modified Cu-AMNs that have been clicked onto *GFP*- or HIV-targeting TFOs showing selective cleavage of the target gene.

Figure I.19: Sequence of the exon 5 of the *EGFR* gene, highlighting the 19 nucleotide polypurine track compatible with triplex formation.

Figure II.1: Structures of: **a**. azide-functionalised monofunctional platinum(II) complexes with DPA-derived ligands; and **b**. the azide-modified prodigiosin target proposed in this project.

Figure II.2: Generation of gene editing metal-TFO hybrids using click chemistry for targeted crosslinking or cleavage.

Figure III.1: Total synthesis of NHS-ester thiazole orange B6 (TO_{B6}).

Figure III.2: Synthesis of Pt-N_3-Oxali.

Figure III.3: Triplex recognition domain on the 5th exon of the *EGFR* gene for parallel triplex formation.

Figure III.4: Preparation of TFO hybrids. **a**. Structure of 5mC. **b**. Structure of amine-modified dU monomer. **c**. Sequence of the CuAAC- and SPAAC-compatible TFOs (C1, C2, C3 and S1, S2, S3). **d**. Amide coupling on the amine-modified dU using NHS-ester TO_{B6}. **e**. Structure of the SPAAC-capable DBCO monomer. **f**. Structure of the CuAAC-capable alkyne-modified dU.

Figure III.5: PAGE showing the conjugation efficiency of TFO hybrids. CuAAC-TFO hybrids (C1-O, C2-O and C3-O lanes 2,4 and. 6) were compared to unclicked TFOs (C1, C2 and C3, lanes 1, 3 and 5) before and after SYBR Gold staining and SPAAC-TFO hybrids (S1-O, S2-O and S3-O lanes 8, 10 and 12) were compared to unclicked TFOs (S1, S2 and S3, lanes 7, 9 and 11) after SYBR Gold staining.

Figure III.6: PAGE of analysis of 100 eq. of Pt(II)-Oxali TFO hybrids (CuAAC-generated hybrids = C1-O, C2-O and C3-O, and SPAAC-generated hybrids = S1-O, S2-O and S3-O) with a 40-mer duplex target (0.5 pmol, 1 eq.) containing the recognition domain together with 1 eq. of a 29-mer *off*-target duplex lacking the recognition domain. Lanes 13 and 18: target duplex alone, lanes 14 and 19: *off*-target duplex alone, lanes 15, 16, 17, 20, 21 and 22: both target- and *off*-target sequences were incubated with 100 eq. of C1-O, C2-O, C3-O, S1-O, S2-O and S3-O, respectively.

Figure IV.1: Structure of bifunctional platinum(II) anticancer agents cisplatin, carboplatin, oxaliplatin, and of monofunctional platinum(II) complexes pyriplatin and phenanthriplatin.

Figure IV.2: Synthetic scheme for the complexation of N_3-benzyl-DPA with platinum(II).

Figure IV.3: Synthetic scheme for the preparation of Pt-N_3-propyl-DPA starting from 3-bromopropyl-1-amine hydrobromide.

Figure IV.4: Interactions of Pt-N_3-propyl-DPA and Pt-N_3-benzyl-DPA with pUC19 showing dose-dependent unwinding of the supercoiled plasmid DNA, characteristic of crosslinking. Complexes (10, 20, 30, 40, 50, 100, 150 or 200 μM) were incubated with pUC19 (400 ng) at 37 °C for 48 h before being analysed onto 1.3% agarose gels.

Figure IV.5: Design of the library of 19-nt TFOs targeting the *EGFR* gene and illustration of SPS and post-synthetic labelling.

Figure IV.6: Structure of the 40-mer target duplex, the labelled shorter target duplex with its 27-nt FAM-labelled target strand and 19-nt Cy5-labelled complementary strand and the *off*-target duplex that does not contain the triplex recognition domain.

Figure IV.7: PAGE analysis of the activity of monofunctional Pt-TFO hybrids B-1, B-3, P-1 and P-3 toward 40-mer target duplex and 29-mer *off*-target duplex across a gradient of Pt-TFO concentration (10, 25, 50 and 100 equivalents) in phosphate buffer after 48 h incubation at 37 °C.

Figure IV.8: Fluorescence recording of the melting temperature for DBCO, Pt-benzyl-DPA and Pt-propyl-DPA hybrids of TFO-1 and TFO-3 and associated first negative derivative, where the T_M is recorded as the temperature where the maximum is reached.

Figure IV.9: Denaturing PAGE experiment showing higher-order bands due to the adduct formation from monofunctional Pt-TFO hybrids B-1, B-3, P-1 and P-3 in the presence of the labelled short target duplex across a gradient of Pt-TFO concentration (10, 50 and 100 equivalents) in phosphate buffer. Lanes 49 and 56: 100 equivalents of DBCO-TFO-1 and DBCO-TFO-3 with labelled short target duplex showing impurities from the (unclicked) alkyne-TFOs.

Figure IV.10: Principe of the PEx inhibition experiment. The recovery of duplex in a control sample is compared to the recovery of duplex after adduct formation in the presence of Pt-TFO

hybrids. 5′-phosphorylate strand is digested by lambda exonuclease. The digestion product was then annealed with a primer and was used as a template for primer extension using vent(exo-) polymerase.

Figure IV.11: PAGE analysis of the PEx inhibition experiment in the presence of Pt-TFO hybrids. First, the underlying duplex (lanes 57, 61, 63, 65, 69 and 71) was digested by lambda exonuclease (lanes 58 and 66), then the primer was added (lanes 59 and 67) followed by the partial recovery of duplex upon primer extension (lanes 60, 62, 64, 68, 70 and 72), showing polymerase inhibition activity of the Pt-TFO hybrids. Densitometry was used to determine the intensity of the underlying duplex in the initial and final samples, and the ratio was plotted to quantify polymerase activity across Pt-TFO hybrids.

Figure V.1: Isolation of prodigiosin, tambjamine E and tetrapyrrole from marine bacteria.

Figure V.2: Reported[22] 3-step synthesis of 4-methoxy-1H,1′H-[2,2′-bipyrrole]-5-carbaldehyde (bi-pyrrole) starting from 4-chloro-3-methoxy-2-(E)-butenoic acid methyl ester.

Figure V.3: First series of attempt to synthesise an azide-functionalised pyrrole, starting from ethyl pyrrole-2-carboxylate.

Figure V.4: Second attempt to prepare an azide-functionalised pyrrole, starting from pyrrole-3-carboxylic acid.

Figure V.5: Proposed synthetic schemes for the preparation of two different amine-functionalised pyrroles for subsequent conversion to azide intermediates.

Figure V.6: First successful attempt for the coupling of bi-pyrrole with a monopyrrole in methanolic HCl.

Figure V.7: Preparation of N-(3-azzidepropyl)-2,4-diethyl-1H-pyrrole-3-carboxamide.

Figure V.8: Preparation of N_3-PD by coupling the bi-pyrrole moiety with N-(3-azidopropyl)-2,4-dimethyl-1H-pyrrol-3-carboxamide in methanolic HCl.

Figure V.9: Conversion of supercoiled (SC) DNA to open circular (OC) and linear (L) DNA upon single or double strand break.

Figure V.10: Cleavage of pUC19 with increasing amounts of [Cu(N_3-PD)(NO_3)$_2$] after 30, 60 or 90 min incubation (top to bottom) at 37 °C in HEPES buffer and NaCl, **a.** in the presence of Na-*L*-asc, and **b.** without Na-*L*-asc. Lanes 1, 11, 21, 31, 41 and 51: pUC19. Lanes 2 – 10, 12 – 20, 22 – 30, 32 – 40, 42 – 50, 52 – 60: pUC19 in the presence of 5, 10, 20, 25, 50, 75, 100, 150 or 200 µM of [Cu(N_3-PD)(NO_3)$_2$].

Figure V.11: PAGE analysis of the cleavage of dodecamers with varying A/T motifs, listed in the table on the right, by [Cu(N_3-PD)(NO_3)$_2$] to assess the sequence preference of the AMN. Lanes 61 – 64: dodecamer 1, lanes 65 – 68 : dodecamer 2, lanes 69 – 72: dodecamer 3, lanes 73-76: dodecamer 4, lanes 77 – 80: dodecamer 5, lanes 81 – 84: dodecamer 6 and lanes 85 – 88: dodecamer 7, in the presence of 100, 500 or 1000 eq. of [Cu(N_3-PD)(NO_3)$_2$].

Figure V.12: Structure of the 40-bp target and 29-bp *off*-target duplexes, design of the library of 19-nt TFOs targeting the *EGFR* gene and illustration of SPS and post-synthetic labelling.

Figure V.13: PAGE reporting the target specific triplex formation of 25, 50 or 100 eq. of hybrids in the presence of target and *off*-target duplexes. Target duplex (lanes 89 and 103), *off*-target duplex (lanes 90 and 104), and PD-1 (lanes 91-93), PD-2 (lanes 94-96), PD-3 (lanes 97-99), PD-4(100-102), Phen-1 (lanes 105-107), Phen-2 (lanes 108-110), Phen-3 (lanes 111-113) and Phen-4 (lanes 114-116) hybrids in the presence of both duplexes.

Figure V.14: Fluorescence recording of the melting temperature for DBCO, PD and Phen hybrids of TFO-2 and TFO-3 and associated first

negative derivative, where the T_M is recorded as the temperature where the maximum is reached.

Figure V.15: Native PAGE (TA) showing the attempts to cleave target duplexes with varying A/T composition on the overhang using PD-2 in the presence of increasing amounts of copper. Lanes 117 – 126: *EGFR* target duplex containing the triplex-binding region, lanes 127 – 136: duplex containing the triplex-binding region and with a 5 x TA overhang and lanes 137 – 146: duplex containing the triplex-binding region and with a 5 x AT overhang.

Figure V.16: **a.** Time-dependent self-activated target-specific cleavage activity of PD-2 in the presence of copper(II). **b.** Time-dependent Na-*L*-asc-mediated target specific cleavage activity of Phen-2 in the presence of copper(II). Lanes 147 and 154: target duplex, lanes 148 and 155: *off*-target duplex. Lane 149 both duplexes in the presence of PD-2, lanes 150-153: lane 149 + $Cu(NO_3)_2$ with increasing incubation time. Lane 156 both duplexes in the presence of Phen-2 and Na-*L*-asc, lanes 157-160: lane 156 + $Cu(NO_3)_2$ with increasing incubation time.

Figure V.17: **a**. Principle of the qPCR quantification of damage showing the difference between an undamaged amplicon and an amplicon that has been damaged. **b**. Evolution of the fold change over time illustrating the progressive damage of the amplicon caused by PD-2 in the presence of copper.

Figure VI.1: Synthesis of N_3-DPPZ and N_3-ImPhen according to the procedure reported by Lauria et al.[21]

Figure VI.2: Synthesis of N_3-PD and N_3-Phen according to the procedure reported in Chapter V.

Figure VI.3: Schematic representation of the self-assembly assay. The first step is the addition of the DBCO-TFO to the duplex for triplex formation, then N_3-ligand is added (N_3-PD, N_3-DPPZ, N_3-ImPhen, N_3-Phen or N_3-benzyl-DPA) and the SPAAC is performed using the duplex as a template. The final step is the

addition of a metal centre to initiate cleavage of the target duplex. All steps are performed in the same sample, without intermediate incubation time.

Figure VI.4: Structure of TFO-2 and TFO-3, 5mC, TO-modified dU and 5′-DBCO modifications, and target and *off*-target duplexes. TFO-2 has 1 TO modification away from the DBCO group and TFO-3 has 2 TO units, one away and one close to DBCO.

Figure VI.5: PAGE analysis showing the self-activated target specific cleavage activity of self-assembled PD-TFO-2 (left) and PD-TFO-3 (right) in the presence of copper. Lanes 1 and 6: target duplex, lanes 2 and 7: *off*-target duplex, lane 3: both duplexes + DBCO-TFO-2, lane 4: lane 3 + N_3-PD, lane 5: lane 4 + $Cu(NO_3)_2$, lane 8: both duplexes + DBCO-TFO-3, lane 9: lane 8 + N_3-PD and lane 10: lane 9 + $Cu(NO_3)_2$.

Figure VI.6: PAGE analysis showing the self-activated target specific cleavage activity of self-assembled PD-TFO-2 in the presence of different metals. Lane 11: target duplex, lane 12: *off*-target duplex, lane 13: both duplexes + DBCO-TFO-2, lane 14: lane 13 + N_3-PD, lane 15: lane 14 + $Cu(NO_3)_2$, lane 16: lane 15 + Na-*L*-asc, lane 17: lane 14 + $FeCl_3$, lane 18: lane 17 + Na-*L*-asc, lane 19: lane 14 + $Zn(OAc)_2$ and lane 20: lane 14 + $Mn(OAc)_2$.

Figure VI.7: **a**. Cartoon representation of the concept of the experiment where PAGE gels are run with cleavage samples at different time points. Densitometry is then used to measure a ratio of intensity for each ligand at each exposure interval. The table in this figure does not reflect any specific result. **b**. Heat map representation of the score for targeted cleavage activity of self-assembled AMN-TFO hybrids in the presence of copper(II) ions. The score was calculated using Formula 1 for each ligand (PD, DPPZ, ImPhen, Phen and benzyl-DPA) at each time point (3, 6, 18 and 24 h). The targeted cleavage activity of DPPZ-, ImPhen-, Phen- and benzyl-DPA-TFO hybrids was measured in the presence of Na-*L*-asc.

Figure A.1.1 ^{1}H-NMR of 3-(5-carboxypentyl)-2-methylbenzo[d]thiazol-3-ium bromide.

Figure A.1.2 ^{1}H-NMR of 4-chloro-1-methylquinolin-1-ium trifluoromethanesulfonate.

Figure A.1.3 ^{1}H-NMR of (E)-3-(5-carboxypentyl)-2-((1-methylquinolin-4(1H)-ylidene)methyl)benzo[d]thiazol-3-ium hexafluorophosphate (TO_{B6}).

Figure A.1.4.1 ^{1}H-NMR of (E)-3-(6-((2,5-dioxopyrrolidin-1-yl)oxy)-6-oxohexyl)-2-((1-methylquinolin-4(1H)-ylidene)methyl)benzo[d]thiazol-3-ium hexafluorophosphate (NHS ester TO_{B6}).

Figure A.1.4.2 IR spectrum of (E)-3-(6-((2,5-dioxopyrrolidin-1-yl)oxy)-6-oxohexyl)-2-((1-methylquinolin-4(1H)-ylidene)methyl)benzo[d]thiazol-3-ium hexafluorophosphate (NHS ester TO_{B6}).

Figure A.1.4.3 ESI-MS of (E)-3-(6-((2,5-dioxopyrrolidin-1-yl)oxy)-6-oxohexyl)-2-((1-methylquinolin-4(1H)-ylidene)methyl)benzo[d]thiazol-3-ium hexafluorophosphate (NHS ester TO_{B6}).

Figure A.1.5 ^{1}H-NMR of Di-tert-boc-2-hydroxy-1,3-diaminopropane.

Figure A.1.6 ^{1}H-NMR of Di-tert-boc-2-methanesulfonyl-1,3-diaminopropane.

Figure A.1.7 ^{1}H-NMR of Di-tert-boc-2-azido-1,3-diaminopropane.

Figure A.1.8.1 ^{1}H-NMR of 2-azidopropane-1,3-diamine dihydrochloride.

Figure A.1.8.2 IR spectrum of 2-azidopropane-1,3-diamine dihydrochloride.

Figure A.1.9.1 ^{1}H-NMR of *cis*-[Pt(2-azidopropane-1,3-diamine)(Oxalate)] (Pt-N_3-Oxali).

Figure A.1.9.2 ^{195}Pt-NMR of *cis*-[Pt(2-azidopropane-1,3-diamine)(Oxalate)] (Pt-N_3-Oxali) with polynomial baseline correction.

Figure A.1.9.3 ^{195}Pt-NMR of *cis*-[Pt(2-azidopropane-1,3-diamine)(Oxalate)] (Pt-N_3-Oxali).

Figure A.1.9.4 IR spectrum of *cis*-[Pt(2-azidopropane-1,3-diamine)(Oxalate)] (Pt-N_3-Oxali).

Figure A.1.9.5 ESI-MS of *cis*-[Pt(2-azidopropane-1,3-diamine)(Oxalate)] (Pt-N_3-Oxali).
Figure A.2.1 HPLC trace of C1-O.
Figure A.2.2 MS chromatogram of C1-O.
Figure A.2.3 HPLC trace of C2-O.
Figure A.2.4 MS chromatogram of C2-O.
Figure A.2.5 HPLC trace of C3-O.
Figure A.2.6 MS chromatogram of C3-O.
Figure A.2.7 HPLC trace and MS chromatogram of S1-O.
Figure A.2.8 HPLC trace and MS chromatogram of S2-O.
Figure A.2.9 HPLC trace of S3-O.
Figure B.1.1: ^{1}H-NMR of platinum (II) (N-(4-azidobenzyl)-1-(pyridin-2-yl)-N-(pyridin-2-ylmethyl)methanamine) chloride (Pt-N_3-benzyl-DPA) in DMSO-d_6.
Figure B.1.2: ^{13}C-NMR of platinum(II) (N-(4-azidobenzyl)-1-(pyridin-2-yl)-N-(pyridin-2-ylmethyl)methanamine) chloride (Pt-N_3-benzyl) in DMSO-d_6.
Figure B.1.3: ^{195}Pt-NMR of platinum(II) (N-(4-azidobenzyl)-1-(pyridin-2-yl)-N-(pyridin-2-ylmethyl)methanamine) chloride (Pt-N_3-benzyl) in DMSO-d_6.
Figure B.1.4: IR spectrum of platinum(II) (N-(4-azidobenzyl)-1-(pyridin-2-yl)-N-(pyridin-2-ylmethyl)methanamine) chloride (Pt-N_3-benzyl).
Figure B.1.5: ESI-MS of platinum(II) (N-(4-azidobenzyl)-1-(pyridin-2-yl)-N-(pyridin-2-ylmethyl)methanamine) chloride (Pt-N_3-benzyl).
Figure B.1.6: ^{1}H-NMR of 3-azidopropyl-1-amine in DMSO-d_6.
Figure B.1.7: ^{1}H-NMR of 3-azido-N,N-bis(pyridin-2-ylmethyl)propan-1-amine (N_3-propyl-DPA) in DMSO-d_6.
Figure B.1.8: ^{13}C-NMR of 3-azido-N,N-bis(pyridin-2-ylmethyl)propan-1-amine (N_3-propyl-DPA) in DMSO-d_6.
Figure B.1.9: IR spectrum of 3-azido-N,N-bis(pyridin-2-ylmethyl)propan-1-amine (N_3-propyl-DPA).
Figure B.1.10: ESI-MS of 3-azido-N,N-bis(pyridin-2-ylmethyl)propan-1-amine (N_3-propyl-DPA).

Figure B.1.11: ^{1}H-NMR of platinum (II) (3-azido-N,N-bis(pyridin-2-ylmethyl)propan-1-amine) chloride (Pt-N_3-propyl) in DMSO-d_6.
Figure B.1.12: ^{13}C-NMR of platinum(II) (3-azido-N,N-bis(pyridin-2-ylmethyl)propan-1-amine) chloride (Pt-N_3-propyl) in DMSO-d_6.
Figure B.1.13: ^{195}Pt-NMR of platinum(II) (3-azido-N,N-bis(pyridin-2-ylmethyl)propan-1-amine) chloride (Pt-N_3-propyl) in DMSO-d_6.
Figure B.1.14: IR spectrum of platinum(II) (3-azido-N,N-bis(pyridin-2-ylmethyl)propan-1-amine) chloride (Pt-N_3-propyl).
Figure B.1.15: ESI-MS of platinum(II) (3-azido-N,N-bis(pyridin-2-ylmethyl)propan-1-amine) chloride (Pt-N_3-propyl).
Figure B.2.1: HPLC trace and MS chromatogram of B-1.
Figure B.2.2: HPLC trace and MS chromatogram of B-2.
Figure B.2.3: HPLC trace of B-3.
Figure B.2.4: HPLC trace and MS chromatogram of B-4.
Figure B.2.5: HPLC trace and MS chromatogram of P-1.
Figure B.2.6: HPLC trace and MS chromatogram of P-2.
Figure B.2.7: HPLC trace of P-3.
Figure B.2.8: MS chromatogram of P-4.
Figure B.2.9: HPLC trace and MS chromatogram of O-1.
Figure B.2.10: HPLC trace and MS chromatogram of O-2.
Figure B.2.11: HPLC trace and MS chromatogram of O-3.
Figure B.3.1: PAGE analysis of SPAAC-generated hybrids.
Figure B.3.2: PAGE analysis of the triplex formation activity of B-2, B-4, P-2 and P-4.
Figure B.3.3: Denaturing PAGE control experiments **a**. showing higher bands presents in TFO-1, TFO-3, B-1, B-3, P-1 and P-3 (100 eq.) with no prior incubation and **b**. showing the adduct formation from Oxali-TFO hybrids O-1 and O-3 in the presence of the labelled short target duplex across a gradient of Pt-TFO concentration (10, 50 and 100 equivalents) in phosphate buffer.
Figure B.3.4: PAGE gels showing the stepwise PEx inhibition experiment for each Pt-TFO hybrid, B-1, P-1, O-1, B-3, P-3 and O-3.

Figure B.3.5: PAGE gel showing the negative control for he PEx inhibition experiment, in the absence of TFO (left), in the presence of DBCO-TFO-1 (middle) or DBCO-TFO-3 (right). The migration of the long target strand is shown in lane 149. 5′-phosphate modified duplex (lane 150) is exposed to lambda exonuclease (lane 151) before addition of the primer (lane 152) and finally vent(exo-) (lane 153, showing recovery of the duplex lane. The same is repeated in the presence of DBCO-TFO-1 (lanes 154-157) and DBCO-TFO-3 (lanes 158-161) showing less duplex recovery.

Figure C.1.1: ^{1}H NMR of 4-methoxy-3-pyrrolin-2-one in $CDCl_3$.

Figure C.1.2: ^{1}H NMR of N-((5-bromo-3-methoxy-2H-pyrrol-2-ylidene)methyl)-N-ethylethanamine in $CDCl_3$.

Figure C.1.3: ^{1}H NMR of 4-methoxy-1H,1'H-[2,2'-bipyrrole]-5-carbaldehyde in DMSO-d_6.

Figure C.1.4: ^{1}H NMR of 3-azidopropyl-1-amine in DMSO-d_6.

Figure C.1.5.1: ^{1}H NMR of N-(3-azidopropyl)-2,4-dimethyl-1H-pyrrole-3-carboxamide in $CDCl_3$.

Figure C.1.5.2: IR spectrum of N-(3-azidopropyl)-2,4-dimethyl-1H-pyrrole-3-carboxamide.

Figure C.1.6.1: ^{1}H NMR of N-(3-azidopropyl)-5-((4'-methoxy-1H,5'H-[2,2'-bipyrrol]-5'-ylidene)methyl)-2,4-dimethyl-1H-pyrrole-3-carboxamide (N_3-PD) in MeOD.

Figure C.1.6.2: ^{13}C NMR of N-(3-azidopropyl)-5-((4'-methoxy-1H,5'H-[2,2'-bipyrrol]-5'-ylidene)methyl)-2,4-dimethyl-1H-pyrrole-3-carboxamide (N_3-PD) in MeOD.

Figure C.1.6.3: IR spectrum of N-(3-azidopropyl)-5-((4'-methoxy-1H,5'H-[2,2'-bipyrrol]-5'-ylidene)methyl)-2,4-dimethyl-1H-pyrrole-3-carboxamide (N_3-PD).

Figure C.1.6.4: MS chromatogram of N-(3-azidopropyl)-5-((4'-methoxy-1H,5'H-[2,2'-bipyrrol]-5'-ylidene)methyl)-2,4-dimethyl-1H-pyrrole-3-carboxamide (N_3-PD).

Figure C.1.7.1: ^{1}H NMR of 5-azido-1,10-phenanthroline in $CDCl_3$.

Figure C.1.7.2: ^{13}C NMR of 5-azido-1,10-phenanthroline in $CDCl_3$.

Figure C.2.1: HPLC trace and MS chromatogram of PD-1.
Figure C.2.2: MS chromatogram of PD-2.
Figure C.2.3: HPLC trace and MS chromatogram of PD-3.
Figure C.2.4: MS chromatogram of PD-4.
Figure C.2.5: HPLC trace and MS chromatogram of Phen-1.
Figure C.2.6: MS chromatogram of Phen-2.
Figure C.2.7: HPLC trace and MS chromatogram of Phen-3.
Figure C.2.8: HPLC trace and MS chromatogram of Phen-4.
Figure C.3.1: Agarose gels showing the impact of ROS scavengers on the cleavage activity of [Cu(N_3-PD)(NO_3)$_2$] a. in the presence of Na-*L*-asc (lanes 161 to 198, concentration of 5, 10, 20 or 25 µM) and b. without Na-*L*-asc (lanes 199 to 237, concentrations of 10, 25, 50 or 100 µM).
Figure C.3.2: Agarose gel showing the impact of major and minor groove binders on the self-activated cleavage activity of [Cu(N_3-PD)(NO_3)$_2$]. Lanes 243 – 246: in the presence of methyl green, lanes 247 – 251: in the presence of netropsin.
Figure D.1.1: ^{1}H NMR spectrum of 1,10-phenanthroline-5,6-dione.
Figure D.1.2: ^{1}H NMR spectrum of nitro DPPZ.
Figure D.1.3: ^{1}H NMR spectrum of amino DPPZ.
Figure D.1.4: ^{1}H NMR spectrum of azido DPPZ.
Figure D.1.5: ^{1}H NMR spectrum of nitro ImPhen.
Figure D.1.6: ^{1}H NMR spectrum of amino ImPhen.
Figure D.1.7: ^{1}H NMR spectrum of azido ImPhen.
Figure D.2.: PAGE analysis showing the target-specific cleavage activity of self-assembled TFO-2 hybrids in the presence of copper, using N_3-PD, N_3-Phen, N_3-DPPZ, N_3-ImPhen or N_3-benzyl-DPA. Except for PD hybrids (lanes 21 - 37), all lanes contain 1 mM Na-*L*-asc. Lane 21: target duplex. Lane 22 *off*-target duplex. Lanes 23, 28, 33: target + *off*-target duplex + TFO-2 + N_3-PD. Lanes 24 - 27, 29 - 32, 34 - 37: lanes 23, 28, 33 + $Cu(NO_3)_2$ with 3, 6, 18 or 24 h incubation. Lanes 38, 55, 72 and 89 : target duplex + Na-*L*-asc. Lanes 39, 56, 73 and 90: *off*-target duplex + Na-*L*-asc. Lanes 40, 45 and 50: target +

off-target duplex + TFO-2 + N_3-Phen + Na-*L*-asc. Lanes 41 - 44, 46 - 49, 51 - 54: lanes 40, 45 and 50 + $Cu(NO_3)_2$ with 3, 6, 18 or 24 h incubation. Lanes 57, 62 and 67: target + *off*-target duplex + TFO-2 + N_3-DPPZ + Na-*L*-asc. Lanes 58 - 61, 63 - 66, 68 - 71: lanes 57, 62 and 67 + $Cu(NO_3)_2$ with 3, 6, 18 or 24 h incubation. Lanes 74, 79 and 84: target + *off*-target duplex + TFO-2 + N_3-ImPhen + Na-*L*-asc. Lanes 75 - 78, 80 - 83, 85 - 88: lanes 74, 79 and 84 + $Cu(NO_3)_2$ with 3, 6, 18 or 24 h incubation. Lanes 91, 96 and 101: target + *off*-target duplex + TFO-2 + N_3-benzyl-DPA + Na-*L*-asc, lanes 92 - 95, 97 - 100, 102 - 105: lanes 91, 96 and 101 + $Cu(NO_3)_2$ with 3, 6, 18 or 24 h incubation.

6 Table of Tables

Table III.1: Calculated and observed mass for CuAAC- and SPAAC-generated Pt-Oxali-TFO hybrids.

Table IV.1: Calculated and measured mass for TFO hybrids. The mass of the hybrids was calculated both I the presence of the labile chloride ligand (left), and without (right).

Table V.1: Temperature of cycles for PCR amplification.

Table V.2: ROS scavengers used in this study and their associated ROS.

Table V.3: Calculated and measured mass for TFO hybrids.

7 List of Abbreviations

5mC	5-methylcytosine
^{13}C NMR	Carbon-13 nuclear magnetic resonance
^{1}H NMR	proton nuclear magnetic resonance
A	Adenine
AMN	Artificial metallo-nuclease
APS	Ammonium persulfate
bp	Base pair
BPL-C6	Bis-1,10-phenanthroline-carbon-6
C	Cytosine
$CDCl_3$	Deuterated chloroform
Cp	Crossing point
CRISPR	Clustered Regularly Interspaced Short Palindromic Repeats
CuAAC	Copper-catalysed azide-alkyne cycloaddition
Cy5	Cyanine-5
DBCO	5′-dibenzocyclooctone
DCC	Dicyclohexylcarbodiimide
DCM	Dichloromethane
DCU	Dublin City University
DI H_2O	Deionised water
DIPEA	Diisopropylethylamine
DMF	Dimethylformamide
DMSO	Dimethyl sulfoxide
DMSO-d_6	Deuterated dimethyl sulfoxide
DMTU	Dimethylthiourea
DNA	Deoxyribonucleic acid
dNTP	Deoxy*N*triphosphate, *N* = adenine, thymine, guanine or cytosine
DPA	Di-(2-picolyl)amine
DPPN	Benzo[*i*]dipyrido[3,2-*a*:2′,3′-*c*]phenazine

DPPZ	Dipyridophenazine
DPQ	Dipyridoquinoxaline
Dr.	Doctor
dsDNA	Double-stranded deoxyribonucleic acid
dU	Deoxyuracil
EDTA	Ethylenediaminetetraacetic
EGFR	Epidermal growth factor receptor gene
Eng	Engineer
ESI	Electrospray ionisation
ETN	European Training Network
FAM	Fluorescein
FDA	Food and Drug Administration
FTIR	Fourier-transform infrared spectroscopy
G	Guanine
GFP	Green fluorescent protein gene
HBTU	Hexafluorophosphate Benzotriazole Tetramethyl Uronium
HEPES	N-2-hydroxyethylpiperazine-N-2-ethane sulfonic acid
HIV	Human immunodeficiency virus
HPLC	High-performance liquid chromatography
ImPhen	Imidazophenanthroline
IPA	Isopropyl alcohol
IR	Infrared Spectroscopy
IEx-HPLC	Ionic exchange high-performance liquid chromatography
L	Linear
LED	Light emitting diode
M.Sc	Master of Science
MeOH	Methanol

mRNA	Messenger ribonucleic acid
MS	Mass spectrometry
Na-*L*-asc	Sodium-*L*-ascorbate
NCI	National Cancer Institute
NHS	N-hydroxysuccinimide
NMR	Nuclear magnetic Resonance
NSCLC	Non-small cell lung cancer
nt	Nucleotide
OC	Open circular
Oda	Octanedioate
PAGE	Polyacrylamide gel electrophoresis
PCR	Polymer chain reaction
PD	Prodigiosin
PEX	Primer extension
PhD	Doctor pf Philosophy
Phen	1,10-phenanthroline
PMO	Phosphorodiamidate morpholino oligomers
PNA	Peptide nucleic acid
PPC	Polynuclear platinum complexes
Prof.	Professor
qPCR	Real-time polymer chain reaction
r.t.	Room temperature
RNA	Ribonucleic acid
ROS	Reactive oxygen species
RP-HPLC	Reverse-phase high-performance liquid chromatography
RSC	Royal Society of Chemistry
SAR	Structure-activity relationship
SC	Supercoiled

SDS	Sodium dodecyl-sulfate
sgRNA	Single guide RNA
SNI-PEX	Single nucleotide incorporation primer extension
SPAAC	Strain-promoted azide-alkyne cycloaddition
SPS	Solid phase synthesis
ssDNA	Single-stranded deoxyribonucleic acid
T	Thymine
TA	Tris-acetate
TAB	Trimethylammonium bicarbonate
TAE	Tris-acetate-EDTA
TALE	Transcription Activator-Like Effector
TALENs	Transcription Activator-Like Effector Nucleases
TBE	Tris-borate-EDTA
TEMED	N, N, N', N'-tetramethylethylenediamine
TEMPO	(2,2,6,6-Tetramethylpiperidin-1-yl)oxyl
Terph	Terephthalate
TFO	Triplex-forming oligonucleotide
THF	Tetrahydrofuran
THPTA	*Tris*-hydroxypropyltriazolylmethylamine
T_M	Melting temperature
TO	Thiazole Orange
TPMA	*Tris*-(2-pyridylmethyl)amine
U	Uracil
UCD	University College Dublin
Z	6-amino-5-nitropyridin-2-one
ZFN	Zinc finger nuclease

8 Abstract

Metallated Triplex-Forming Oligonucleotides as Inducers of Sequence-Selective Chemical Modifications

Malou Coche

Since the discovery of the anticancer activity of cisplatin, many metal complexes have been investigated for gene-targeting therapies, such as monofunctional platinum(II) complexes or copper-based artificial metallo-nucleases (AMNs). Monofunctional platinum(II) complexes have shown gene silencing activity alternative to traditional *cis*-platinum(II) complexes, while copper-AMNs are known to oxidatively cleave DNA. The cleavage activity is often dependent on the introduction of a reductant, but some ligands, such as the marine alkaloid prodigiosin, display 'self-activated' or unattended cleavage activity. Although DNA targeting metallodrugs often lack specificity, recent literature has shown that this can be remediated through their covalent attachment to triplex-forming oligonucleotides (TFOs) using click chemistry. However, the efficacy of the resulting hybrids is hampered by endogenous DNA repair mechanisms and low triplex stability. It also remains to be established whether robust DNA interactions can be achieved with bulkier monofunctional platinum(II)-TFO conjugates, or if self-activated, triplex-mediated cleavage can lead to more efficient DNA degradation.

Here, we report the design and synthesis of novel *EGFR*-targeting TFO hybrids using both azide-functionalised prodigiosin analogues and monofunctional platinum(II) complexes, conjugated *via* strain-promoted azide-alkyne cycloaddition (SPAAC). After optimising TFOs for triplex recognition and conjugation efficacy, the activity of the resulting hybrids was comprehensively characterised. Using PAGE, their target-specific interactions with duplex DNA were visualised, while Primer Extension assays qualitatively determined the inhibition of enzymatic activity of Pt(II)-TO hybrids following triplex formation. Our findings demonstrate that prodigiosin-TFO hybrids achieve significant self-activated and target-specific DNA cleavage in the presence of copper, leading to potent gene silencing activity. Conversely, monofunctional platinum(II)-TFO hybrids exhibit robust target-specific DNA interaction, effectively inhibiting downstream enzymatic activity. This work establishes a promising platform for developing new metallodrug conjugates to overcome resistance mechanisms in targeted cancer therapy.

Chapter I

Introduction

April 2026

1 Introduction

Deoxyribonucleic acid (DNA), the carrier of genetic information, adopts a double helical structure (Figure I.1.a), first elucidated in 1953 by Watson and Crick,[1] Franklin,[2] and Wilkins.[3] Each strand is composed of a sugar-phosphate backbone, and strands interact together through hydrogen bond complementary base pairing between purine (adenine (A) or guanine (G)) and pyrimidine (thymine (T) or cytosine (C)) nucleobases (Figure I.1.b). The sequence of DNA and its recognition by enzymes underpin replication and transcription processes, central to gene expression and cellular regulation. Briefly, DNA is transcribed by RNA polymerase,[4] which produces complementary RNA that contains a 2′-hydroxyl group on the ribose unit and uracil (U) in place of T.[5] The RNA is spliced to remove introns, leaving only exons for recognition by ribosomes during translation, thereby expressing proteins. Mutations within DNA can disrupt these mechanisms, potentially leading to aberrant protein production or disease progression.[6] Gene silencing aims to target genetic disorders to prevent protein expression from a compromised gene.[7] This can be achieved by cleavage or interaction of molecules with DNA to prevent cellular machinery recognition.[8]

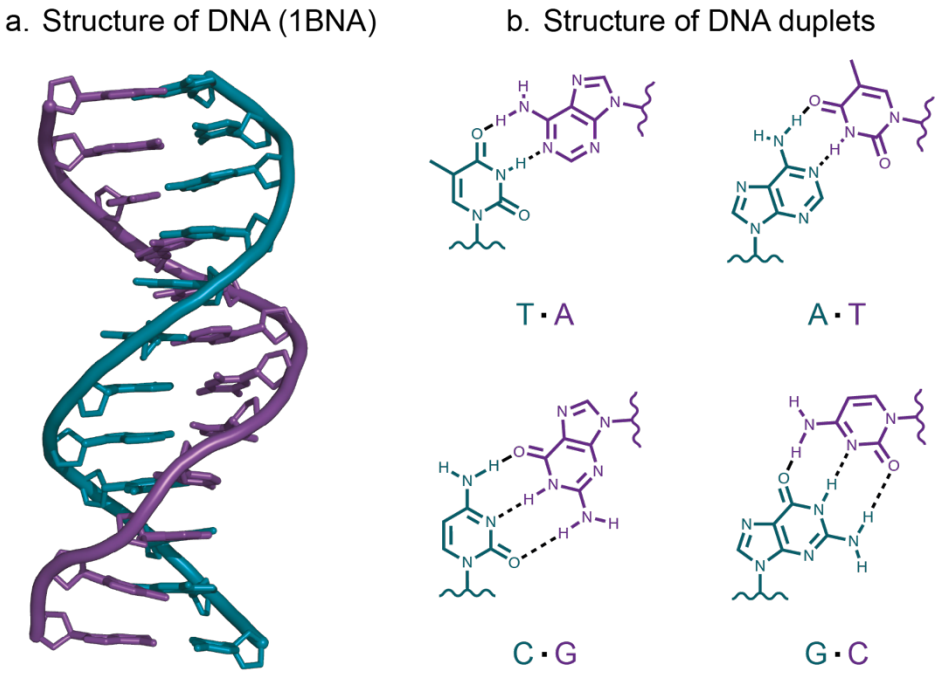


Figure I.1: **a**. Structure of B DNA (1BNA). **b**. Structure of DNA duplets showing Watson-Crick hydrogen bonds between nucleobases.

The unique structure of DNA affords many diverse non-covalent ligand interactions, including; i) major or minor groove binding; ii) intercalation between base pairs; and iii) electrostatic interaction with the negatively charged backbone[9] (Figure I.2). The asymmetric binding mode of nucleobases is responsible for the presence of a major and a minor groove on B-DNA.[1] Groove binding compounds typically contain unfused aromatic rings that maintain rotational freedom, thereby allowing the molecules to fit into the major or minor groove of DNA, without significantly disturbing the DNA structure.[10] DNA intercalators, on the other hand, usually display fused aromatic rings resulting in planar compounds that are able to insert between two base pairs. Intercalation does not interfere with Watson-Crick hydrogen bonds but results in local unwinding of the DNA.[11] Intercalating ligands are frequently employed in metal drug design due to their ability to anchor reactive centres within the DNA helix. Some compounds combine intercalation with groove binding, resulting in threading intercalation, which is often paired with slow binding constant.[12, 13] Electrostatic interactions are also observed, due to the high density of negative charge on the DNA backbone. Many DNA conformations rely on counterion stabilization, where the presence of a metal cation is necessary for stability.[14] DNA strands can also adopt higher-order structures

such as DNA triplexes,[15] G-quadruplexes,[16] i-motifs,[17] three-way junctions[18] and Holliday junctions.[19] These structures are involved in many biological processes and are a valuable target for nucleic acid therapies.[20] Understanding how ligand architecture dictates these interactions is therefore essential for the rational design of gene-targeting agents.

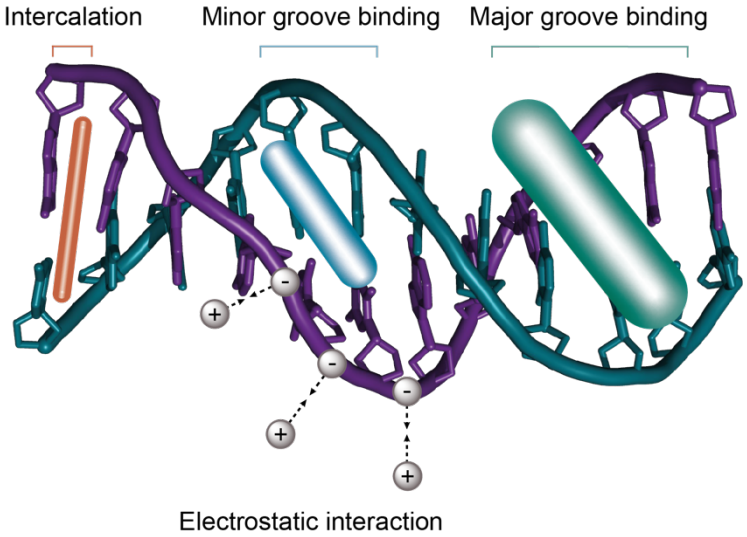


Figure I.2: Common non-covalent B-DNA binding modes showing major and minor groove binding, intercalation, and electrostatic interaction.

1.1 Interaction of metal complexes with DNA

1.1.1 Use of metals in medicine

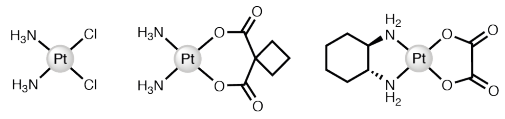
Metals play indispensable biological roles as cofactors, or structural elements and are found as: i) insoluble metal salts (e.g. calcium salts composing bones[21]); ii) soluble aqueous ions that are required for several regulatory processes (e.g. calcium[22] and magnesium[23] involved in cell signalling); or iii) complexes bearing biological ligands or large molecules (e.g. iron,[24] zinc,[25] or copper[26] involved in enzymatic functions).[27] Yet, their intrinsic reactivity also imparts cytotoxic potential,[28] which has long been exploited in medicine as displayed in: i) bismuth salts for the treatment of dyspepsia emerging around 1780;[29] ii) gold cyanides that were initially investigated for the treatment of tuberculosis by Robert Koch in the early 20th century[30] and later lead to the discovery of Auranofin,[31] a second generation gold compound that was used to treat rheumatoid arthritis;[32] iii) arsenic compounds including Ehrlich's Salvarsan discovered in 1909 and used to treat syphilis;[33] or iv) antimony drugs that were the main treatment for decades for leishmaniasis (e.g.

Pentostam).[34] The therapeutic use of metal complexes relies on exploiting their properties while controlling their toxicity, a balance achieved most notably in platinum-based anticancer drugs.[35]

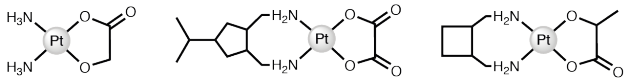
1.1.2 Platinum-based anticancer agents

Cisplatin is a square planar *cis*-platinum(II) complex (Figure I.3.a) that can crosslink DNA through the covalent binding of the N7 positions of two adjacent purine nucleobases. This crosslink results in distortion of the double-helix DNA, which prevents enzymatic activity, thereby triggering gene silencing and cell-death.[36, 37] Cisplatin preferably crosslinks two intrastrand guanines, but some intrastrand guanine and adenine, as well as a small fraction of interstrand guanine crosslinks have been observed (Figure I.3.b). Since cisplatin received FDA approval in 1978 for the chemotherapeutic treatment of cancer, two more *cis*-platinum(II) drugs have been approved worldwide, carboplatin and oxaliplatin, while nedaplatin, heptaplatin and lobaplatin have been approved regionally in Asia[38] (Figure I.3.a). Structure-Activity Relationship (SAR) studies of *cis*-platinum(II) complexes revealed the importance of the square-planar coordination geometry, the neutral overall charge, the presence of two labile ligands positioned *cis* to one another, as well as two inert ligands in the remaining coordination sites.[39] Overall, *cis*-platinum(II) drugs are the most widely used chemotherapeutic agents for cancer treatment. Despite their wide use, *cis*-platinum(II) agents can be affected by acquired platinum resistance in cancer cells[40] and are usually associated with many side effects stemming from dose limiting toxicity profiles such as nephrotoxicity.[41]

a. cis-platinum(II) drugs approved for cancer treatment



Cisplatin Carboplatin Oxaliplatin



Nedaplatin Heptaplatin Lobaplatin

b. Adducts formed by the crosslinking of cis-platinum(II) to purines

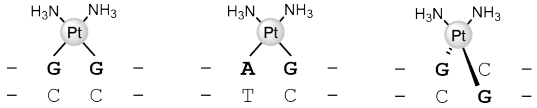


Figure I.3: **a**. Structure of clinically approved *cis*-platinum(II) anticancer agents. **b**. Adducts generated by *cis*-platinum(II) crosslinking on two intrastrand guanines, intrastrand adenine and guanine, and interstrand guanines.

To limit *off*-target effects, platinum(IV) pro-drugs have been developed, based on the principle that platinum(IV) is kinetically inert, therefore significantly less toxic than platinum(II), and can be activated by the reducing environment at the tumour site. The reduction of Pt(IV) to Pt(II) changes the geometry of the complex from six-coordinate octahedral to four-coordinate square planar geometry[42] (Figure I.4.a). Platinum(IV) can therefore be functionalized with a variety of bio-active ligands on the axial position, that are released upon reduction, together with the cytotoxic Pt(II) complex. So far, four Pt(IV) drugs have entered clinical trials: tetraplatin;[43, 44] LA-12;[45, 46] iproplatin;[47] and satraplatin[48] (Figure I.4.b), showing the emerging potential of platinum(IV) based therapeutics.

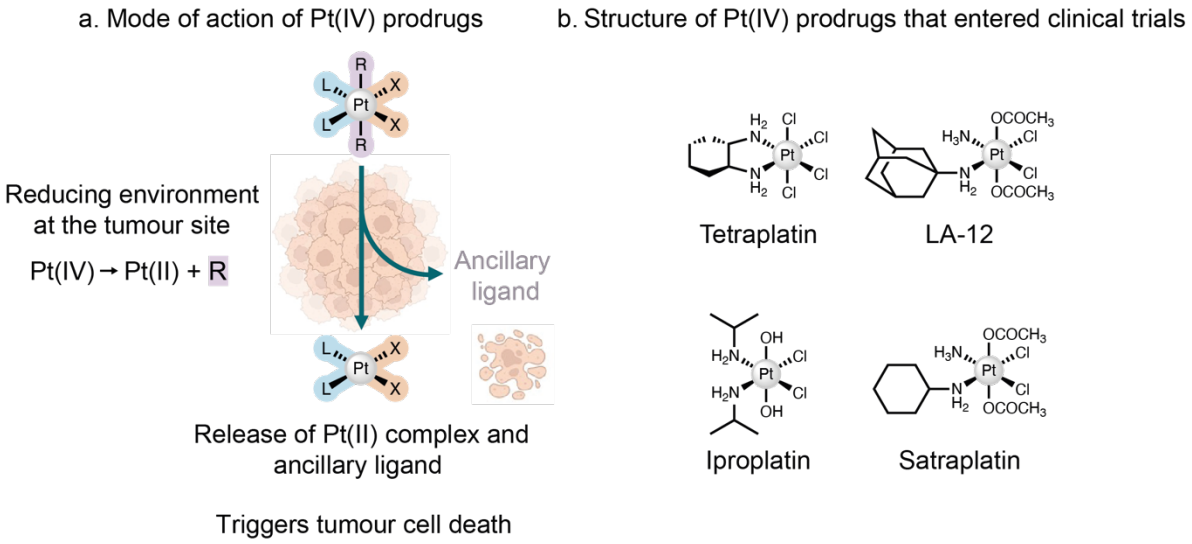
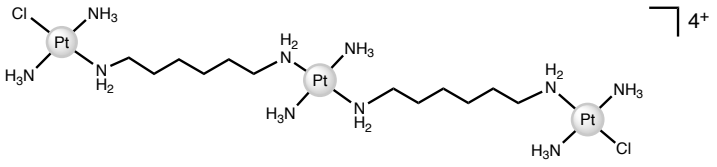


Figure I.4: **a**. Reduction of platinum(IV) with non-leaving group ligands (L), leaving group ligands (X) and axial ligands (R) to platinum(II), releasing axials ligands at tumour site. **b**. Structure of platinum(IV) drug candidates that entered clinical trials.

A second example of non-*cis*-platinum(II) platinum complexes that have entered clinical trials are the polynuclear platinum complexes (PPCs). BBR3464 (Triplatin, Figure I.5) is a trinuclear Pt(II) complex that engages in long-range crosslinking driven by two labile ligands coordinated to each terminal Pt(II), developed by Farrell and co-workers.[49] BBR3464 showed anticancer activity in a broad spectrum of cancer cell-lines that differs from that of *cis*-platinum(II) drugs,[50] and entered clinical trials. Phase I was successful in identifying the maximum tolerated dose[51] and showed promising results on breast cancer for the combination of BBR3464 with 5-fluorouracil[52] but clinical trials were stop in phase II due to pharmacokinetic issues.[53]



BBR3464 (triplatin)

Figure I.5: Structure of a trinuclear platinum(II) complex, BBR3464 (triplatin) developed by Farrell and co-workers.[49]

Some PPCs, such as the fully *trans*-symmetric, non-covalent TriplatinNC[54] complex and its recently reported trackable derivative, N_3-TriplatinNC,[55] display a unique mode of action, called the phosphate clamp (Figure I.6), that differs from that of Pt(II) and Pt(IV) complexes. This binding

mode is defined by well-spaced positively charged square planar platinum nuclei interacting with the negatively charged non-bridging oxygen atoms on the phosphate group of DNA backbone. The electrostatic interaction is accompanied by minor groove spanning and backbone tracking and can result in DNA condensation through interaction of one PPC with more than one DNA molecules.[56] NCI-60 profiling showed that trinuclear PPCs produce activity fingerprints that do not overlap with cisplatin, characteristic of a distinct cytotoxicity signature, supporting a novel mechanism of action and motivating continued exploration of these scaffolds as DNA-targeting agents and trackable probes.[55]

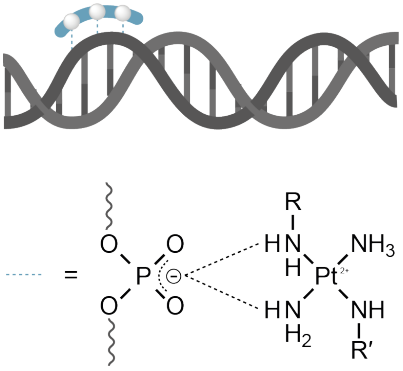


Figure I.6: Schematic representation of the phosphate clamp binding mode of PPCs.

Another promising class of platinum complexes for cancer treatment is the monofunctional platinum(II) class. Interestingly, these complexes do not adhere to traditional SAR studies related to *cis*-platinum(II), and therefore were not expected to display any DNA-binding activity.[39] However, they have shown some potential as anticancer agents. The first monofunctional platinum(II) compounds that were reported had the general formula $[Pt(NH_3)_2(Am)Cl]^+$ (where Am = either a heterocyclic amide based on pyridine, pyrimidine, purine or piperidine, or a saturated amine ligand), and showed activity that differs from that of *cis*-platinum(II).[57] Pyriplatin and phenanthriplatin (Figure I.7.a) were submitted for NCI-60 screening and targeted different cancer cell lines than cisplatin and its analogues, suggesting a distinct mode of action from the traditional bifunctional crosslinking.[58, 59] The promising activity displayed by pyriplatin lead to the development of Phenanthriplatin, where the pyridine ligand is replaced with a bulkier intercalating ligand, phenanthridine. This drug candidate showed higher cellular uptake than cisplatin, was less subject to

inactivation by biomolecules, and was efficient at inhibiting transcription.[59] It has been predicted that upon binding to DNA—through the empty coordination site after the loss of the chloride ligand—the bulkier group on the complex intercalates DNA and further impedes the activity of enzymes (figure I.7.b).[40] Consequently, monofunctional platinum(II) complexes have been developed bearing groups with increasing steric hinderance and capable of intercalating DNA.

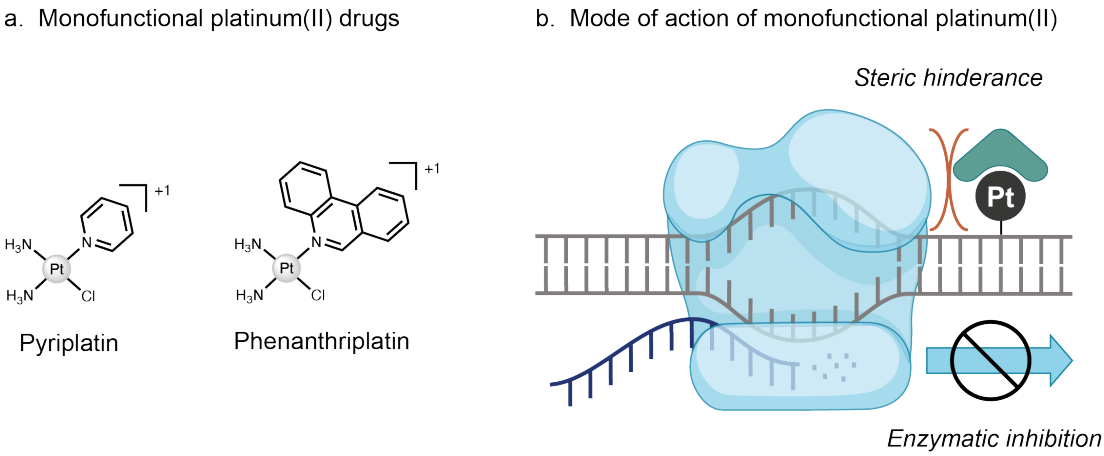


Figure I.7: **a**. Structure of pyriplatin and phenanthriplatin, two promising monofunctional platinum(II) anticancer agents. **b**. Inhibition of enzymatic activity by monofunctional platinum(II) assisted by steric repulsion by the ligand.

Collectively, these studies demonstrate the structural adaptability of platinum complexes and their capacity for diverse DNA interactions. However, despite their clinical success, Pt(II)-based drugs remain limited by systemic toxicity due to a lack of gene-level specificity. While emerging monofunctional Pt(II) systems offer an opportunity to combine Pt(II)-reactivity with DNA anchoring, these compounds would benefit from conjugation to sequence-specific vectors.

1.1.3 Copper-based artificial metallo-nucleases

Artificial metallo-nucleases (AMNs) are a class of metal complexes that aim to mimic the activity of natural nuclease enzymes. While copper plays an essential role in many biological processes, recent work has identified copper-dependant cell proliferation, and, interestingly, a heightened dependence of tumour cells on copper.[60, 61] Copper complexes have long been recognised for their ability to promote oxidative cleavage of nucleic acids through Fenton-type chemistry. Sigman's reagent, reported in 1979, is a copper complex prepared

in situ using copper(II) and an excess of 1,10-phenanthroline (Phen).[62] This complex combines redox active copper ion with two semi-intercalating ligand 1,10-phenanthroline, and displays oxidative DNA damage of the DNA backbone through the production of reactive oxygen species (ROS) in the presence of a reductant, causing single strand breaks.[63]

The Kellett group[64] investigated the impact of the extension of phenanthroline-derived ligands on binding activity and cleavage activity, using dipyridoquinoxaline (DPQ), dipyridophenazine (DPPZ) and benzo[*i*]dipyrido[3,2-*a*:2′,3′-*c*]phenazine (DPPN). The extended aromaticity increased planarity and π-stacking interactions, effectively anchoring the metal centre in proximity to the phosphate backbone and led to enhanced DNA recognition and cleavage, compared to Sigman's reagent.[64] However, these *bis*-substituted copper complexes showed high dissociation rate of the second ligand, limiting their stability. This can be addressed by covalently binding the two phenanthroline moieties with a serinol bridge, for instance, in the case of Clip-Phen,[65] which displays higher stability and better cleavage activity than $Cu(Phen)_2$.[66] Although highly efficient, early Cu(II) complexes lacked control over cleavage selectivity, producing random strand breaks.

To improve activity and solubility, ligand scaffolds such as *tris*-(2-pyridylmethyl)amine (TPMA)[67] and di-(2-picolyl)amine (DPA),[68] were introduced. These nitrogen-rich ligands stabilised Cu(II) in aqueous media and provided a well-defined coordination environment, that facilitated redox cycling between Cu(II) and Cu(I). $[Cu(TPMA)(N,N)]^{2+}$ and $[Cu(DPA)(N,N)]^{2+}$ have shown higher solution stability compared to $Cu(Phen)_2$ and display unique DNA oxidation properties.[68]

Cleavage can also be improved through the design of ligands with multiple copper chelating sites, thereby increasing the concentration of copper per molecule.[69-74] The dinuclear complexes $[Cu(Terph)(Phen)]^{2+}$ and $[Cu(Oda)(Phen)]^{2+}$ (where Terph = terephthalate and Oda = octanedioate) (Figure I.8) display selective antiproliferative activity on solid epithelial cancers that differ from the reported activity of cisplatin. Additionally, both dinuclear copper complexes have shown to be 10-100 times more active than their mononuclear counterparts.[74] Collectively, these efforts demonstrate how subtle changes in ligand architecture can fine-tune both reactivity and

selectivity of Cu-AMNs, providing a versatile chemical space for the design of DNA-cleaving agents.

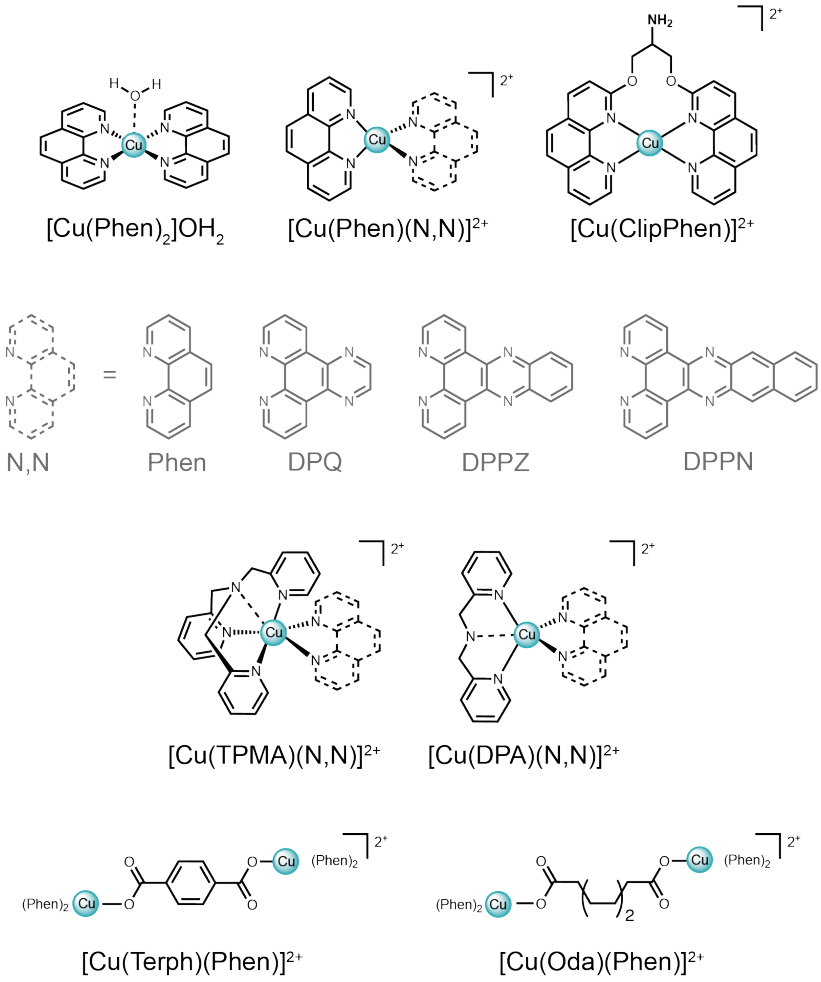


Figure I.8: Evolution of phenanthroline based Cu-AMNs from *bis*-phenanthroline complexes to caging ligands and binuclear Cu-AMNs.

A major challenge in the field of Cu-AMNs remains the dependence on exogenous reductants to trigger DNA oxidation. [75] Some reported systems have shown reductant-free or 'self-activated' copper cleavage activity, such as colibactin[76], di-copper complexes such as Cu2-BPL-C6,[77] or the marine alkaloid prodigiosin (PD)[78] (Figure I.9.a). PD is a naturally occurring red pigment produced mainly by bacteria found in marine sponges, such as *Pseudoalteromonas*[79] or *Serratia marcescens*.[80] It is studied for its anticancer, antimicrobial, and immunosuppressive activity.[81, 82] The pyrrolylpyrromethene prodiginine scaffold consists of 3 aromatic pyrroles, in which the third pyrrole ring is linked by an methylene bridge, resulting in a potential N,N,N

coordination site compatible with copper. PD has a C-6 methoxy group on the second pyrrole, which is thought to be linked to its antibacterial activity.[83]

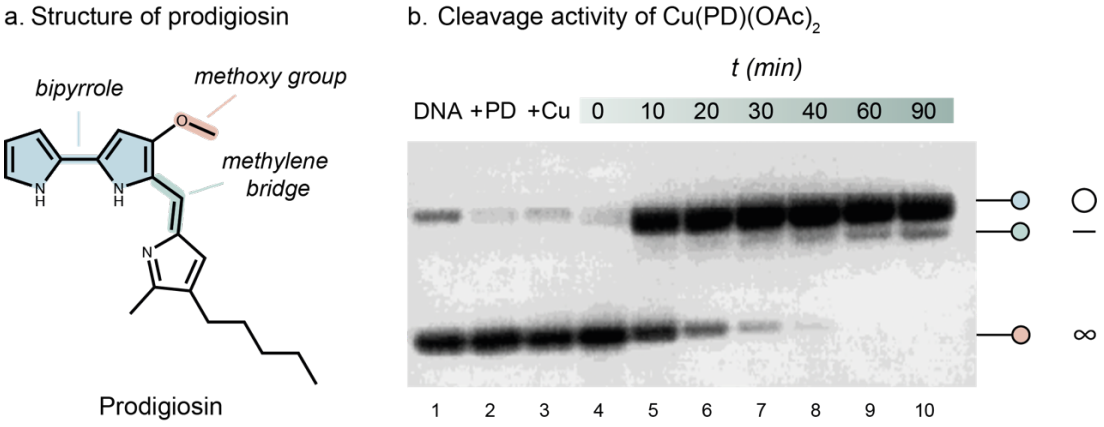


Figure I.9: **a**. Structure of prodigiosin with the bipyrrole motif (blue), the methoxy group (orange) and the methylene bridge (green). **b**. Cleavage of supercoiled DNA by prodigiosin in the presence of copper generating single and double strand breaks. (Figure adapted from Melvin et al.).[78]

The self-activation property of Cu-PD is attributed to the redox-activity of the bi-pyrrole motif, which facilitates electron transfer to the coordinated copper centre.[84] This also gives rise to the formation of blue tetrapyrrole moieties during chemical synthesis, [85] which are also commonly found in prodiginines natural sources.[86] Subsequent studies established that copper complexes of PD derivatives can also induce DNA damage in mild conditions, without a reductant, distinguishing them from classical Cu-Phen-type AMNs. The intrinsic redox activity of the bi-pyrrole motif provides an attractive route toward reductant-independent metallo-nuclease systems that function in biologically relevant environments. The evolution of Cu-based AMNs reflects a progression from simple, reductant-driven systems to structurally sophisticated, ligand-controlled architectures. Through rational design of the coordination sphere and incorporation of redox-active ligands such as PD, it becomes possible to combine efficiency, stability and self-activation. Building on this, Cu-AMNs can be explored as self-activated oxidative agents and investigated for their potential combination with target specific scaffolds for sequence-selective DNA cleavage.

1.2 Targeted metal therapies using triplex-forming oligonucleotides

Justified by the high relevance of DNA as a therapeutic target, many metal-based drugs have been developed for specific gene-targeted therapies. Gene silencing is a very prominent research field, especially following the great success of sequence targeted nuclease technologies such as Zinc Finger Nucleases (ZFNs),[87] Transcription Activator-Like Effector Nucleases (TALENs)[88] and Clustered Regularly Interspaced Short Palindromic Repeats (CRISPR).[89] These gene editing technologies rely on the combination of a DNA cleaving moiety with a sequence recognition entity. ZFNs and TALENs exploit the cleavage domain of Fok I, a type II restriction endonuclease.[90] Target recognition is then controlled by peptide chains, or zinc finger domains, in the case of ZFNs,[87] or by transcription activator-like effector (TALE) protein, in the case of TALENs.[91] CRISPR is inspired by natural defence mechanism against infection, found in prokaryotic cells.[92] Briefly, this method relies on the combination of a single guide RNA (sgRNA), which is the recognition moiety, with a DNA cleaving entity, Cas9, which is able to cleave DNA through a hydrolytic pathway.[89] In 2020, Emmanuelle Charpentier and Jennifer Doudna were awarded the Nobel Price for their work on CRISPR-Cas9, which has been accompanied by a surge in the interest in sequence specific gene editing technologies. These groundbreaking examples highlight the potential for the combination of gene-recognition moieties with DNA damaging agents for targeted therapies.

1.2.1 Triplex-forming oligonucleotides

Triplex-forming oligonucleotides (TFOs) represent a powerful strategy for sequence-selective recognition of duplex DNA. Triplex structures were first reported by Rich *et. al.*[15] in 1957, when a three-stranded structure was generated by a polyriboadenylic acid and two polyribouracylic acid strands. This work pioneered the field of triplexes and TFOs. TFOs are single stranded oligonucleotides designed to bind the major groove of double-stranded DNA (dsDNA) through Hoogsteen hydrogen bonding to purine-rich tracts[93] (Figure I.10). TFOs align either parallel or antiparallel to the purine-rich, or ‘target’, strand of the duplex, forming distinct triplets. Parallel triplexes, in which the TFO runs in the same 5′ to 3′ direction as its target strand, are generally more

stable than their antiparallel analogues.[94] This sequence-selective recognition makes TFOs particularly attractive scaffolds for gene silencing through site-selective modifications or targeted DNA cleavage.

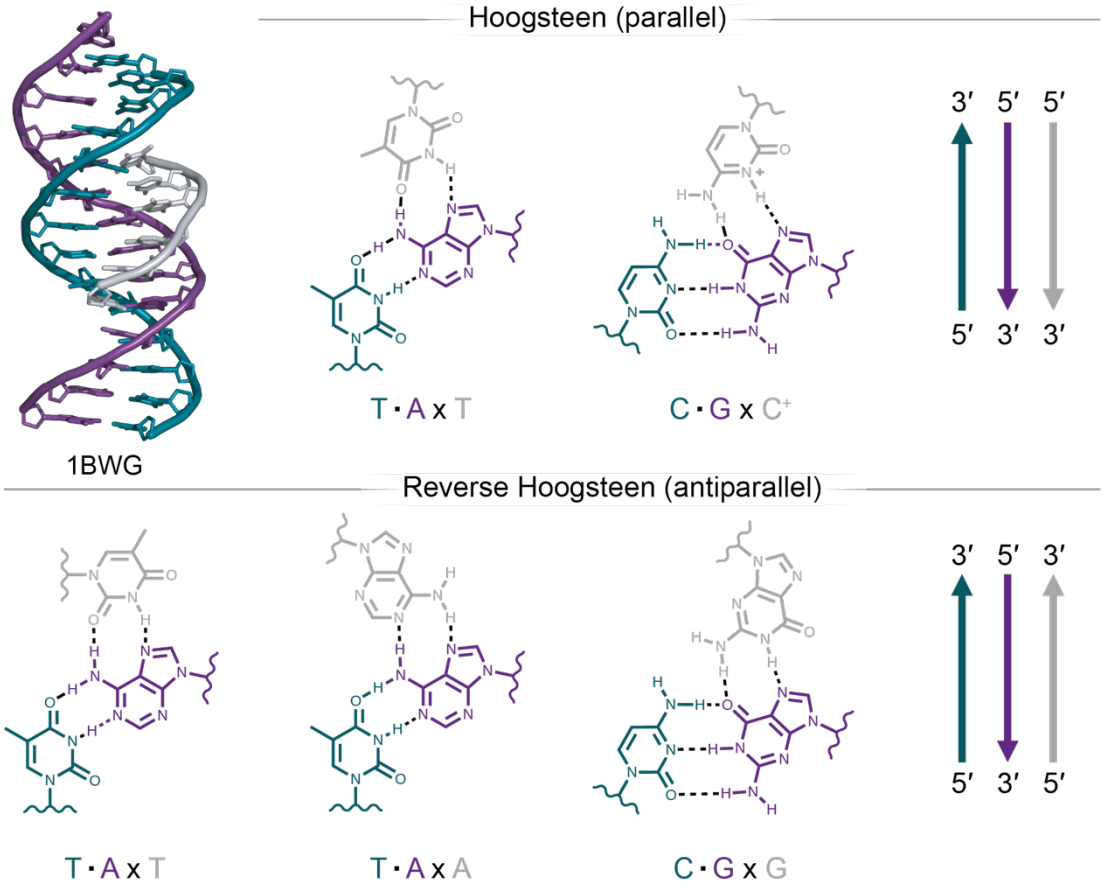


Figure I.10: Structure of triplexes (1BWG) and of base triplets in the case of parallel and antiparallel triplex formation, displaying Watson-Crick hydrogen bindings (·) between complementary (green) and target strand (purple) and hydrogen bonding (x) of the TFO strand (grey) on the Hoogsteen face of DNA duplets.

Triplex formation is highly sensitive to sequence compositions. Uninterrupted polypurine tracts represent the most favourable targets, whereas interruptions or GC-rich regions significantly reduce affinity. Beyond base composition, duplex structure also plays a critical role, as local helical parameters, groove width, and backbone flexibility can influence accessibility of the Hoogsteen face. Moreover, high-order DNA organisation, such as DNA supercoiling or chromatin compaction, affect the thermodynamic and kinetic accessibility of triplex target sites *in vivo*.[95, 96]

Despite their high sequence selectivity, the use of TFOs in biological contexts is limited by the intrinsic instability of triplex structures under

physiological conditions. Several factors contribute to this including: i) electrostatic repulsion between the three negatively charged backbones; ii) the requirement for C protonation at the N3 position to form the C·GxC$^+$ triplets, which demand mildly acidic conditions; and iii) the sensitivity to interruptions of the polypurine target. Electrostatic repulsion between the three negatively charged strands presents a major thermodynamic barrier to triplex formation. Divalent and trivalent metal ions such as Mg^{2+}, are therefore critical for stabilising triplex structures by shielding phosphate repulsion. Extensive chemical modification strategies have therefore been developed to enhance triplex stability and broaden their biological utility. Among the most effective and accessible modifications are: i) the substitution of canonical nucleobases with modified nucleobases (e.g. replacing C with 5-methylcytosine (5mC)[97] or the Z nucleobase (where Z = 6-amino-5-nitropyridin-2-one));[98] ii) the incorporation of triplex stabilizing moieties (e.g. exploiting the intercalation properties of thiazole orange (TO));[99, 100] iii) the use of chemical motifs that can anchor the TFO to its target, such as the crosslinking agent psoralen;[101, 102] and iv) the use of artificial backbones within the TFO (e.g. phosphorodiamidate morpholino oligomers (PMO) or peptide nucleic acids (PNA));[103].

The replacement of C with 5mC (Figure I.11.a) enables protonation of the TFO strand and stable triplex formation closer to physiological pH.[104] The methyl substituent also improves π-stacking and hydrophobic interaction within the major groove. More recently, the Z nucleobase was shown to further improve TFOs, enabling triplex formation at neutral pH. The Z nucleobase is an uncharged alternative to protonated C, and is therefore able to form two hydrogen bonds with the C·G duplet at physiological pH.[98] A second strategy involves embedding the intercalating ligand TO (Figure I.11.b) within the TFO strand. TO fluoresces upon intercalation, providing both enhanced stability and a useful spectroscopic handle for triplex formation monitoring. Multiple TO units strategically spaced along the sequence have been shown to significantly increase the melting temperature (T_M) of triplexes.[100] Psoralen intercalates between DNA base pairs and, upon UV irradiation, can bind DNA. This reaction can form either monoadducts or interstrand crosslinks, depending on whether one or two T residues are involved. These crosslinks effectively lock the TFO to its target duplex, enhancing both stability and functional persistence.[105]

Finally, neutral backbones such as PMO[106] or PNA[107] (Figure I.11.c) mitigate electrostatic repulsion by replacing the negatively charged phosphodiester linkage with neutral analogues. These modifications not only increase triplex stability but also enhance cellular uptake and resistance to enzymatic degradation.[108, 99, 104, 109]

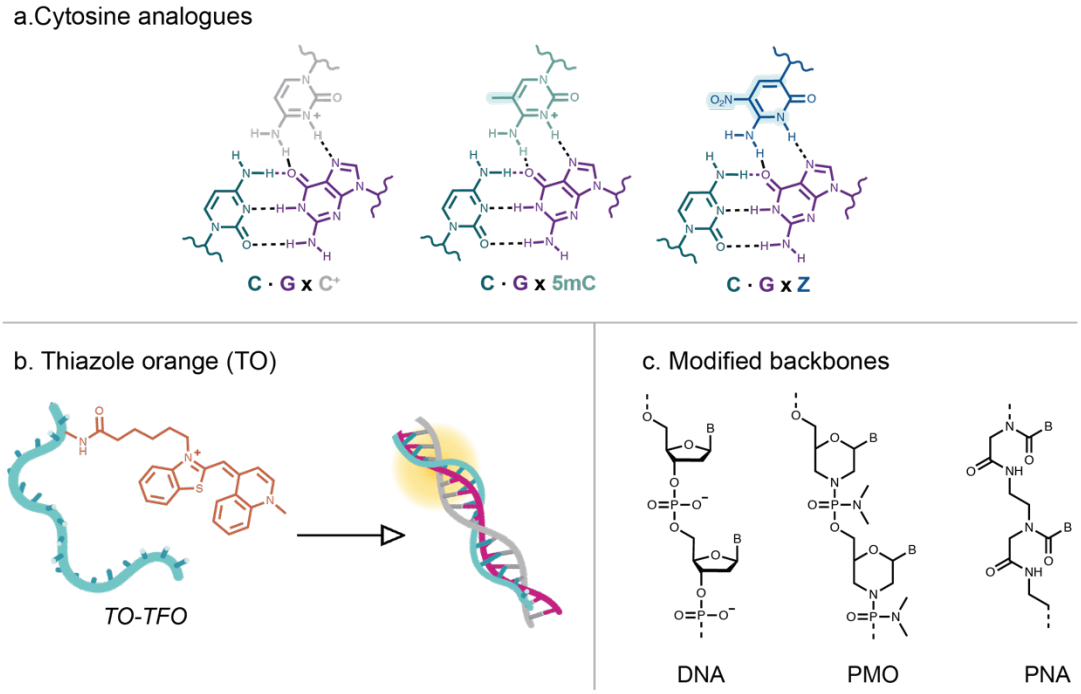


Figure I.11: **a**. Structure of triplets formed by cytosine and its analogues with increased triplex stabilisation, 5mC and Z. **b**. Use of thiazole orange (TO) for triplex stabilisation and triplex formation provbe **c**. Comparison of DNA phosphodiester backbone, phosphorodiamidate morpholino oligomer (PMO) and peptide nucleic acid (PNA) backbones.

Two main methods are available to synthesise TFOs, solid-phase synthesis (SPS)[110, 111] and enzymatic synthesis.[112] SPS (Figure I.12) remains the most established route for short to medium-length oligonucleotides.[113] It proceeds through iterative cycles of detritylation, coupling, capping and oxidation starting from a 3′-bond monomer attached to a solid support. SPS provides a precise positional control of base insertion and can therefore be used for insertion of chemical modifications—such as alkyne or amine functionalities—making it particularly well-suited to post-synthetic conjugation strategies like click chemistry. However, it is not compatible with oxidatively active or nucleobase-reactive modifications, which can interfere with synthesis or deprotection steps.

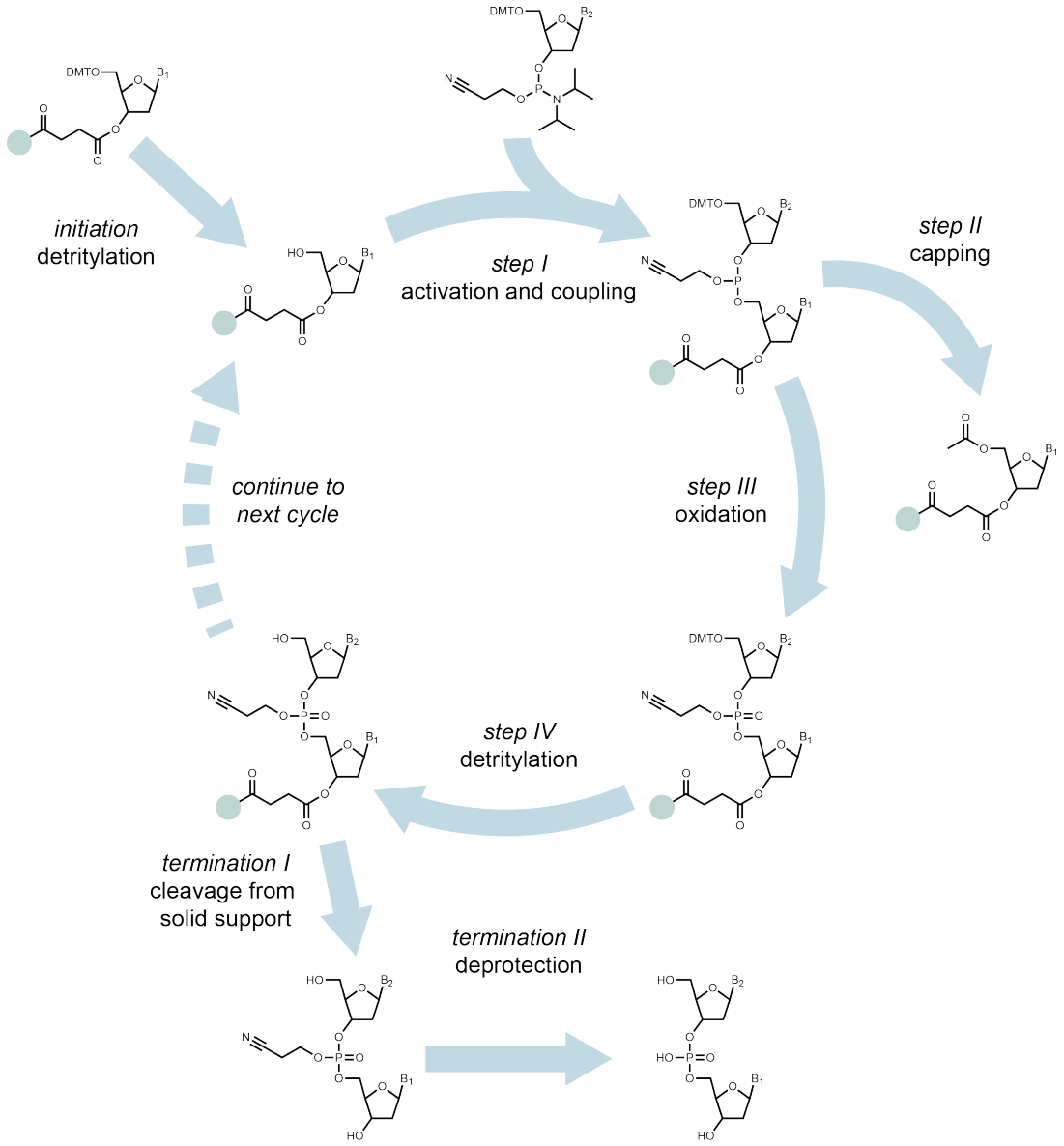


Figure I.12: Cycle of solid phase synthesis (SPS) of oligonucleotide.

Enzymatic methods, particularly single-nucleotide incorporation primer extension (SNI-PEX) (Figure I.13) circumvent these limitations. In this approach, DNA polymerases extend a primer strand annealed to a complementary template, using triphosphate substrates.[112] The Hocek group reported the first example of an enzymatically prepared AMN-TFO hybrid.[114] More recently, the Kellett group have reported the enzymatic synthesis of a DPA-TFO hybrid and its comparison to a SPS-derived equivalent.[115] The SNI-PEX method enables site-specific incorporation of functionalised nucleotides under mild-conditions. The complementary template, often biotinylated, facilitates magnetic separation and recovery of the functionalised TFO. The

enzymatic method thus complements SPS by enabling the preparation of long or sensitive sequences that are not amenable to automated systems.[116]

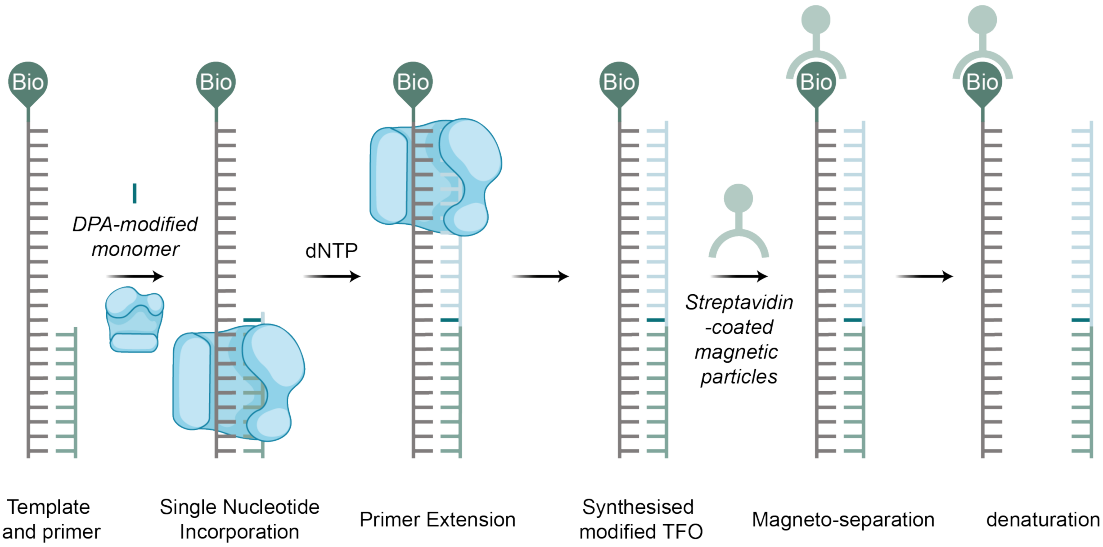


Figure I.13: Schematic representation of the incorporation of a DPA clicked monomer into a TFO sequence *via* SNI-PEX enzymatic oligonucleotide synthesis.

The capability of TFOs to target defined DNA sequences underpins their use in antigene applications,[117] where transcription can be inhibited through triplex formation at promoter or coding regions. Because TFOs can be chemically synthesised, modified and conjugated with high precision, they provide useful vectors for hybrid biomaterial constructs that can couple recognition ability of nucleic acids with reactivity of small-molecule drugs or metal centres.

1.2.2 Platinum(II)-TFO hybrids

TFOs provide an elegant framework for sequence-specific DNA recognition and modification, making them an ideal vector for directing reactive metal complexes such as Pt(II) to defined sequences. The first Pt(II)-modified oligonucleotide was reported by Orgel *et al.*,[118] who synthesised a Pt(II)-oligomer bearing a cysteamine linker at the 5′-end for post synthetic platination (Figure I.14.a). The resulting hybrid displayed efficient crosslinking of dsDNA and promising inhibition of DNA polymerase I activity, demonstrating the potential of Pt(II)-oligonucleotide conjugates for targeted gene modulation.

Subsequent studies sought to introduce Pt(II) prior to oligonucleotide synthesis. Lippard *et al.*[119] and Lippert *et al.*[120] independently reported the automated SPS preparation of Pt(II)-TFO hybrids, functionalising G (Figure

I.14.b) or T (Figure I.14.c) residues respectively. To prevent undesired crosslinking during SPS, the Pt(II) coordination sphere was fully saturated. These early hybrids were obtained in modest yields (below 30 %), reflecting the synthetic challenges associated with incorporating metal centres before SPS.

In 1998, Leng *et al*.[121] explored post-synthetic modification strategies, attaching *trans*-Pt(II) centres to C (Figure I.14.d) and G (Figure I.14.b) residues. While G labelling was successful, selective attachment to C proved difficult within polypyrimidine sequences, underscoring the need for improved orthogonality in Pt(II)-oligonucleotide coupling. To address these limitations, Reedijk *et al.*[122] later developed a protected platinated monomers compatible with SPS, featuring a platinated C6 amine linker on the phosphate backbone (Figure I.14.e). This approach enabled the controlled incorporation of Pt(II) into oligonucleotides but required multiple protection and deprotection steps, resulting in low overall yields.

Building on this, Reedijk and Lippert[123] successfully synthesised Pt(II)-PNA hybrids *via* SPS, yielding a range of PNA probes platinated through the N7 position of G (Figure I.14.b). Despite this progress, pre-synthesis labelling strategies were not developed further, with later studies shifting toward post-synthetic platination, which offered greater flexibility and milder reaction conditions.

In 2002, McLaughlin *et al.*[124, 125] reported several polythymine TFOs with ethylenediamine linkers at the 5′ end to facilitate efficient Pt(II) complexation (Figure I.14.f). The resulting Pt(II)-TFO hybrids formed stable adducts with target DNA through sequence-directed crosslinking. Miller and coworkers[126, 127] expanded this approach, reporting *trans*- and *cis*-Pt(II)-TFO hybrids *via* conjugation at G (Figure I.14.b) and C (Figure I.14.g) bases. These hybrids showed robust triplex stability upon crosslinking, even in the presence of C interruptions within the target strand. However, their tolerance toward interruption of the homopurine motif remained lower than that of analogues with standard nucleobases substitutions.[128]

The Miller group later reported a series of improved *trans*-Pt(II)-TFO hybrids.[129,130,131] Pt(II) centres were attached to the N7 position of terminal G at both the 5′ and 3′ ends of oligopyrimidine sequences (Figure I.14.b),[129]

enabling inhibition of translation *in vitro* and in *E.coli via* covalent crosslinking. Further developments yielded hybrids capable of transcription inhibition[130] and androgen receptor-targeted Pt(II)-TFOs showing modest knockdown of messenger RNA (mRNA) and protein expression in transfected prostate cancer cells.[131] Collectively, this early work showed the therapeutic potential of the combining the cytotoxicity of Pt(II) with the gene-targeting precision of TFOs, while also revealing the need for improved coupling methodologies.

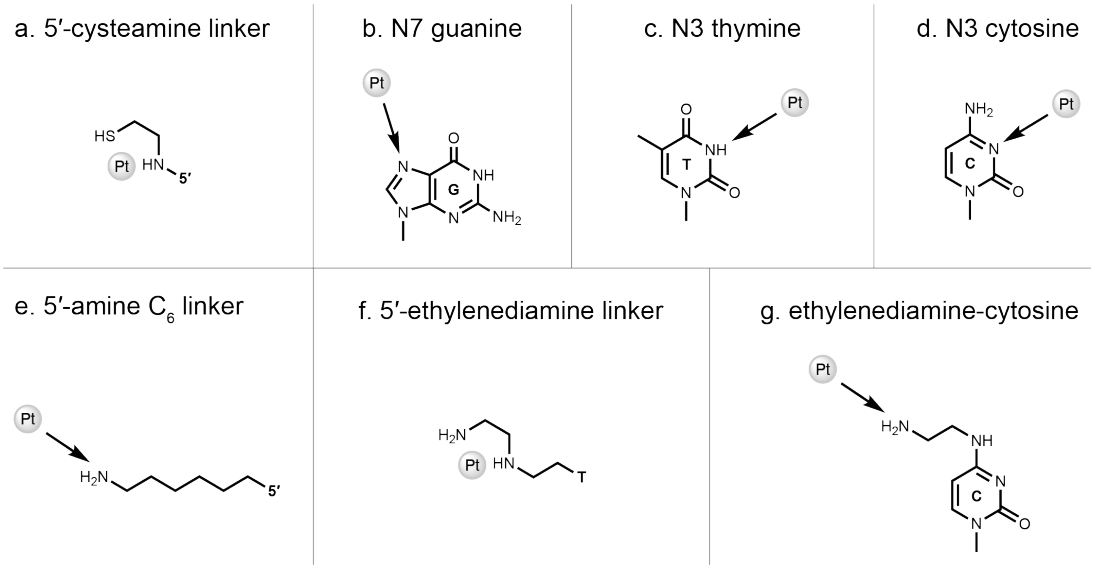


Figure I.14: Early strategies for the platination of oligonucleotides for target-specific DNA crosslinking.

To overcome the synthetic limitations of early Pt-TFO conjugation strategies, click chemistry, particularly azide-alkyne cycloaddition, has emerged as an efficient and reliable method for metal-TFO hybrids generation (Figure I.15).[93] The Nobel Prize-awarded biorthogonal reactions can proceed *via* copper-catalysed (CuAAC) or strain-promoted (SPAAC) mechanisms,[132] and was first used on nucleic acid for labelling with fluorophores,[133] and was later optimised by Carell *et al.*,[134] enabling high yield even with highly alkyne-functionalised TFOs. This led to a wide range of available click chemistry building blocks for nucleic acid, usable to develop click-capable TFOs. Commercially available alkyne handles can be introduced at almost any site along the TFO sequence using standard SPS-compatible monomers, enabling the modulable conjugation of azide-functionalised metal complexes to alkyne-modified TFOs. CuAAC typically affords faster reaction kinetics and higher

conversion rates,[135] while SPAAC offers a metal-free alternative—advantageous when working with redox-sensitive metal complexes.[136, 137]

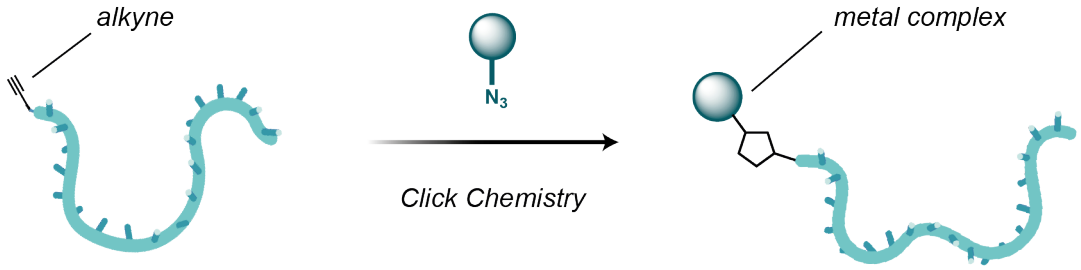
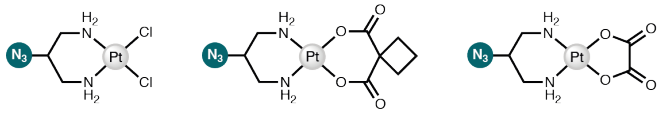


Figure I.15: Use of click chemistry for labelling alkyne-modified TFOs with azide-functionalised metal centres.

The Kellett group[138] has successfully applied click chemistry conditions to attach azide-derivatives of cisplatin, oxaliplatin and carboplatin (Figure I.16) to green fluorescent protein gene (*GFP*)-targeting TFOs bearing alkyne modifications. Incorporation of TO units was used to further enhance triplex formation and provided fluorescence readouts for hybrid formation. Subsequent studies by the same group[139] employed an amine-alkyne nucleobase monomer to introduce both TO and carboplatin on the same nucleobase, producing hybrids with superior triplex stability and enhanced crosslinking activity compared to non-TO-labelled analogues. This versatile click-based approach established a robust platform for the modular assembly of platinum-TFO conjugates and opened the possibility of generating diverse hybrid libraries with programmable DNA-binding and reactivity profiles.



Pt-N_3-Cis Pt-N_3-Carbo Pt-N_3-Oxali

Figure I.16: Structure of azide functionalised cisplatin, carboplatin and oxaliplatin that have been clicked onto *GFP*-targeting TFOs for target-specific DNA crosslinking.

1.2.3 TFO-oxidative AMN hybrids: toward targeted DNA cleavage

In parallel with crosslinking Pt(II)-TFO conjugates, efforts have been made to develop sequence-targeted oxidative AMNs capable of DNA cleavage using oligonucleotides. The first such system was reported in 1985 when Dervan *et al.*[140] described an Fe(II)-EDTA-oligonucleotide hybrid linked *via* a T residue (Figure I.17.a). The SPS-prepared 19-nucleotide (nt) hybrid cleaved its

pBR322 target specifically over a 16-nt span, consistent with cleavage mediated by diffusible ROS. A similar hybrid featuring Fe(II)-EDTA at the 5′-terminus (Figure I.17.b) was later reported,[141] confirming the reproducibility of this strategy.

Later, Sigman and coworkers[142] introduced a glycamido-phenanthroline-oligonucleotide conjugate (Figure I.17.c), which exhibited a narrower cleavage site in the presence of copper, suggesting the involvement of non-diffusible ROS species. Even though these early hybrids demonstrated site-selective activity, the hybridisation to their target required disruption of the duplex DNA target.

Subsequent reports of Fe(II)-EDTA-TFO hybrids targeted the Hoogsteen face of duplex DNA without interfering with duplex bonds.[143-145] These systems required buffers stabilising A-form DNA and acidic pH to enable triplex formation, which unfortunately impaired the cleavage activity of the iron centre. In 1989, Helene's group[146] achieved a major advance by demonstrating site-specific double strand DNA cleavage using Cu(Phen)-modified TFOs in the presence of a reductant. As opposed to Sigman's hybrids, these hybrids bound the Hoogsteen face of duplex DNA through a stable triplex architecture and used a more flexible linker between the Phen and oligonucleotide (Figure I.17.d), improving accessibility to the target site.

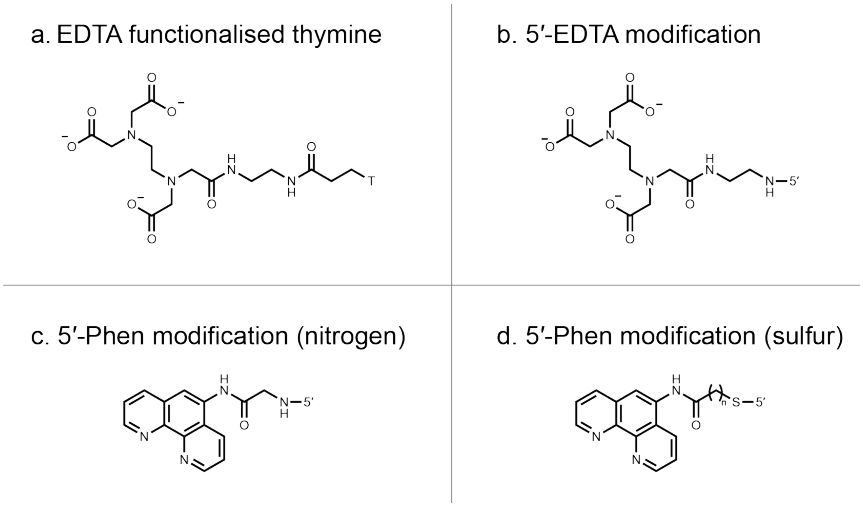


Figure I.17: Reported EDTA- and Phen-functionalised oligonucleotides for targeted oxidative DNA cleavage.

Alternative strategies explored at this time included hydrolysis-mediated cleaving hybrids,[147-149] manganese-porphyrin TFO conjugates[150] and oligonucleotide Cu(II)/Co(III) metallodesferal constructs.[151] Although active, these systems often suffer from easily cleaved linkers, ion-dependant triplex stability, and complex synthetic routes.

In 2020, the European Training Network “ClickGene” significantly contributed to the field of AMN-TFO hybrids by introducing click-assembled hybrids. For example, Lauria *et al*.[152] reported the efficient attachment of phenanthroline derivatives to TFOs targeting the *GFP* using azide-alkyne cycloaddition. The Kellett group later expanded this chemistry to include various polypyridyl copper complexes,[153, 115] yielding hybrids that achieved sequence-specific cleavage of the target *GFP* duplex, in the presence of sodium-*L*-ascorbate (Na-*L*-asc), with negligible *off*-target activity. In parallel, the Hocek group[154] introduced an azide-functionalised Clip-Phen derivative for hybridisation to human immunodeficiency virus (HIV)-targeting TFOs (Figure I.18) yielding promising hybrids with potential therapeutic activity. These new constructs, based on well-characterised copper-mediated reductant-dependant cleaving ligands, demonstrated selective oxidative cleavage of target DNA in the presence of Na-*L*-asc, while benefitting from the robustness and modularity of click chemistry. Collectively, these studies established click conjugation as a general and efficient route to diverse TFO-AMN systems, overcoming the synthetic and stability limitations of earlier generation hybrids.[155]

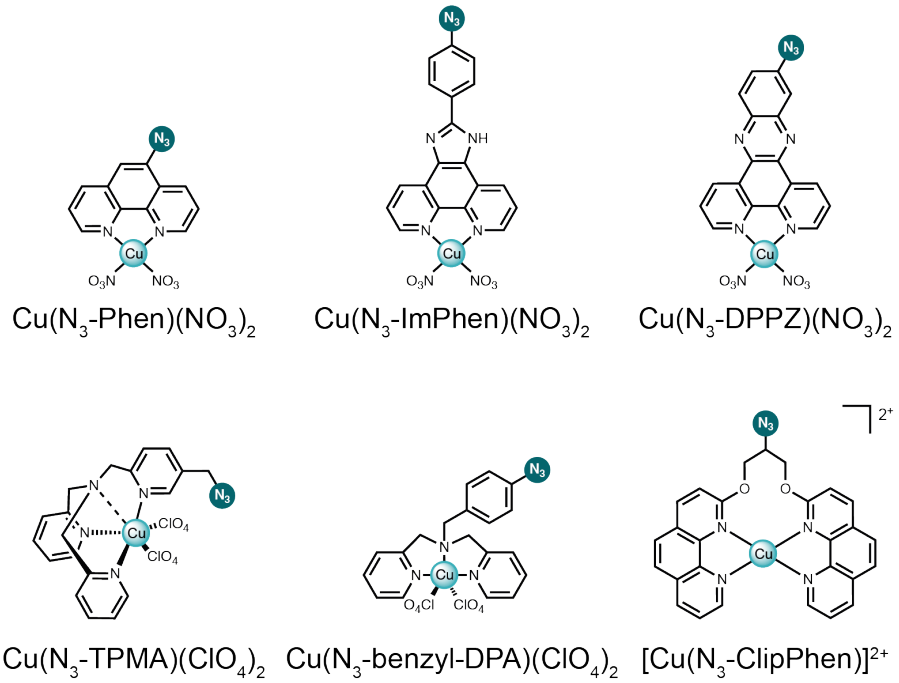


Figure I.18: Structure of azide-modified Cu-AMNs that have been clicked onto *GFP*- or HIV-targeting TFOs showing selective cleavage of the target gene.

1.2.4 The epidermal growth factor receptor gene as a therapeutic target

The reported metal-TFO hybrids generated *via* click chemistry to date have targeted the *GFP* gene or the HIV sequence—models of convenience or targeting a virus, that are not part of the human genome. To advance toward applications in cancer therapy, attention has turned to oncogenes, that are part of the human genome. The epidermal growth factor receptor (*EGFR*) gene is overexpressed in several tumour types, including lung cancer[156], and promotes uncontrolled cellular proliferation and survival of tumour cells.[157] Importantly, exon 5 of the *EGFR* gene contains a 19-base pair (bp) polypurine tract (Figure I.19), making it an ideal substrate for TFO binding. Effective parallel triplex formation requires an extended purine stretch to enable stable hydrogen bonding between the TFO and its duplex target, competing with the electrostatic repulsion among the three negatively charged strands.

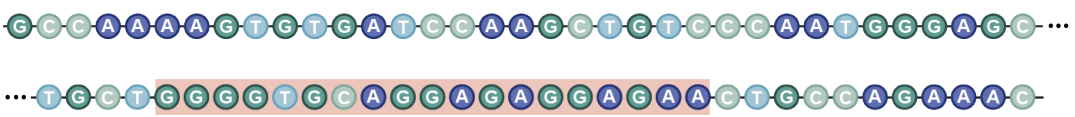


Figure I.19: Sequence of the exon 5 of the *EGFR* gene, highlighting the 19 nucleotide polypurine track compatible with triplex formation.

Targeting the endogenous, cancer-relevant *EGFR* sequence, which is a major focus of this thesis, represents a significant step toward translating metal-TFO hybrids from model systems to therapeutically meaningful contexts, particularly for the development of *EGFR*-directed gene-silencing conjugates.

TFOs have been investigated for gene silencing, transcription inhibition, or genome editing by targeting a promoter regions or coding sequences. Despite the rise of CRISPR-based genome editing technologies, TFOs remain uniquely valuable due to their protein-free targeting mechanism, and compatibility with chemical functionalisation. In this context, the development of metal-TFO hybrids capable of adduct formation or DNA cleavage at therapeutically relevant loci represents a strategic evolution of triplex technology. Targeting disease-associated genes, such as the *EGFR*, extends triplex chemistry from model systems to clinically meaningful genomic contexts and underscores the translational potential of modular, click-assembled metal-TFO hybrids.

2 References

[1] Watson, J. D.; Crick, F. H. *Nature.* **1953**, *171,* (4356), 737-738.
[2] Franklin, R. E.; Gosling, R. G. *Nature.* **1953**, *171,* (4356), 740-741.
[3] Wilkins, M. H.; Stokes, A. R.; Wilson, H. R. *Nature.* **1953**, *171,* (4356), 738-740.
[4] Pabo, C. O.; Sauer, R. T. *Annu Rev Biochem.* **1992**, *61,* (1), 1053-1095.
[5] Balvay, L.; Libri, D.; Fiszman, M. Y. *Bioessays.* **1993**, *15,* (3), 165-169.
[6] Taylor, R. W.; Turnbull, D. M. *Nat Rev Genet.* **2005**, *6,* (5), 389-402.
[7] Bestor, T. H. *J Clin Invest.* **2000**, *105,* (4), 409-411.
[8] Sánchez-Pérez, Y.; Soto-Reyes, E.; García-Cuellar, C. M.; Cacho-Díaz, B.; Santamaría, A.; Rangel-López, E. *Cns Neurol Disord-Dr.* **2017**, *16,* (10), 1090-1098.
[9] Strekowski, L.; Wilson, B. *Mutat Res.* **2007**, *623,* (1-2), 3-13.
[10] Goodsell, D. a. D., R. E. *Journal of Medicinal Chemistry.* **1986**, *29,* (5), 727-733.
[11] Long, E. C.; Barton, J. K. *Accounts Chem Res.* **1990**, *23,* (9), 271-273.
[12] Paramanathan, T.; Vladescu, I.; McCauley, M. J.; Rouzina, I.; Williams, M. C. *Nucleic Acids Res.* **2012**, *40,* (11), 4925-4932.
[13] Venugopal, S.; Sharma, V.; Mehra, A.; Singh, I.; Singh, G. *Chem Biol Drug Des.* **2022**, *100,* (4), 580-598.
[14] Cherstvy, A. G. *Phys Chem Chem Phys.* **2011**, *13,* (21), 9942-9968.
[15] Felsenfeld, G.; Davies, D. R.; Rich, A. *J Am Chem Soc.* **1957**, *79,* (8), 2023-2024.
[16] Gellert, M.; Lipsett, M. N.; Davies, D. R. *Proc Natl Acad Sci U S A.* **1962**, *48,* (12), 2013-2018.
[17] Gehring, K.; Leroy, J. L.; Gueron, M. *Nature.* **1993**, *363,* (6429), 561-565.
[18] Leonard, C. J.; Berns, K. I. *Prog Nucleic Acid Res Mol Biol.* **1994**, *48*, 29-52.
[19] Holliday, R. *Genetical Research.* **2009**, *5,* (2), 282-304.
[20] Tateishi-Karimata, H.; Sugimoto, N. *Chem Commun (Camb).* **2020**, *56,* (16), 2379-2390.
[21] Posner, A. S. *Physiol Rev.* **1969**, *49,* (4), 760-792.
[22] Clapham, D. E. *Cell.* **1995**, *80,* (2), 259-268.
[23] Wu, N.; Veillette, A. *Nature.* **2011**, *475,* (7357), 462-463.
[24] Rouault, T. A. *Nat Chem Biol.* **2006**, *2,* (8), 406-414.
[25] Coleman, J. E. *Curr Opin Chem Biol.* **1998**, *2,* (2), 222-234.
[26] Cass, A. E.; Hill, H. A. *Ciba Found Symp.* **1980**, *79*, 71-91.
[27] Lehninger, A. L. *Physiol Rev.* **1950**, *30,* (3), 393-429.
[28] Mertz, W. *Nutr Rev.* **1993**, *51,* (10), 287-295.
[29] Tillman, L. A.; Drake, F. M.; Dixon, J. S.; Wood, J. R. *Aliment Pharmacol Ther.* **1996**, *10,* (4), 459-467.
[30] Benedek, T. G. *J Hist Med Allied Sci.* **2004**, *59,* (1), 50-89.
[31] Finkelstein, A. E.; Walz, D. T.; Batista, V.; Mizraji, M.; Roisman, F.; Misher, A. *Ann Rheum Dis.* **1976**, *35,* (3), 251-257.
[32] Shaw, C. F. *Chem Rev.* **1999**, *99,* (9), 2589-2600.
[33] Engman, M. F.; Mook, W. H.; Marchildon, J. W. *Journal of the American Medical Association.* **1911**, *LVI,* (2).
[34] Goodwin, L. G. *Trans R Soc Trop Med Hyg.* **1995**, *89,* (3), 339-341.
[35] Thompson, K. H.; Orvig, C. *Science.* **2003**, *300,* (5621), 936-939.

[36] Roberts, J. J.; Thomson, A. J. *Prog Nucleic Acid Res Mol Biol.* **1979**, *22*, 71-133.
[37] Todd, R. C.; Lippard, S. J. *Metallomics.* **2009**, *1,* (4), 280-291.
[38] Kelland, L. *Nat Rev Cancer.* **2007**, *7,* (8), 573-584.
[39] Cleare, M. J.; Hoeschele, J. D. *Bioinorganic Chemistry.* **1973**, *2,* (3), 187-210.
[40] Johnstone, T. C.; Wilson, J. J.; Lippard, S. J. *Inorganic Chemistry.* **2013**, *52,* (21).
[41] A., A. S. *Biomedical & Pharmacology Journal.* **2019**, *12,* (1), 7-15.
[42] Xu, Z. F.; Wang, Z. G.; Deng, Z. Q.; Zhu, G. Y. *Coordination Chemistry Reviews.* **2021**, *442*.
[43] Anderson, W. K.; Quagliato, D. A.; Haugwitz, R. D.; Narayanan, V. L.; Wolpert-DeFilippes, M. K. *Cancer Treat Rep.* **1986**, *70,* (8), 997-1002.
[44] Plaxe, S. C.; Braly, P. S.; Freddo, J. L.; McClay, E.; Christen, R. D.; Kirmani, S.; Kim, S.; Heath, D.; Howell, S. B. *Gynecol Oncol.* **1993**, *51,* (1), 72-77.
[45] Horvath, V.; Soucek, K.; Svihalkova-Sindlerova, L.; Vondracek, J.; Blanarova, O.; Hofmanova, J.; Sova, P.; Kozubik, A. *Invest New Drugs.* **2007**, *25,* (5), 435-443.
[46] Sova, P.; Mistr, A.; Kroutil, A.; Zak, F.; Pouckova, P.; Zadinova, M. *Anti-Cancer Drug.* **2006**, *17,* (2), 201-206.
[47] Creaven, P. J.; Madajewicz, S.; Pendyala, L.; Mittelman, A.; Pontes, E.; Spaulding, M.; Arbuck, S.; Solomon, J. *Cancer Treat Rep.* **1983**, *67,* (9), 795-800.
[48] McKeage, M. J.; Raynaud, F.; Ward, J.; Berry, C.; O'Dell, D.; Kelland, L. R.; Murrer, B.; Santabarabara, P.; Harrap, K. R.; Judson, I. R. *J Clin Oncol.* **1997**, *15,* (7), 2691-2700.
[49] Qu, Y.; Appleton, T. G.; Hoeschele, J. D.; Farrell, N. *Inorganic Chemistry.* **1993**, *32,* (11), 2591-2593.
[50] Farrell, N. P., Spinelli, A. *Royal Society of Chemistry.* **1999**, (8), 125-134.
[51] Sessa, C.; Capri, G.; Gianni, L.; Peccatori, F.; Grasselli, G.; Bauer, J.; Zucchetti, M.; Vigano, L.; Gatti, A.; Minoia, C.; et al. *Ann Oncol.* **2000**, *11,* (8), 977-983.
[52] Gourley, C.; Cassidy, J.; Edwards, C.; Samuel, L.; Bisset, D.; Camboni, G.; Young, A.; Boyle, D.; Jodrell, D. *Cancer Chemother Pharmacol.* **2004**, *53,* (2), 95-101.
[53] Hensing, T. A.; Hanna, N. H.; Gillenwater, H. H.; Gabriella Camboni, M.; Allievi, C.; Socinski, M. A. *Anticancer Drugs.* **2006**, *17,* (6), 697-704.
[54] Komeda, S.; Moulaei, T.; Woods, K. K.; Chikuma, M.; Farrell, N. P.; Williams, L. D. *J Am Chem Soc.* **2006**, *128,* (50), 16092-16103.
[55] O'Carroll, S.; Slator, C.; de Paiva, R. E. F.; Newsome, C.; Searle, B.; Kk, S.; Whittle, S.; Catley, T. E.; Scoditti, S.; Mnich, K.; et al. *Nucleic Acids Res.* **2025**, *53,* (13).
[56] Prisecaru, A.; Molphy, Z.; Kipping, R. G.; Peterson, E. J.; Qu, Y.; Kellett, A.; Farrell, N. P. *Nucleic Acids Res.* **2014**, *42,* (22), 13474-13487.
[57] Hollis, L. S.; Amundsen, A. R.; Stern, E. W. *J Med Chem.* **1989**, *32,* (1), 128-136.
[58] Lovejoy, K. S.; Serova, M.; Bieche, I.; Emami, S.; D'Incalci, M.; Broggini, M.; Erba, E.; Gespach, C.; Cvitkovic, E.; Faivre, S.; et al. *Mol Cancer Ther.* **2011**, *10,* (9), 1709-1719.

[59] Park, G. Y.; Wilson, J. J.; Song, Y.; Lippard, S. J.; Park, G. Y.; Wilson, J. J.; Song, Y.; Lippard, S. J. *Proceedings of the National Academy of Sciences.* **2012**, *109,* (30).
[60] Ge, E. J.; Bush, A. I.; Casini, A.; Cobine, P. A.; Cross, J. R.; DeNicola, G. M.; Dou, Q. P.; Franz, K. J.; Gohil, V. M.; Gupta, S.; et al. *Nat Rev Cancer.* **2022**, *22,* (2), 102-113.
[61] Messina, M. S.; Torrente, L.; Pezacki, A. T.; Humpel, H. I.; Li, E. L.; Miller, S. G.; Verdejo-Torres, O.; Padilla-Benavides, T.; Brady, D. C.; Killilea, D. W.; et al. *Proc Natl Acad Sci U S A.* **2025**, *122,* (3), e2412816122.
[62] Sigman, D. S.; Graham, D. R.; D'Aurora, V.; Stern, A. M. *J Biol Chem.* **1979**, *254,* (24), 12269-12272.
[63] Sigman, D. S.; Mazumder, A.; Perrin, D. M. *Chem Rev.* **1993**, *93,* (6).
[64] Molphy, Z.; Prisecaru, A.; Slator, C.; Barron, N.; McCann, M.; Colleran, J.; Chandran, D.; Gathergood, N.; Kellett, A. *Inorg Chem.* **2014**, *53,* (10), 5392-5404.
[65] Pitie, M.; Donnadieu, B.; Meunier, B. *Inorg Chem.* **1998**, *37,* (14), 3486-3489.
[66] Pitié, M.; Boldron, C.; Gornitzka, H.; Hemmert, C.; Donnadieu, B.; Meunier, B. *Eur J Inorg Chem.* **2003**, (3), 528-540.
[67] Fantoni, N. Z.; Molphy, Z.; Slator, C.; Menounou, G.; Toniolo, G.; Mitrikas, G.; McKee, V.; Chatgilialoglu, C.; Kellett, A. *Chem-Eur J.* **2019**, *25,* (1), 221-237.
[68] Fantoni, N. Z.; Molphy, Z.; O'Carroll, S.; Menounou, G.; Mitrikas, G.; Krokidis, M. G.; Chatgilialoglu, C.; Colleran, J.; Banasiak, A.; Clynes, M.; et al. *Chem-Eur J.* **2021**, *27,* (3), 971-983.
[69] Humphreys, K. J.; Karlin, K. D.; Rokita, S. E. *J Am Chem Soc.* **2002**, *124,* (27), 8055-8066.
[70] Ito, T.; Thyagarajan, S.; Karlin, K. D.; Rokita, S. E. *Chem Commun.* **2005**, (38), 4812-4814.
[71] Li, L.; Karlin, K. D.; Rokita, S. E. *J Am Chem Soc.* **2005**, *127,* (2), 520-521.
[72] McStay, N.; Slator, C.; Singh, V.; Gibney, A.; Westerlund, F.; Kellett, A. *Nucleic Acids Res.* **2021**, *49,* (18), 10289-10308.
[73] Molphy, Z.; Montagner, D.; Bhat, S. S.; Slator, C.; Long, C.; Erxleben, A.; Kellett, A. *Nucleic Acids Res.* **2018**, *46,* (19), 9918-9931.
[74] Slator, C.; Molphy, Z.; McKee, V.; Long, C.; Brown, T.; Kellett, A. *Nucleic Acids Res.* **2018**, *46,* (6), 2733-2750.
[75] McGivern, T. J. P.; Afsharpour, S.; Marmion, C. J. *Inorganica Chimica Acta.* **2018**, *472*, 12-39.
[76] Li, Z.-R.; Li, J.; Cai, W.; Lai, J. Y. H.; McKinnie, S. M. K.; Zhang, W.-P.; Moore, B. S.; Zhang, W.; Qian, P.-Y.; Li, Z.-R.; et al. *Nature Chemistry 2019 11:10.* **2019**, *11,* (10).
[77] Poole, S.; Aning, O. A.; McKee, V.; Catley, T.; Nielsen, A. Y.; Thisgaard, H.; Johansson, P.; Menounou, G.; Hennessy, J.; Slator, C.; et al. *Nucleic Acids Res.* **2025**, *53,* (1).
[78] Melvin, M. S.; Tomlinson, J. T.; Saluta, G. R.; Kucera, G. L.; Lindquist, N.; Manderville, R. A. *J Am Chem Soc.* **2000**, *122,* (26), 6333-6334.
[79] Sakai-Kawada, F. E.; Ip, C. G.; Hagiwara, K. A.; Awaya, J. D. *Front Microbiol.* **2019**, *10*, 1715.
[80] Suryawanshi, R. K.; Patil, C. D.; Borase, H. P.; Salunke, B. K.; Patil, S. V. *Appl Biochem Biotechnol.* **2014**, *173,* (5), 1209-1221.

[81] D'Alessio, R.; Bargiotti, A.; Carlini, O.; Colotta, F.; Ferrari, M.; Gnocchi, P.; Isetta, A.; Mongelli, N.; Motta, P.; Rossi, A.; et al. *J Med Chem.* **2000**, *43,* (13), 2557-2565.
[82] Montaner, B.; Perez-Tomas, R. *Curr Cancer Drug Targets.* **2003**, *3,* (1), 57-65.
[83] Arivizhivendhan, K. V.; Boopathy, R.; Maharaja, P.; Mary, R. R.; Sekaran, G. *Rsc Advances.* **2015**, *5,* (84), 68621-68631.
[84] Melvin, M. S.; Calcutt, M. W.; Noftle, R. E.; Manderville, R. A. *Chem Res Toxicol.* **2002**, *15,* (5), 742-748.
[85] Guyard, L., Hapiot, P., Neta, P. *J. Phys. Chem. B.* **1997**, *101,* (29), 5698-5706.
[86] Wang, X.; Isbrandt, T.; Christensen, E. O.; Melchiorsen, J.; Larsen, T. O.; Zhang, S. D.; Gram, L. *Microbiol Spectr.* **2021**, *9,* (2), e0117121.
[87] Pabo, C. O.; Peisach, E.; Grant, R. A. *Annu Rev Biochem.* **2001**, *70*, 313-340.
[88] Boch, J.; Scholze, H.; Schornack, S.; Landgraf, A.; Hahn, S.; Kay, S.; Lahaye, T.; Nickstadt, A.; Bonas, U. *Science.* **2009**, *326,* (5959), 1509-1512.
[89] Doudna, J. A.; Charpentier, E. *Science.* **2014**, *346,* (6213), 1258096.
[90] Gaj, T.; Gersbach, C. A.; Barbas, C. F. *Trends Biotechnol.* **2013**, *31,* (7), 397-405.
[91] Bogdanove, A. J.; Voytas, D. F. *Science.* **2011**, *333,* (6051), 1843-1846.
[92] Charpentier, E. *Embo Mol Med.* **2015**, *7,* (4), 363-365.
[93] Fantoni, N. Z.; El-Sagheer, A. H.; Brown, T. *Chem Rev.* **2021**, *121,* (12), 7122-7154.
[94] Fox, K., R. ; Brown, T.; Rusling, D. A. *Chemical Biology.* **2018**, *Chapter 1*, 1-32.
[95] Chandrasekaran, A. R.; Rusling, D. A. *Nucleic Acids Res.* **2018**, *46,* (3).
[96] Pyne, A. L. B.; Noy, A.; Main, K. H. S.; Velasco-Berrelleza, V.; Piperakis, M. M.; Mitchenall, L. A.; Cugliandolo, F. M.; Beton, J. G.; Stevenson, C. E. M.; Hoogenboom, B. W.; et al. *Nature Communications.* **2021**, *12,* (1).
[97] Xodo, L. E.; Manzini, G.; Quadrifoglio, F.; van der Marel, G. A.; van Boom, J. H. *Nucleic Acids Res.* **1991**, *19,* (20), 5625-5631.
[98] Rusling, D. A. *Nucleic Acids Res.* **2021**, *49,* (13), 7256-7266.
[99] Klimkowski, P.; De Ornellas, S.; Singleton, D.; El-Sagheer, A. H.; Brown, T. *Org Biomol Chem.* **2019**, *17,* (24), 5943-5950.
[100] Walsh, S.; El-Sagheer, A. H.; Brown, T. *Chem Sci.* **2018**, *9,* (39), 7681-7687.
[101] Havre, P. A.; Gunther, E. J.; Gasparro, F. P.; Glazer, P. M. *Proc Natl Acad Sci U S A.* **1993**, *90,* (16), 7879-7883.
[102] Takasugi, M.; Guendouz, A.; Chassignol, M.; Decout, J. L.; Lhomme, J.; Thuong, N. T.; Helene, C. *Proc Natl Acad Sci U S A.* **1991**, *88,* (13), 5602-5606.
[103] Fox, K. R.; Brown, T. *Biochemical Society Transactions.* **2011**, *39,* (2).
[104] Leitner, D.; Schroder, W.; Weisz, K. *Biochemistry-Us.* **2000**, *39,* (19), 5886-5892.
[105] Li, H.; Broughton-Head, V. J.; Peng, G.; Powers, V. E.; Ovens, M. J.; Fox, K. R.; Brown, T. *Bioconjug Chem.* **2006**, *17,* (6), 1561-1567.

[106] Lacroix, L.; Arimondo, P. B.; Takasugi, M.; Helene, C.; Mergny, J. L. *Biochem Biophys Res Commun.* **2000**, *270,* (2), 363-369.
[107] Wittung, P.; Nielsen, P.; Norden, B. *Biochemistry-Us.* **1997**, *36,* (26), 7973-7979.
[108] Hansen, M. E.; Bentin, T.; Nielsen, P. E. *Nucleic Acids Res.* **2009**, *37,* (13), 4498-4507.
[109] Torigoe, H.; Sasaki, K.; Katayama, T. *J Biochem.* **2009**, *146,* (2), 173-183.
[110] Beaucage, S. L.; Caruthers, M. H. *Tetrahedron Letters.* **1981**, *22,* (20), 1859-1862.
[111] Caruthers, M. H. *Science.* **1985**, *230,* (4723), 281-285.
[112] Langer, P. R.; Waldrop, A. A.; Ward, D. C.; Langer, P. R.; Waldrop, A. A.; Ward, D. C. *Proceedings of the National Academy of Sciences.* **1981**, *78,* (11).
[113] Pon, R. T. **1993**.
[114] Menova, P.; Cahova, H.; Plucnara, M.; Havran, L.; Fojta, M.; Hocek, M. *Chem Commun (Camb).* **2013**, *49,* (41), 4652-4654.
[115] McGorman, B.; Fantoni, N. Z.; O'Carroll, S.; Ziemele, A.; El-Sagheer, A. H.; Brown, T.; Kellett, A. *Nucleic Acids Res.* **2022**, *50,* (10), 5467-5481.
[116] Goodchild, J. *Bioconjugate Chem.* **1990**, *1,* (3), 165-187.
[117] Miller, P. S. *Prog Nucleic Acid Re.* **1996**, *52*, 261-291.
[118] Chu, B. C.; Orgel, L. E. *Nucleic Acids Res.* **1989**, *17,* (12), 4783-4798.
[119] Manchanda, R.; Dunham, S. U.; Lippard, S. J. *J Am Chem Soc.* **1996**, *118,* (21), 5144-5145.
[120] Schliepe, J.; Berghoff, U.; Lippert, B.; Cech, D. *Angew Chem Int Edit.* **1996**, *35,* (6), 646-648.
[121] Bernal-Mendez, E.; Sun, J.-s.; González-Vílchez, F.; Leng, M. *New Journal of Chemistry.* **1998**, *22,* (12), 1479-1483.
[122] Schmidt, K. S.; Filippov, D. V.; Meeuwenoord, N. J.; van der Marel, G. A.; van Boom, J. H.; Lippert, B.; Reedijk, J. *Angewandte Chemie International Edition.* **2000**, *39,* (2), 375-377.
[123] Schmidt, K. S.; Boudvillain, M.; Schwartz, A.; van der Marel, G. A.; van Boom, J. H.; Reedijk, J.; Lippert, B. *Chemistry.* **2002**, *8,* (24), 5566-5570.
[124] Sharma, S. K.; McLaughlin, L. W. *J Am Chem Soc.* **2002**, *124,* (33), 9658-9659.
[125] Sharma, S. K.; McLaughlin, L. W. *J Inorg Biochem.* **2004**, *98,* (10), 1570-1577.
[126] Campbell, M. A.; Mason, T. M.; Miller, P. S. *Can J Chem.* **2007**, *85,* (4), 241-248.
[127] Campbell, M. A.; Miller, P. S. *J Biol Inorg Chem.* **2009**, *14,* (6), 873-881.
[128] Mergny, J. L.; Sun, J. S.; Rougee, M.; Montenaygarestier, T.; Barcelo, F.; Chomilier, J.; Helene, C. *Biochemistry-Us.* **1991**, *30,* (40), 9791-9798.
[129] Campbell, M. A.; Miller, P. S. *Bioconjugate Chem.* **2009**, *20,* (12).
[130] Graham, M. K.; Miller, P. S. *J Biol Inorg Chem.* **2012**, *17,* (8), 1197-1208.
[131] Graham, M. K.; Brown, T. R.; Miller, P. S. *Biochemistry-Us.* **2015**, *54,* (13), 2270-2282.
[132] Kolb, H. C.; Finn, M. G.; Sharpless, K. B. *Angew Chem Int Ed Engl.* **2001**, *40,* (11), 2004-2021.
[133] Seo, T. S.; Li, Z.; Ruparel, H.; Ju, J. *J Org Chem.* **2003**, *68,* (2), 609-612.

[134] Gierlich, J.; Burley, G. A.; Gramlich, P. M.; Hammond, D. M.; Carell, T. *Org Lett.* **2006**, *8,* (17), 3639-3642.
[135] Luu, T.; Gristwood, K.; Knight, J. C.; Jörg, M. *Bioconjugate Chem.* **2024**, *35,* (6).
[136] Agard, N. J.; Prescher, J. A.; Bertozzi, C. R. *J Am Chem Soc.* **2004**, *126,* (46), 15046-15047.
[137] Cabrera, D. G.; Koivisto, B. D.; Leigh, D. A. *Chemical Communications.* **2007**, (41).
[138] Hennessy, J.; McGorman, B.; Molphy, Z.; Farrell, N. P.; Singleton, D.; Brown, T.; Kellett, A. *Angew Chem Int Ed Engl.* **2022**, *61,* (3), e202110455.
[139] Hennessy, J.; Klimkowski, P.; Singleton, D.; Gibney, A.; Coche, M.; Farrell, N. P.; El-Sagheer, A. H.; Brown, T.; Kellett, A. *RSC Medicinal Chemistry.* **2023**.
[140] Dreyer, G. B.; Dervan, P. B. *Proc Natl Acad Sci U S A.* **1985**, *82,* (4), 968-972.
[141] Chu, B. C.; Orgel, L. E. *Proc Natl Acad Sci U S A.* **1985**, *82,* (4), 963-967.
[142] Chen, C. H.; Sigman, D. S. *Proc Natl Acad Sci U S A.* **1986**, *83,* (19), 7147-7151.
[143] Moser, H. E.; Dervan, P. B. *Science.* **1987**, *238,* (4827), 645-650.
[144] Strobel, S. A.; Dervan, P. B. *Science.* **1990**, *249,* (4964), 73-75.
[145] Strobel, S. A.; Moser, H. E.; Dervan, P. B. *J Am Chem Soc.* **1988**, *110,* (23), 7927-7929.
[146] Francois, J. C.; Saison-Behmoaras, T.; Barbier, C.; Chassignol, M.; Thuong, N. T.; Helene, C. *Proc Natl Acad Sci U S A.* **1989**, *86,* (24), 9702-9706.
[147] Komiyama, M.; Shiiba, T.; Takahashi, Y.; Takeda, N.; Matsumura, K.; Kodama, T. *Supramolecular Chemistry.* **1994**, *4,* (1), 31-34.
[148] Komiyama, M.; Takeda, N.; Takahashi, Y.; Uchida, H.; Shiiba, T.; Kodama, T.; Yashiro, M. *Journal of the Chemical Society-Perkin Transactions 2.* **1995**, (2), 269-274.
[149] Zelder, F. H.; Mokhir, A. A.; Kramer, R. *Inorg Chem.* **2003**, *42,* (26), 8618-8620.
[150] Bigey, P.; Pratviel, G.; Meunier, B. *Nucleic Acids Res.* **1995**, *23,* (19), 3894-3900.
[151] Joshi, R. R.; Ganesh, K. N. *Biochim Biophys Acta.* **1994**, *1201,* (3), 454-460.
[152] Lauria, T.; Slator, C.; McKee, V.; Müller, M.; Stazzoni, S.; Crisp, A. L.; Carell, T.; Kellett, A. *Chem-Eur J.* **2020**, *26,* (70), 16782-16792.
[153] Fantoni, N. Z.; McGorman, B.; Molphy, Z.; Singleton, D.; Walsh, S.; El-Sagheer, A. H.; McKee, V.; Brown, T.; Kellett, A. *Chembiochem.* **2020**, *21,* (24), 3563-3574.
[154] Panattoni, A.; El-Sagheer, A. H.; Brown, T.; Kellett, A.; Hocek, M. *Chembiochem.* **2020**, *21,* (7), 991-1000.
[155] Fantoni, N. Z.; Brown, T.; Kellett, A. *Chembiochem.* **2021**, *22,* (13), 2184-2205.
[156] Santos, G. D.; Shepherd, F. A.; Tsao, M. S. *Annu Rev Pathol-Mech.* **2011**, *6*, 49-69.
[157] Nicholson, R. I.; Gee, J. M.; Harper, M. E. *Eur J Cancer.* **2001**, *37 Suppl 4*, S9-15.

Chapter II

Project Rationale

April 2026

1 Project rationale

Metal complexes have played a central role in the development of chemotherapeutic agents for cancer treatment since the discovery of *cis*-platinum(II) drugs. Cisplatin and its derivatives, carboplatin and oxaliplatin, exert their cytotoxicity through DNA crosslinking, thereby disrupting cell machinery.[1] The clinical success of traditional crosslinking agents has inspired the design of new platinum-based drugs with alternative coordination environments and mechanisms of action[2] such as monofunctional platinum(II) complexes. Such examples include pyriplatin[3] and phenanthriplatin[4], which are capable of forming a single covalent bond with DNA and inhibit enzymatic activity. These systems are of particular interest as they can be chemically altered to incorporate aromatic ligands to facilitate enhanced DNA interaction.

In parallel, copper complexes have been extensively explored as artificial metallo-nucleases (AMNs) owing to their ability to oxidatively cleave DNA.[5] Using this principle, the drug candidate elesclomol[6] successfully entered clinical trials, and reached phase III before being discontinued.[7] While phenanthroline (Phen)-based Cu-AMNs have demonstrated efficient nuclease activity,[8] their therapeutic application has been hindered by limited selectivity and reliance on reductants for activation. Recent work on alternative ligand frameworks, such as di-copper complexes,[9, 10] colibactin[11] or the natural marine alkaloid prodigiosin,[12] has revealed that auto-catalytic or 'self-activating' Cu-AMNs can be generated, broadening the scope of metal-based DNA cleaving agents.

Despite their remarkable DNA reactivity, both platinum and copper complexes typically suffer from poor specificity, leading to *off*-target effects and dose-limiting toxicity. To overcome these limitations, research has shifted towards the conjugation of reactive metal centres to sequence-selective targeting vectors, most notably triplex-forming oligonucleotides (TFOs).[13-18] TFOs are single-stranded DNA that bind duplex DNA *via* Hoogsteen hydrogen bonds, allowing precise recognition of defined genomic sequences. Early Pt(II)- and Cu(II)-TFO hybrids demonstrated the potential of combining the chemical reactivity of metal complexes with the sequence specificity of TFOs, but their preparation remained challenging.[19]

The advent of click chemistry, particularly copper-catalysed azide-alkyne cycloaddition (CuAAC) and strain-promoted azide-alkyne cycloaddition (SPAAC), provided a powerful platform for generating metal-TFO hybrids.[20] While the application of TFOs is still limited by poor triplex stability, extensive methods have been developed for the modification of TFOs for enhanced triplex stability, including chemical modification such as 5-methylcytosine (5mC)[21], known to reduce the reliance on low pH for triplex formation, and the incorporation of thiazole orange (TO), which stabilises triplexes through intercalation.[22, 23] These strategies have been applied to TFOs targeting human immunodeficiency virus (HIV)[24] and the green fluorescent protein (*GFP*)[25-28] gene as proof-of-concept, and have shown enhanced targeting activity. Extending this work to biologically relevant human targets, such as the epidermal growth factor receptor (*EGFR*) gene—overexpressed in several cancers[29]—provides a meaningful step toward therapeutic application, as the *EGFR* sequence contains a polypurine motif compatible with triplex recognition.

This thesis aims to develop and evaluate metal-functionalised TFO hybrids that combine enhanced triplex stability with DNA damage activity for potential gene-silencing applications. Two classes of azide-modified metal complexes are investigated, monofunctional platinum(II) complexes with tridentate di-(2-picolyl)amine (DPA)-derived ligands (Figure II.1.a) and the copper complex of a prodigiosin derivative (Figure II.1.b).

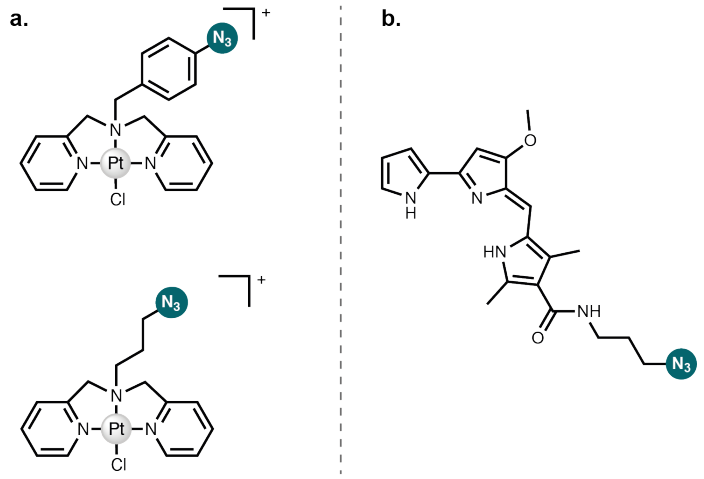


Figure II.1: Structures of: **a**. azide-functionalised monofunctional platinum(II) complexes with DPA-derived ligands; and **b**. the azide-modified prodigiosin target proposed in this project.

The approach integrates click chemistry as a modular conjugation platform to tether the active metal complexes to *EGFR*-targeting TFOs, to achieve either covalent DNA binding or oxidative cleavage (Figure II.2). Building on this, we developed a self-assembly assay to rapidly screen ligand-metal combinations for their compatibility with TFO click functionalisation and sequence-specific DNA cleavage activity. This approach establishes a versatile platform for the rapid evaluation of optimal conditions for AMN-TFO hybrid design.

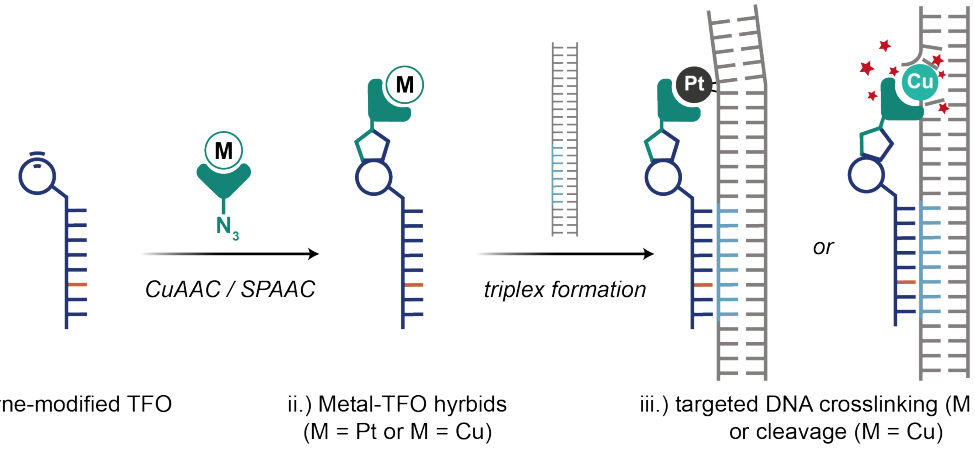


Figure II.2: Generation of gene editing metal-TFO hybrids using click chemistry for targeted crosslinking or cleavage.

The overall objectives of this thesis are: i) to develop *EGFR*-targeting TFOs and evaluate CuAAC and SPAAC conjugation strategies for optimally attaching Pt(II) chemotypes; ii) to prepare azide-functionalised monofunctional platinum(II) complexes bearing DPA-derived ligands (Figure II.1.a) and compare their DNA reactivity to that of earlier reported *cis*-platinum(II) analogues; iii) to evaluate and compare the adduct-formation efficiency of monofunctional Pt(II)-TFO hybrids with that of *cis*-Pt(II)-TFOs; iv) to design and synthesise a new azide-functionalised prodigiosin marine alkaloid (Figure II.1.b) capable of promoting copper-mediated, self-activated DNA cleavage; v) to investigate the sequence selectivity and DNA cleavage activity of prodigiosin-TFO hybrids in the presence of copper; and vi) to exploit the versatility of SPAAC to rapidly screen ligands for Cu-AMN-TFO hybrid applications.

2 References

[1] A., A. S. *Biomedical & Pharmacology Journal.* **2019**, *12,* (1), 7-15.

[2] Johnstone, T. C.; Wilson, J. J.; Lippard, S. J. *Inorganic Chemistry.* **2013**, *52,* (21).

[3] Lovejoy, K. S.; Serova, M.; Bieche, I.; Emami, S.; D'Incalci, M.; Broggini, M.; Erba, E.; Gespach, C.; Cvitkovic, E.; Faivre, S.; et al. *Mol Cancer Ther.* **2011**, *10,* (9), 1709-1719.

[4] Park, G. Y.; Wilson, J. J.; Song, Y.; Lippard, S. J.; Park, G. Y.; Wilson, J. J.; Song, Y.; Lippard, S. J. *Proceedings of the National Academy of Sciences.* **2012**, *109,* (30).

[5] Sigman, D. S.; Graham, D. R.; D'Aurora, V.; Stern, A. M. *J Biol Chem.* **1979**, *254,* (24), 12269-12272.

[6] Chen, S.; Sun, L.; Koya, K.; Tatsuta, N.; Xia, Z.; Korbut, T.; Du, Z.; Wu, J.; Liang, G.; Jiang, J.; et al. *Bioorg Med Chem Lett.* **2013**, *23,* (18), 5070-5076.

[7] O'Day, S. J.; Eggermont, A. M.; Chiarion-Sileni, V.; Kefford, R.; Grob, J. J.; Mortier, L.; Robert, C.; Schachter, J.; Testori, A.; Mackiewicz, J.; et al. *J Clin Oncol.* **2013**, *31,* (9), 1211-1218.

[8] Molphy, Z.; Prisecaru, A.; Slator, C.; Barron, N.; McCann, M.; Colleran, J.; Chandran, D.; Gathergood, N.; Kellett, A. *Inorg Chem.* **2014**, *53,* (10), 5392-5404.

[9] A, K.; M, O. C.; M, M.; M, M.; P, L.; G, R.; V, M.; B, C.; M, W.; S, M.; et al. *Dalton transactions (Cambridge, England : 2003).* **2011**, *40,* (5).

[10] Poole, S.; Aning, O. A.; McKee, V.; Catley, T.; Nielsen, A. Y.; Thisgaard, H.; Johansson, P.; Menounou, G.; Hennessy, J.; Slator, C.; et al. *Nucleic Acids Res.* **2025**, *53,* (1).

[11] Li, Z.-R.; Li, J.; Cai, W.; Lai, J. Y. H.; McKinnie, S. M. K.; Zhang, W.-P.; Moore, B. S.; Zhang, W.; Qian, P.-Y.; Li, Z.-R.; et al. *Nature Chemistry 2019 11:10.* **2019**, *11,* (10).

[12] Melvin, M. S.; Tomlinson, J. T.; Saluta, G. R.; Kucera, G. L.; Lindquist, N.; Manderville, R. A. *J Am Chem Soc.* **2000**, *122,* (26), 6333-6334.

[13] Bernal-Mendez, E.; Sun, J.-s.; González-Vílchez, F.; Leng, M. *New Journal of Chemistry.* **1998**, *22,* (12), 1479-1483.

[14] Chen, C. H.; Sigman, D. S. *Proc Natl Acad Sci U S A.* **1986**, *83,* (19), 7147-7151.

[15] Francois, J. C.; Saison-Behmoaras, T.; Barbier, C.; Chassignol, M.; Thuong, N. T.; Helene, C. *Proc Natl Acad Sci U S A.* **1989**, *86,* (24), 9702-9706.

[16] Miller, P. S. *Prog Nucleic Acid Re.* **1996**, *52*, 261-291.

[17] Moser, H. E.; Dervan, P. B. *Science.* **1987**, *238,* (4827), 645-650.

[18] Strobel, S. A.; Moser, H. E.; Dervan, P. B. *J Am Chem Soc.* **1988**, *110,* (23), 7927-7929.

[19] Schliepe, J.; Berghoff, U.; Lippert, B.; Cech, D. *Angew Chem Int Edit.* **1996**, *35,* (6), 646-648.

[20] Fantoni, N. Z.; El-Sagheer, A. H.; Brown, T. *Chem Rev.* **2021**, *121,* (12), 7122-7154.

[21] Leitner, D.; Schroder, W.; Weisz, K. *Biochemistry-Us.* **2000**, *39,* (19), 5886-5892.

[22] Klimkowski, P.; De Ornellas, S.; Singleton, D.; El-Sagheer, A. H.; Brown, T. *Org Biomol Chem.* **2019**, *17,* (24), 5943-5950.
[23] Walsh, S.; El-Sagheer, A. H.; Brown, T. *Chem Sci.* **2018**, *9,* (39), 7681-7687.
[24] Panattoni, A.; El-Sagheer, A. H.; Brown, T.; Kellett, A.; Hocek, M. *Chembiochem.* **2020**, *21,* (7), 991-1000.
[25] Fantoni, N. Z.; McGorman, B.; Molphy, Z.; Singleton, D.; Walsh, S.; El-Sagheer, A. H.; McKee, V.; Brown, T.; Kellett, A. *Chembiochem.* **2020**, *21,* (24), 3563-3574.
[26] Hennessy, J.; Klimkowski, P.; Singleton, D.; Gibney, A.; Coche, M.; Farrell, N. P.; El-Sagheer, A. H.; Brown, T.; Kellett, A. *RSC Medicinal Chemistry.* **2023**.
[27] Hennessy, J.; McGorman, B.; Molphy, Z.; Farrell, N. P.; Singleton, D.; Brown, T.; Kellett, A. *Angew Chem Int Ed Engl.* **2022**, *61,* (3), e202110455.
[28] Lauria, T.; Slator, C.; McKee, V.; Müller, M.; Stazzoni, S.; Crisp, A. L.; Carell, T.; Kellett, A. *Chem-Eur J.* **2020**, *26,* (70), 16782-16792.
[29] Mitsudomi, T.; Yatabe, Y. *Febs Journal.* **2010**, *277,* (2), 301-308.

Chapter III

Development and optimisation of TFO probes compatible with click chemistry for *EGFR*-targeted interactions

April 2026

1 Introduction

Platinum-based chemotherapeutics such as cisplatin and its derivatives oxaliplatin and carboplatin remain among the most widely used agents in cancer treatment.[1] Their use has however long been hindered by severe side effects, such as nephrotoxicity,[2] which arise from the lack of specificity to tumours and *off*-target DNA binding. One strategy to address these challenges involves tethering platinum complexes to gene-targeting vectors to improve tumour specificity and reduce systemic toxicity.[3]

Triplex-forming oligonucleotides (TFOs) have emerged as a promising tool for such targeted activity.[4-6] TFOs are single-stranded oligonucleotides that sequence-specifically bind duplex DNA through the formation of hydrogen bonds on the Hoogsteen face of DNA duplets. Parallel TFOs target extended polypurine tracts of DNA, allowing for site-specific DNA recognition that can be exploited for targeted delivery of small molecules or metal complexes. However, the stability of such triplexes under physiological conditions remains a limitation due to their low binding affinity and slow association kinetics at neutral pH. Chemical modifications such as 5-methylcytosine (5mC)[7] or thiazole orange (TO)[8] have been shown to significantly enhance triplex stability owing to 5mC being protonated at higher pH than canonical cytosine, and the stabilising intercalating property of TO.

With the advent of biorthogonal click chemistry,[9] new opportunities have emerged for the functionalisation of oligonucleotides. Copper-catalysed (CuAAC) and strain-promoted (SPAAC) azide-alkyne cycloadditions are widely used click reactions for this purpose.[10] These reactions, combined with solid-phase synthesis (SPS) of oligonucleotides,[11] enable site-specific attachment of diverse functional groups to DNA. Previous studies have demonstrated that CuAAC can be used to label internally octadiynyl-modified TFOs with *cis*-platinum(II) complexes,[12, 5] yielding hybrids capable of targeting a specific DNA sequence and forming intrastrand platinum adducts.

The CuAAC reaction is widely used for oligonucleotides functionalisation, but requires a copper(I) catalysis, typically generated *in situ* by reducing Cu(II) with a reductant, such as sodium-*L*-ascorbate (Na-*L*-asc), under inert atmosphere. These conditions can interfere with redox-active metal

ions, such as Pt(IV) complexes,[13-15] or multidentate metal-binding ligands, potentially disrupting coordination with the desired metal centre.[16] It also often requires high-performance liquid chromatography (HPLC) purification to remove copper residues,[17, 18] reducing yields and further increasing procedural complexity. By contrast, SPAAC proceeds under mild, copper-free, conditions[19] and may be more suited in biological environment.[20, 21] However, SPAAC typically requires longer reaction times[22, 23] and may show lower conversion rates.[23] Additionally, cycloalkynes, the strained alkyne substrates required for SPAAC, suffer from poor long-term stability and a propensity to undergo rearrangements, yielding products of identical molecular mass, but lacking the critical alkyne moiety.[24]

The aim of this chapter is to develop and optimise TFO probes that are compatible with click chemistry for epidermal growth factor receptor (*EGFR*)-targeted interactions. The compatibility of CuAAC and SPAAC for the functionalisation of TFOs with an azide-modified oxaliplatin analogue are assessed by developing two families of TFOs targeting the *EGFR*. For that reason, TFOs bearing an internal octadiynyl modification for CuAAC, and a TFO featuring a 5′-dibenzocyclooctone (DBCO) group for SPAAC were prepared. This work also aims to investigate the effect of 5mC and TO modification on triplex formation and stability. Therefore, both sets of TFOs incorporated modifications such as 5mC or TO to enhance triplex formation and each TFO was conjugated to an azide-modified oxaliplatin analogue. The resulting hybrids were evaluated for their purity, triplex-forming capabilities, and *EGFR*-targeting efficacy.

2 Materials and Methods

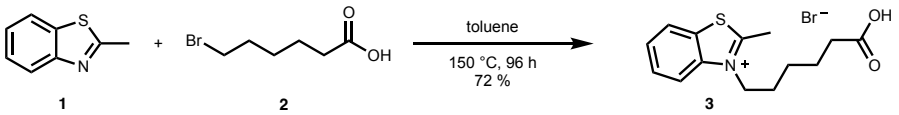
2.1 General method

Chemical reagents and high-performance liquid chromatography (HPLC) grade solvents were purchased from Merck, Tokyo Chemical Industry (TCI) or Fisher Scientific and used without further purification. ^{1}H and ^{195}Pt-NMR spectra were recorded on a Brucker AC 600 MHz NMR spectrometer. FTIR measurements were performed on a PerkinElmer Spectrum Two spectrometer. Electrospray ionization mass spectrometry (ESI-MS) was performed by collaborators in the University of Bath. All spectra are reported in Chapter VIII section A.1. Mass spectrometry for oligonucleotides was conducted by collaborators in ATDBio. All spectra are reported in Chapter VIII section A.2. PAGE gels were visualised on a Syngene G:Box Mini 9 gel documentation system and all samples were quenched with loading dye (6×, 2.5% Ficoll®-400, 11 mM EDTA, 3.3 mM Tris-HCl, 0.017% SDS, 0.015% bromophenol blue, pH 8.0, Thermo Fisher) before loading on PAGE gels. PAGE gels were prepared using 29:1 acrylamide:bis-acrylamide in the presence of Tris Acetate (TA, pH 6.0, 50 mM), $MgCl_2$ (5 mM), NaCl (75 mM), TEMED (Thermo Fisher Scientific, 0.2%) and ammonium persulfate (APS, 0.05%). Octadiynyl-modified TFOs were synthesised using solid-phase synthesis according to standard methods[25] and deprotected using aqueous ammonia. TFOs were purified *via* reverse phase HPLC (RP-HPLC) in 0.1 M trimethylammonium bicarbonate (TAB) with 10–30% acetonitrile and desalted using NAP-25 columns (Cytiva). CuAAC-capable TFOs were labelled with TO and Pt-N_3-Oxali, prepared according to Hennessy *et al.*,[5] during a secondment to the group of Prof. Tom Brown in the University of Oxford using NHS ester TO_{B6}.[8] 5′-DBCO TFOs were synthesised and labelled with TO similarly by collaborators in ATDBio.

2.2 Synthesis of NHS-ester TO_{B6}

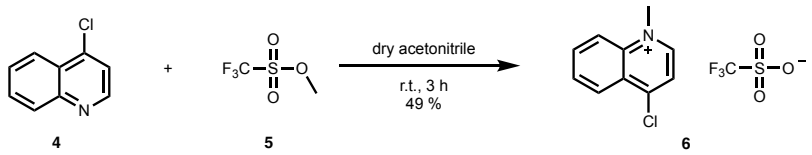
Reaction protocols were adapted from the literature method as reported by Klimkowski *et al*.[26] Spectroscopy data for all compounds was confirmed with the literature.

2.2.1 Synthesis of 3-(5-carboxypentyl)-2-methylbenzo[d]thiazol-3-ium bromide



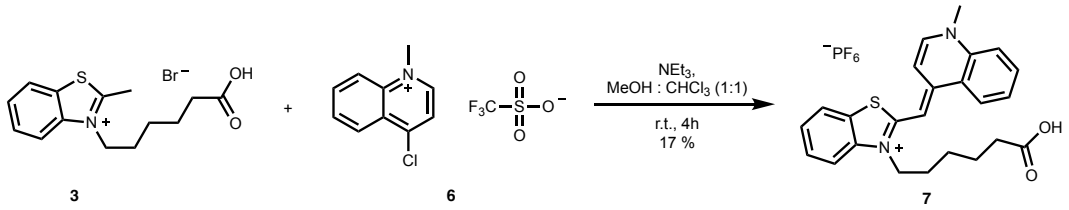
In 10 mL toluene, 6-bromohexanoic acid (4.135 g, 21.20 mmol, 1 eq.) was dissolved and 2-methylbenzothiazole (3.8 mL, 29.87 mmol, 1.4 eq.) was added. The resulting mixture was stirred under reflux at 150 °C for 96 h. After cooling down to room temperature, the obtained precipitate was isolated by filtration and washed with 5 x 15 mL diethyl ether, yielding 5.219 g, 15.23 mmol of an off-white powder with a 72% yield. ^{1}H NMR (DMSO-d_6) δ (ppm) 12.05 (s, 1H), 8.43 (m, 1H), 8.33 (d, J = 8.5 Hz, 1H), 7.89 (ddd, J = 8.5, 7.2, 1.3 Hz, 1H), 7.80 (ddd, J = 8.2, 7.2, 1.0 Hz, 1H), 4.70 (t, 2H), 3.21 (s, 3H), 2.23 (t, J = 7.3 Hz, 2H), 1.85 (quint, J = 7.8 Hz, 2H), 1.56 (quint, J = 7.3 Hz, 2H), 1.48 – 1.43 (m, 2H).

2.2.2 Synthesis of 4-chloro-1-methylquinolin-1-ium trifluoromethanesulfonate



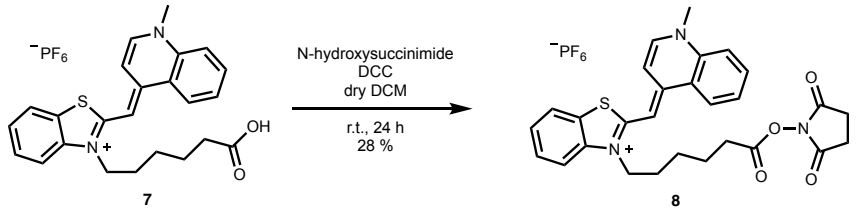
To a solution of 4-chloroquinoline (996.2 mg, 6.09 mmol, 1 eq.) in 10 mL dry acetonitrile, methyl trifluoromethanesulfonate (666 µL, 6.09 mmol, 1 eq.) was added. The mixture was stirred at room temperature (r.t.) under inert atmosphere for 3 h before 10 mL of diethyl ether were added. The resulting precipitate was isolated by gravity filtration and washed with diethyl ether, yielding 981.8 mg, 3.00 mmol of white crystals with a 49% yield. ^{1}H NMR (DMSO-d_6) δ (ppm) 9.50 (d, *J* = 6.3 Hz, 1H), 8.63 – 8.56 (m, 2H), 8.51 (d, *J* = 6.3 Hz, 1H), 8.38 (ddd, *J* = 8.7, 7.0, 1.4 Hz, 1H), 8.19 (ddd, *J* = 8.2, 7.0, 1.0 Hz, 1H), 4.61 (s, 3H).

2.2.3 Synthesis of (E)-3-(5-carboxypentyl)-2-((1-methylquinolin-4(1H)-ylidene)methyl)benzo[d]thiazol-3-ium hexafluorophosphate (TO_{B6})



4-chloro-1-methylquinolin-1-ium trifluoromethanesulfonate (586.0 mg, 1.79 mmol, 1.2 eq.) was dissolved in 20 mL dry DCM and 3-(5-carboxypentyl)-2-methylbenzo[d]thiazol-3-ium bromide (513.2 mg, 1.49 mmol, 1 eq.) was added together with 20 mL of dry MeOH and anhydrous triethylamine (0.5 mL, 3.73 mmol, 2.5 eq.). The mixture was stirred covered from light at room temperature for 15 min before 300 mL diethyl ether was added to reveal a precipitate that was isolated by vacuum filtration and washed with diethyl ether. The crude product was redissolved in 21 mL THF and 20 mL H_2O before addition of LiOH (114.2 mg, 4.77 mmol, 3.2 eq.). The mixture was stirred at room temperature in the dark overnight. 16 mL of 2.5% HCl were added, and the product was extracted using 4 x 40 mL of a 4:1 mixture of DCM/IPA. The organic phase was dried over $MgSO_4$, filtered and evaporated under reduced pressure affording 0.73 g, 1.3 mmol of a red powder. Salt metathesis was performed by adding $NaPF_6$ (1.120 g, 6.66 mmol, 5 eq. of the intermediate product) to a stirred solution of the red powder in 600 mL of a 10:34 mix of IPA/H_2O. The mixture was stirred in the dark at room temperature overnight before the precipitate was isolated by vacuum filtration and washed with 2 x 10 mL of 4:1 DCM/IPA and 2 x 15 mL H_2O, yielding 135.7 mg, 0.25 mmol of TO_{B6} with a 17% yield. ^{1}H NMR (DMSO-d_6) δ (ppm) 8.74 (dd, J = 8.8, 1.4 Hz, 1H), 8.62 (d, J = 7.2 Hz, 1H), 8.09 – 8.01 (m, 3H), 7.80 (ddd, J = 8.3, 6.9, 1.3 Hz, 1H), 7.78 (d, J = 8.3 Hz, 1H), 7.61 (ddd, J = 8.4, 7.3, 1.3 Hz, 1H), 7.45 – 7.39 (m, 2H), 6.94 (s, 1H), 4.63 (t, J = 7.5 Hz, 2H), 4.18 (s, 3H), 2.20 (t, J = 7.3 Hz, 2H), 1.81 (quint, J = 7.6 Hz, 2H), 1.59 (quint, J = 7.3 Hz, 2H), 1.51 – 1.46 (m, 2H).

2.2.4 *Synthesis of (E)-3-(6-((2,5-dioxopyrrolidin-1-yl)oxy)-6-oxohexyl)-2-((1-methylquinolin-4(1H)-ylidene)methyl)benzo[d]thiazol-3-ium hexafluorophosphate (NHS ester TO_{B6})*



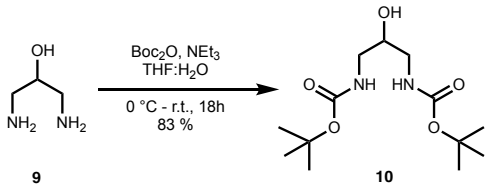
7 8

Under inert atmosphere, a solution of dicyclohexylcarbodiimide (101.3 mg, 0.49 mmol, 2 eq.) in 20 mL DMF was added to TO_{B6} (135.7 mg, 0.25 mmol, 1 eq.) followed by a solution of N-hydroxysuccinimide (85.1 mg, 0.74 mmol, 3 eq.) in 20 mL DMF. The resulting mixture was stirred in the dark under inert atmosphere overnight. 50 mL of 5% HCl were added, and the product was extracted with 3 x 30 mL DCM. Combined organic phases were washed with 3 x 20 mL H_2O, dried over $MgSO_4$ and evaporated to dryness before being purified by column chromatography using a 10 – 50% gradient of acetonitrile in DCM, yielding 87.0 mg, 0.13 mmol of NHS ester TO_{B6} with a 54% yield. ^{1}H NMR (DMSO-d_6) δ (ppm) 8.74 (d, *J* = 8.4 Hz, 1H), 8.63 (d, *J* = 7.2 Hz, 1H), 8.09 – 8.01 (m, 3H), 7.81 – 7.76 (m, 2H), 7.63 – 7.60 (m, 1H), 7.45 – 7.40 (m, 2H), 6.94 (s, 1H), 4.63 (t, *J* = 7.5 Hz, 2H), 4.19 (s, 3H), 2.80 (s, 4H), 2.69 (t, *J* = 7.3 Hz, 2H), 1.85 (q, *J* = 7.7 Hz, 2H), 1.72 (q, *J* = 7.5 Hz, 2H), 1.59 (q, *J* = 8.1 Hz, 2H). IR (cm^{-1}): 2925, 2865, 1813, 1783, 1734, 1666, 1616, 1545, 1506, 1465, 1377, 1322, 1226, 1206, 1164, 834, 754, 557. ESI-MS calc. for $C_{28}H_{28}N_3O_4S^+$ $[M]^+$: 502.18. Found: 502.18.

2.3 Synthesis of Pt-N_3-Oxali

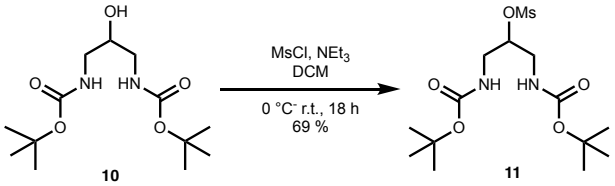
Reaction protocols were adapted from the literature method as reported by Hennessy *et al*[5]. Spectroscopy data for all compounds was coherent with the literature.

2.3.1 Synthesis of Di-tert-boc-2-hydroxy-1,3-diaminopropane



To a solution of 1,3-diamino-2-propanol (2.000 g, 22.19 mmol, 1 eq.) and triethylamine (6.2 mL, 44.38 mmol, 2 eq.) in a 1:1 THF/H_2O mix (80 ml) stirring at 0 °C was added di-tert-butyl dicarbonate (12.112 g, 55.48 mmol, 2.5 eq.) in THF (40 ml). The resulting solution was stirred at r.t. overnight. THF was removed in vacuo and approx. 40 ml of distilled H_2O was added to the solution before extraction with ethyl acetate (3 x 50 ml). Organic layer was dried over $MgSO_4$, and solvent removed in vacuo to yield 5.368 g, 18.49 mmol, of the desired product as a white solid, with an 83% yield. ^{1}H NMR ($CDCl_3$) δ (ppm) 5.11 (s, 2H), 3.74 (tt, J = 5.6, 4.7 Hz, 1H), 3.27 – 3.14 (m, 4H), 1.44 (s, 18H).

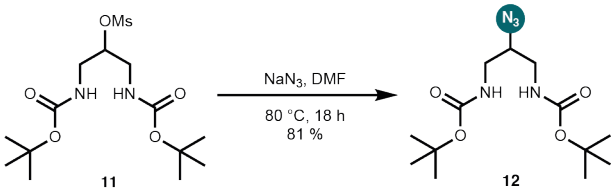
2.3.2 Synthesis of Di-tert-boc-2-methanesulfonyl-1,3-diaminopropane



Di-tert-boc-2-hydroxy-1,3-diaminopropane (2.872 g, 9.89 mmol, 1 eq.) and triethylamine (4.1 mL, 29.42 mmol, 3 eq.) were dissolved in 70 ml anhydrous DCM under an argon atmosphere. Methanesulfonyl chloride (1.5 mL, 19.76 mmol, 2 eq.) was dissolved in 20 ml anhydrous DCM and added dropwise with stirring over 30 minutes at 0 °C. The mixture was allowed to gradually warm to r.t. and stirred overnight. 30 ml DI H_2O was added to the mixture to react with excess MsCl and stirred for 4 h. The organic layer was isolated and washed with 25 mL 10% $NaHCO_3$ and 2 x 30 mL brine. The organic layer was dried over $MgSO_4$ and evaporated to dryness under reduced pressure to afford 3.202 g (8.69 mmol) of a pale yellow/beige solid, with an 88% yield. ^{1}H NMR

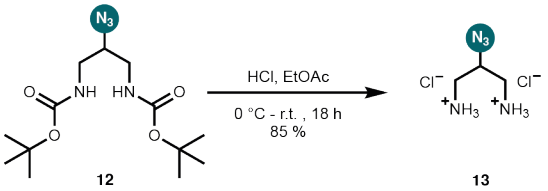
($CDCl_3$) δ (ppm) 5.15 (s, 2H), 4.66 (s, 1H), 3.52 – 3.48 (m, 2H), 3.39 – 3.29 (dt, J = 14.9, 5.8 Hz, 2H), 3.10 (s, 3H), 1.44 (s, 18H).

2.3.3 Synthesis of Di-tert-boc-2-azido-1,3-diaminopropane



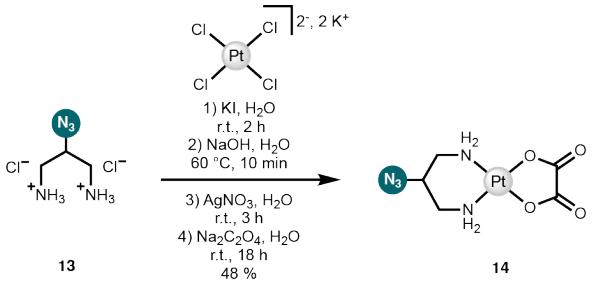
To a solution of di-tert-boc-2-methanesulfonyl-1,3-diaminopropane (3.000 g, 8.16 mmol, 1 eq.) in 20 ml anhydrous DMF, NaN_3 (2.122 g, 32.64 mmol, 4 eq.) was added and the mixture was stirred at 80 °C for 18 h. The mixture was allowed to cool to ambient temperature, poured into approx. 20 ml DI H_2O and further cooled to 0 °C prior to filtering to obtain 2.155 g, 6.83 mmol of a white solid product, with an 84% yield. ^{1}H NMR ($CDCl_3$) δ (ppm) 5.05 (s, 2H), 3.65 (t, J = 5.8 Hz, 1H), 3.39 – 3.37 (m, 2H), 3.14 – 3.11 (dd, J = 13.4, 6.8 Hz, 2H), 1.45 (s, 18H).

2.3.4 Synthesis of 2-azidopropane-1,3-diamine dihydrochloride



To a solution of di-tert-boc-2-azido-1,3-diaminopropane (2.000 g, 6.34 mmol, 1 eq.) in ethyl acetate (15 ml) was added 7.4 mL of aqueous 6 M HCl, dropwise with stirring at 0 °C. The reaction mixture was stirred at 0 °C for 30 mins followed by stirring for 18 h at r.t. and cooling at 5 °C overnight. The resulting white precipitate was filtered and washed several times with ethyl acetate to afford 880.1 mg, 4.68 mmol of the product as a white crystalline solid, with a 74% yield. ^{1}H NMR (DMSO-d_6) δ (ppm) 8.47 (s, 6H), 4.28 – 4.23 (ddt, J = 12.9, 8.8, 4.5 Hz, 1H), 3.17 – 3.14 (dd, J = 13.5, 3.9 Hz, 2H), 2.92 – 2.89 (dd, J = 13.5, 9.1 Hz, 2H). IR (cm^{-1}): 3061, 2956, 2886, 2850, 2536, 2135, 2079, 1592, 1511, 1471, 1361, 1280, 1203, 1082.

2.3.5 *Synthesis of* cis-*[Pt(2-azidopropane-1,3-diamine)(Oxalate)] (Pt-N_3-Oxali)*



To a solution of K_2PtCl_4 (300.0 mg, 0.72 mmol, 1 eq.) in approx. 8 ml DI H_2O was added KI (1.200 g, 7.23 mmol, 10 eq.) and the mixture was stirred for 2 h. A solution of 2-azidopropane-1,3-diamine dihydrochloride (136.2 mg, 0.72 mmol, 1 eq.) in 3 ml aqueous NaOH (57.9 g, 1.45 mmol, 2 eq.) was then added dropwise to the stirring mixture. Subsequently, the entire mixture was then heated at 60 °C for 10 mins, cooled to 0 °C and filtered to obtain brown/ tan solid product. Sequential washes with DI H_2O, MeOH and diethyl ether (5 x 5 ml) followed by drying over vacuum afforded *cis*-[Pt(2-azidopropane-1,3-diamine)I_2] as a brown solid. *Cis*-[Pt(2-azidopropane-1,3-diamine)I_2] (351.7 g, 0.62 mmol, 1 eq.) was suspended in approx. 30 ml DI H_2O and a 5 ml aqueous solution of $AgNO_3$ (212.2 mg, 1.25 mmol, 2 eq.) was then added dropwise with stirring. The solution was stirred for 3 h before filtering through a 0.22 µm Millipore pad to remove AgI. An aqueous solution (4 mL) of sodium oxalate (188.4 mg, 1.40 mmol, 1 eq.) was added to the retained filtrate and the entire solution was stirred for 18 h in the dark. The solution was filtered through a 0.45 µm Millipore pad to obtain 126.3 mg, 0.32 mmol of a grey solid, with a 72% yield. ^{1}H NMR (DMSO-d_6) δ (ppm) 5.77 (d, J = 11.7 Hz, 2H), 5.44 (d, J = 9.9 Hz, 2H), 4.00 – 3.98 (m, 1H), 2.62 - 2.58 (m, 2H), 2.56 - 2.52 (m, 2H). ^{195}Pt NMR (129 MHz, DMSO-d_6) δ -1972.17. IR (cm^{-1}): 3182, 3092, 2106 (N_3), 1654, 1388, 1248, 1212, 818. ESI-MS calc. for $C_5H_9N_5O_4{}^{195}Pt^+$ $[M+Na]^+$: 421.02. Found: 421.02.

2.4 Post-synthetic labelling of TFOs

2.4.1 One-pot TO_{B6} NHS ester (8) and CuAAC labelling of octadiynyl-modified TFOs.

TFO (20 nmol) was dissolved in 12 µL of carbonate buffer ($NaHCO_3$/Na_2CO_3, 0.5 M pH 8.7), and NHS-ester TO_{B6} (8, 400 nmol, 20 eq. for one TO incorporation, and 800 nmol, 40 eq. for the incorporation of two TO) was added. The resulting mixture was stirred at 25 °C for 2.5 h. 170 µL of Millipore water, 210 µL of DMF, Pt-N_3-Oxali (14, 200 nmol, 10 eq.) and Cu-THPTA (200 nmol, 10 eq.) were added. The resulting solution was degassed with argon for 5 min, and Na-*L*-asc (400 nmol, 20 eq.) was added. The solution was stirred at 30 °C for 18 h in the dark, before being desalted over a NAP 5 column, and purified *via* RP-HPLC (45 to 80% gradient of A: 0.1 M triethylamine bicarbonate in 1:1 acetonitrile/H_2O, pH 7.3, in B: 0.1 M triethylamine bicarbonate in H_2O, pH 7.3). The resulting hybrids were characterised by mass spectrometry. Expected and observed ESI-MS results for the molecular ion masses are as shown in Table III.1.

2.4.2 SPAAC-labelling of 5'-DBCO TO-labelled TFOs

In a total volume of 50 µL of 9:1 molecular grade (NF) H_2O / dimethylformamide, TO-labelled DBCO-TFO (1 nmol) and Pt-N_3-Oxali (10 nmol, 10 eq.) were mixed and incubated at 37 °C, 300 rpm for 18 h. The Pt-Oxali-TFOs were then subjected to NAP-5 column purification, were freeze-dried overnight, and characterised by mass spectrometry. Expected and observed ESI-MS results for the molecular ion masses are as shown in Table III.1.

2.5 PAGE characterisation of the Pt(II)-TFO hybrids

2.5.1 Migration profile of the hybrids

CuAAC and SPAAC reactions were monitored by PAGE. Pt-TFO hybrids (30 pmol) were diluted in molecular biology grade H_2O to reach a total volume of 10 µL, and 2 µL loading dye was added. Non-clicked control octadiynyl-TFOs or DBCO-TFOs were prepared similarly. All samples were loaded onto gels prepared as described in section 2.1. PAGE was run in 50 mM TA buffer pH 6.0 at 70 V for 4 h and visualised as described in section 2.1.

2.5.2 Triplex formation activity of CuAAC- and SPAAC-generated Pt(II)-TFO hybrids

Samples were prepared in a total volume of 10 µL containing target duplex (0.5 pmol) and TFO hybrids (50 pmol, 100 eq. to target duplex) in phosphate buffer (10 mM PO_4^{3-}, 150 mM NaCl, 10 mM $MgCl_2$, pH 6.0) and incubated at 37 °C for 1 h. Loading dye was added and the samples were loaded onto gels prepared as described in general methods. PAGE was run in 50 mM TA buffer pH 6.0 at 70 V for 4 h and visualised as described in section 2.1.

3 Results and discussion

3.1 Synthesis of NHS ester TO_{B6} and Pt-N_3-Oxali

3.1.1 Synthesis of NHS ester TO_{B6}

A carboxylic acid thiazole orange with a C6 linker on the benzothiazole moiety (TO_{B6}) was synthesised according to the method reported by Walsh *et al*.[8] and Klimkowski *et al.*[25] before being activated with an NHS ester (Figure III.1). Briefly, 2-methylbenzothiazole was condensed with the alkylating agent 6-bromohexanoic acid with a 72% yield, while 4-chloroquinoline was methylated by the halo-alkylating agent methyl trifluoromethanesulfonate creating the quinolinium salt with a 49% yield. The obtained intermediates were then condensed, with the thiazole intermediate acting as a nucleophile, attaching at the 2-position of the benzothiazolium ring to form the methylene bridge linking the benzothiazole to the quinoline moiety. Salt metathesis was then performed, yielding the PF_6^- salt of TO_{B6} with a 17% yield. Finally, the NHS ester-activated TO_{B6} was prepared by activation of the carboxylic acid group using DCC, followed by esterification using *N*-hydroxysuccinimide with a 28% yield. Each intermediate of the synthesis was protected from light to prevent degradation of the fluorophore.

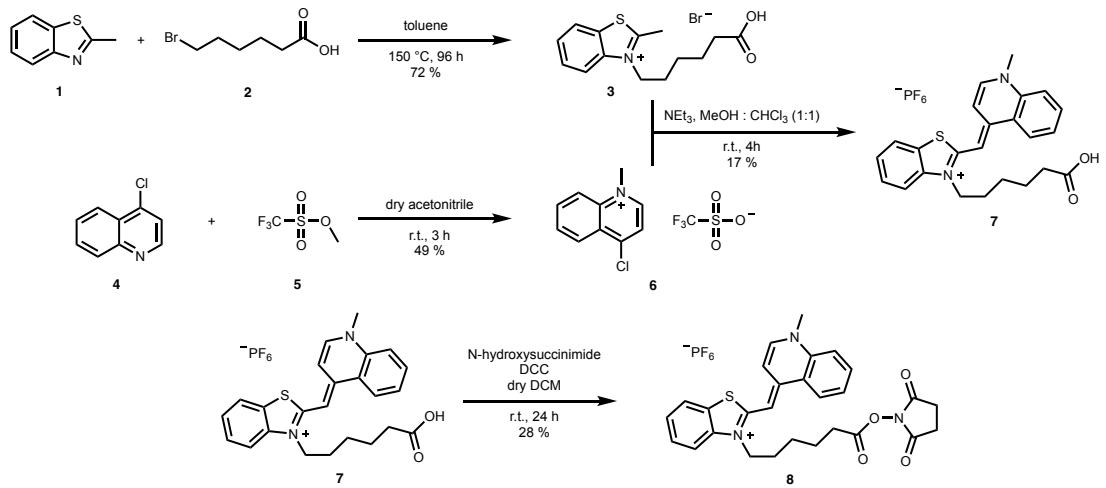


Figure III.1: Total synthesis of NHS-ester thiazole orange B6 (TO_{B6}).

3.1.2 Synthesis of Pt-N_3-Oxali

Pt-N_3-Oxali was prepared using the procedure reported by Hennessy *et al.*[5] (Figure III.2). Here, 1,3-diamino-2-propanol was protected using Boc_2O, with an 83% yield. The hydroxy-group on di-tert-boc-2-hydroxy-1,3-

diaminopropane was then activated by mesylation, using methanesulfonyl chloride with an 88% yield. As the sulfonate group was a good leaving group, it enabled the substitution with an azide, using sodium azide in DMF. The azide ligand obtained with an 84% yield was finally deprotected and conserved as a salt to increase the stability and safety of the ligand, as it contains a high nitrogen to carbon ratio. This stable crystalline salt, obtained with an 80% yield has been shown to be an efficient bidentate chelator for *cis*-platinum(II) while enabling great click orthogonality. In parallel, the chloride ligands of tetrachloroplatinate(II) were substituted with iodine ligands, enabling the *cis*-coordination of the 2-azidopropane-1,3-diamine dihydrochloride ligand. Silver nitrate was used to replace the iodine ligands by nitrate for efficient coupling of the oxalate ligand. Pt-N_3-Oxali was fully characterised by MS, IR and NMR, which were all coherent with literature value. Due to the labile nature of the ancillary ligand, and the presence of azide on the complexes, the compounds were stored in the dark and at low temperature. This synthetic route allowed the preparation of azide-functionalised oxaliplatin analogue, which retains the labile ligand present in the well-studied model, but the inert ligands are replaced by 2-azidopropane-1,3-diamine compatible with square planar coordination sphere while enabling click chemistry labelling of alkyne-modified TFOs.

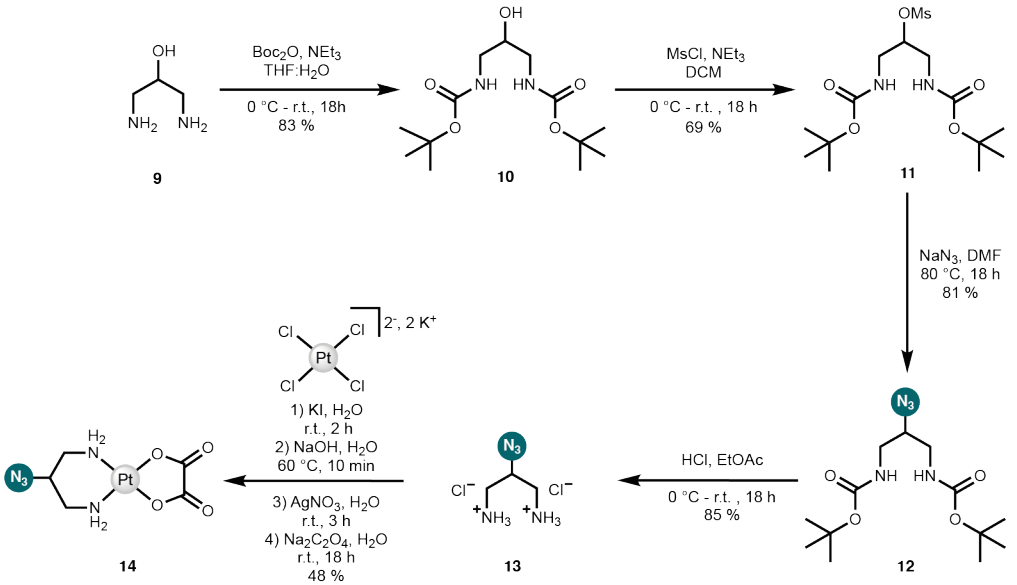


Figure III.2: Synthesis of Pt-N_3-Oxali.

3.2 Target selection and TFO design

3.2.1 Targeting the EGFR-*gene*

The *EGFR* gene encodes a receptor protein present at the surface of cells that signals cell growth and development.[27] This gene is overexpressed in various cancer types, including non-small cell lung cancer (NSCLC), breast cancer, head and neck tumours, and brain cancer,[28-30] leading to cell proliferation and survival, which favours disease progression and resistance to standard therapy.[31] Targeting TFOs to the *EGFR* gene could therefore have therapeutic applications in cancer treatment. TFOs containing 19 nucleotides were designed to target exon 5 of the *EGFR* gene, which has a poly-purine tract with only two pyrimidine interruptions, or inversion sites, compatible with triplex formation (Figure III.3). To target this coding region of the gene, parallel triplexes were designed, with T and protonated C forming Hoogsteen hydrogen bonds with AT and GC base pairs, generating the base triplets T·AxT and C·GxC$^+$, respectively. The two inversion sites present on the target strand were paired with G, T or A (*vide infra*). The TFO sequence was long enough to promote stable triplex formation and to minimise the potential of alternative binding sites within the target gene. The target region was investigated for any obvious secondary structure such as a G-quadruplex or a stem-loop. These motifs could emerge if 4 repetitions of at least 3 adjacent G were present and separated by 1 to 7 nucleotides ($G_{\geq 3}N_{1\text{-}7}G_{\geq 3}N_{1\text{-}7}G_{\geq 3}N_{1\text{-}7}G_{\geq 3}$) in the case of G-quadruplexes,[32] or by two complementary motifs of 3 nucleotides (or more) separated by up to 10 nucleotides in the case of stem-loops. Finally, a target duplex, which is a 40 bp region of the *EGFR* gene that contains the triplex recognition domain, was also synthesised.

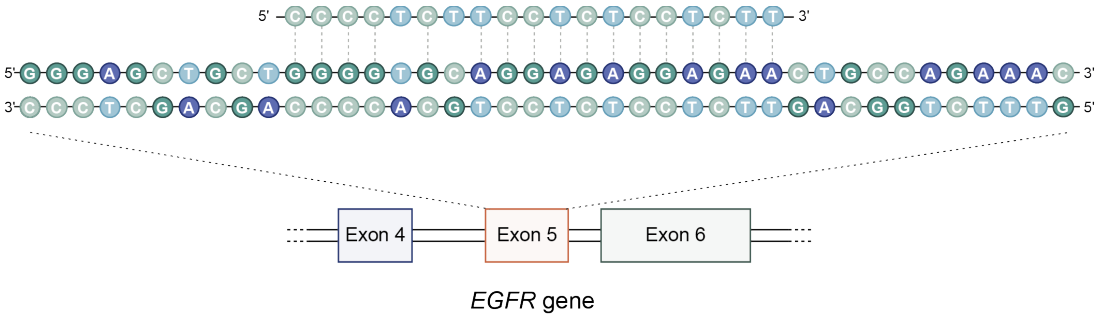


Figure III.3: Triplex recognition domain on the 5th exon of the *EGFR* gene for parallel triplex formation.

3.2.2 Optimisation of TFOs for triplex stabilisation

To improve the binding affinity of the TFOs to the target duplex, various modifications were incorporated within the TFO sequence. All cytosine nucleobases in the TFOs were replaced with 5mC (Figure III.4.a.), which is known to improve binding kinetics at neutral pH. Two positions were selected for the introduction of an amine-modified nucleobase for TO incorporation (Figure III.4.b.), one proximate to the 5′-end (X_1) and the other to the 3′-end (X_2) (Figure III.4.c.). Position (X_1) is close to an inversion site, and to the internal octadiynyl modification of CuAAC-compatible TFOs. To investigate the impact of both the location and the number of TO incorporations, three different TFOs were designed for each family of probes. TFO construct 1 (C1 for the CuAAC compatible TFO, and S1 for the SPAAC compatible congener) contain one TO modification at position (X_1), TFO construct 2 (C2 and S2) have 1 TO at position (X_2), and TFO construct 3 (C3 and S3) have two TO modifications, with one at (X_1) and the second at (X_2). This design also sought to determine if the presence of a TO modification binding at an inversion site could help overcome destabilisation. Additionally, the probe design enabled analysis of whether the presence of TO close to the CuAAC site in C1 and C3 could help address the destabilisation resulting from the Pt(II) complex, or instead generated hindrance and further destabilisation.

Studies have examined the effect of TFO nucleobase interactions at inversion sites with G and T found to induce the least destabilisation when aligned opposite an inversion site within the target duplex. Whether the target strand has a T or a C, the alignment of a G base is least destabilising, followed closely by T.[33] In the case of the CuAAC-compatible TFOs, the T and C inversions were paired with an A and a G, respectively, according to Watson-Crick base pairing, while in the SPAAC-compatible TFOs, the T and C interruptions were both paired with a T (see underlined nucleotides in Figure III.4.c). T was selected instead of G as the TFOs needed to be compatible with monofunctional Pt(II) complexes, which can covalently bind to a single G nucleobase.[34] As T was reported to be the second most stabilising base at an inversion site after G, it was selected at both inversion positions in the SPAAC-compatible TFOs to minimise unwanted crosslinking during subsequent SPAAC labelling with monofunctional Pt(II).

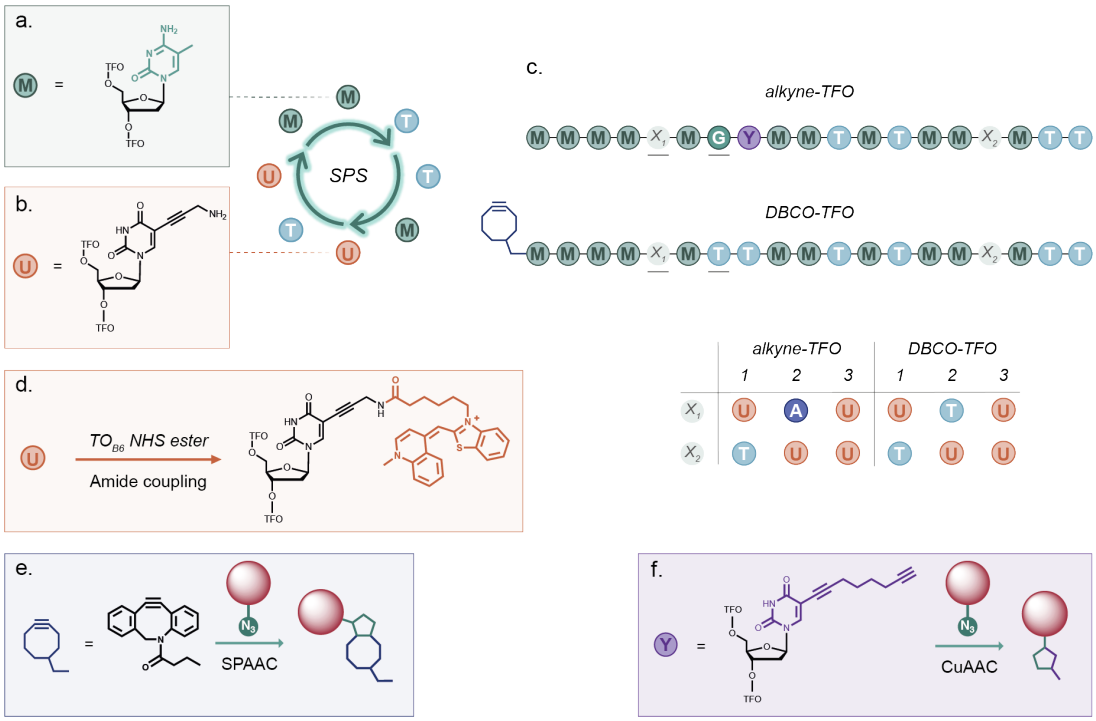


Figure III.4: Preparation of TFO hybrids. **a**. Structure of 5mC. **b**. Structure of amine-modified dU monomer. **c**. Sequence of the CuAAC- and SPAAC-compatible TFOs (C1, C2, C3 and S1, S2, S3). **d**. Amide coupling on the amine-modified dU using NHS-ester TO$_{B6}$. **e**. Structure of the SPAAC-capable DBCO monomer. **f**. Structure of the CuAAC-capable alkyne-modified dU.

3.2.3 Strategies for labelling of TFOs

To site-specifically incorporate two different moieties on the TFOs, *i.e.* TO and oxaliplatin in this chapter, two different labelling methods were selected. Click chemistry and amide coupling are the standard for nucleic acid labelling, and do not interfere with each other. SPS enabled the custom insertion of an amide-modified nucleobase (Figure III.4.d.) at any desired position. This nucleobase is a suitable substrate for NHS ester coupling and using the NHS-ester activated TO$_{B6}$ allowed for a more efficient labelling in milder conditions than using the carboxylic acid alternative, which was important given the small scale at which the reactions were performed. The TO labelling was performed in carbonate buffer, without any coupling agent, and the reaction was complete after 2.5 hours.

A SPAAC-compatible, DBCO modification (Figure III.4.e.) was introduced post-synthetically onto the phosphate backbone at the 5′ end. As SPS synthesises the DNA from the 3′ to the 5′ end, adding the DBCO at the 5′-end, *i.e.* at the end of the final SPS cycle, avoided exposing DBCO to the conditions of SPS which could degrade the DBCO group. For CuAAC, an

alkyne-modified nucleobase (Figure III.4.f.) was inserted at position 8 on the TFOs. The TO labelling and CuAAC were completed in the same reaction without isolating or purifying the intermediate, but HPLC purification was required post-synthetically. In the case of the DBCO-modified TFOs, the SPAAC reaction on the TO-TFOs yielded hybrids with sufficient purity without the need for HPLC purification.

3.3 Comparative investigation of CuAAC and SPAAC for TFO conjugation with Oxaliplatin

3.3.1 Efficiency of the click labelling of TFOs

Although the CuAAC reaction has been traditionally favoured for its high reaction kinetics and yield, its reliance on a copper(I) catalyst and reducing environment can present a challenge when used with metal complexes. On the other hand, the main experimental advantage of SPAAC over CuAAC for TFO labelling with *cis*-Pt(II) complexes is that there is no need for copper-catalysis or a reducing environment. SPAAC is usually associated with slower reaction rates than CuAAC, but in this work we found that both CuAAC and SPAAC worked best with relatively longer incubation times (18 h).

The efficiency of SPAAC and CuAAC was assessed qualitatively by MS analysis and PAGE migration profile. In the case of CuAAC-generated hybrids, the only hybrids obtained were C2-O and C3-O according to MS. Additionally, C1 did not yield the expected Pt(II) hybrid (C1-O), only TO-labelled C1. (Table III.1). In the case of SPAAC-generated hybrids, the expected mass was observed for S1-O and S2-O both, but S3-O did not yield interpretable traces for MS analysis. This has been consistently observed for Pt(II) hybrids of C3.

Table III.1: Calculated and observed mass for CuAAC- and SPAAC-generated Pt-Oxali-TFO hybrids.

		expected	*observed*
CuAAC	1	6672	6362
	2	6771	6679
	3	7214	7210
SPAAC	1	7013	7009
	2	7013	7009
	3	7440	/

3.3.2 Apparent purity of the hybrids

To further assess the efficiency of the click reactions, the PAGE migration profile of both CuAAC- and SPAAC-generated hybrids was established (Figure III.5). Here, each hybrid was loaded onto a PAGE gel next to the unclicked TFO. In accordance with MS, PAGE showed that C1 did not successfully click to Pt-N_3-Oxali since the migration of the product (C1-O, lane 2) was identical to the unclicked TFO-1 (C1, lane 2). CuAAC-generated hybrids TFO-2 (C2-O, lane 4) and 3 (C3-O, lane 6) displayed more than one band, which were difficult to differentiate on PAGE. Overall, SPAAC appeared to be more efficient as it generated one distinct higher band (SPAAC-products of S1 (S1-O, lane 8), S2 (S2-O, lane 10) and S3 (S3-O, lane 12)). This higher band is indicative of a specie with higher molecular weight, distinct from the unclicked TFOs (S1 in lane 7, S2 in lane 9 and S3 in lane 11). The highest conversion rate was observed for S1-O. All products were visible prior to SYBR Gold staining, proving that the TO labelling was successful. Non-clicked TFO was observed for each hybrid, whether it was generated *via* SPAAC or CuAAC, however SPAAC-hybrids display sharper bands. The reduced purity of CuAAC-generated hybrids might arise from side reactions promoted under copper-catalysed conditions, unwanted crosslinking of the TFO interfering with the CuAAC, metal ion exchange from Pt(II) to Cu(II), or impact of the reducing environment during CuAAC on the Pt(II) complex, highlighting the limitation of CuAAC compared to SPAAC.

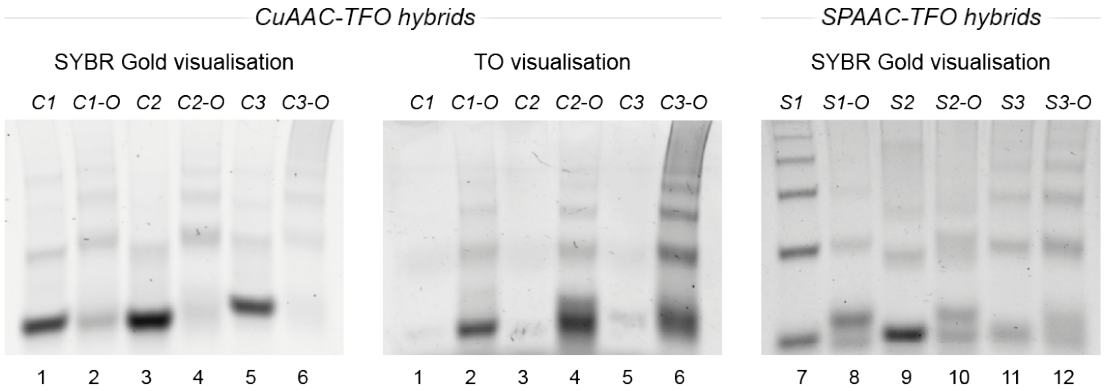


Figure III.5: PAGE showing the conjugation efficiency of TFO hybrids. CuAAC-TFO hybrids (C1-O, C2-O and C3-O lanes 2,4 and. 6) were compared to unclicked TFOs (C1, C2 and C3, lanes 1, 3 and 5) before and after SYBR Gold staining and SPAAC-TFO hybrids (S1-O, S2-O and S3-O lanes 8, 10 and 12) were compared to unclicked TFOs (S1, S2 and S3, lanes 7, 9 and 11) after SYBR Gold staining.

3.3.3 Triplex formation

Following the successful isolation of both CuAAC- and SPAAC-generated hybrids, each hybrid was tested for its ability to form a DNA triplex (Figure III.6). The TFO hybrids (100 eq.) were incubated with a 40-mer duplex DNA containing the recognition domain and a 29-mer *off*-target duplex lacking the recognition domain. The recognition domain contains a high amount of G, making it a compatible duplex for crosslinking by the oxaliplatin motif. The target duplex also displays a crosslinking site in the 5′-overhang, in proximity of the location of the DBCO modification. While the *off*-target duplex lacks the TFO recognition domain, it retains sites compatible with platinum(II) intrastrand crosslinking rendering it a suitable control for detecting non-specific crosslinking.

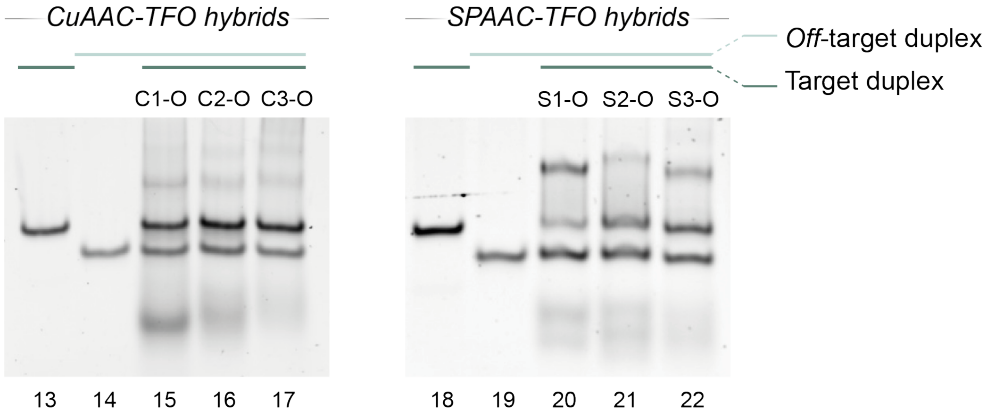


Figure III.6: PAGE of analysis of 100 eq. of Pt(II)-Oxali TFO hybrids (CuAAC-generated hybrids = C1-O, C2-O and C3-O, and SPAAC-generated hybrids = S1-O, S2-O and S3-O) with a 40-mer duplex target (0.5 pmol, 1 eq.) containing the recognition domain together with 1 eq. of a 29-mer *off*-target duplex lacking the recognition domain. Lanes 13 and 18: target duplex alone, lanes 14 and 19: *off*-target duplex alone, lanes 15, 16, 17, 20, 21 and 22: both target- and *off*-target sequences were incubated with 100 eq. of C1-O, C2-O, C3-O, S1-O, S2-O and S3-O, respectively.

Upon analysing the PAGE gel, lanes 20 and 22 show a higher-order band above the TFO, target and *off*-target duplexes, indicative of triplex formation. These results show that only the SPAAC-generated hybrids S1-O and S3-O could form stable triplexes in the tested conditions. S1-O and S3-O correspond to TFOs bearing the TO modification closest to the inversion site and to the TFO carrying two TO units, respectively, and both display the strongest triplex formation activity. This showed that, in the case of CuAAC-

generated hybrids, the presence of 5mC and TO units did not improve the binding affinity of the TFOs to the target duplex enough to enable triplex formation. Further experiments could be designed to probe this effect and understand if the positioning of the oxaliplatin motif in the TFO construct is directly responsible for mediating the binding kinetics. For instance, identical TFOs could be developed where the DBCO and octadiynyl monomers were inserted at the same location and any inversion sites were targeted with the same triplet nucleobase. In summary, combining the PAGE profile and MS analysis of the hybrids, strong justification now exists to select SPAAC chemistry over CuAAC for the functionalisation of TFOs with *cis*-Pt(II) moieties.

4 Conclusion

In this chapter, two libraries of *EGFR*-targeting TFO hybrids were synthesised– one compatible with CuAAC and the other with SPAAC chemistries. Both sets incorporated 5mC and TO modifications to enhance triplex formation, and the influence of the number of TO modifications and their positioning towards TFO binding affinity was investigated.

These results demonstrate the conjugation of Pt-N_3-Oxali to TFOs *via* click chemistry proceeded more efficiently through SPAAC than CuAAC methods. This enhancement is likely due to the milder, catalyst-free conditions of SPAAC in contrast to the somewhat harsher, copper-dependant and reductive conditions required for CuAAC reactions. Although neither approach achieved full conversion to the Pt-TFO hybrids, and required the same reaction time, SPAAC yielded hybrids of satisfactory purity according to PAGE, without further need for HPLC purification. In contrast, CuAAC-derived hybrids exhibited lower purity on PAGE, even after HPLC purification, or in the case of TFO-1, did not yield the expected hybrid.

Using PAGE analysis, significant triplex formation was observed exclusively for SPAAC-labelled hybrids. More specifically, S1-O and S3-O demonstrated the most intense triplex band, with no depletion of the off-target band. However, this finding cannot be directly attributed to the click chemistry method alone, as the hybrids differ not only in their conjugation strategy but also in the base composition across homopurine interruptions and Pt(II) positioning. It is plausible that binding of Pt(II) within the recognition domain disrupts hydrogen bonding, thereby impairing triplex formation.

Together, these findings provide a comparative evaluation of CuAAC and SPAAC for functionalising *EGFR*-targeting TFOs containing oxaliplatin derivatives. SPAAC emerged as the more robust and purification-friendly method under the tested conditions. Consequently, SPAAC was adopted for the functionalisation of *EGFR*-targeting TFOs in subsequent chapters.

5 References

[1] Kelland, L. *Nat Rev Cancer.* **2007**, *7,* (8), 573-584.
[2] Arany, I.; Safirstein, R. L. *Semin Nephrol.* **2003**, *23,* (5), 460-464.
[3] Schultz, P. G.; Taylor, J. S.; Dervan, P. B. *J Am Chem Soc.* **1982**, *104,* (24), 6861-6863.
[4] Chu, B. C.; Orgel, L. E. *Nucleic Acids Res.* **1989**, *17,* (12), 4783-4798.
[5] Hennessy, J.; McGorman, B.; Molphy, Z.; Farrell, N. P.; Singleton, D.; Brown, T.; Kellett, A. *Angew Chem Int Ed Engl.* **2022**, *61,* (3), e202110455.
[6] Miller, P. S. *Prog Nucleic Acid Re.* **1996**, *52*, 261-291.
[7] Fox, K., R. ; Brown, T.; Rusling, D. A. *Chemical Biology.* **2018**, *Chapter 1*, 1-32.
[8] Walsh, S.; El-Sagheer, A. H.; Brown, T. *Chem Sci.* **2018**, *9,* (39), 7681-7687.
[9] Kolb, H. C.; Finn, M. G.; Sharpless, K. B. *Angew Chem Int Ed Engl.* **2001**, *40,* (11), 2004-2021.
[10] Fantoni, N. Z.; El-Sagheer, A. H.; Brown, T. *Chem Rev.* **2021**, *121,* (12), 7122-7154.
[11] Pon, R. T. **1993**.
[12] Hennessy, J.; Klimkowski, P.; Singleton, D.; Gibney, A.; Coche, M.; Farrell, N. P.; El-Sagheer, A. H.; Brown, T.; Kellett, A. *RSC Medicinal Chemistry.* **2023**.
[13] Basu, U.; Banik, B.; Wen, R.; Pathak, R. K.; Dhar, S. *Dalton Transactions.* **2016**, *45,* (33).
[14] Farrer, N. J.; Griffith, D. M. *Current Opinion in Chemical Biology.* **2020**, *55*.
[15] Pathak, R. K.; McNitt, C. D.; Popik, V. V.; Dhar, S. *Chemistry – A European Journal.* **2014**, *20,* (23).
[16] Cabrera, D. G.; Koivisto, B. D.; Leigh, D. A. *Chemical Communications.* **2007**, (41).
[17] Doe, E.; Hayth, H. L.; Brumett, R.; Khisamutdinov, E. F. *International Journal of Molecular Sciences.* **2023**, *24,* (5).
[18] Kandler, R.; Benaragama, Y.; Bera, M.; Wang, C.; Samiha, R. A.; Sameera, W. M. C.; Das, S.; Nag, A. *Molecules.* **2024**, *29,* (9).
[19] Agard, N. J.; Prescher, J. A.; Bertozzi, C. R. *J Am Chem Soc.* **2004**, *126,* (46), 15046-15047.
[20] Farrer, N. J.; Sharma, G.; Sayers, R.; Shaili, E.; Sadler, P. J. *Dalton Trans.* **2018**, *47,* (31), 10553-10560.
[21] Ragab, S. S. *RSC Adv.* **2025**, *15,* (14), 10583-10601.
[22] Li, L.; Zhang, Z. *Molecules.* **2016**, *21,* (10).
[23] Luu, T.; Gristwood, K.; Knight, J. C.; Jörg, M. *Bioconjugate Chem.* **2024**, *35,* (6).
[24] Mbua, N. E.; Guo, J.; Wolfert, M. A.; Steet, R.; Boons, G. J. *Chembiochem.* **2011**, *12,* (12), 1912-1921.
[25] El-Sagheer, A. H.; Brown, T. *J Am Chem Soc.* **February 27, 2009**, *131,* (11).
[26] Klimkowski, P.; De Ornellas, S.; Singleton, D.; El-Sagheer, A. H.; Brown, T. *Org Biomol Chem.* **2019**, *17,* (24), 5943-5950.
[27] Byeon, H. K.; Ku, M.; Yang, J. *Exp Mol Med.* **2019**, *51*.
[28] Mitsudomi, T.; Yatabe, Y. *Febs Journal.* **2010**, *277,* (2), 301-308.

[29] Park, H. S.; Jang, M. H.; Kim, E. J.; Kim, H. J.; Lee, H. J.; Kim, Y. J.; Kim, J. J.; Kang, E.; Kim, S. W.; Kim, I. A.; et al. *Modern Pathol.* **2014**, *27,* (9), 1212-1222.
[30] Xu, H. S.; Zong, H. L.; Ma, C.; Ming, X.; Shang, M.; Li, K.; He, X. G.; Du, H.; Cao, L. *Oncol Lett.* **2017**, *14,* (1), 512-516.
[31] Franovic, A.; Gunaratnam, L.; Smith, K.; Robert, I.; Patten, D.; Lee, S. *Proceedings of the National Academy of Sciences of the United States of America.* **2007**, *104,* (32), 13092-13097.
[32] Garant, J. M.; Perreault, J. P.; Scott, M. S. *Bioinformatics.* **2017**, *33,* (22), 3532-3537.
[33] Mergny, J. L.; Sun, J. S.; Rougee, M.; Montenaygarestier, T.; Barcelo, F.; Chomilier, J.; Helene, C. *Biochemistry-Us.* **1991**, *30,* (40), 9791-9798.
[34] Johnstone, T. C.; Wilson, J. J.; Lippard, S. J. *Inorganic Chemistry.* **2013**, *52,* (21).

Chapter IV

Development of Monofunctional Azide-modified Platinum(II) Complexes and SPAAC-labelling of TFO Probes for *EGFR*-specific Coordination Activity

April 2026

1 Introduction

The recognition of DNA as a primary target for anticancer therapy has driven extensive development of gene-targeted therapies, most notably platinum(II) complexes. The standard chemotherapeutic treatment for many tumour types, particularly solid epithelial tumours,[1] often involves platinum(II) agents such as cisplatin[2] and its derivatives oxaliplatin and carboplatin[3] (Figure IV.1). These *cis*-platinum(II) compounds exert their cytotoxicity through DNA crosslinking, a coordinative interaction that interferes with replication and transcription of DNA, leading to cell death.[4] However, the emergence of acquired and intrinsic resistance to traditional *cis*-platinum(II) therapies highlighted the necessity for developing new classes of cytotoxic complexes.[5]

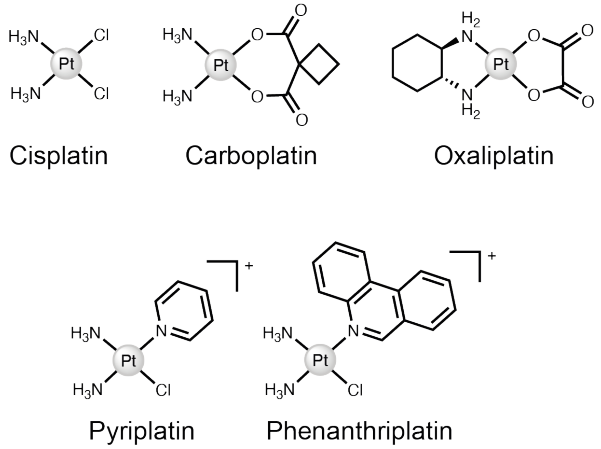


Figure IV.1: Structure of bifunctional platinum(II) anticancer agents cisplatin, carboplatin, oxaliplatin, and of monofunctional platinum(II) complexes pyriplatin and phenanthriplatin.

Monofunctional platinum(II) complexes are a novel subclass of anti-tumour platinum(II) complexes.[6-8] Unlike bifunctional platinum(II) species, they form a single coordinative bond with DNA, often in combination with an intercalating aromatic ligand that enhances DNA binding or provides inhibitory effects on enzymes such as topoisomerase.[9] The ligand is also involved in steric repulsion of enzymes, further inhibiting replication and transcription, as illustrated by the phenanthridine ligand in phenanthriplatin[8] or the pyridine moiety in pyriplatin.[7] These monofunctional complexes retain significant anticancer potential while exhibiting distinct mechanism of DNA damage. Nevertheless, the application of platinum(II) chemotherapeutics remains limited by *off*-target effects and the challenge of achieving gene-level selectivity.[10]

One method to improve sequence specificity involves tethering platinum(II) complexes to triplex-forming oligonucleotides (TFOs).[11-13] TFOs are a single strand of oligonucleotide that sequence-specifically bind duplex DNA through the formation of hydrogen bonds with the Hoogsteen face of DNA duplets in the major groove of DNA.[14] Early studies combining bifunctional platinum(II) species with TFOs demonstrated the feasibility of this approach, enabling target-specific interactions. Miller and coworkers[15-17] notably showed the attachment of bifunctional platinum(II) species *via* replacement of one of the labile ligands, resulting in monofunctional Pt-TFO constructs. While active, early hybrids were constrained by inefficient conjugation chemistry and limited triplex stability.[18] Subsequent work employing copper-catalysed or strain promoted azide-alkyne cycloaddition (CuAAC or SPAAC, respectively) improved conjugation efficiency.[19, 20] The resulting hybrids were optimised using thiazole orange (TO) and 5-methylcytosine (5mC) modifications within the TFO sequence. These modifications are known to enhance the potential of TFOs through increased binding affinity with the target duplex *via* intercalation for TO[21, 22] and compatibility close to neutral pH conferred by 5mC.[23] The developed *cis*-Pt-TO-TFO hybrids showed remarkable target-specific crosslinking activity, especially in the case of the oxaliplatin-derived hybrids. [19, 20]

This chapter aims to develop new click-compatible monofunctional Pt(II) complexes and assess their potential upon TFO hybridisation as an alternative to *cis*-Pt(II) systems. TFOs were designed to target a polypurine strand on the epidermal growth factor receptor (*EGFR*) gene, a gene overexpressed in several cancers such as lung cancer.[24] The conjugates were prepared using copper-free SPAAC conditions and evaluated for their ability to form stable triplexes and sequence-specific Pt(II) adduct formation. Additionally, the enzymatic inhibition of hybridised monofunctional Pt-TFO hybrids was evaluated and directly compared to oxaliplatin-TFO analogues to assess the influence of monofunctional versus bifunctional design.

2 Materials and Methods

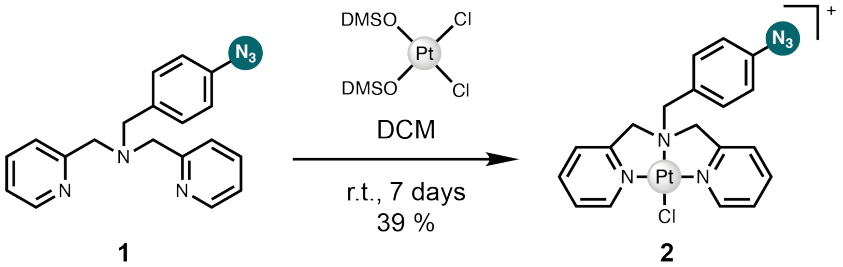
2.1 General method

Chemicals and high-performance liquid chromatography (HPLC) grade solvents were purchased from Merck, Tokyo Chemical Industry (TCI) or Fisher Scientific and used without further purification. Enzymes and their buffers were purchased from New England Biolabs and used according to recommended protocols. ^{1}H, ^{13}C and ^{195}Pt-NMR spectra were recorded on a Brucker AC 600 MHz NMR spectrometer. FTIR measurements were performed on a PerkinElmer Spectrum Two spectrometer. Electrospray ionisation-mass spectrometry (ESI-MS) was performed by collaborators in the University of Bath. All spectra are reported in Chapter VIII section B.1. Mass spectrometry for oligonucleotides was conducted by collaborators in ATDBio. HPLC traces and MS chromatograms are reported in Chapter VIII section B.2. Agarose and PAGE gels were visualised on a Syngene G:Box Mini 9 gel documentation system and all samples were quenched with loading dye (6×, 2.5% Ficoll®-400, 11 mM EDTA, 3.3 mM Tris-HCl, 0.017% SDS, 0.015% bromophenol blue, pH 8, Thermo Fisher) before loading on agarose or PAGE gels. Agarose gels were prepared by dissolving agarose in tris-acetate-EDTA (TAE, Fisher Scientific, 1×) and adding SYBR Safe (Thermo Fisher Scientific) and heating the mixture before casting and leaving it cool for 1 h. PAGE gels were prepared using 29:1 acrylamide:bis-acrylamide in the presence of either tris-borate-EDTA (TBE, Fisher Scientific, 1×) or tris-acetate (TA, pH 6.0, 50 mM), TEMED (Thermo Fisher Scientific, 0.2%) and ammonium persulfate (APS, 0.05%). In the case of denaturing gels, urea (42%) is added. In the case of TA gels, $MgCl_2$ (5 mM) and NaCl (75 mM) are added. Thermal melting (T_M) analyses were carried out on a Light Cycler® 480 II (Roche) using SYBR Green I master mix (Roche) when specified. Fluorescence was recorded across a temperature range from 20 °C to 99 °C, with a ramp rate of 0.6 °C/s and 10 acquisitions per °C. 5′-DBCO TFOs were synthesised and labelled with TO by collaborators in ATDBio. The phosphate buffer used for sample preparation contained 10 mM PO_4^{3-}, 150 mM NaCl, 2 mM $MgCl_2$, at pH 6.0.

2.2 Synthesis of Pt-N_3-Benzyl-DPA and Pt-N_3-Propyl-DPA

N-(4-azidobenzyl)-1-(pyridin-2-yl)-N-(pyridin-2-ylmethyl)methanamine was prepared by a coworker according to the literature method reported by McGorman *et al.*[25]

2.2.1 *Synthesis of Pt-N_3-benzyl-DPA*

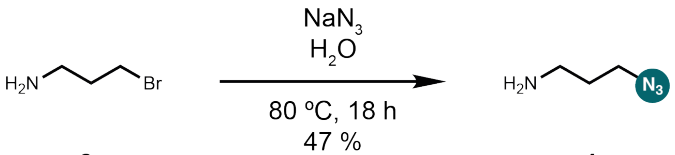


1 **2**

N-(4-azidobenzyl)-1-(pyridin-2-yl)-N-(pyridin-2-ylmethyl)methanamine (89.1 mg, 0.27 mmol, 1.1 eq.) was dissolved in DCM (30 mL) and $[Pt(DMSO)_2Cl_2]$ (103.5 mg, 0.25 mmol, 1 eq.) was added. The resulting mixture was stirred in darkness for 7 days. Diethyl ether was added to the solution revealing a grey precipitate that was isolated by vacuum filtration and further dried under vacuum, affording 54.4 mg, 0.10 mmol of [Pt(N_3-benzyl-DPA)Cl]·Cl (39% yield). ^{1}H NMR (600 MHz, DMSO-d_6) δ (ppm): 8.64 – 8.62 (m, 1H), 8.15 (td, *J* = 7.8, 1.6 Hz, 1H), 7.78 (m, 1H), 7.63 (d, *J* = 7.8 Hz, 1H), 7.53 (t, *J* = 6.7 Hz, 1H), 6.85 (m, 1H), 5.38 (d, *J* = 15.7 Hz, 1H), 4.90 (d, *J* = 15.7 Hz, 1H), 4.32 (s, 1H). ^{13}C NMR (151 MHz, DMSO-d_6) δ (ppm): 166.03, 149.35, 141.23, 135.02, 125.32, 123.89, 119.07, 68.28. ^{195}Pt NMR (129 MHz, DMSO-d_6) δ (ppm): -2363.83. IR (cm^{-1}): 3369.7, 3036, 2925.7, 2115.74, 2078, 1614.3, 1603.1, 1505.6, 1447.2, 1284.0, 1128.2. ESI-MS calc. for $C_{19}H_{18}ClN_6{}^{195}Pt^+$ $[M]^+$: 560.09. Found: 560.09.

2.2.2 Synthesis of N_3-propyl-DPA

2.2.2.1 Synthesis of 3-azidopropyl-1-amine

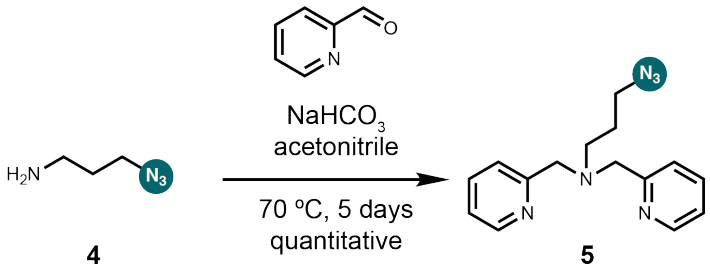


3 **4**

3-bromopropyl-1-amine hydrobromide (1.000 g, 4.57 mmol, 1 eq.) was dissolved in DI H_2O (4 mL) and sodium azide (891.2 mg, 13.70 mmol, 3 eq.)

was added. The resulting mixture was then refluxed overnight. After cooling down to room temperature, diethyl ether (20 mL) was added, the mixture was cooled to 0 °C and potassium hydroxide (1.000 g) was added. The aqueous layer was isolated and extracted with 3 x 20 mL portions of diethyl ether. The combined organic layers were dried over $MgSO_4$ and evaporated under reduced pressure to afford 389.1 mg, 2.15 mmol of 3-azidopropyl-1-amine as a colourless oil with a 47% yield. ^{1}H NMR (DMSO-d_6) δ (ppm): 3.37 (t, 2H), 2.58 (t, 2H), 1.58 (quint, 2 H).

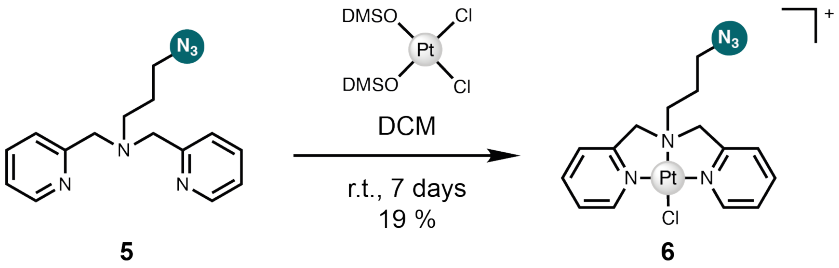
2.2.2.2 Synthesis of 3-azido-N,N-bis(pyridin-2-ylmethyl)propan-1-amine (N_3-propyl-DPA)



4 5

2-chloromethylpyridine hydrochloride (2.863 g, 17.46 mmol, 4 eq.) was dissolved in dry acetonitrile (40 mL) under inert atmosphere and $NaHCO_3$ (3.666 g, 43.64 mmol, 10 eq.) was added at 0 °C, followed by the slow addition of 3-azidopropan-1-amine (790.1 mg, 4.36 mmol, 1 eq.). The resulting red mixture was refluxed at 70 °C under inert atmosphere in the dark for 5 days. The solution was filtered to remove $NaHCO_3$ and the filtrate was evaporated and re-suspended in DCM before being washed with 5 x 10 mL portions of DI H_2O, dried over $MgSO_4$ and evaporated to dryness under reduced pressure, affording 1.240 g, 4.39 mmol of 3-azido-N,N-bis(pyridin-2-ylmethyl)propan-1-amine as a brown oil with quantitative yield. ^{1}H NMR (DMSO-d_6) δ (ppm): 8.48 (ddd, J = 4.9, 1.8, 0.9 Hz, 2 H), 7.77 (td, J = 7.6, 1.8 Hz, 2 H), 7.51 (dt, J = 7.8, 1.1 Hz, 2H), 7.25 (ddd, J = 7.5, 4.8, 1.2 Hz, 2H), 3.73 (s, 4H), 3.34 (t, 2H), 2.53 – 2.50 (t, 2H), 1.74 – 1.69 (quint, J = 6.8 Hz, 2H). ^{13}C NMR (DMSO-d_6) δ (ppm): 159.72, 149.21, 136.91, 123.13, 122.56, 60.22, 51.10, 49.21, 26.52. IR (cm^{-1}): 3053.0, 3009.3, 2926.2, 2820.9, 2092.8, 1588.6, 1569.0, 1472.6, 1432.4, 1251.3, 1146.6. ESI-MS calc. for $C_{15}H_{18}N_6^{195}$ $[M+Na]^+$: 305.15. Found: 305.15.

2.2.3 Synthesis of Pt-N_3-propyl-DPA



5 **6**

3-azido-N,N-bis(pyridin-2-ylmethyl)propan-1-amine (83.1 mg, 0.29 mmol, 1.1 eq.) was dissolved in DCM (30 mL) and [Pt(DMSO)$_2$Cl$_2$] (113.2 mg, 0.27 mmol, 1 eq.) was added. The resulting mixture was stirred in darkness for 7 days. Diethyl ether was added to the solution revealing a brown precipitate that was isolated by vacuum filtration and further dried under vacuum, affording 26.4 mg, 0.05 mmol of [Pt(N_3-propyl-DPA)Cl]·Cl (19% yield). ^{1}H NMR (600 MHz, DMSO-d_6) δ (ppm): 8.79 (d, *J* = 5.8 Hz, 2H), 8.29 (td, *J* = 7.8, 1.5 Hz, 2H), 7.80 (m, 2H), 7.67 (m, 3H), 5.35 (d, *J* = 15.8 Hz, 2H), 4.82 (d, *J* = 15.9 Hz, 2H), 3.32 (d, *J* = 10.5 Hz, 2H), 3.08 – 3.05 (m, 2H), 1.75 (dt, *J* = 14.9, 6.6 Hz, 2H). ^{13}C NMR (151 MHz, DMSO-d_6) δ (ppm): 166.07, 149.59, 141.87, 125.93, 124.03, 68.25, 61.88, 47.97. ^{195}Pt NMR (129 MHz, DMSO-d_6) δ (ppm): -2349.28. IR (cm^{-1}): 3431.8, 3381.4, 3031.5, 2936, 2094.7, 1613.5, 1478.4, 1443.7, 1285.6, 1252.6, 1111.9. ESI-MS calc. for $C_{15}H_{18}ClN_6{}^{195}Pt^+$ $[M]^+$: 512.09. Found: 512.09.

2.3 Interaction of the monofunctional Pt(II) complexes with plasmid DNA

Samples were prepared in a total volume of 20 µL in HEPES buffer (80 mM) containing supercoiled pUC19 DNA (400 ng), NaCl (25 mM), and increasing concentration of Pt-N_3-benzyl-DPA or Pt-N_3-propyl-DPA (between 0 and 200 µM). After incubation at 37 °C for 24 h, the reactions were quenched by the addition of 3 µL of 6× loading dye (Thermo Fisher R0611) and loaded onto a 1.3% agarose gel. The gel was run in 1× TAE buffer at 70 V for 90 min before being stained with SYBR Safe and visualised as described in section 2.1.

2.4 Synthesis of oligonucleotides

2.4.1 NHS-ester labelling of duplex strands

Single stranded oligonucleotides (20 nmol, 1 eq.) were firstly dissolved in carbonate buffer (12 µL, 0.5 M $NaHCO_3/Na_2CO_3$, pH = 8.75). NHS ester cyanine-5 (Cy-5) or fluorescein (FAM) (400 nmol, 20 eq.) was added, and the resulting mixture was stirred at 25 °C for 2.5 h. The mixture was desalted over a NAP 5 column, and purified by ionic exchange high-performance liquid chromatography (IEx-HPLC), using a 25 to 60% gradient of Tris-HCl (20 mM), NaCl (1 M,pH 8.0) in Tris-HCl (20 mM, pH 8.0). The fractions collected were desalted over a NAP 25 column and freeze-dried before being characterised by mass spectrometry. Expected and observed ESI-MS results for the molecular ion masses are as shown in Table IV.1.

2.4.2 SPAAC-labelling of TFOs

In a total volume of 800 µL of phosphate buffer, TO-labelled DBCO-TFO (15 nmol, 1 eq.) and either Pt-N_3-benzyl-DPA or Pt-N_3-propyl-DPA (150 nmol, 10 eq.) were mixed and incubated at 30 °C, at 600 rpm for 3 h. The Pt-TFOs were then subjected to NAP-10 column purification and were freeze-dried overnight. The resulting hybrids were characterised by mass spectrometry. Expected and observed ESI-MS results for the molecular ion masses are as shown in Table IV.1.

2.5 Triplex formation of Pt-TFO hybrids

2.5.1 Triplex formation analysis via *PAGE*

Samples were prepared in a total volume of 10 µL containing the target duplex (0.5 pmol), *off*-target duplex (0.5 pmol) and TFO hybrids (50 pmol, 100 eq.) in phosphate buffer and incubated at 37 °C for 1 h or 48 h. Loading dye was added and the samples were loaded onto PAGE gel which was run in 50 mM TA buffer at 70 V for 4 h. The gels were visualised as described in section 2.1.

2.5.2 Melting temperature recording

In a total volume of 20 µL, TFO hybrid (50 pmol, 10 eq.) was added to the target duplex (5 pmol, 1 eq.) in phosphate buffer. Samples were prepared in triplicates and incubated at 37 °C for 48 h before the fluorescence was recorded using a Light Cycler® 480 II (Roche) instrument. For TFO-4 hybrids,

SYBR Green (10 μL) was added prior to measurement. The fluorescence was recorded across a gradient of temperature up to 99 °C, with 10 fluorescence measurements recorded per °C. Thermal melting curves were analysed and graphed using GraphPad Prism 10 software. T_M values were calculated as the temperature where the first negative derivative of the melting curve reaches a maximum. The T_M values reported for each hybrid represent the average of triplicate measurements.

2.6 Target-specific crosslinking of EGFR *duplex by Pt-TFO hybrids determined by fluorescence denaturation*

Samples were prepared in a total volume of 10 μL containing fluorophore-labelled truncated target duplex (1 pmol, 1 eq.) in phosphate buffer with increasing equivalents of Pt-TFO hybrids (10, 25, 50 and 100 eq.). The resulting samples were incubated at 37 °C for 48 h, and glycerol (5 μL) was added. The samples were then loaded onto a denaturing TBE gel and run in 1× TBE buffer at 300 V for 1 h. The gels were visualised using a multiplex protocol on a Syngene G:Box Mini 9 gel documentation system. 3 images were recorded and overlapped with red, blue or green LED excitation and 705 nm, 525 nm or 605 nm filter to separately visualise Cy5, FAM, or TO respectively.

2.7 Inhibition of polymerase enzyme activity

A target duplex with a 5′-phosphate-labelled complementary strand (0.5 pmol, 1 eq.) was incubated with Pt-TFO (50 pmol, 100 eq.) at 37 °C for 48 h in 3 μL phosphate buffer. ThermoPol (1 μL of 10× concentration) was added to all samples followed by lambda exonuclease (1 μL of 2 u/μL) to relevant samples. The 5′-phosphate strand was digested at 37 °C for 30 min. Primer (1.5 μM of 10 μM) was added followed by dNTPs (1.5 μL of 10 mM) and vent(exo-) polymerase (1 μL of 2 u/μL) to the relevant samples, before further incubation at 37 °C for 30 min. Water was added to control samples to reach a total volume of 10 μM. All samples were quenched by the addition of loading dye (2 μL) before being loaded onto 1× TBE native PAGE, run at 150 V for 1.5 h. Gels were visualised as described in section 2.1.

3 Results and discussion

3.1 Synthesis of N_3-propyl-DPA and Pt-N_3-DPA complexes

Monofunctional platinum(II) complexes bearing an azide handle were developed to enable biorthogonal conjugation to alkyne-modified TFOs *via* click chemistry. Both Pt-N_3-benzyl-DPA and Pt-N_3-propyl-DPA were designed to promote monofunctional crosslinking through a labile chloride ligand, and a tridentate DPA-based ligand. The N_3-benzyl-DPA was expected to exhibit rotational freedom and greater steric shielding, whereas the aliphatic propyl analogue was conceived as a more flexible variant.

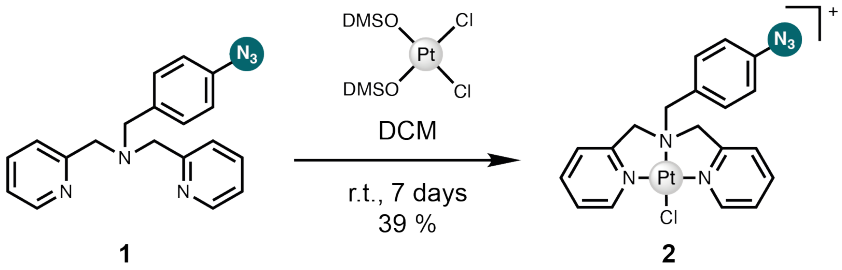


Figure IV.2: Synthetic scheme for the complexation of N_3-benzyl-DPA with platinum(II).

N_3-benzyl-DPA was prepared according to the method reported by McGorman *et al.*[25] and coordinated with platinum(II) upon treatment with one equivalent of *cis*-[Pt(DMSO)$_2$Cl$_2$] using 1.1 equivalents of the ligand (Figure IV.2). The reaction was protected from light and stirred for several days to ensure full completion of the complexation without degrading the light-sensitive azide-ligand, affording [Pt(N_3-benzyl-DPA)Cl]·Cl in 39% yield.

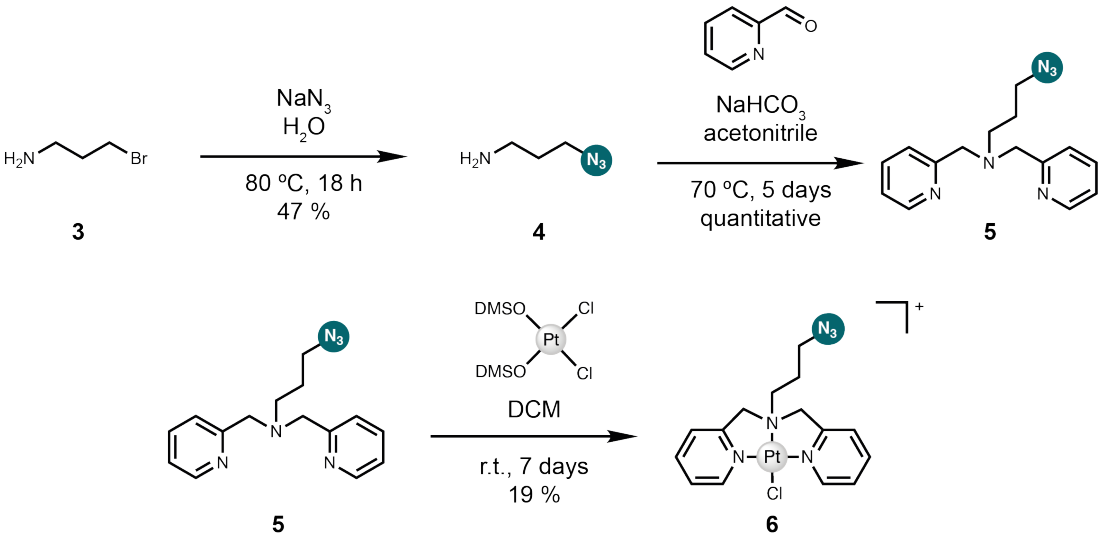


Figure IV.3: Synthetic scheme for the preparation of Pt-N_3-propyl-DPA starting from 3-bromopropyl-1-amine hydrobromide.

The N_3-propyl-DPA ligand was prepared in two steps (Figure IV.3). Firstly, nucleophilic substitution of 3-bromopropyl-1-amine with sodium azide produced 3-azidopropylamine, which was then condensed with two equivalents of picolinaldehyde to yield the desired tertiary amine quantitatively. Coordination of the ligand to platinum(II) followed the same procedure as for the benzyl analogue, providing the monofunctional Pt-N_3-propyl-DPA complex [Pt(N_3-propyl-DPA)Cl]·Cl in 19% yield. Both complexes displayed the expected spectroscopic characteristics, confirming successful synthesis. These compounds were next evaluated for their native interactions with plasmid DNA and subsequent conjugation to TFOs.

3.2 Crosslinking of supercoiled plasmid DNA

The ability of Pt-N_3-benzyl-DPA and Pt-N_3-propyl-DPA to interact with DNA was investigated using pUC19 plasmid DNA as a substrate and visualised on an agarose gel (Figure IV.4). Increasing concentrations of each complex induced progressive migration shift towards the supercoiled form, characterised by the slower migration property of the plasmid across the complex gradient. Interestingly, Pt-N_3-benzyl-DPA induced full the least migration at 100 µM whereas Pt-N_3-propyl-DPA required 150 µM to achieve the same effect. This dose-dependent behaviour confirmed interactions with DNA by both complexes as a result of unwinding. This is characteristic of crosslinking in the case of bifunctional platinum(II) compounds, or monoadduct formation in the case of monofunctional platinum(II) complexes.[26] The observation validated these complexes as suitable candidates for conjugation to TFOs for sequence-specific coordinative interactions.

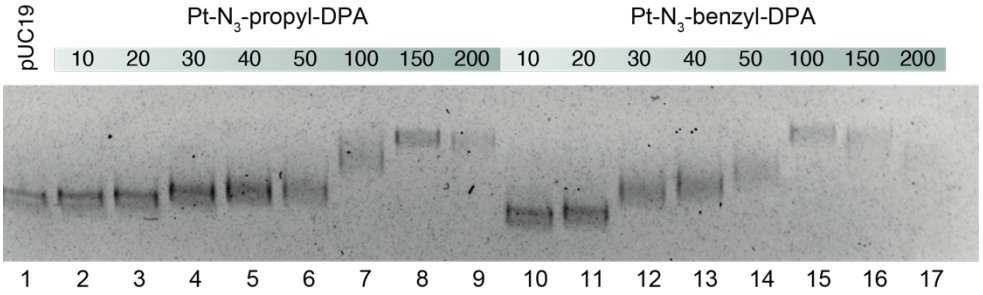


Figure IV.4: Interactions of Pt-N_3-propyl-DPA and Pt-N_3-benzyl-DPA with pUC19 showing dose-dependent unwinding of the supercoiled plasmid DNA, characteristic of crosslinking. Complexes (10, 20, 30, 40, 50, 100, 150 or 200 µM) were incubated with pUC19 (400 ng) at 37 °C for 48 h before being analysed onto 1.3% agarose gels.

3.3 *Synthesis of oligonucleotides*

3.3.1 SPAAC-labelling of the TFOs

Four alkyne-modified TFOs were designed to recognise a polypurine motif located within exon 5 of the *EGFR* gene, potentially enabling parallel triplex binding (Figure IV.5). SPAAC chemistry was selected for copper-free conjugation of the Pt(II) complexes, following the results described in Chapter III for Pt-N_3-Oxali hybridisation. Each TFO contained a 5′-dibenzocyclooctyne (DBCO) modification and 5mC was used instead of cytosine for improved binding affinity with the target duplex. TO intercalators were incorporated *via* amide coupling to further enhance triplex stability: TFO-1 and TFO-2 carried one TO units (in position X_1 or X_2, respectively), TFO-3 contained two TO units (in positions X_1 and X_2), while TFO-4 served as an unmodified control.

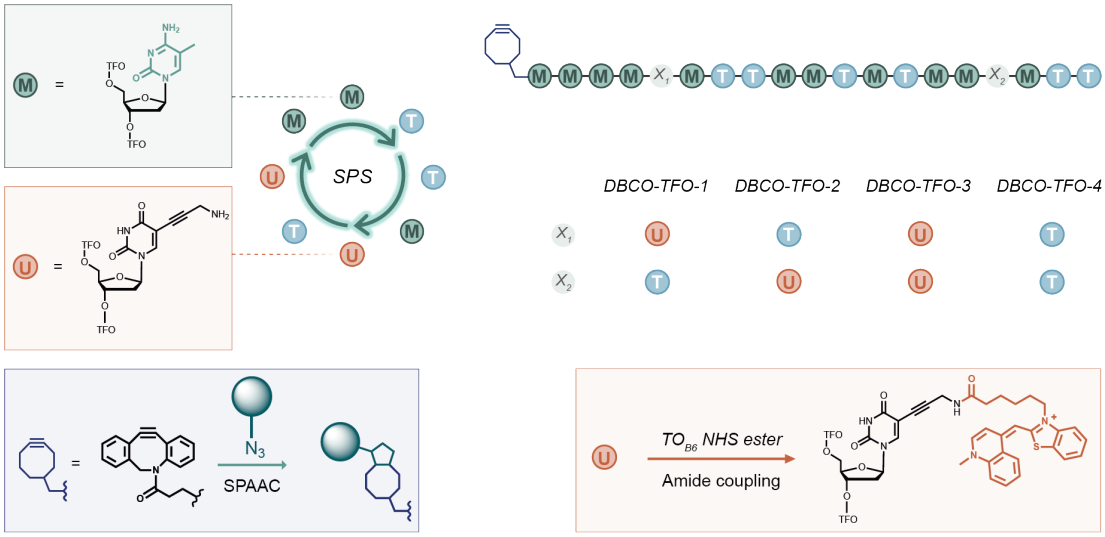


Figure IV.5: Design of the library of 19-nt TFOs targeting the *EGFR* gene and illustration of SPS and post-synthetic labelling.

The azide-functionalised Pt(II) complexes were conjugated to DBCO-modified TFOs in phosphate buffer (10 mM PO_4^{3-}, 150 mM NaCl, 2 mM $MgCl_2$, pH 6.0) to prevent undesired crosslinking to the TFO, which would compete with SPAAC. Here, ten equivalents of Pt-N_3 complex were reacted with one equivalent of DBCO-TFO at 37 °C for 3 h. PAGE analysis of TFO-1 and TFO-3 hybrids (Figure B.3.1) showed significant conversion to Pt-TFO hybrids, without need for further purification.

HPLC/MS analysis (Chapter VIII section B.2) confirmed successful conjugation for hybrids derived from TFO-1, 2 and 4 (Table IV.1), with recorded masses matching theoretical values. TFO-3 derivatives did not yield

interpretable traces. Collectively, PAGE and MS results confirmed the generation of Pt-TFO hybrids and validated SPAAC as a robust method for generating monofunctional Pt-TFO hybrids.

Table IV.1: Calculated and measured mass for TFO hybrids. The mass of the hybrids was calculated both in the presence of the labile chloride ligand (left), and without (right).

Hybrid	Calculated mass	Observed mass
B-1	7266 / 7231	7224
B-2	7266 / 7231	7263
B-3	7693 / 7658	/
B-4	6838 / 6803	6800
P-1	7218 / 7183	7177
P-2	7218 / 7183	7215
P-3	7645 / 7610	/
P-4	6790 / 6755	6753
O-1	7103 / 7013	7009
O-2	7103 / 7013	7009
O-3	7533 / 7443	/

TFO	*1*	*2*	*3*	*4*
X_1	U	T	U	T
X_2	T	U	U	T
+Pt-benzyl-DPA	B-1	B-2	B-3	B-4
+Pt-propyl-DPA	P-1	P-2	P-3	P-4
+Pt-Oxali	O-1	O-2	O-3	/

3.3.2 Preparation of the target and off*-target duplexes*

To investigate the activity of the monofunctional Pt-TFO hybrids, three duplexes were synthesised: a 40-mer target duplex, a shorter fluorescently labelled target duplex, and a 29-mer *off*-target duplex (Figure IV.6). The sequences were designed around the 19-nt triplex recognition domain of the *EGFR* gene, with flanking regions providing appropriate context for hybridisation. The shorter target duplex was designed with sequences of different lengths (27-nt on the target strand, and a truncated 19-nt complementary strand) and labelled with different fluorophores. Using amide coupling, the target strand was labelled with fluorescein (FAM) and the

complementary strand with cyanine-5 (Cy5). This design enabled electrophoretic characterisation of each strand with direct visualisation with selective excitation filters. The *off*-target duplex contained a randomised sequence with the same flanking regions as the long target duplex. Guanine (G) residues were present throughout the duplexes to provide potential coordination sites for the hybridised monofunctional Pt(II) complexes. Each duplex also included at least one pair of adjacent G bases to facilitate comparison with *cis*-Pt(II) analogues.

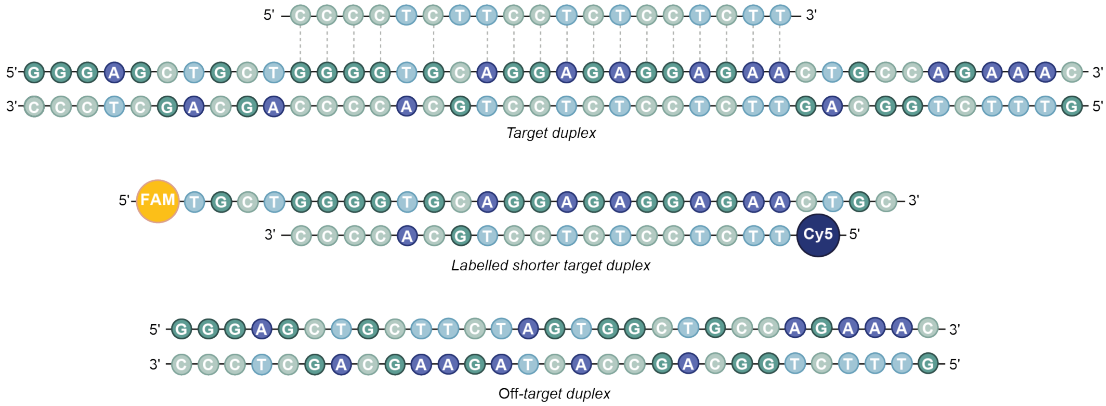


Figure IV.6: Structure of the 40-mer target duplex, the labelled shorter target duplex with its 27-nt FAM-labelled target strand and 19-nt Cy5-labelled complementary strand and the *off*-target duplex that does not contain the triplex recognition domain.

3.4 Triplex recognition by monofunctional Pt-TFO hybrids

The sequence-specific triplex recognition of all monofunctional Pt-TFO hybrids was initially evaluated by PAGE using the 40-mer target and *off*-target duplexes (Figure B.3.2). Hybrids derived from TFO-2 and 4 did not form triplexes at appreciable levels and were therefore excluded from further analysis, whereas hybrids of TFO-1 and 3 formed distinct triplexes with the target duplex. No binding to the *off*-target duplex was detected, confirming sequence specificity of the hybrids. The experiment was repeated with a 48 h incubation time to allow for the formation of potential monofunctional coordinative Pt(II) bonds with the target duplex (Figure IV.7). Here, hybrids derived from TFO-3, Pt-benzyl-DPA-TFO-3 (B-3), and Pt-propyl-DPA-TFO-3 (P-3) generated more intense triplex bands than their TFO-1 counterparts (B-1 and P-1, respectively), consistent with the presence of two TO units enhancing triplex association. P-1 and P-3 produced slightly more intensive triplex bands than the B-1 and B-3, possibly due to the unencumbered

coordination environment about the Pt(II) centre. For all hybrids, maximal triplex intensity was achieved at 100 equivalents of TFO.

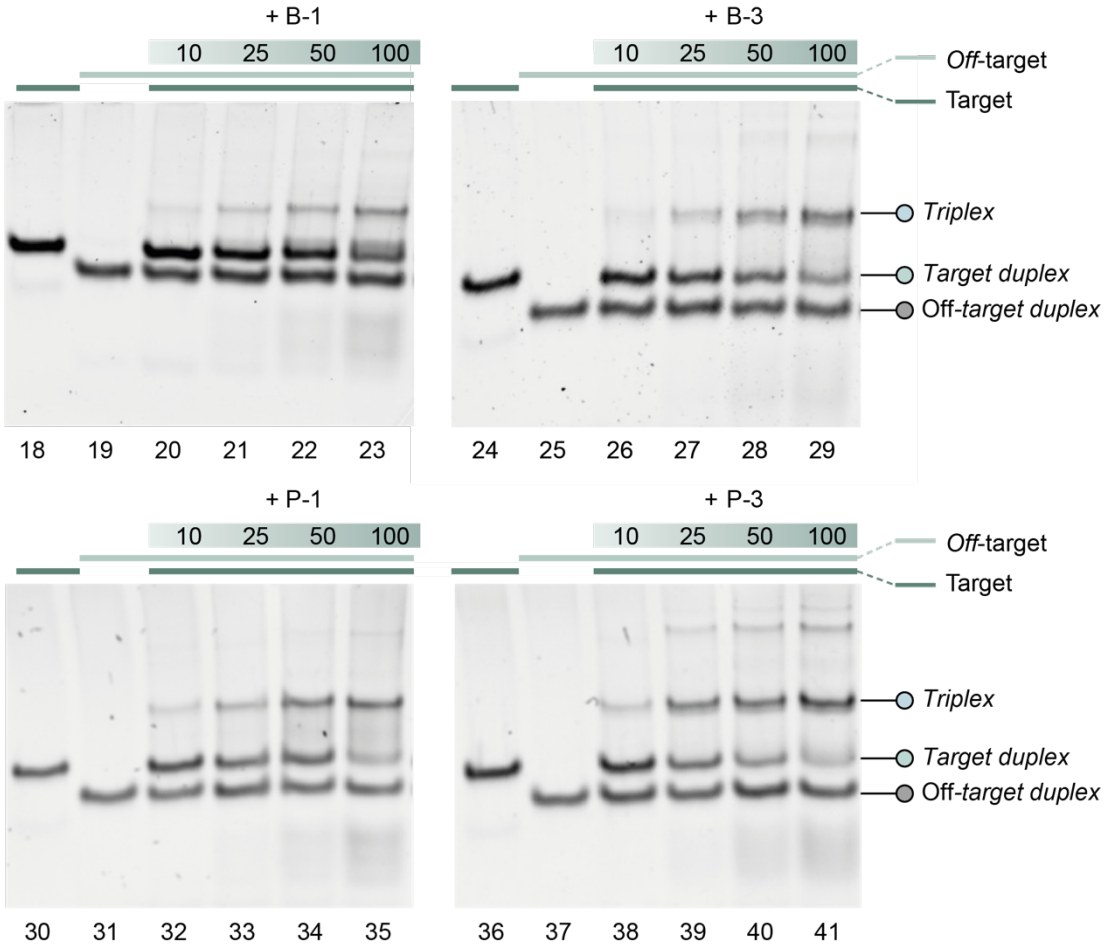


Figure IV.7: PAGE analysis of the activity of monofunctional Pt-TFO hybrids B-1, B-3, P-1 and P-3 toward 40-mer target duplex and 29-mer *off*-target duplex across a gradient of Pt-TFO concentration (10, 25, 50 and 100 equivalents) in phosphate buffer after 48 h incubation at 37 °C.

Next, thermal denaturation experiments exploiting TO fluorescence were used to quantify triplex association (Figure. IV.8). As the temperature increased, loss of TO intercalation caused by melting (dissociation) of the TFO from the duplex led to decreased fluorescence, which allowed determination of the melting temperature (T_M) for each hybrid. All Pt-TFO hybrids exhibited T_M values above 50 °C (51.3 °C, 50.8 °C, 50.2 °C and 51.1 °C for P-1, P-3, B-1 and B-3 respectively), indicating thermally stable triplexes at physiological temperature. In comparison, the parent DBCO-TFO displayed higher T_M values (55.0 °C for DBCO-TFO-1 and 66.8 °C for DBCO-TFO-3), indicating

that Pt(II) conjugation slightly destabilised the structure, which was also observed for recently reported *cis*-Pt-modified TFO hybrids.[20]

Interestingly, the negative fluorescence derivative curve for P-3 revealed two distinct melting events (50.8 °C and 60.3 °C), likely corresponding to sequential melting of each TO unit. DBCO-TFO-3 and B-3 exhibited similar, less-pronounced biphasic behaviour. Overall, the results confirm that Pt-TFO hybrids preserve strong triplex-forming capacities, with stability sufficient for Pt-adduct formation and enzymatic analyses.

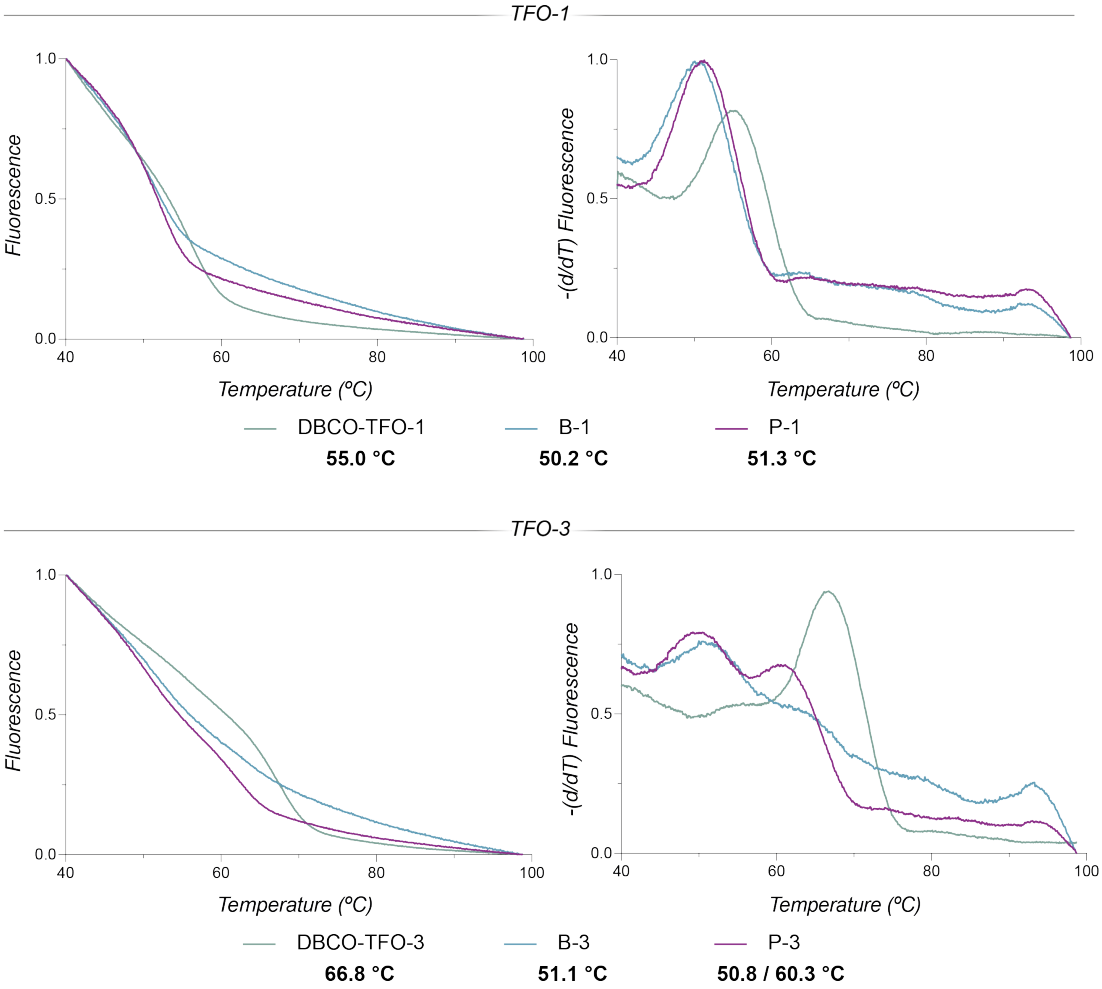


Figure IV.8: Fluorescence recording of the melting temperature for DBCO, Pt-benzyl-DPA and Pt-propyl-DPA hybrids of TFO-1 and TFO-3 and associated first negative derivative, where the T_M is recorded as the temperature where the maximum is reached.

3.5 Target specific crosslinking of EGFR *duplex by Pt-TFO hybrids (fluorescent denaturing experiment)*

Denaturing PAGE analysis was used to probe irreversible coordinative interactions of the monofunctional Pt-TFO hybrids towards fluorescently labelled short target duplex (Figure IV.9). This duplex, containing two strands

of discrete length and labelled with FAM or Cy5, enabled independent visualisation of each component (i.e. the purine-rich target strand or pyrimidine-rich complement strand) following electrophoretic separation. Pt(II) hybrids B-1, B-3, P-1 and P-3 were incubated with the duplex prior to denaturing PAGE, which disrupted both Hoogsteen and Watson-Crick hydrogen bonds, ensuring that only coordinatively linked species remained associated.

New, higher-molecular-weight bands were detected and increased in intensity with hybrid concentration. These bands were visible under the TO/FAM channel but absent from the Cy5 channel, indicating that they consisted of coordinative adducts between the FAM-labelled target strand and the TO-labelled Pt-TFO hybrids. The absence of corresponding Cy5 signal excluded association with the complementary strand, confirming that the interaction was selective to the target strand, consistent with its high G-content. P-1 and P-3 yielded slightly brighter higher-order bands than B-1 and B-3, suggesting a slightly stronger binding affinity of the Pt-propyl-DPA-TFO hybrids toward the target duplex than their Pt-benzyl-DPA-TFO analogues.

Control experiments verified that these adducts arose from the reaction of the Pt-TFO hybrids with the duplex, rather than from impurities, by comparing the results with controls with no incubation. In these controls, no adduct can form due to the lack of incubation, and therefore are indicative of higher-order bands that are not due to adduct formation. DBCO-TFO-1 and DBCO-TFO-3 produced distinctive higher bands, present even following short incubation times (Figure B.3.3.a). These did not overlap with the adducts observed for the Pt(II) conjugate after incubation. Similarly, when Pt-TFO hybrids were analysed without prior incubation (Figure B.3.3.a), only a faint higher band was observed, that did not overlap with the adducts generated during incubation. These results demonstrated that the higher-molecular-weight bands observed after incubation (Figure IV.9) were generated specifically through the interaction of the monofunctional Pt-TFO hybrids with the purine-rich target strand.

The monofunctional Pt-TFO hybrids were then compared to the Pt-Oxali-TFO hybrids developed in Chapter III, which are based on *cis*-Pt(II) chemotype drugs. These hybrids also showed the same activity towards the

target duplex, but to a lesser extent (Figure B.3.3.b). The reduced activity can be attributed to the requirement of the oxaliplatin analogue for adjacent G sites, limiting their potential binding locations. In contrast, monofunctional Pt(II) complexes react with isolated G residues, resulting in greater adduct-formation yield. Collectively, these results confirm that the designed Pt-DPA-TFO conjugates engage in target-specific irreversible covalent binding of the *EGFR* duplex consistent with coordinative Pt-adduct formation, with the Pt-propyl-DPA-TFO hybrids seeming to display a slightly better binding affinity than their benzylic analogues. This could be attributed to the higher flexibility of the propyl handle compared to the benzyl analogue.

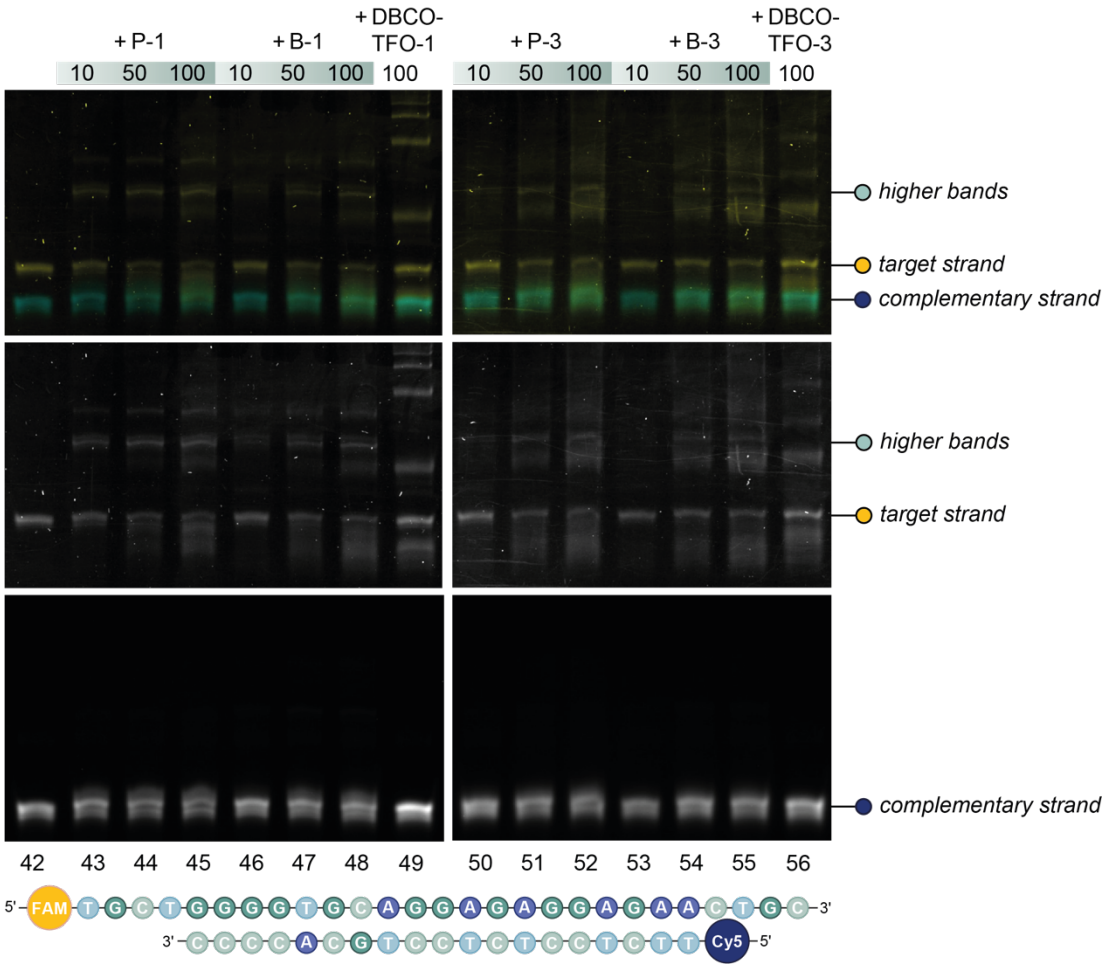
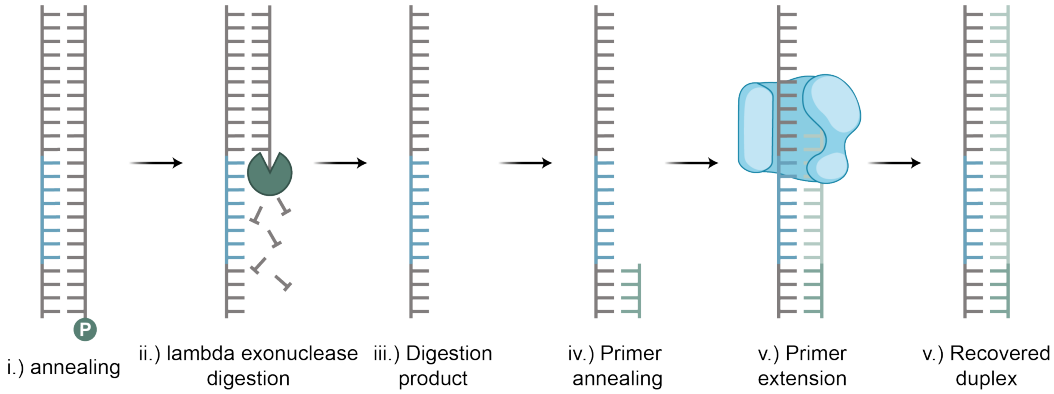


Figure IV.9: Denaturing PAGE experiment showing higher-order bands due to the adduct formation from monofunctional Pt-TFO hybrids B-1, B-3, P-1 and P-3 in the presence of the labelled short target duplex across a gradient of Pt-TFO concentration (10, 50 and 100 equivalents) in phosphate buffer. Lanes 49 and 56: 100 equivalents of DBCO-TFO-1 and DBCO-TFO-3 with labelled short target duplex showing impurities from the (unclicked) alkyne-TFOs.

3.6 Primer extension inhibitory studies

To evaluate whether Pt-TFO affected enzymatic processing of DNA, a Primer Extension (PEX) inhibition assay was designed (Figure IV.10). Here, a 40-bp target duplex containing a 5′-phosphorylated complementary strand was designed for selective digestion of the complementary strand using lambda exonuclease. This yielded a template for vent(exo-) DNA polymerase—an enzyme with higher fidelity than *Taq* known to process difficult templates—to access and potentially extend if the monofunctional Pt-DNA adducts can be read-through. The resulting products were analysed by native 1× TBE PAGE (Figure B.3.4) and quantified by densitometry (Figure IV.11).

a. Primer extension principle



b. Primer extension inhibition by triplex-mediated Pt(II) adduct formation

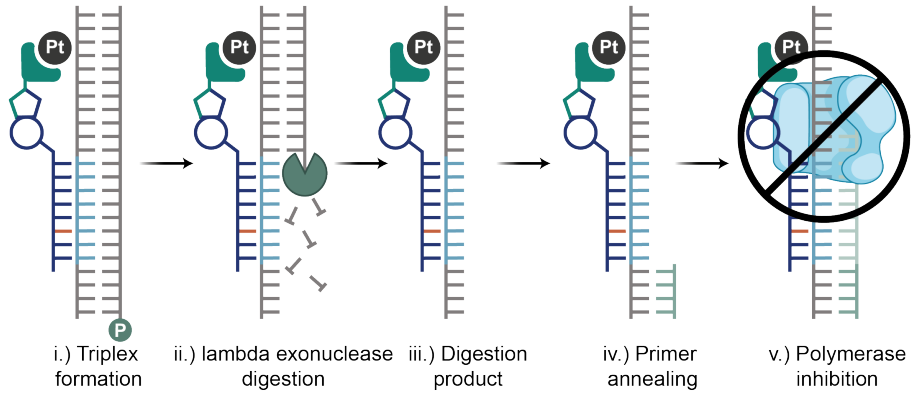
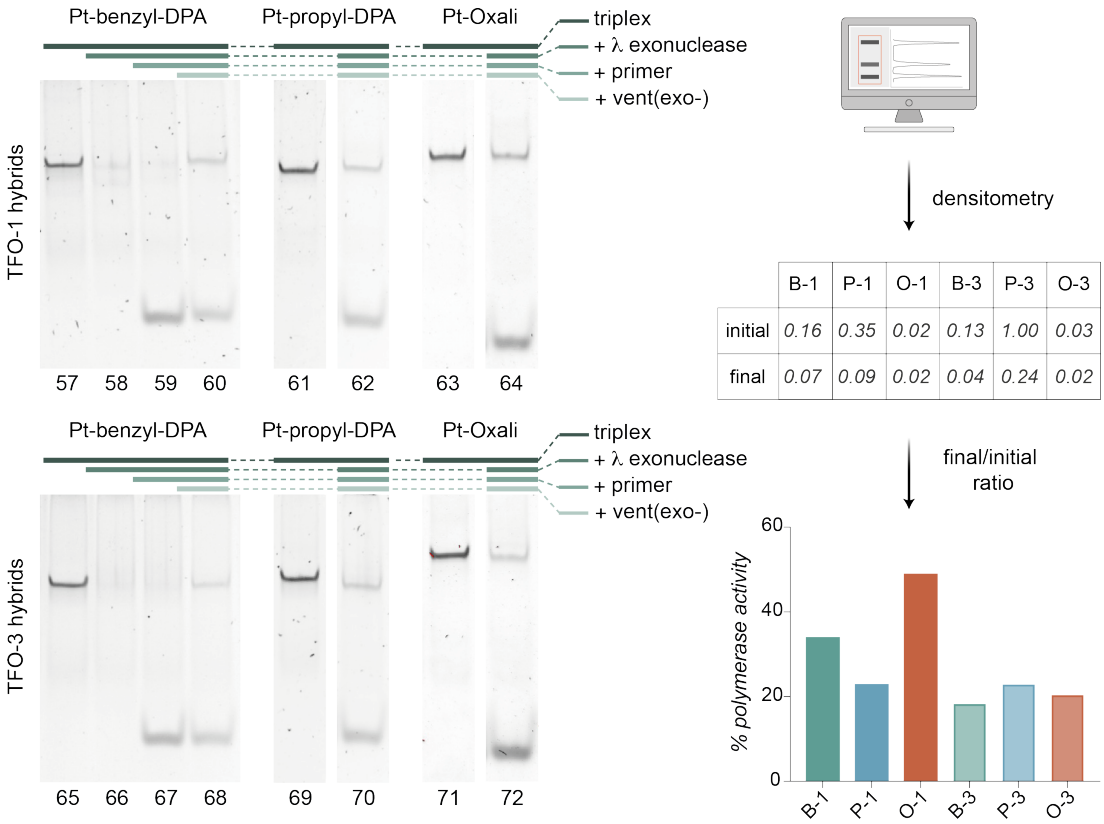


Figure IV.10: Principle of the PEX inhibition experiment. The recovery of duplex in a control sample is compared to the recovery of duplex after adduct formation in the presence of Pt-TFO hybrids. 5′-phosphorylate strand is digested by lambda exonuclease. The digestion product was then annealed with a primer and was used as a template for primer extension using vent(exo-) polymerase.

In the duplex control (Figure B.3.5), exonuclease digestion produced the expected single-stranded product, and subsequent polymerase extension regenerated approximately 60% of the original duplex signal. The same protocol was then applied to samples with DBCO-TFO-1 and yielded similar recovery, indicating that the unmodified TFO-1 did not interfere with enzymatic read-through. In contrast, DBCO-TFO-3 partially inhibited vent(exo-) polymerase extension, consistent with its higher TO content and enhanced triplex formation kinetics.

Importantly, introduction of Pt-TFO hybrids significantly inhibited read-through by the polymerase enzyme. Here, hybrids derived from TFO-1 reduced the recovery percentage to 20-50% while those derived from TFO-3 resulted in less than 30% recovery. These data indicate that the Pt-TFO hybrids hindered polymerase progression in accordance with the formation of coordinative monofunctional Pt-DNA adducts. Interestingly, the higher inhibitory properties observed for monofunctional Pt(II) conjugates relative to *cis*-Pt(II) analogues suggests that steric hinderance from the tridentate DPA ligand further impedes vent(exo-) polymerase access to the template. Collectively, these findings confirm that monofunctional Pt-TFO hybrids can act as sequence specific inhibitors of DNA synthesis, consistent with their ability to introduce site-selective covalent modifications.



	B-1	P-1	O-1	B-3	P-3	O-3
initial	*0.16*	*0.35*	*0.02*	*0.13*	*1.00*	*0.03*
final	*0.07*	*0.09*	*0.02*	*0.04*	*0.24*	*0.02*

Figure IV.11: PAGE analysis of the PEX inhibition experiment in the presence of Pt-TFO hybrids. First, the underlying duplex (lanes 57, 61, 63, 65, 69 and 71) was digested by lambda exonuclease (lanes 58 and 66), then the primer was added (lanes 59 and 67) followed by the partial recovery of duplex upon primer extension (lanes 60, 62, 64, 68, 70 and 72), showing polymerase inhibition activity of the Pt-TFO hybrids. Densitometry was used to determine the intensity of the underlying duplex in the initial and final samples, and the ratio was plotted to quantify polymerase activity across Pt-TFO hybrids.

4 Conclusion

In this chapter, monofunctional Pt(II) complexes incorporating DPA-based ligands were successfully synthesised. These complexes were hybridised with TFOs *via* SPAAC chemistry. The copper-free SPAAC conjugation strategy provided an efficient and reproducible means of metalating TFOs under mild conditions, avoiding potential degradation associated with CuAAC. The reactions proceeded without the need for purification, confirming the reliability of SPAAC for post-synthetic functionalisation of oligonucleotides.

Following the characterisation of the hybrids, their target-specific activity was assessed. Here, biophysical studies established the Pt-TFO hybrids maintained an ability to form stable and sequence-specific triplexes with the *EGFR* target duplex, with no detectable *off*-target association. While the incorporation of the Pt(II) complex led to modest triplex destabilisation compared with parent DBCO-TFOs, the melting temperatures remained above 50 °C, indicating sufficient thermal stability for biological applications. The presence of TO intercalators contributed to enhanced binding affinity as evidenced by more intense triplex bands for derivatives of TFO-3.

Next, denaturing PAGE provided evidence of Pt(II) coordinative bond formation between the Pt-TFO hybrids and the purine-rich target strand of the *EGFR* duplex, confirming the intended monofunctional adduct formation mechanism. The absence of similar interactions with the complementary TFO strand, together with attenuated activity by *cis*-Pt(II) controls reflects the ability of monofunctional Pt(II) complexes to react with isolated G residues. Finally, inhibition of polymerase read-through in the primer-extension assay with vent(exo-) polymerase demonstrated that these covalent adducts are not only structurally stable but are also functionally active, effectively blocking enzymatic processing at defined DNA loci. Taken together, the data highlights the dual functionality of monofunctional Pt-TFO hybrids where the TFO scaffold ensures precise molecular recognition through triplex formation, while the Pt(II) centre confers irreversible chemical reactivity toward G residues.

These results establish a new class of click chemistry generated monofunctional Pt-TFO conjugates capable of selective DNA recognition and covalent modification. The combination of high SPAAC efficiency, triplex

stability, irreversible covalent adduct formation, and enzymatic inhibition marks a significant advancement in the development of DNA targeting metal-TFO systems. Building on the findings, the following chapter explores the application of this efficient SPAAC methodology and the robust triplex-forming properties of the TFO scaffolds to develop artificial metallo-nuclease (AMN)-TFO hybrids capable of target specific DNA damage.

5 References

[1] Zhang, C.; Xu, C.; Gao, X.; Yao, Q. *Theranostics.* **2022**, *12,* (5), 2115-2132.

[2] Rosenberg, B.; VanCamp, L.; Trosko, J. E.; Mansour, V. H. *Nature.* **1969**, *222,* (5191), 385-386.

[3] Kelland, L. *Expert Opinion on Investigational Drugs.* **2007**, *16,* (7).

[4] Khoury, A.; Deo, K. M.; Aldrich-Wright, J. R. *J Inorg Biochem.* **2020**, *207*, 111070.

[5] Johnstone, T. C.; Wilson, J. J.; Lippard, S. J. *Inorganic Chemistry.* **2013**, *52,* (21).

[6] Jin, S.; Guo, Y.; Guo, Z.; Wang, X. *Pharmaceuticals (Basel).* **2021**, *14,* (2).

[7] Lovejoy, K. S.; Serova, M.; Bieche, I.; Emami, S.; D'Incalci, M.; Broggini, M.; Erba, E.; Gespach, C.; Cvitkovic, E.; Faivre, S.; et al. *Mol Cancer Ther.* **2011**, *10,* (9), 1709-1719.

[8] Park, G. Y.; Wilson, J. J.; Song, Y.; Lippard, S. J.; Park, G. Y.; Wilson, J. J.; Song, Y.; Lippard, S. J. *Proceedings of the National Academy of Sciences.* **2012**, *109,* (30).

[9] Zhang, H.; Yang, T.; Wang, Y.; Wang, Z.; Zhu, Z.; Guo, Z.; Wang, X. *Dalton Trans.* **2021**, *50,* (1), 304-310.

[10] Florea, A. M.; Busselberg, D. *Cancers (Basel).* **2011**, *3,* (1), 1351-1371.

[11] Manchanda, R.; Dunham, S. U.; Lippard, S. J. *J Am Chem Soc.* **1996**, *118,* (21), 5144-5145.

[12] Miller, P. S. *Prog Nucleic Acid Re.* **1996**, *52*, 261-291.

[13] Schmidt, K. S.; Boudvillain, M.; Schwartz, A.; van der Marel, G. A.; van Boom, J. H.; Reedijk, J.; Lippert, B. *Chemistry.* **2002**, *8,* (24), 5566-5570.

[14] Fox, K., R. ; Brown, T.; Rusling, D. A. *Chemical Biology.* **2018**, *Chapter 1*, 1-32.

[15] Campbell, M. A.; Mason, T. M.; Miller, P. S. *Can J Chem.* **2007**, *85,* (4), 241-248.

[16] Campbell, M. A.; Miller, P. S. *J Biol Inorg Chem.* **2009**, *14,* (6), 873-881.

[17] Graham, M. K.; Brown, T. R.; Miller, P. S. *Biochemistry-Us.* **2015**, *54,* (13), 2270-2282.

[18] Schmidt, K. S.; Filippov, D. V.; Meeuwenoord, N. J.; van der Marel, G. A.; van Boom, J. H.; Lippert, B.; Reedijk, J. *Angewandte Chemie International Edition.* **2000**, *39,* (2), 375-377.

[19] Hennessy, J.; Klimkowski, P.; Singleton, D.; Gibney, A.; Coche, M.; Farrell, N. P.; El-Sagheer, A. H.; Brown, T.; Kellett, A. *RSC Medicinal Chemistry.* **2023**.

[20] Hennessy, J.; McGorman, B.; Molphy, Z.; Farrell, N. P.; Singleton, D.; Brown, T.; Kellett, A. *Angew Chem Int Ed Engl.* **2022**, *61,* (3), e202110455.

[21] Klimkowski, P.; De Ornellas, S.; Singleton, D.; El-Sagheer, A. H.; Brown, T. *Org Biomol Chem.* **2019**, *17,* (24), 5943-5950.

[22] Walsh, S.; El-Sagheer, A. H.; Brown, T. *Chem Sci.* **2018**, *9,* (39), 7681-7687.

[23] Xodo, L. E.; Manzini, G.; Quadrifoglio, F.; van der Marel, G. A.; van Boom, J. H. *Nucleic Acids Res.* **1991**, *19,* (20), 5625-5631.

[24] Santos, G. D.; Shepherd, F. A.; Tsao, M. S. *Annu Rev Pathol-Mech.* **2011**, *6*, 49-69.

[25] McGorman, B.; Fantoni, N. Z.; O'Carroll, S.; Ziemele, A.; El-Sagheer, A. H.; Brown, T.; Kellett, A. *Nucleic Acids Res.* **2022**, *50,* (10), 5467-5481.
[26] Lovejoy, K. S.; Todd, R. C.; Zhang, S.; McCormick, M. S.; D'Aquino, J. A.; Reardon, J. T.; Sancar, A.; Giacomini, K. M.; Lippard, S. J. *Proc Natl Acad Sci U S A.* **2008**, *105,* (26), 8902-8907.

Chapter V

Prodigiosin Modified Triplex-Forming Oligonucleotide Hybrids Enable Self-Activated DNA Cleavage

April 2026

1 Introduction

DNA is the universal carrier of genetic information and underpins all essential biological processes. Strategies that enable the selective silencing or modification of DNA have significant potential for the treatment and prevention of genetic disorders. One promising approach is the induction of oxidative damage using artificial metallo-nucleases (AMNs).[1] Copper-based AMNs (Cu-AMNs) are of particular interest due to their ability to generate reactive oxygen species (ROS) capable of inducing single- or double-strand breaks in nucleic acids.[2]

In 2000, Manderville and coworkers reported the ability of the marine alkaloid prodigiosin (PD) to generate double strand cleavage in the presence of copper.[3] Notably, this copper-mediated oxidative cleavage occurs autocatalytically without the requirement for an external reductant (e.g. sodium-L-ascorbate, (Na-*L*-asc)), in contrast to the majority of reported AMNs.[4] This property makes PD an attractive candidate for DNA-targeted therapeutic applications. PD is a member of the prodiginine family of natural products, which are predominantly isolated from marine sponge-associated bacteria, along with tambjamine E,[5] and dipyrrolyldipyrromethene prodigiosin (tetrapyrrole)[6, 7] (Figure V.1). Tambjamine E and other prodiginines have also been reported for their Cu-mediated DNA cleavage activity.[8, 4, 9] Beyond its nuclease activity, PD has been investigated for anticancer, immunosuppressive and antimicrobial properties, broadening its relevance in medicinal chemistry.[10]

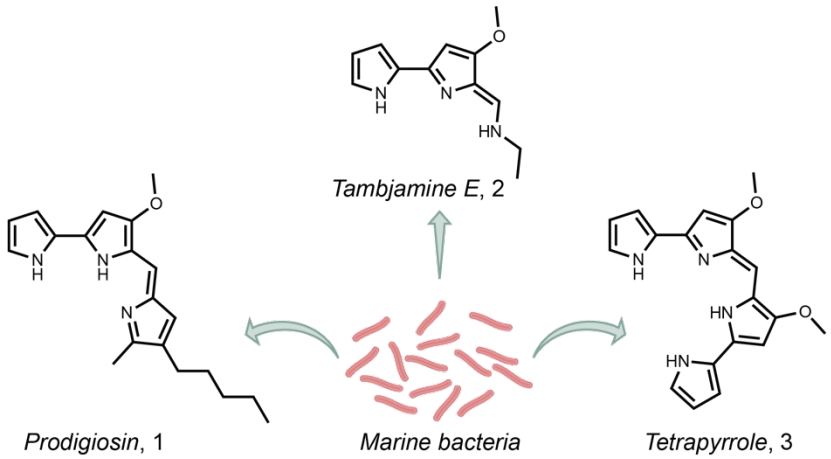


Figure V.1: Isolation of prodigiosin, tambjamine E and tetrapyrrole from marine bacteria.

Despite their potent cleavage activity, Cu-AMNs generally suffer from a lack of sequence specificity, limiting their application in targeted gene therapies. This can be remediated by covalently tethering the nuclease moiety to a sequence-specific recognition element, such as a triplex-forming oligonucleotide (TFO).[11, 12] TFOs sequence-specifically bind to the major groove of duplex DNA *via* Hoogsteen hydrogen bonding.[13] Triplex association kinetics can be improved through chemical modifications[14] such as thiazole orange (TO)[15, 16]—an intercalating dye that stabilises DNA triplexes *via* π-π stacking—or 5-methylcytosine (5mC) that can replace cytosines on the TFO to improve binding at neutral pH.[17]

In recent years, click chemistry, more specifically copper-catalysed azide-alkyne cycloaddition (CuAAC), has been used to attach copper caging ligands[18, 19] and phenanthroline-based[20, 19] AMNs to TFOs. These hybrids combined high target specificity with efficient DNA cleavage. However, the systems were dependant on the addition of a reductant to activate the nuclease activity, which complicates biological applications and reduces *in vivo* compatibility.

Strain-promoted azide-alkyne cycloaddition (SPAAC) offers an alternative conjugation method to CuAAC chemistry that avoids the use of a copper catalyst and is operated under milder conditions.[21] In this chapter, SPAAC was used to attach an azide-modified PD analogue (N_3-PD) to alkyne-modified TFOs. The total synthesis of this analogue is reported here, and we found the azide-derivative retained autocatalytic activity, eliminating the requirement for an external reductant. TFO scaffolds were optimised for triplex stability by incorporating one or two TO units and substituting cytosines with 5mC. The aim of this chapter is to evaluate the potential of PD-modified TFO hybrids for triplex formation and self-activated targeted cleavage activity.

2 Materials and Methods

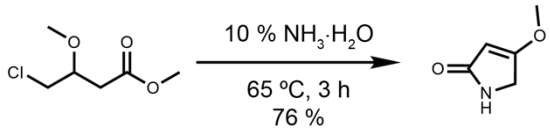
2.1 General methods

Chemicals and high-performance liquid chromatography (HPLC) grade solvents were purchased from Merck, Tokyo Chemical Industry (TCI) or Fisher Scientific and used without further purification. ^{1}H and ^{13}C NMR spectra were recorded on a Bruker AC 600 MHz NMR spectrometer. FTIR measurements were performed on a PerkinElmer Spectrum Two spectrometer. Electrospray ionization mass spectrometry (ESI-MS) was performed by collaborators in the University of Bath. All spectra are reported in Chapter VIII section C.1. Mass spectrometry for oligonucleotides was conducted by collaborators in ATDBio and HPLC traces and MS chromatograms are reported in Chapter VIII section C.2. Agarose and PAGE gels were visualised on a Syngene G:Box Mini 9 gel documentation system and all samples were quenched with loading dye (6×, 2.5% Ficoll®-400, 11 mM EDTA, 3.3 mM Tris-HCl, 0.017% SDS, 0.015% bromophenol blue, pH 8.0, Thermo Fisher) before loading on agarose or PAGE gels. Agarose gels were prepared by dissolving agarose in Tris-acetate-EDTA (TAE, Fisher Scientific, 1×) and adding SYBR Safe (Thermo Fisher Scientific) and heating the mixture before casting and leaving it to cool for 1 h. PAGE gels were prepared using 29:1 acrylamide:bis-acrylamide in the presence of Tris-Acetate (TA, pH 6.0, 50 mM) or tris-borate-EDTA (TBE, Fisher Scientific, 1×) buffer, TEMED (Thermo Fisher Scientific, 0.2%) and ammonium persulfate (APS, 0.05%). In the case of denaturing gels, urea (42%) was added. In the case of TA gels, $MgCl_2$ (5 mM) and NaCl (75 mM) were added. PAGE gels were stained with SYBR Gold (20 mL of 1× solution, Thermo Fisher Scientific) before visualisation on the Syngene G:Box Mini 9 gel documentation system. *EGFR* plasmid was purchased from Addgene. Real-time PCR (qPCR) and thermal melting (T_M) analyses were carried out on a Light Cycler® 480 II (Roche) using SYBR Green I master mix (Roche) as specified. Fluorescence was recorded across a temperature range from 20 °C to 99 °C, with a ramp rate of 0.6 °C/s and 10 acquisitions per °C. 5′-DBCO TFOs were synthesised and labelled with TO by collaborators in ATDBio.

2.2 Synthesis of an azide-functionalised prodigiosin analogue

The synthesis of 4-methoxy-1H,1′H-[2,2′-bipyrrole]-5-carbaldehyde was adapted from the literature method as reported by Kancharla *et al.*[22] Spectroscopy data for all reported compounds was confirmed with the literature.

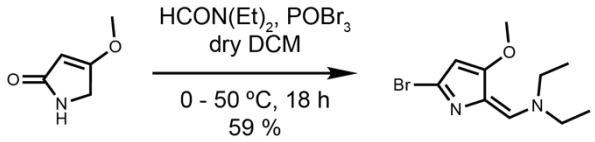
2.2.1 Synthesis of 4-methoxy-3-pyrrolin-2-one



4 **5**

4-chloro-3-methoxy-2-(E)-butenoic acid methyl ester (640.1 mg, 3.89 mmol, 1 eq.) was dissolved in H_2O (3.8 mL) and ammonia (1.5 mL, 31.24 mmol, 8 eq.) was added at 0 °C. The solution was allowed to return to room temperature before being stirred at 65 °C for 5 h. After cooling down, the mixture was extracted with 6 x 10 mL dichloromethane. The aqueous layer was heated at 65 °C for another 2.5 h before being extracted with 3 x 10 mL dichloromethane. Combined organic layers were dried over $MgSO_4$ and evaporated under reduced pressure, affording 335.1 mg, 2.96 mmol of 4-methoxy-3-pyrrolin-2-one as light-yellow crystals, with a 76% yield. ^{1}H NMR ($CDCl_3$) δ (ppm): 5.55 (brs, 1H), 5.08 (s, 1H), 3.93 (s, 2H), 3.82 (s, 3 H).

2.2.2 Synthesis of N-((5-bromo-3-methoxy-2H-pyrrol-2-ylidene)methyl)-N-ethylethanamine

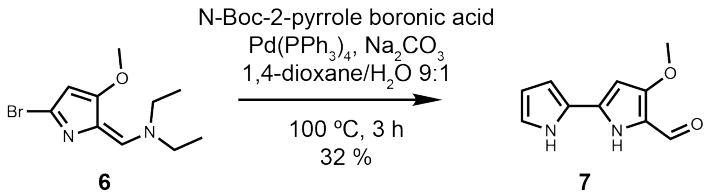


5 **6**

N,N-diethyl formamide (1182 µL, 10.61 mmol, 3 eq.) was diluted in dry dichloromethane (15 mL) and a solution of phosphorus(V) oxybromide (2.534 g, 8.84 mmol, 2.5 eq.) in dry dichloromethane (30 mL) was added dropwise at 0 °C, revealing a white solid that was ground with a spatula, before the mixture was further stirred at 0 °C for 1 h under inert atmosphere. 4-methoxy-3-pyrrolin-2-one (400.3 mg, 3.54 mmol 1 eq.) was then transferred into the reaction flask using dry DCM (10 mL) and the mixture was refluxed at 50 °C under inert atmosphere overnight. After cooling to room temperature, the mixture was poured onto ice-cold water (100 mL), and the pH was raised using

aqueous NaOH (2.5 mL, 5 M). After vigorous stirring for 30 min, the product was extracted using 3 x 50 mL DCM. The combined organic layers were washed with 3 x 20 mL DI H_2O and 3 x 20 mL brine before being dried over Na_2SO_4 and further dried under reduced pressure. The crude product was then purified over a silica column using an ethyl acetate in hexane (0 to 100%) eluent, yielding 539.8 mg, 2.08 mmol of N-((5-bromo-3-methoxy-2H-pyrrol-2-ylidene)methyl)-N-ethylethanamine as a brown oil with a 59% yield. ^{1}H NMR ($CDCl_3$) δ (ppm): 7.00 (s, 1H), 5.60 (s, 1H), 4.12 (q, *J* = 7.1 Hz, 2H), 3.76 (s, 3H), 3.40 (q, *J* = 7.2 Hz, 2H), 1.29 (q, *J* = 7.2 Hz, 6H).

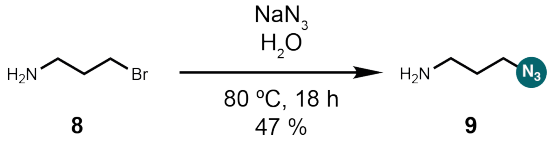
2.2.3 Synthesis of 4-methoxy-1H,1'H-[2,2'-bipyrrole]-5-carbaldehyde



6 **7**

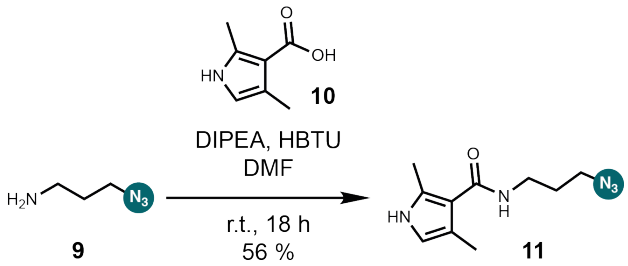
To a solution of N-((5-bromo-3-methoxy-2H-pyrrol-2-ylidene)methyl)-N-ethylethanamine (573 mg, 2.21 mmol, 1 eq.) in dioxane (9 mL) was added N-boc-2-pyrrole boronic acid (700 mg, 3.32 mmol, 1.5 eq.). The resulting mixture was purged with nitrogen at 0 °C before being transferred into a flask containing a solution of Na_2CO_3 (703 mg, 6.63 mmol, 3 eq.) and $Pd(PPh_3)_4$ (256 mg, 0.022 mmol, 0.1 eq.) in DI H_2O (1 mL) under nitrogen atmosphere. The resulting mixture was refluxed at 100 °C for 3 h. After cooling down to room temperature, the solution was poured onto ice cold water (70 mL) and the pH was lowered to 7.0 using HCl (2 M), revealing a precipitate that was isolated by vacuum filtration, washed with DI H_2O, acetone, chloroform and diethyl ether, affording 134.3 mg, 0.71 mmol of 4-methoxy-1H,1′H-[2,2′-bipyrrole]-5-carbaldehyde as a light yellow crystalline powder with a 32% yield. ^{1}H NMR (DMSO-d_6) δ (ppm): 11.42 (s, 1H), 11.24 (s, 1H), 9.29 (s, 1H), 6.91 (td, *J* = 2.6, 1.5 Hz, 1H), 6.75 (brs, 1H), 6.27 (d, *J* = 2.6 Hz, 1H), 6.12 (dt, *J* = 3.5, 2.4 Hz, 1H), 3.83 (s, 3H).

2.2.4 *Synthesis of 3-azidopropyl-1-amine*



3-bromopropyl-1-amine hydrobromide (1.000 g, 4.57 mmol, 1 eq.) was dissolved in H_2O (4 mL) and sodium azide (891.2 mg, 13.70 mmol, 3 eq.) was added. The resulting mixture was then refluxed overnight. After cooling down to room temperature, diethyl ether (20 mL) was added, the mixture was cooled at 0 °C and potassium hydroxide (1.000 g) was added. The aqueous layer was isolated and extracted with 3 x 20 mL diethyl ether. The combined organic layers were dried over $MgSO_4$ and evaporated under reduced pressure to afford 389.1 mg, 2.15 mmol of 3-azidopropyl-1-amine as a colourless oil with a 47% yield. ^{1}H NMR (DMSO-d_6) δ (ppm) 3.37 (t, *J* = 6.8 Hz, 2H), 2.58 (t, *J* = 6.7 Hz, 2H), 1.59 (m, 2H).

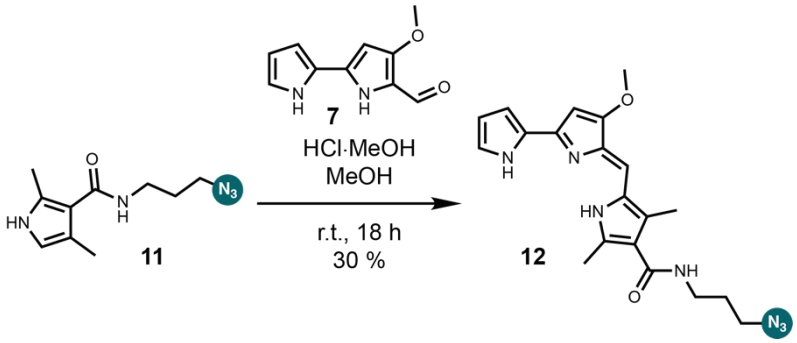
2.2.5 *Synthesis of N-(3-azidopropyl)-2,4-dimethyl-1H-pyrrole-3-carboxamide*



2,4-dimethyl-1H-pyrrole-3-carboxylic acid (472.0 mg, 3.39 mmol, 1 eq.) was dissolved in dry DMF (20 mL) and 3-azidopropyl-1-amine (1.837 g, 10.14 mmol, 3 eq.) was added, followed by DIPEA (1296 µL, 7.44 mmol, 2.2 eq.) at 0 °C. The resulting mixture was stirred at 0 °C for 30 min before HBTU (1.924 g, 5.07 mmol, 1.5 eq.) was added. The mixture was flushed with dry nitrogen and further stirred at room temperature in the dark overnight. Ethyl acetate (20 mL) was added, and the mixture was washed with 3 x 15 mL H_2O and 3 x 15 mL brine before being dried over $MgSO_4$ and evaporated to dryness under reduced pressure. The crude product was purified by silica chromatography column using ethyl acetate as a mobile phase, yielding 419.8 mg, 1.90 mmol of N-(3-azidopropyl)-2,4-dimethyl-1H-pyrrole-3-carboxamide with a 56% yield. ^{1}H NMR ($CDCl_3$) δ (ppm): 7.87 (brs, 1H), 6.40 (s, 1H), 5.80 (brs, 1H), 3.53 (q, *J* = 6.5 Hz, 2H), 3.46 (t, *J* = 6.6 Hz, 2H), 2.51 (s, 3H), 2.27 (s, 3H), 1.92 (quint,

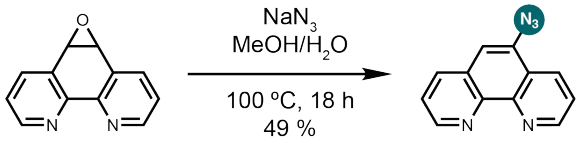
J = 6.6 Hz, 2H). IR (cm^{-1}): 3436, 3270, 2926, 2868, 2094, 1715, 1622, 1569, 1530, 1509, 1437, 841, 557.

2.2.6 Synthesis of N-(3-azidopropyl)-5-((4'-methoxy-1H,5'H-[2,2'-bipyrrol]-5'-ylidene)methyl)-2,4-dimethyl-1H-pyrrole-3-carboxamide (N_3-PD)



After the preparation of fresh MeOH.HCl (3 M, 0.5 mL acetyl chloride in 2.0 mL dry MeOH at 0 °C), 4-methoxy-1H,1'H-[2,2'-bipyrrole]-5-carbaldehyde (308.1 mg, 1.62 mmol, 1eq.) was dissolved in dry MeOH (15 mL) under inert atmosphere, and N-(3-azidopropyl)-2,4-dimethyl-1H-pyrrole-3-carboxamide (536.9 mg, 2.43 mmol, 1.5 eq.) was added. The mixture was cooled to 0 °C and MeOH.HCl (1.5 mL, 3 M) was added dropwise. The resulting mixture was stirred at room temperature under inert atmosphere in the dark overnight. The reaction mixture was then evaporated to dryness under reduced pressure and the crude product was purified by column chromatography using ethyl acetate, affording 190.4 mg, 0.48 mmol of *N*-(3-azidopropyl)-5-((4'-methoxy-1*H*,5'*H*-[2,2'-bipyrrol]-5'-ylidene)methyl)-2,4-dimethyl-1*H*-pyrrole-3-carboxamide with a 30% yield. ^{1}H NMR (MeOD) δ (ppm) 7.01 (dd, *J* = 2.5, 1.3 Hz, 1H), 6.75 (d, *J* = 2.2 Hz, 2H), 6.25 (dd, *J* = 3.6, 2.5 Hz, 1H), 6.08 (s, 1H), 3.92 (s, 3H), 3.44 (t, *J* = 6.8 Hz, 4H), 2.52 (s, 3H), 2.30 (s, 3H), 1.88 (quint, *J* = 6.8 Hz, 2H). ^{13}C (MeOD) δ (ppm) 167.9, 122.2, 112.4, 112.4, 110.6, 109.7, 95.0, 57.6, 48.9, 48.4, 36.6, 28.6, 11.5, 9.0. IR (cm^{-1}): 3245, 2957, 2921, 2873, 2852, 2094, 1702, 1623, 1609, 1600, 1539, 1447, 1436, 1374, 1361, 1153, 1136, 1111. ESI-MS calc. for $C_{20}H_{24}N_7O_2$ $[M+H]^+$:394.1991. Found: 394.1990.

2.2.7 *Synthesis of 5-azido-1,10-phenanthroline (N_3-Phen)*



13 **14**

The synthesis of 5-azido-1,10-phenanthroline was adapted from the method reported by Lauria *et al.*[20] 5,6-epoxy-5,6-dihydro-[1,10]-phenanthroline (400.0 mg, 2.04 mmol, 1 eq.) and sodium azide (396.2 mg, 6.09 mmol, 3 eq.) were dissolved in H_2O/methanol (15 mL, 4:1). The resulting mixture was refluxed at 100 °C for 18 h in darkness. The reaction was then cooled to room temperature and poured onto ice-cold water (20 mL). The resulting precipitate was isolated by gravity filtration, washed with 5 x 15 mL H_2O and dried under nitrogen for 30 min before being further dried on a Schlenk line overnight, in the dark, affording 5-azido-1,10-phenanthroline (221.2 mg, 1.00 mmol) with a 49% yield. ^{1}H NMR ($CDCl_3$) δ 9.24 (dd, J = 4.5, 1.7 Hz, 1H), 9.13 (dd, J = 4.4, 1.6 Hz, 1H), 8.55 (dd, J = 8.3, 1.7 Hz, 1H), 8.19 (dd, J = 8.1, 1.7 Hz, 1H), 7.66 (ddd, J = 21.3, 8.2, 4.3 Hz, 2H), 7.50 (s, 1H). ^{13}C NMR ($CDCl_3$) δ 151.26, 149.72, 146.65, 144.24, 135.45, 134.65, 131.38, 128.27, 123.62, 123.39, 123.08, 112.36.

2.3 Preliminary DNA cleavage activity assessment

All reactions were quenched by the addition of 3 µL of loading dye and loaded onto a 1.3% agarose gel. All gels were run in 1× TAE buffer at 70 V for 90 min.

2.3.1 *Cleavage of pUC19 in the presence of Na-L-asc*

Samples were prepared in a total volume of 20 µL in HEPES buffer (80 mM, pH 7.2) containing supercoiled pUC19 DNA (400 ng), NaCl (25 mM), Na-*L*-asc (1 mM), and increasing concentrations of [Cu(N_3-PD)(NO_3)$_2$], ranging from 0 µM to 200 µM. Samples were incubated at 37 °C for 30, 60 or 90 min before being quenched and loaded on 1.3% agarose gels. Gels were visualised as mentioned in section 2.1.

2.3.2 *Self-activated pUC19 cleavage profile*

The samples were prepared in a total volume of 20 µL in HEPES buffer (80 mM, pH 7.2) containing supercoiled pUC19 DNA (400 ng), NaCl (25 mM), and increasing concentrations of [Cu(N_3-PD)(NO_3)$_2$], ranging from 0 µM to 200 µM. Samples were incubated at 37 °C for 30, 60 or 90 min before being quenched

and loaded on 1.3% agarose gels. Gels were visualised as mentioned in section 2.1.

2.3.3 Mechanistic studies of pUC19 cleavage

The samples were prepared in a total volume of 20 µL in HEPES buffer (80 mM, pH 7.2) containing supercoiled pUC19 DNA (400 ng), NaCl (25 mM), scavenger (1 mM of either tiron, L-methionine, D-mannitol, NaN_3, DMTU, *L*-histidine, D_2O or TEMPO) and [Cu(N_3-PD)(NO_3)$_2$] (10 µM, 25 µM, 50 µM or 100 µM). For the mechanistic investigation of Na-*L*-asc-activated cleavage, Na-*L*-asc was added in each lane to reach 1 mM concentration and [Cu(N_3-PD)(NO_3)$_2$] was added reaching concentrations of 5 µM, 10 µM, 20 µM or 25 µM. Samples were incubated at 37 °C for 60 min before being quenched and loaded on 1.3% agarose gels. Gels were visualised as mentioned in section 2.1.

2.3.4 Groove-preference of [Cu(N_3-PD)(NO_3)$_2$]

Supercoiled pUC19 DNA (400 ng) was incubated at 37 °C for 1 h with either methyl green or netropsin (80 µM), which are known to reside in the major or minor groove, respectively. The samples were then prepared in a total volume of 20 µL in HEPES buffer (80 mM, pH 7.2) containing DNA (400 ng), NaCl (25 mM) and increasing concentration of [Cu(N_3-PD)(NO_3)$_2$] (10 µM, 25 µM, 50 µM or 100 µM). Samples were incubated at 37 °C for 60 min before being quenched and loaded on 1.3% agarose gels. Gels were visualised as mentioned in section 2.1.

2.3.5 Sequence-specific cleavage preference of [Cu(N_3-PD)(NO_3)$_2$]

Dodecamers of different A and T composition (1 pmol) were incubated at 37 °C for 1 h in the presence of increasing amounts of [Cu(N_3-PD)(NO_3)$_2$] (100, 500 or 1000 eq.) in phosphate buffer (10 mM PO_4^{3-}, 150 mM NaCl, 10 mM $MgCl_2$, pH 6.0). The samples were then quenched with 2 µL loading dye and loaded onto 50 mM TA native gels and PAGE was run at 70 V for 4 h. Gels were visualised after SYBR Gold staining as mentioned in section 2.1.

2.4 SPAAC labelling of 5'-DBCO modified TFOs

2.4.1 Preparation of PD-TFO hybrids

In a total volume of 800 µL in H_2O / acetonitrile (9:1), N_3-PD (200 nmol, 10 eq.) was treated with DBCO-labelled TFO (20 nmol, 1 eq.). The resulting mixture was incubated at 37 °C, 300 rpm for 1 h. biology grade H_2O (200 µL) was added to the reaction mixture for NAP-10 column purification, before freeze-drying.

2.4.2 Preparation of phenanthroline-TFO hybrids

Phenanthroline-TFO hybrids were prepared similarly on a smaller scale. In a total volume of 80 µL in H_2O / acetonitrile (9:1), N_3-phenanthroline (20 nmol, 10 eq.) was reacted with DBCO-labelled TFO (2 nmol, 1 eq.). The resulting mixture was incubated at 37 °C, 300 rpm for 1 h. biology grade H_2O (20 µL) was added to the reaction mixture for NAP-5 column purification, before freeze-drying.

2.4.3 SPAAC monitoring with denaturing PAGE

SPAAC-reactions were monitored by denaturing 20% acrylamide gel electrophoresis in 1× TBE. Hybrids and DBCO-TFOs (30 pmol) were prepared in 10 µL biology grade H_2O and loading dye (2 µL) was added. The gels were run at 150 V for 3 h and visualised after staining with SYBR Gold as mentioned in section 2.1.

2.5 Triplex formation of PD-TFO and Phen-TFO hybrids

2.5.1 PAGE visualisation of triplex formation

Samples were prepared in a total volume of 10 µL containing the target duplex (0.5 pmol) in phosphate buffer (10 mM PO_4^{3-}, 150 mM NaCl, 10 mM $MgCl_2$, pH 6.0) with increasing equivalents of TFO hybrids (20, 50 and 100 eq.). The resulting samples were incubated at 37 °C for 1 h, and loading dye (2 µL) was added. The samples were then loaded onto a 20% acrylamide TA, pH 6.0, native gel, and PAGE was run in 50 mM TA buffer at 70 V for 4 h. The gels were visualised after staining with SYBR Gold as mentioned in section 2.1.

2.5.2 Thermal melting studies

In a total volume of 20 µL, TFO hybrid (50 pmol, 10 eq.) was added to the target duplex (5 pmol, 1 eq.) in phosphate buffer (10 mM PO_4^{3-}, 150 mM NaCl, 10 mM $MgCl_2$, pH 6.0). Samples were prepared in triplicates and incubated at 37 °C for 1 h before the fluorescence was recorded using a Light Cycler® 480 II (Roche) instrument across a gradient of temperature up to 99 °C, with 10 fluorescence measurements recorded per °C. For hybrids of TFO-4, SYBR Green I master mix (10 µL, Roche) was added prior to measurements. Thermal melting curves obtained by the Light Cycler® software were exported and analysed and graphed using GraphPad Prism 10 software. T_M was calculated as the temperature where the first negative derivative of the melting curve reaches a maximum. The reported T_M values reported for each hybrid was the average of the triplicates.

2.6 Qualitative Cleavage Activity assessment of the PD-TFO Hybrids

2.6.1 Initial investigations of the cleavage activity of PD-TFO hybrids

Cleavage experiments were carried out in the presence of different duplexes containing the triplex-binding region (0.5 pmol, 1 eq. of each) in a total volume of 10 µL phosphate buffer (10 mM PO_4^{3-}, 150 mM NaCl, 10 mM $MgCl_2$, pH 6.0). TFO hybrid (50 pmol, 100 eq.) was added followed by $Cu(NO_3)_2$ (in varying amounts). In the case of Na-*L*-asc-mediated cleavage activity assessment, Na-*L*-asc (1 mM) was added to each sample. The resulting samples were incubated at 37 °C for increasing incubation time, quenched by the addition of loading dye (2 µL) and loaded onto 20% acrylamide native TA gels, pH 6.0, along with target and *off*-target duplex controls. PAGE was run at 70 V for 4 h. The gels were visualised after staining with SYBR Gold as mentioned in section 2.1.

2.6.2 Comparison of PD-TFO and Phen-TFO hybrids using PAGE

Cleavage experiments were carried out in the presence of target and *off*-target duplex (0.5 pmol, 1 eq. of each) in a total volume of 10 µL phosphate buffer (10 mM PO_4^{3-}, 150 mM NaCl, 10 mM $MgCl_2$, pH 6.0). TFO hybrid (50 pmol, 100 eq.) was added followed by $Cu(NO_3)_2$ (250 pmol, 500 eq.). In the case of Phen-TFO hybrids, Na-*L*-asc (1 mM) was added to each sample. The resulting

samples were incubated at 37 °C for increasing incubation time, quenched by the addition of loading dye (2 µL) and loaded onto 20% acrylamide native TA gels, pH 6.0, along with target and *off*-target duplex controls. PAGE was run at 70 V for 4 h. The gels were visualised after staining with SYBR Gold as mentioned in section 2.1.

2.6.3 Amplicon expression

PCR amplification was completed using a thermocycler on 32 samples in parallel, in a total volume of 50 µL containing 1× Taq buffer (PCR Biosystems), *EGFR* plasmid (2 µL of 1 ng/µL), reverse and forward primers (1 µL of 10 µM each) and Taq polymerase (0.25 µL of 5 u/µL, PCR Biosystems). The samples were incubated as shown in Table V.1.

Table V.1: Temperature of cycles for PCR amplification.

NUMBER OF CYCLES	TEMPERATURE (°C)	DURATION (SEC)	STEP
1	95	60	Initial denaturing
40	95	15	Denaturing
	50	15	Primer annealing
	72	60	Extension
1	4	300	Cooling

The amplicon was isolated using the PCR clean-up kit (New England Biolab (NEB)) and all samples were gathered.

2.6.4 qPCR quantification of damage

Each cleavage sample was prepared in triplicates, and for each triplicate, a reference sample was prepared. Briefly, in 2.5 µL of phosphate buffer (10 mM PO_4^{3-}, 150 mM NaCl, 10 mM $MgCl_2$, pH 6.0), the 89 bp amplicon (0.25 pmol, 1 eq.) was reacted with PD-TFO hybrid (25 pmol, 100 eq.). Samples were split in half and $Cu(NO_3)_2$ (500 eq.) was added to the cleavage sample, while biology grade H_2O was added to its reference sample. Both reference and cleavage samples were incubated for 1, 6, 24 h or 30 h at 37 °C. 96-well plates were prepared by adding the sample (2.5 x 10^5 dilution) to a mixture containing SYBR Green I master mix (Roche), the forward and reverse primers (1 µL of 10 µM each) and PCR grade water. qPCR was performed using a Light Cycler® 480 II (Roche) instrument and the associated Light Cycler® 480 II software

(Roche). For each sample and reference pair, three replicates were loaded onto the plates, and the final reported value is the average across both the technical and biological replicates.

3 Results and discussion

3.1 Synthesis of N_3-PD

3.1.1 Synthesis of the bi-pyrrole moiety

The total synthesis of an azide modified PD analogue was developed using the earlier synthetic strategy for PD scaffolds reported by Kancharla *et al*.[22] The first key intermediate, 4-methoxy-1H,1'H-[2,2'-bipyrrole]-5-carbaldehyde, is prepared in 3 steps, starting from 4-chloro-3-methoxy-2-(E)-butenoic acid methyl ester[23, 24] (Figure V.2). The first step is a cyclisation step driven by basic conditions, yielding 4-methoxy-3-pyrrolin-2-one in 76% yield. This reaction is compatible with scale-up and does not require further purification before the activation with $POBr_3$ and coupling of a diethyl formamide, affording N-((5-bromo-3-methoxy-2H-pyrrol-2-ylidene)methyl)-N-ethylethanamine with a 59% yield. The last step was adapted from the literature and was optimised to give 4-methoxy-1H,1'H-[2,2'-bipyrrole]-5-carbaldehyde in 32% yield. The activated bromide pyrrole is coupled to a Boc-protected pyrrole boronic acid, catalysed by tetrakis(triphenylphosphine)palladium(0) in basic conditions. No further purification for these intermediates was required.

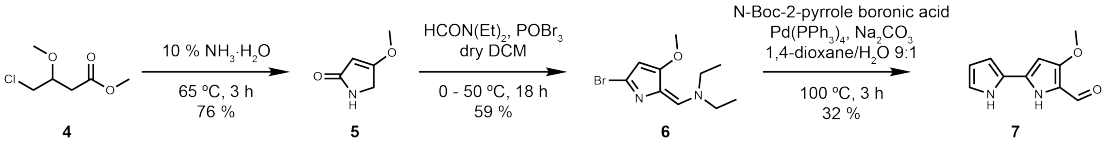


Figure V.2: Reported[22] 3-step synthesis of 4-methoxy-1H,1′H-[2,2′-bipyrrole]-5-carbaldehyde (bi-pyrrole) starting from 4-chloro-3-methoxy-2-(E)-butenoic acid methyl ester.

3.1.2 Optimising the synthesis of an azide-functionalised mono-pyrrole derivative

The main challenge in the total synthesis of the azide-PD was the preparation of an azide-functionalised mono-pyrrole intermediate. Various synthetic routes were investigated, based on previously reported work.[25, 23, 22, 26] The first route was adapted from Kancharla *et al.*[22] starting from ethyl pyrrole-2-carboxylate (Figure V.3). This synthesis includes a Friedel-Crafts acylation followed by a

reduction of the generated ketone, before decarboxylation using ethylene glycol in the presence of NaOH. Despite many trials for the reduction step—including the use of $NaBH_4$, $LiAlH_4$ and hydrazine hydrate—no product was obtained, according to proton NMR. These structures can be identified by three characteristic pyrrolic protons. The N-H proton and the two C-H protons are usually characterised by peaks between 6-8 ppm. Although the order of the synthetic steps was inverted or condensed in various attempts, no suitable pyrrole product was obtained.

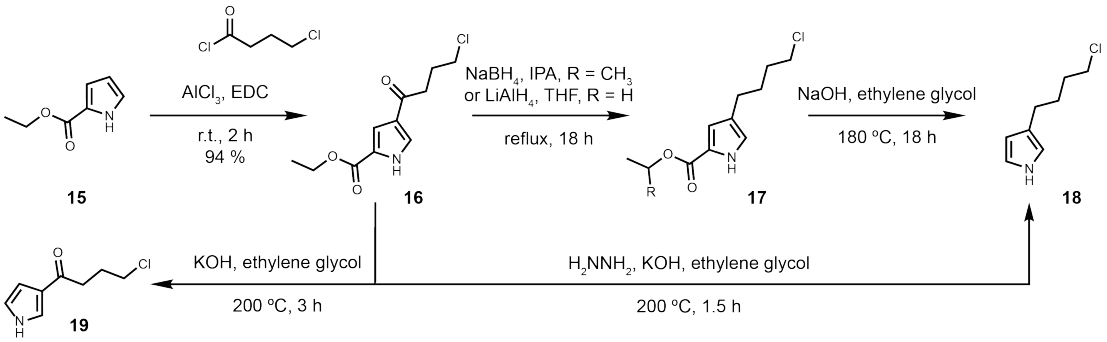


Figure V.3: First series of attempt to synthesise an azide-functionalised pyrrole, starting from ethyl pyrrole-2-carboxylate.

A second pathway was designed using more straightforward functionalisation such as the amide coupling of pyrrole-3-carboxylic acid to an amine using HBTU and DIPEA with 3-chloropropylamine hydrochloride, leading to N-(3-chloropropyl)-1H-pyrrole-3-carboxamide in 47% yield (Figure V.4). Using sodium azide, the chloride was substituted to give N-(3-azidopropyl)-1H-pyrrole-3-carboxamide with a 49% yield. Unfortunately, the coupling of N-(3-azidopropyl)-1H-pyrrole-3-carboxamide with 4-methoxy-1H,1'H-[2,2'-bipyrrole]-5-carbaldehyde was unsuccessful.

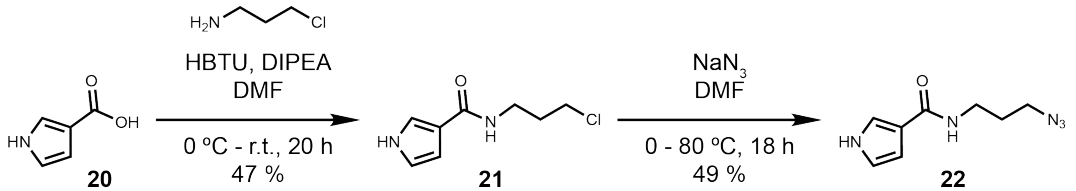


Figure V.4: Second attempt to prepare an azide-functionalised pyrrole, starting from pyrrole-3-carboxylic acid.

Two additional pathways were then developed based on patented synthesis (Figure V.5).[27] These pathways were developed to investigate if the presence of the carbonyl group adjacent to pyrrole was interfering with the prodigiosin coupling. In both pathways, the first step was successful with a high yield, but no reducing agent yielded results during attempts to reduce the alkene and the cyano/nitro group simultaneously.

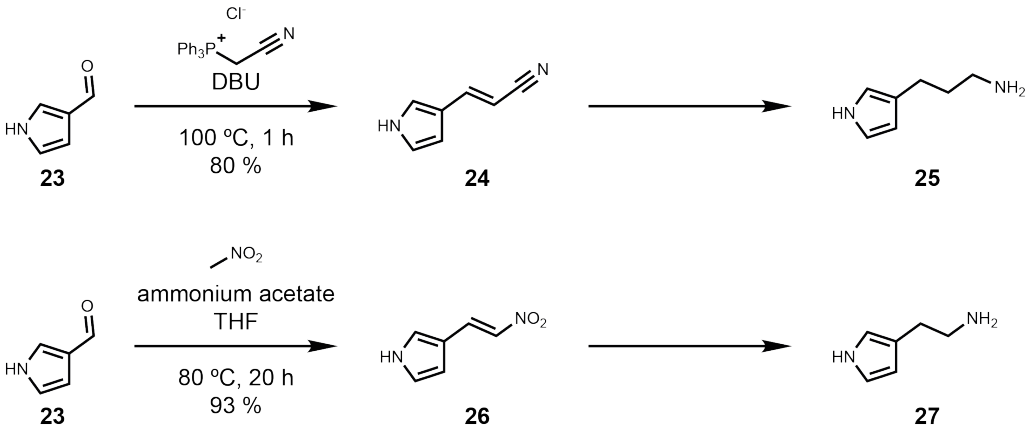


Figure V.5: Proposed synthetic schemes for the preparation of two different amine-functionalised pyrroles for subsequent conversion to azide intermediates.

With these synthetic approaches proving unsuccessful, an alternative explanation for the failed prodigiosin coupling was tested. A precursor was identified bearing substituent on three of the pyrrole ring carbons, leaving only a single position available for coupling with 4-methoxy-1H,1'H-[2,2'-bipyrrole]-5-carbaldehyde. Before functionalisation of the mono-pyrrole, a first prodigiosin scaffold coupling reaction was tried with 2,4-dimethyl-1H-pyrrole-3-carboxylic acid (Figure V.6). The precursors were dissolved in dry methanol under inert conditions and catalytic amount of freshly prepared methanolic hydrochloric acid was added. After stirring at room temperature overnight and in darkness a red solid was isolated and purified by chromatography column (0 – 10% MeOH in DCM). The ^{1}H NMR analysis confirmed the successful isolation of the red PD analogue.

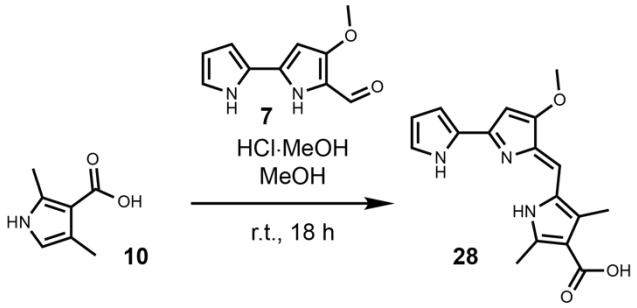


Figure V.6: First successful attempt for the coupling of bi-pyrrole with a monopyrrole in methanolic HCl.

3.1.3 Synthesis of N-(3-azidopropyl)-2,4-dimethyl-1H-pyrrole-3-carboxamide

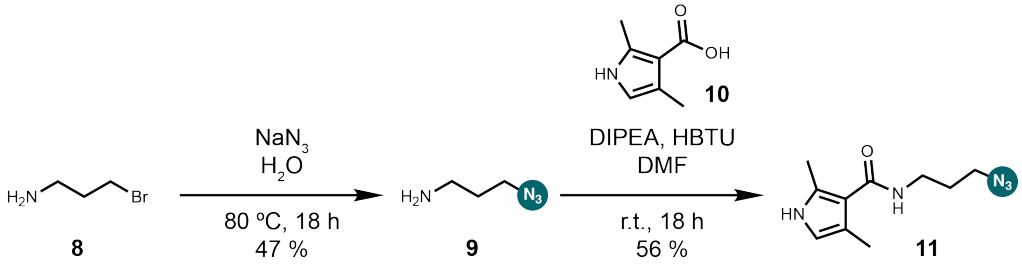


Figure V.7: Preparation of N-(3-azzidepropyl)-2,4-diethyl-1H-pyrrole-3-carboxamide.

Following the successful coupling of 2,4-dimethyl-1H-pyrrole-3-carboxylic acid to 4-methoxy-1H,1'H-[2,2'-bipyrrole]-5-carbaldehyde, a synthetic pathway was elaborated (Figure V.7) starting from 3-bromopropan-1-amine, which was converted to the corresponding azide using sodium azide in DI H_2O yielding clean 3-azidopropan-1-amine with a 47% yield. An amide coupling was then performed in the presence of HBTU and DIPEA to attach the C3 azide linker to 2,4-dimethyl-1H-pyrrole-3-carboxylic acid, yielding N-(3-azidopropyl)-2,4-dimethyl-1H-pyrrole-3-carboxamide with a 56% yield, after chromatography column purification. The structure was confirmed by ^{1}H NMR and IR spectroscopy, with an absorption band at 2094 cm^{-1} confirming the presence of the azide. The NMR spectra of N-(3-azidopropyl)-2,4-dimethyl-1H-pyrrole-3-carboxamide shows the 2 methyl groups, the proton on the free carbon of the pyrrole ring and the C3 linker protons, each presenting a unique splitting pattern. Although the amine protons are not showing in $CDCl_3$, the splitting of the peak of the hydrogens attached to the carbon in the alpha position of the amide group incorporates the presence of the secondary amine proton, showing up as a quartet, instead of a triplet.

3.1.4 Coupling of the bi-pyrrole moiety and the azide-functionalised pyrrole

The final step in the total synthesis of the azide-functionalised prodigiosin analogue involved the coupling between the bi-pyrrole moiety and the azide-functionalised pyrrole (Figure V.8). The synthesis of many reported prodigiosin analogues include this final step, where the bi-pyrrole is coupled to a mono-pyrrole unit under inert condition, catalysed by methanolic HCl.

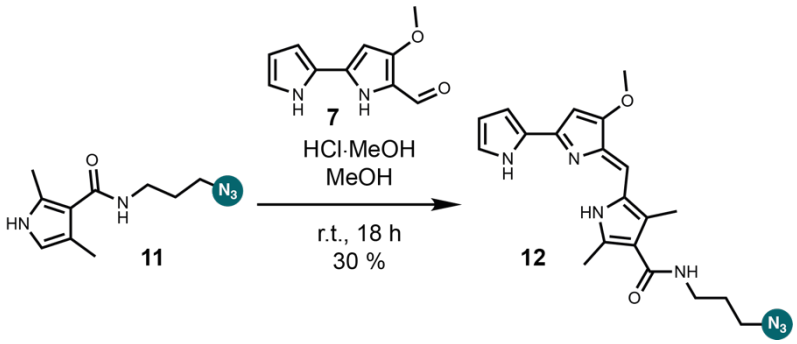


Figure V.8: Preparation of N_3-PD by coupling the bi-pyrrole moiety with N-(3-azidopropyl)-2,4-dimethyl-1H-pyrrol-3-carboxamide in methanolic HCl.

3.2 Preliminary biophysical activity assessment

3.2.1 DNA cleavage assay

The freshly synthesised N_3-PD was assessed for its DNA cleavage activity in the presence of copper(II) using the supercoiled plasmid DNA vector, pUC19. Upon single-strand cleavage, supercoiled DNA adopts the open circular form. The linear form is obtained either in the case of double strand break or a second single-strand break (Figure V.9). Supercoiled (SC), open circular (OC) and linear (L) DNA have different migration profiles within gel electrophoresis and can therefore be discriminated. As SC DNA is condensed and tightly packed, it travels the furthest on the gel. OC DNA travels the least on agarose gel due to its bulky relaxed circular state, while L form migrates between SC and OC. To assess the cleavage potential of N_3-PD in the presence of copper(II), pUC19 was incubated with increasing concentrations of N_3-PD and copper(II) nitrate, in the presence of NaCl using HEPES buffer (80 mM, pH 7.2).

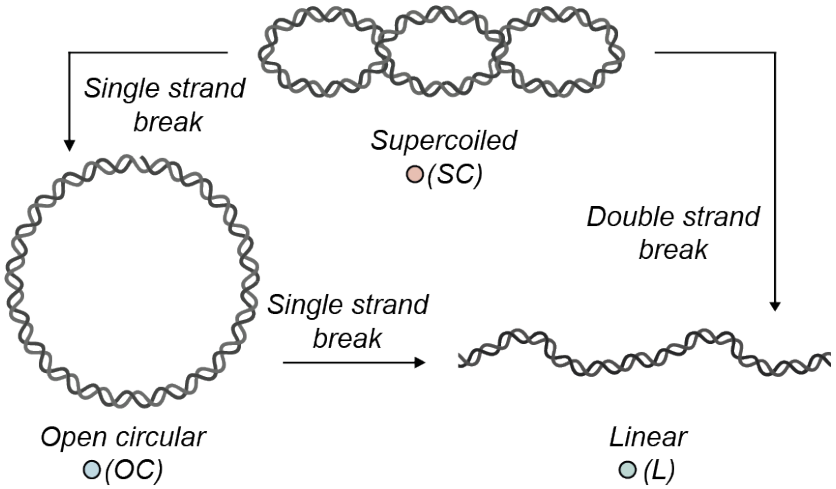


Figure V.9: Conversion of supercoiled (SC) DNA to open circular (OC) and linear (L) DNA upon single or double strand break.

3.2.2 Na-L-asc-mediated and self-activated cleavage activity of [Cu(N_3-PD)(NO_3)$_2$]

The cleavage profile of N_3-PD in the presence of copper(II) was assessed both with (Figure V.10.a), and without (Figure V.10.b) Na-*L*-asc, which is commonly used with Cu-AMNs to reduce Cu(II) to Cu(I) and initiate the ROS production. Prodiginines such as PD are known to undergo self-activation, *i.e.* cleave DNA without the requirement for an external reductant and so experiments were also performed in the absence of exogenous reductant.

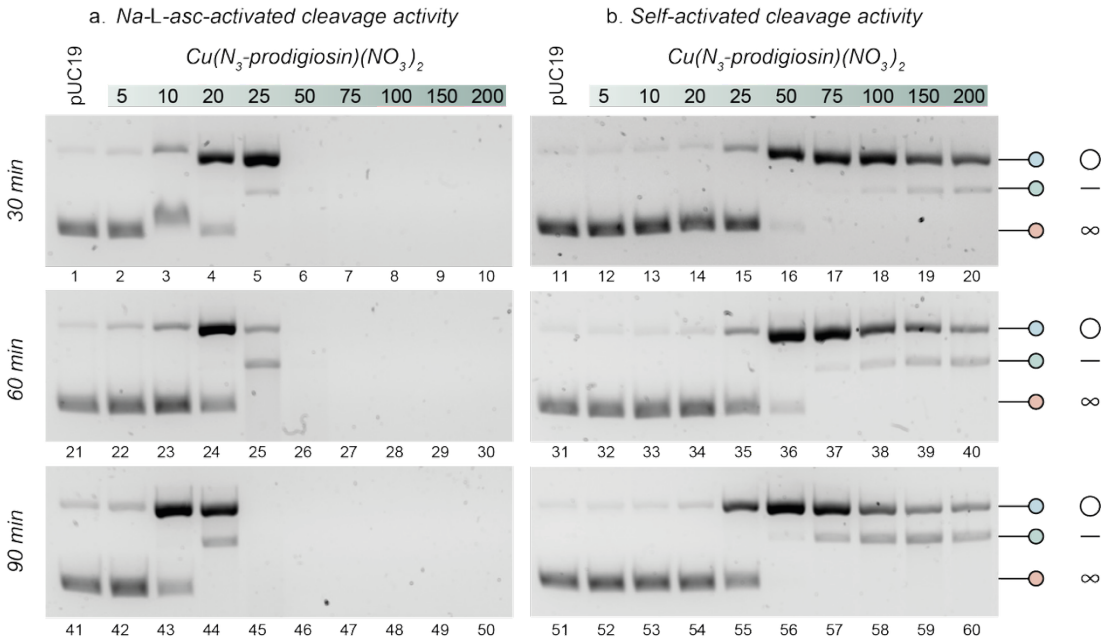


Figure V.10: Cleavage of pUC19 with increasing amounts of [Cu(N_3-PD)(NO_3)$_2$] after 30, 60 or 90 min incubation (top to bottom) at 37 °C in HEPES buffer and NaCl, **a.** in the presence of Na-*L*-asc, and **b.** without Na-*L*-asc. Lanes 1, 11, 21, 31, 41 and 51: pUC19. Lanes 2 – 10, 12 – 20, 22 – 30, 32 – 40, 42 – 50, 52 – 60: pUC19 in the presence of 5, 10, 20, 25, 50, 75, 100, 150 or 200 μM of [Cu(N_3-PD)(NO_3)$_2$].

In the absence of added reduction, complete relaxation of pUC19 was observed upon exposure to 50 μM of the complex for all three exposure times, demonstrating the self-activated cleavage ability of N_3-PD. In the presence of Na-*L*-asc, pUC19 was completely cleaved upon exposure to 25 μM of the complex (after 30 min and 60 min incubation at 37 °C) and at 20 μM following 90 min incubation at 37 °C. [Cu(N_3-PD)(NO_3)$_2$] also generated linear DNA under both Na-*L*-asc- and self-activated cleavage conditions. This confirmed the novel PD derivative retained self-activated DNA cleaving activity commonly associated with prodiginines.

3.2.3 Mechanistic studies

The cleavage experiments with pUC19 were next repeated in the presence of ROS scavengers as well as groove binders to characterise the cleavage activity. Each ROS scavengers is known to sequester a specific ROS or mixture thereof (Table V.2).[28, 29] Thus, using several scavengers one at a time and observing the increased or decreased cleavage activity can aid the identification of ROS involved in the cleavage mechanism. In parallel, cleaving DNA in the presence of a major or a minor groove binder can help to assess

the groove-preference of an AMN. In this experiment, if the preferred groove is occupied prior to the introduction of the Cu-AMN, inhibition of cleavage activity would be expected.

Table V.2: ROS scavengers used in this study and their associated ROS.

REAGENT	ROS/GROOVE PREFERENCE
Tiron	Superoxide ($O_2^{\bullet-}$)
L-methionine	Hypochlorous acid, hydroxyl, peroxide, superoxide (HOCl, $^{\bullet}OH$, H_2O_2, $O_2^{\bullet-}$)
D-mannitol	Hydroxyl ($^{\bullet}OH$)
NaN_3	Singlet oxygen ($^1O_2$)
DMTU	Peroxide (H_2O_2)
L-histidine	Singlet oxygen ($^1O_2$)
D_2O	Singlet oxygen stabiliser ($^1O_2$)
TEMPO	Diffusive superoxide ($O_2^{\bullet-}$)
Methyl green	Major groove
Netropsin	Minor groove

Interestingly, the Na-*L*-asc-activated and self-activated cleavage show different activity in the presence of ROS scavengers. The self-activated cleavage activity of [Cu(N_3-PD)(NO_3)$_2$] was completely inhibited in the presence of tiron, *L*-methionine and *L*-histidine, and mildly impacted by the presence of DMTU, NaN_3 and netropsin. These results seem to indicate that the self-activated activity of [Cu(N_3-PD)(NO_3)$_2$] mostly involves pathways linked to singlet oxygen and superoxide production. In the case of the Na-*L*-asc-activated cleavage activity of [Cu(N_3-PD)(NO_3)$_2$], DMTU and tiron prevented the cleavage while TEMPO, *L*-histidine and NaN_3 had a milder impact, suggesting the major involvement of peroxide and superoxide radicals as well as a minor contribution by singlet oxygen (Figure C.3.1).

The presence of a competitive binder in the minor groove only mildly reduced the cleavage activity while the presence of a major groove binder slightly enhanced cleavage activity, suggestive a preference for cleavage in the minor groove (Figure C.3.2).

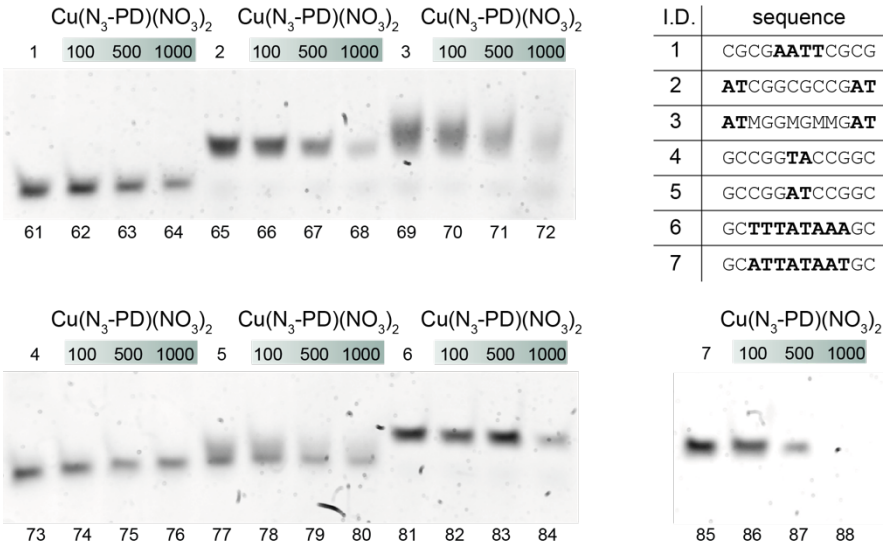
To investigate sequence preference for DNA cleavage by [Cu(N_3-PD)(NO_3)$_2$], dodecamers were examined that vary in overall AT-content, the presence of AT/TA steps, along with 5mC modifications (Figure V.11). The two most reactive substrates, dodecamer 7, followed closely by 6, both share a

high density of AT-content. In contrast, 4 and 5 are predominantly GC-rich and did not show significant cleavage. This suggests that high overall AT-content enhances susceptibility to cleavage by the complex.

A more detailed comparison between 7 and 6 reveals an additional layer of selectivity. Although both sequences are AT-rich, 7 contains more continuous AT/TA steps, whereas 6 presents a less alternating arrangement of A and T. The higher cleavage observed for 7 therefore suggests that, additionally to the high AT-content, the organisation of A and T into extended AT/TA steps motifs represents the most favourable environment for the complex. This is also supported by the lack of significant cleavage observed for 1 despite having a more AT-rich sequence than 4 and 5.

Finally, a comparison of 2 and 3 provides further insight into the role of groove accessibility. The presence of 5mC on 3, which sterically perturbs the major groove, did not impede the cleavage efficiency compared to the unmodified dodecamer 2. Consistent with the results presented above, these results point toward a preference for cleavage in the minor groove.

Taken together, the cleavage pattern demonstrates that [Cu(N_3-PD(NO_3)$_2$] shows distinct sequence preference, favouring AT-rich regions and, more specifically, continuous AT/TA step motifs, while remaining largely unaffected by modifications that restrict the major groove.



I.D.	sequence
1	CGCG**AATT**CGCG
2	**AT**CGGCGCCG**AT**
3	**AT**MGGMGMMG**AT**
4	GCCGG**TA**CCGGC
5	GCCGG**AT**CCGGC
6	GC**TTTATAAA**GC
7	GC**ATTATAAT**GC

Figure V.11: PAGE analysis of the cleavage of dodecamers with varying A/T motifs, listed in the table on the right, by [Cu(N_3-PD)(NO_3)$_2$] to assess the sequence preference of the AMN. Lanes 61 – 64: dodecamer 1, lanes 65 – 68 : dodecamer 2, lanes 69 – 72: dodecamer 3, lanes 73-76: dodecamer 4, lanes 77 – 80: dodecamer 5, lanes 81 – 84: dodecamer 6 and lanes 85 – 88: dodecamer 7, in the presence of 100, 500 or 1000 eq. of [Cu(N_3-PD)(NO_3)$_2$].

3.3 SPAAC-labelling of the TFOs

A library of four SPAAC-compatible TFOs was designed as described in previous chapters. Briefly, the TFOs were optimised for triplex formation by replacing all cytosines by 5mC. TFO-1 and TFO-2 incorporate one TO modification either proximate to the 5′-end (TFO-1) or to the 3′-end (TFO-2), and TFO-3 which has two TO motifs. The TFOs were labelled with TO using amide coupling between NHS-ester TO_{B6} and an amine-modified deoxy-uracil (dU) nucleobase. TFO-4 has no TO modification and served as a control. All TFOs possessed a 5′-DBCO modification to enable SPAAC-labelling using azide-functionalised ligands (Figure V.12).

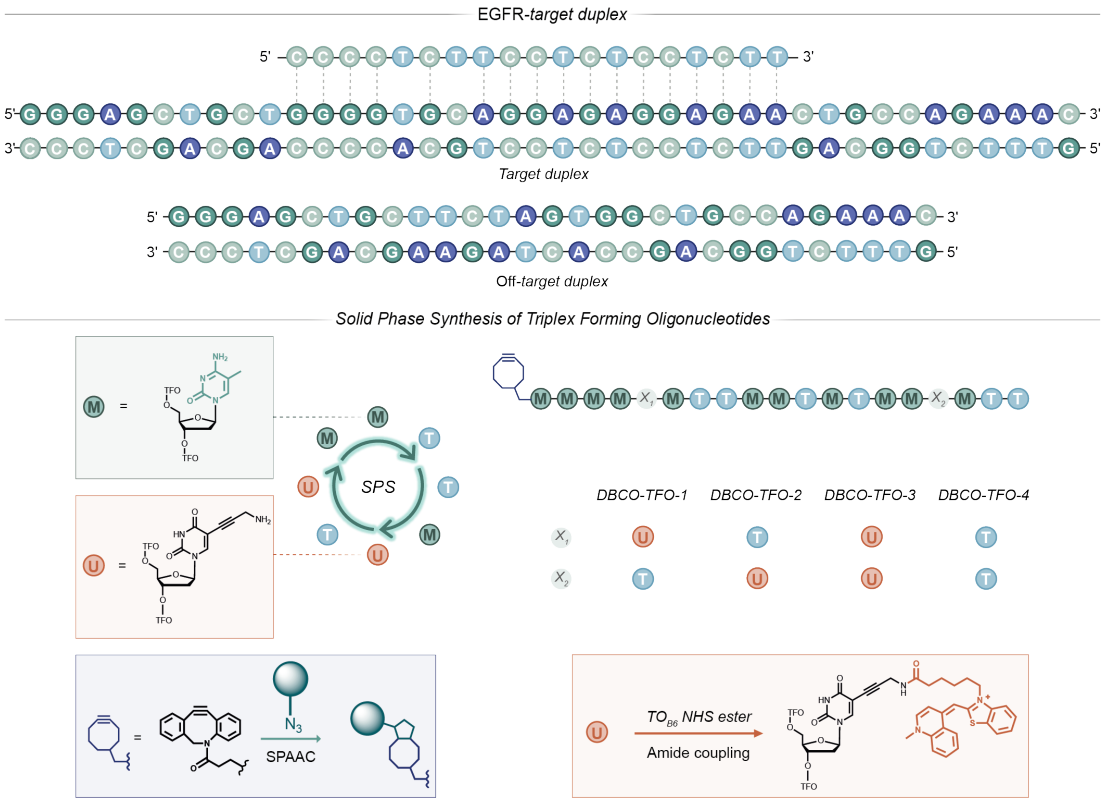


Figure V.12: Structure of the 40-bp target and 29-bp *off*-target duplexes, design of the library of 19-nt TFOs targeting the *EGFR* gene and illustration of SPS and post-synthetic labelling.

N_3-PD and N_3-Phen were attached to the DBCO-TFOs using SPAAC. The use of a strained alkyne allowed for straightforward functionalisation of TFOs that did not necessitate additional reagents such as copper or Na-*L*-asc, or an inert atmosphere. Here, 10 equivalents of the N_3-ligand in acetonitrile were reacted with 1 equivalent of DBCO-TFO in biology grade H_2O. After incubation at 37 °C for 1 h, the excess of N_3-ligand was removed by NAP column desalting. PAGE analysis showed significant conversion to PD-TFO and Phen-TFO hybrids, without the need for further purification. The successful SPAAC functionalisation was confirmed with mass spectrometry. Expected and observed ESI-MS results for the molecular ion masses are as shown in Table V.3.

Table V.3: Calculated and measured mass for TFO hybrids.

Hybrid	Calculated mass	Observed mass
PD-TFO-1	7098	7096
PD-TFO-2	7098	7096
PD-TFO-3	7525	7523
PD-TFO-4	6670	6671
Phen-TFO-1	6926	6923
Phen-TFO-2	6926	6924
Phen-TFO-3	7353	7350
Phen-TFO-4	6498	6499

3.4 Triplex formation experiments

The target duplex was incubated with increasing equivalents of PD-TFO and Phen-TFO hybrids, leading to triplex formation, which was observed by PAGE analysis (Figure V.13). Here, PD-TFO-1 (PD-1), PD-TFO-2 (PD-2) and PD-TFO-3 (PD-3) all formed triplexes, with the highest intensity bands associated with triplex formation observed with 100 equivalents of hybrid. PD-TFO-4 (PD-4), the TFO lacking TO modifications, did not produce detectable higher-order triplex band formation. In the case of Phen-TFO hybrids, Phen-TFO-1 (Phen-1) and Phen-TFO-3 (Phen-3) showed greater triplex band formation than Phen-TFO-2 (Phen-2), while Phen-TFO-4 (Phen-4) was inactive. Although PD-1 and PD-2 formed triplexes with comparable signal intensity on PAGE, PD-2 was selected over PD-1 for further analyses because its triplex band was distinctly better resolved and free of the diffuse background observed under the PD-1 triplex band, which could interfere with subsequent band densitometry quantification. Similarly, for both Phen- and PD-TFO hybrids, TFO-3 resulted in sharp triplex bands without background noise, therefore TFO-2 and TFO-3 hybrids were selected for further analysis.

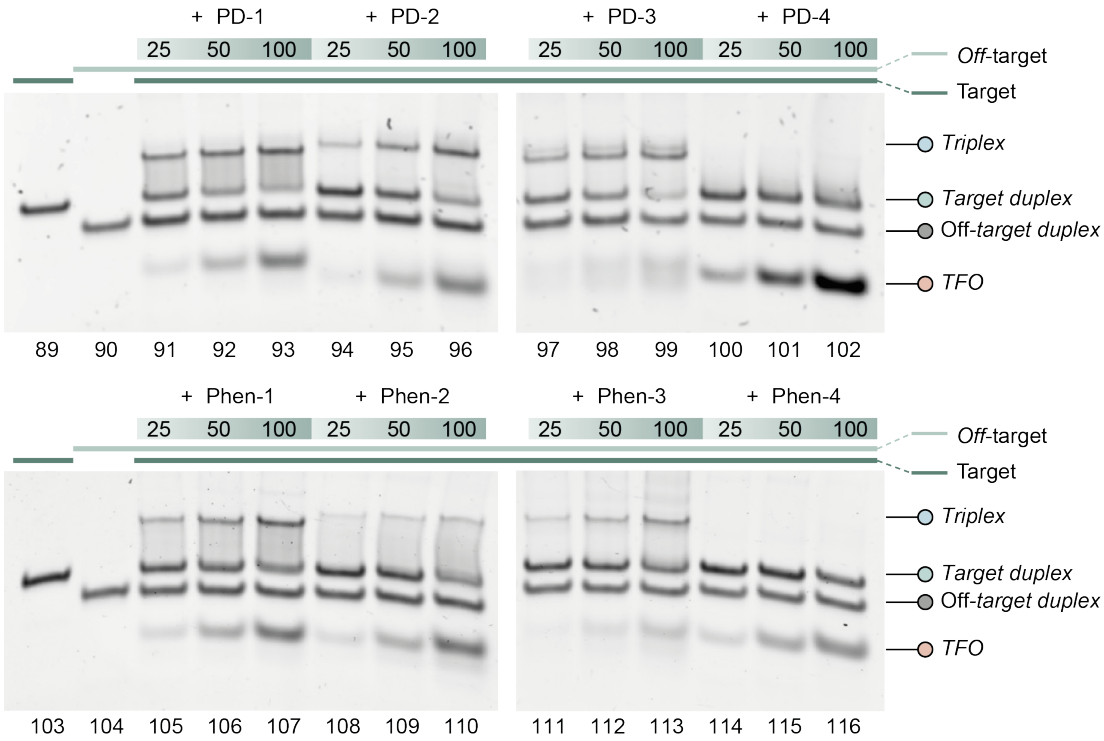


Figure V.13: PAGE reporting the target specific triplex formation of 25, 50 or 100 eq. of hybrids in the presence of target and *off*-target duplexes. Target duplex (lanes 89 and 103), *off*-target duplex (lanes 90 and 104), and PD-1 (lanes 91-93), PD-2 (lanes 94-96), PD-3 (lanes 97-99), PD-4(100-102), Phen-1 (lanes 105-107), Phen-2 (lanes 108-110), Phen-3 (lanes 111-113) and Phen-4 (lanes 114-116) hybrids in the presence of both duplexes.

The melting temperature of PD-2- and PD-3-containing triplexes was measured using intrinsic TO fluorescence and compared to that of the equivalent DBCO-TFOs and phenanthroline-functionalised TFOs (Figure V.14). As the temperature increased and the TFO dissociated from the duplex target, the TO units were expelled from the duplex and their fluorescence was quenched. The resulting fluorescence across temperature profiles were differentiated, and the maximum of the negative derivative was recorded as the melting temperature (T_M) of the triplex. The reported T_M value corresponds to the average of three replicates.

PD-2 displayed a higher T_M than DBCO-TFO-2 (56.3 °C compared to 54.9 °C), and PD-3 and DBCO-TFO-3 hybrids exhibited similar melting temperatures (66.6 °C and 66.8 °C respectively). This suggests that the presence of PD can contribute to the stability of the triplex, when it is positioned away from the TO unit. Furthermore, when compared to their Phen analogues, both PD-2 and PD-3 hybrids showed substantially higher melting temperature.

This suggests that, in this context, the Phen unit does not contribute positively to triplex stability, while the PD unit provides additional stabilisation to the triplex structure.

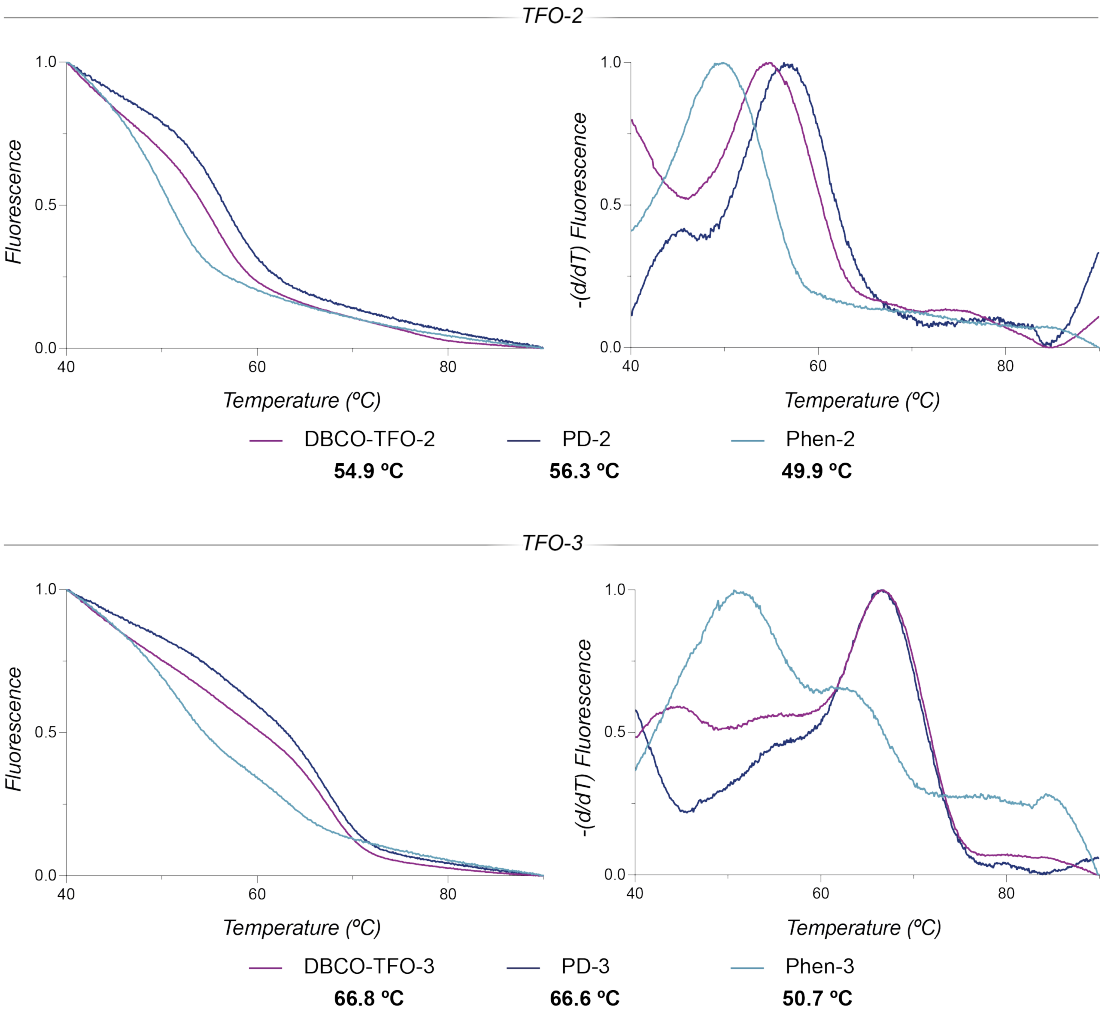


Figure V.14: Fluorescence recording of the melting temperature for DBCO, PD and Phen hybrids of TFO-2 and TFO-3 and associated first negative derivative, where the T_M is recorded as the temperature where the maximum is reached.

3.5 Self-activated target specific cleavage of the EGFR *duplex*

3.5.1 Investigations on the cleavage activity of PD-2 in the presence of copper

The cleavage profile of PD-2 was investigated in the presence of the target and *off*-target duplexes, using 100 equivalents of PD-2 per duplex. The initial attempts were performed with 1 equivalent of copper per PD-2. Unfortunately, no damage was observed, even in the presence of Na-*L*-asc. To investigate the cleavage further, duplex targets with a series of overhangs with different sequence contexts were acquired. These duplexes still contain the appropriate

triplex recognition domain but possess different A and T composition in the overhang region, proximate to where the PD motif would associate upon triplex formation. In parallel, the impact of a gradient of copper on the cleavage activity was investigated. We hypothesised that the PD ligand might be a weaker binder of copper(II) within the TFO construct as compared to the standalone ligand, or that other donors within the construct compete directly with PD for the available copper(II) ion. In the presence of increased copper(II) ions, PD-2 cleaved targeted duplexes without affecting the *off*-target, and that the cleavage was independent of the sequence present on the 5′-overhang of the target strand. Based on these results, a ratio of 5 eq. of copper per PD-2 was selected for further analysis.

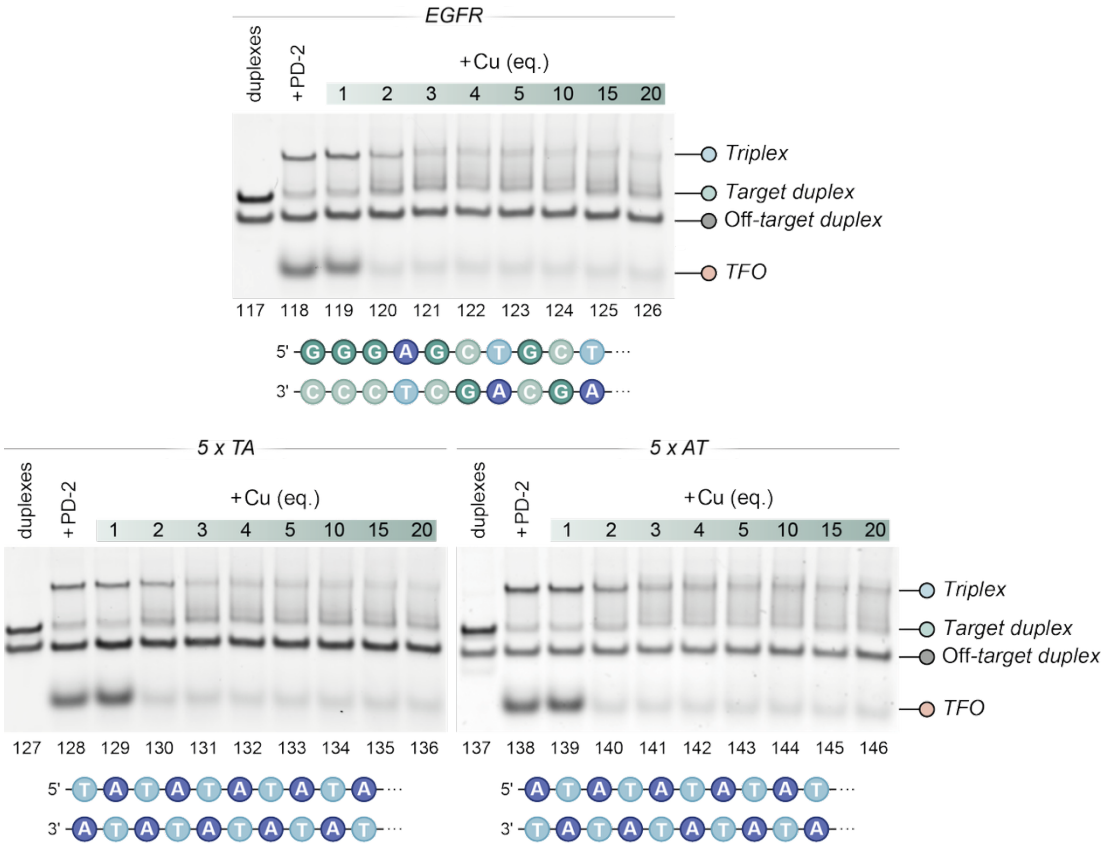


Figure V.15: Native PAGE (TA) showing the attempts to cleave target duplexes with varying A/T composition on the overhang using PD-2 in the presence of increasing amounts of copper. Lanes 117 – 126: *EGFR* target duplex containing the triplex-binding region, lanes 127 – 136: duplex containing the triplex-binding region and with a 5 x TA overhang and lanes 137 – 146: duplex containing the triplex-binding region and with a 5 x AT overhang.

3.5.2 PAGE analysis of target specific cleavage activity

The time-dependent cleavage activity of Cu-AMN-TFO hybrids were investigated against target and *off*-target duplexes using PAGE visualisation. Here, a concentration of 100 equivalents of AMN-TFO was selected to promote efficient triplex formation, and 5 equivalents of $Cu(NO_3)_2$ per AMN-TFO were introduced to trigger the cleavage. The cleavage activity of PD-TFOs were investigated without Na-*L*-asc (Figure V.16.a) while in the case of the Phen-TFO hybrids, Na-*L*-asc was required to produce damage (Figure V.16.b). PD-2 exhibited pronounced cleavage activity in the absence of a reductant, as shown by the depletion of both triplex and duplex bands between 2- and 18-hours of incubation. While PD-3 formed suitable triplexes, it was found to yield negligible cleavage activity (Figure S.V.4). By contrast, Phen-2 required the addition of Na-*L*-asc to induce cleavage and although depletion of the target duplex band was identified, no significant triplex band formation was identified. Importantly, none of the hybrids displayed detectable *off*-target cleavage across all time points. As observed earlier, excess copper(II) present in the assay was found to promote self-cleavage of the TFO, and although this did not prevent targeted cleavage activity, it does represent a limitation of the design. This effect could be remediated by modifying the TFO from phosphoramidite to phosphorothioate backbones, which are known to protect oligonucleotides from nuclease degradation, and help cell penetration.[30]

These results show that PD-TFO hybrids are the first self-activated, triplex-mediated, target-specific copper metallo-nucleases. Thus, PD-2 can induce sequence-specific damage in the presence of copper, without the need for an external reductant. In contrast, Phen-2 only cleaved DNA in the presence of a reductant, highlighting the unique properties of PD as a Cu-AMN ligand. The difference between the PD- and the Phen-TFO hybrid could be justified by the enhanced triplex association of PD-TFO, even though that parameter alone is not sufficient for good cleavage, as demonstrated by PD-3. Collectively, these results show the novelty and potential of PD-TFO conjugates as a new class of self-activated, target-specific DNA cleaving agents, offering a promising platform for further development of AMN-TFO systems.

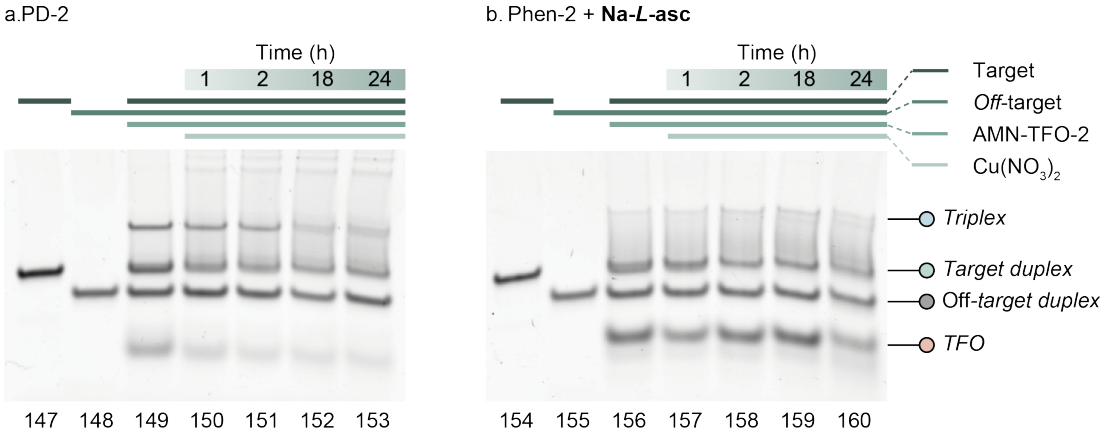


Figure V.16: **a.** Time-dependent self-activated target-specific cleavage activity of PD-2 in the presence of copper(II). **b.** Time-dependent Na-*L*-asc-mediated target specific cleavage activity of Phen-2 in the presence of copper(II). Lanes 147 and 154: target duplex, lanes 148 and 155: *off*-target duplex. Lane 149 both duplexes in the presence of PD-2, lanes 150-153: lane 149 + $Cu(NO_3)_2$ with increasing incubation time. Lane 156 both duplexes in the presence of Phen-2 and Na-*L*-asc, lanes 157-160: lane 156 + $Cu(NO_3)_2$ with increasing incubation time.

3.5.3 qPCR quantification of the cleavage activity of the PD-TFO-2 hybrid.

An 89 bp amplicon of the *EGFR* plasmid containing the triplex-binding region was incubated with PD-2 in the presence of copper(II) across time and analysed by qPCR. DNA cleavage prevents amplification of the full-length amplicon, leading to a measurable reduction in intact template available for amplification (Figure V.17.a). The Roche LightCycler II instrument quantified this by measuring the crossing point (Cp), defined as the PCR cycle at which amplification reaches detectable exponential growth. A higher Cp value indicates a lower concentration of template DNA, as additional cycles are required to reach the detection threshold.

Each exposure was measured in technical triplicates, and the Cp of the cleaved sample was averaged and compared with that of an undamaged control. A sample reference was also prepared, which contained the same initial amount of DNA and PD-2 but without copper. Ratios were normalised using the LightCycler software (Roche), which applies the following equation (Formula 1) to calculate the fold change:

$$\text{Fold-change} = 2^{\text{Cp(control tgt)-Cp(control ref)+Cp(sample ref)-Cp(sample tgt)}}$$

Formula 1: Fold-change as calculated by the LightCycler II software (Roche) using the threshold cycle of sample and control target and reference samples. The fold-change decreases as the amount of DNA in the target sample decreases.

Plotting the fold-change over time (Figure V.17.b) revealed progressive DNA damage, with over 50% cleavage observed after 6 h, and between 80–90% cleavage observed after 24 h.

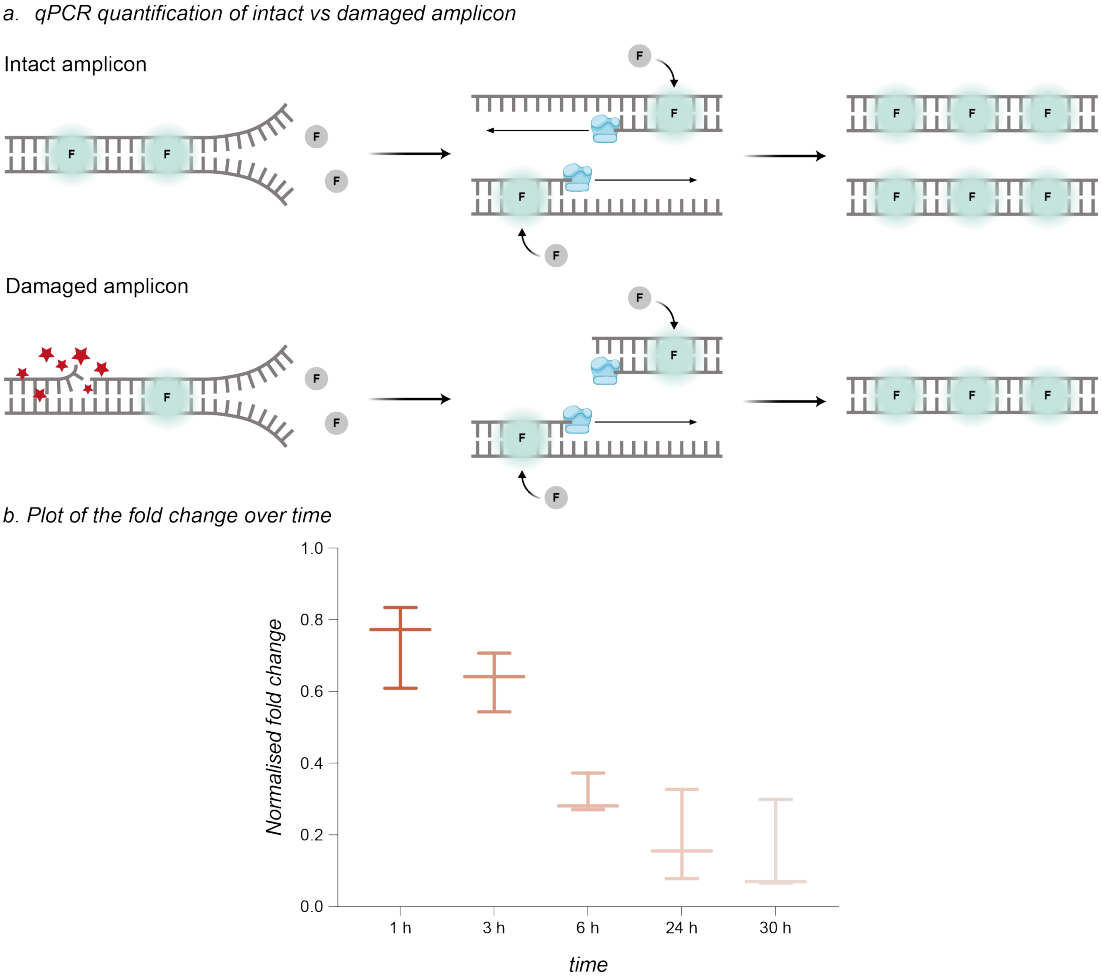


Figure V.17: **a**. Principle of the qPCR quantification of damage showing the difference between an undamaged amplicon and an amplicon that has been damaged. **b**. Evolution of the fold change over time illustrating the progressive damage of the amplicon caused by PD-2 in the presence of copper.

4 Conclusion

In this chapter, a novel azide-functionalised prodigiosin ligand was successfully synthesised by combining an azide-modified mono-pyrrole derivative with a bi-pyrrole intermediate. This represents the first reported example of a prodigiosin derivative specifically tailored for biorthogonal conjugation, enabling direct attachment to oligonucleotide scaffolds *via* copper-free click chemistry.

The copper-mediated nuclease activity of N_3-PD was investigated using supercoiled plasmid DNA, in the presence and absence of Na-*L*-asc to demonstrate the self-activated cleavage properties of the novel PD analogue. Agarose gel electrophoresis confirmed efficient cleavage, showing conversion of supercoiled DNA to both open circular and linear forms. Complete cleavage was observed at 20 μM in the presence of Na-*L*-asc and more interestingly, cleavage activity was preserved even in the absence of a reductant. The cleavage mechanism was next studied for the involvement of specific ROS, groove selectively and sequence preference, revealing singlet oxygen- and superoxide-dependant mechanisms, with a slight preference for cleavage in the minor groove of DNA. Additionally, the cleavage showed a preference for high AT-content and continuous AT/TA step motifs. These findings reinforce the strong potential of prodigiosin scaffolds as redox-active ligands for DNA damaging applications.

To further enhance the potential of the novel PD analogue, it was then conjugated to a library of alkyne-modified *EGFR*-targeting TFOs *via* SPAAC. The SPAAC reactions proceeded with high efficiency, short reaction times, and did not require purification. These hybrids were shown to form stable triplexes with their target duplex, confirming the TFO scaffolds retained their recognition capability post conjugation. The PD-TFO hybrids were then compared to DBCO-TFO and Phen-TFO analogues, revealing the PD motif did not reduce triplex association, but rather contributed to enhanced thermal stabilisation of the DNA triplex. Indeed, the T_M values recorded for PD-TFOs was slightly higher than the non-modified DBCO-TFO variant, while also being significantly higher than Phen-TFO analogues.

Importantly, PD-2 demonstrated self-activated target-specific cleavage activity in the absence of an external reductant, distinguishing it from previously reported click-generated AMN-TFO hybrids. More specifically, in this study, PD-2 was compared to Phen-2 and showed much greater DNA damaging propensity. No *off*-target cleavage was observed, highlighting the sequence specificity of these hybrids towards the *EGFR* gene. Overall, these hybrids are the first example of click chemistry generated AMN-TFO conjugates targeting a gene from the human genome with potential applications in targeted chemotherapy. While these hybrids could be enhanced by using a phosphorothioate backbone, they provide a powerful platform for site-specific DNA silencing and expand the repertoire of AMN towards clinically relevant targets such as the *EGFR* gene. Building on these findings, the efficiency of SPAAC conjugation and robust triplex stability of these PD-TFO hybrids provided a strong foundation for developing new strategies to accelerate ligand evaluation. In the following chapter, these features are harnessed in a novel self-assembly assay that enables rapid screening of ligands and metal centres for application in AMN-TFO design.

5 References

[1] Gibney, A.; Kellett, A. *Chemistry – A European Journal.* **2024**.
[2] Fantoni, N. Z.; Brown, T.; Kellett, A. *Chembiochem.* **2021**, *22,* (13), 2184-2205.
[3] Melvin, M. S.; Tomlinson, J. T.; Saluta, G. R.; Kucera, G. L.; Lindquist, N.; Manderville, R. A. *J Am Chem Soc.* **2000**, *122,* (26), 6333-6334.
[4] Montaner, B.; Perez-Tomas, R. *Curr Cancer Drug Targets.* **2003**, *3,* (1), 57-65.
[5] Picott, K. J.; Deichert, J. A.; deKemp, E. M.; Schatte, G.; Sauriol, F.; Ross, A. C. *MedChemComm.* **2019**, *10,* (3).
[6] Wang, X.; Isbrandt, T.; Christensen, E. O.; Melchiorsen, J.; Larsen, T. O.; Zhang, S. D.; Gram, L. *Microbiol Spectr.* **2021**, *9,* (2), e0117121.
[7] Wasserman, H. H.; Friedland, D. J.; Morrison, D. A. *Tetrahedron Letters.* **1968**, *9,* (6).
[8] Melvin, M. S.; Calcutt, M. W.; Noftle, R. E.; Manderville, R. A. *Chem Res Toxicol.* **2002**, *15,* (5), 742-748.
[9] Sumit Borah; Matt S. Melvin; Niels Lindquist; Manderville, R. A. *J Am Chem Soc.* **1998**.
[10] Sakai-Kawada, F. E.; Ip, C. G.; Hagiwara, K. A.; Awaya, J. D. *Front Microbiol.* **2019**, *10*, 1715.
[11] Chen, C. H.; Sigman, D. S. *Proc Natl Acad Sci U S A.* **1986**, *83,* (19), 7147-7151.
[12] Strobel, S. A.; Moser, H. E.; Dervan, P. B. *J Am Chem Soc.* **1988**, *110,* (23), 7927-7929.
[13] Fantoni, N. Z.; El-Sagheer, A. H.; Brown, T. *Chem Rev.* **2021**, *121,* (12), 7122-7154.
[14] Fox, K., R. ; Brown, T.; Rusling, D. A. *Chemical Biology.* **2018**, *Chapter 1*, 1-32.
[15] Klimkowski, P.; De Ornellas, S.; Singleton, D.; El-Sagheer, A. H.; Brown, T. *Org Biomol Chem.* **2019**, *17,* (24), 5943-5950.
[16] Walsh, S.; El-Sagheer, A. H.; Brown, T. *Chem Sci.* **2018**, *9,* (39), 7681-7687.
[17] Leitner, D.; Schroder, W.; Weisz, K. *Biochemistry-Us.* **2000**, *39,* (19), 5886-5892.
[18] McGorman, B.; Fantoni, N. Z.; O'Carroll, S.; Ziemele, A.; El-Sagheer, A. H.; Brown, T.; Kellett, A. *Nucleic Acids Res.* **2022**, *50,* (10), 5467-5481.
[19] Panattoni, A.; El-Sagheer, A. H.; Brown, T.; Kellett, A.; Hocek, M. *Chembiochem.* **2020**, *21,* (7), 991-1000.
[20] Lauria, T.; Slator, C.; McKee, V.; Müller, M.; Stazzoni, S.; Crisp, A. L.; Carell, T.; Kellett, A. *Chem-Eur J.* **2020**, *26,* (70), 16782-16792.
[21] Agard, N. J.; Prescher, J. A.; Bertozzi, C. R. *J Am Chem Soc.* **2004**, *126,* (46), 15046-15047.
[22] Kancharla, P.; Li, Y. X.; Yeluguri, M.; Dodean, R. A.; Reynolds, K. A.; Kelly, J. X. *Journal of Medicinal Chemistry.* **2021**, *64,* (12), 8739-8754.
[23] Dairi, K.; Tripathy, S.; Attardo, G.; Lavallée, J. F. *Tetrahedron Letters.* **2006**, *47,* (15), 2605-2606.
[24] Li, J.; Zhang, Q.; Yin, J.; Yu, C.; Cheng, K.; Wei, Y.; Hao, E.; Jiao, L. *Org Lett.* **2016**, *18,* (21), 5696-5699.

[25] D'Alessio, R.; Bargiotti, A.; Carlini, O.; Colotta, F.; Ferrari, M.; Gnocchi, P.; Isetta, A.; Mongelli, N.; Motta, P.; Rossi, A.; et al. *J Med Chem.* **2000**, *43,* (13), 2557-2565.
[26] Nisha, K. K. a. V. K. *RSC Adv.* **2015**, *5*, 10899-10920.
[27] Tait, B. C., M. Methods of Modulating CFTR Activity. 2014.
[28] Molphy, Z.; Prisecaru, A.; Slator, C.; Barron, N.; McCann, M.; Colleran, J.; Chandran, D.; Gathergood, N.; Kellett, A. *Inorg Chem.* **2014**, *53,* (10), 5392-5404.
[29] Slator, C.; Molphy, Z.; McKee, V.; Long, C.; Brown, T.; Kellett, A. *Nucleic Acids Res.* **2018**, *46,* (6), 2733-2750.
[30] Saran, R.; Huang, Z.; Liu, J. *Coordination Chemistry Reviews.* **2021**, *428*.

Chapter VI

Self-assembly of AMN-TFO Hybrids Enables Facile Target-specific DNA Damage Screening

April 2026

1 Introduction

Artificial metallo-nucleases (AMNs) are a class of metal complexes that aim to mimic the activity of natural nucleases by causing strand breaks in DNA. AMNs have emerged as a powerful tool in gene therapies since the discovery of copper-phenanthroline[1] (Cu-Phen) and iron-ethylenediaminetetraacetic acid[2] (Fe-EDTA). Copper-, iron- and manganese-based AMNs (Cu-AMNs, Fe-AMNs and Mn-AMNs) are reported to cleave DNA through oxidative damage by producing reactive oxygen species (ROS).[3] Other classes of AMN include zinc-based AMNs (Zn-AMNs) which generally cleave DNA through hydrolytic pathways.[4]

Cu-AMNs are among the best studied, and a variety of ligands have been produced for optimal design, each offering different balances of DNA affinity, redox activity and metal coordination.[5] For example, phenanthroline-derived ligands such as dipyridophenazine[6] (DPPZ) and imidazophenanthroline[7] (ImPhen) have been studied for their increased planar aromaticity, imparting higher intercalation activity and thereby anchoring the metal centre within the DNA helix. Other examples such as benzyl-di-(2-picolyl)amine (benzyl-DPA) were developed as copper caging ligands, providing increased denticity and thereby stabilising the resulting complex during redox cycling processes central to ROS generation.[8]

Most reported Cu-AMNs require the presence of an external reductant, typically sodium-*L*-ascorbate (Na-*L*-asc), to reduce the Cu(II) to Cu(I) and generate ROS for DNA cleavage. However, some ligands can promote self-activated cleavage in the absence of added reductant. Examples include phenanthroline derivatives such as *bis*-phenanthroline phthalate,[9] bipyridine and terpyridine derivatives such as anthracenyl-terpyridine,[10] as well as natural products, such as prodigiosin (PD),[11] introduced in Chapter I and further discussed in Chapter V. PD is a natural marine alkaloid[12] known to intercalate DNA and generate ROS-mediated DNA damage in the presence of copper, without the need for a reductant.[11] PD has also been reported to form stable complexes with iron[13] and zinc.[14, 15]

However, AMNs remain challenged by the lack of site-specific DNA cleavage, as most AMNs rely on non-specific binding interactions and thus

could induce *off*-target genomic damage.[16] To address this, oligonucleotide-based targeting vectors such as triplex-forming oligonucleotides (TFOs) have been employed.[17, 18] TFOs are single-stranded oligonucleotides that sequence-specifically bind DNA through the formation of hydrogen bonds on the Hoogsteen face of DNA duplets.[19] Therefore, TFOs allow the localisation of functional groups directly adjacent to a target site. AMNs can be tethered to TFOs *via* click chemistry, such as copper-catalysed azide alkyne cycloaddition (CuAAC) and strain-promoted azide-alkyne cycloaddition (SPAAC).[20-22] Previous work has shown the use of CuAAC and SPAAC to attach Cu-AMNs to TFO using azide-functionalised phenanthroline derivatives (Phen, DPPZ, ImPhen[21] and Clip-Phen[22]) and caging ligands (benzyl-DPA[23] and TPMA[20] ligands). These hybrids were isolated and purified before being reacted with their target and *off*-target duplexes, in the presence of copper and Na-*L*-asc, and were shown to generate promising targeted cleavage activity with little-to-no *off*-target damage.

In this chapter, a self-assembly strategy is explored for generating AMN-TFO hybrids, enabling facile screening of TFOs, metal ions, and ligands for AMN applications. In this approach, all components—the target duplex, an *off*-target duplex, a DBCO-modified TFO, an azide-functionalised ligand and a metal salt—were combined simultaneously. The AMN-TFO conjugate forms *in situ* through SPAAC using the target DNA as a template. This method circumvents the need for pre-synthesised hybrids and their purification and enables rapid evaluation of different ligand-metal combinations for target-specific DNA cleavage.

The aim of this work is to assess the feasibility of SPAAC-mediated self-assembled AMN-TFO hybrids targeting the *EGFR*-gene and to evaluate its application for fast screening of metal centres and ligands. Different transition metals used in AMN systems (Cu, Fe, Zn and Mn) were compared for the cleavage activity of PD-TFO hybrids. The novel PD ligand was compared to Cu-AMN-ligands that have previously been tethered to TFOs (DPPZ, ImPhen, Phen and benzyl-DPA).[21, 23] Emphasis was placed on comparing activity against target and *off*-target duplexes to determine the degree of sequence specificity achieved through this self-assembly strategy.

2 Materials and Methods

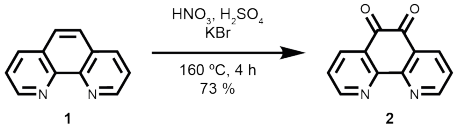
2.1 General methods

Chemicals and high-performance liquid chromatography (HPLC) grade solvents were purchased from Merck, Tokyo Chemical Industry (TCI) or Fisher Scientific and used without further purification. ^{1}H-NMR spectra were recorded on a Brucker AC 600 MHz NMR spectrometer. All spectra are reported in Chapter VIII section D.1. All samples were quenched with loading dye (6×, 2.5% Ficoll®-400, 11 mM EDTA, 3.3 mM Tris-HCl, 0.017% SDS, 0.015% bromophenol blue, pH 8.0, Thermo Fisher) before loading on gels. PAGE gels were prepared using 29:1 acrylamide:bis-acrylamide using Tris-Acetate (TA, pH 6.0, 50 mM) buffer, $MgCl_2$ (5 mM), NaCl (75 mM) TEMED (Thermo Fisher Scientific, 0.2%) and ammonium persulfate (APS, 0.05%). PAGE was run at 70 V for 4 h in 50 mM TA pH 6.0 buffer, and gels were visualised on a Syngene G:Box Mini 9 gel documentation system. Target and *off*-target duplexes were purchased from Integrated DNA Technologies.

2.2 Synthesis azide-functionalised ligands

11-azidodipyrido[3,2-*a*:2',3'-*c*]phenazine (N_3-DPPZ) and 2-(4-azidophenyl)-1H-imidazo[4,5-*f*]-1,10-phenanthroline (N_3-ImPhen) were prepared according to the method reported by Lauria *et al*.[21] with slight modifications, and the NMR spectra were compared to the literature. The synthesis of N-(3-azidopropyl)-5-((4'-methoxy-1H,5'H-[2,2'-bipyrrol]-5'-ylidene)methyl)-2,4-dimethyl-1H-pyrrole-3-carboxamide (N_3-PD) and 5-azido-1,10-phenanthroline (N_3-Phen) was carried out as described in previous chapters. N-(4-azidobenzyl)-1-(pyridin-2-yl)-N-(pyridin-2-ylmethyl)methanamine (N_3-benzyl-DPA) was synthesised by a coworker as reported in literature.[23]

2.2.1 Synthesis of 1,10-phenanthroline-5,6-dione

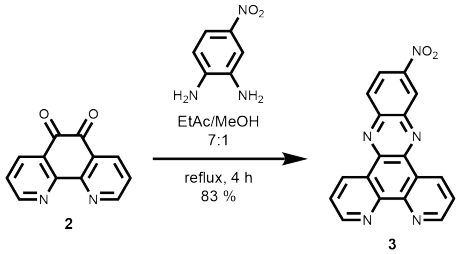


1,10-phenanthroline (4.400 g, 22.21 mmol, 1 eq.) and potassium bromide (4.000 g, 33.60 mmol, 1.5 eq.) were ground and dissolved in a mixture of H_2SO_4 (40 mL) and HNO_3 (20 mL) at 0 °C. The mixture was allowed to return to room temperature before it was refluxed at 160 °C for 4 h. After cooling down

to room temperature, the reaction was poured onto crushed ice (400 mL), and the pH was adjusted to 4.0 using NaOH (5 M). The product was extracted with chloroform (6 x 100 mL), dried over $MgSO_4$ and dried under reduced pressure. The resulting yellow powder was recrystallised in methanol, affording 1,10-phenanthroline-5,6-dione (3.397 g, 16.16 mmol) as yellow crystals with a 73% yield. ^{1}H NMR ($CDCl_3$) δ 9.13 (dd, *J* = 4.7, 1.8 Hz, 2H), 8.52 (dd, *J* = 7.8, 1.8 Hz, 2H), 7.60 (dd, *J* = 7.8, 4.7 Hz, 2H).

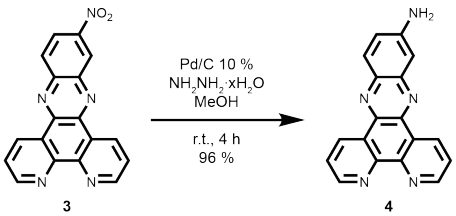
2.2.2 Synthesis of N_3-DPPZ

2.2.2.1 Synthesis of 11-nitrodipyrido[3,2-*a*:2',3'-*c*]phenazine (nitro-DPPZ)



1,10-phenanthroline-5,6-dione (2.000 g, 9.52 mmol, 1 eq.) was suspended in a mixture of methanol/ethyl acetate (1:2, 150 mL) and heated until complete dissolution. 4-nitrobenzene-1,2-diamine (1.457 g, 9.51 mmol, 1 eq.) was added and the reaction was stirred under reflux for 4 h. The mixture was cooled to room temperature, and the resulting precipitate was isolated by vacuum filtration and washed with ice-cold ethyl acetate, yielding nitro-DPPZ (2.598 g, 7.94 mmol) as a grey powder with an 83% yield. ^{1}H NMR ($CDCl_3$) δ 9.77 (d, *J* = 8.0 Hz, 2H), 9.46 (s, 2H), 9.33 (dd, *J* = 2.5, 0.6 Hz, 1H), 8.73 (dd, *J* = 9.3, 2.5 Hz, 1H), 8.57 (d, *J* = 9.2 Hz, 1H), 7.97 (s, 2H).

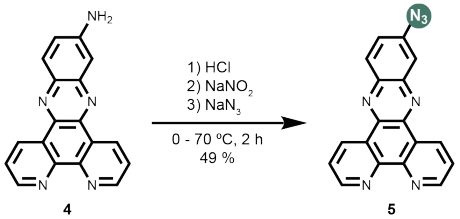
2.2.2.2 Synthesis of 11-aminodipyrido[3,2-*a*:2',3'-*c*]phenazine (amino-DPPZ)



Under nitrogen atmosphere, nitro-DPPZ (300.0 mg, 0.92 mmol, 1 eq.) and palladium on carbon (35.4 mg, catalytic amounts) were suspended in ethanol (100 mL) and the mixture was refluxed before hydrazine hydrate (5 mL,

approx. 100 eq.) was added. The reaction was further refluxed for 4 h and the hot mixture was filtered over a celite pad. The filtrate was evaporated to dryness under reduced pressure, resulting in an orange powder that was washed with diethyl ether, yielding amino-DPPZ (263.4 mg, 0.89 mmol) with a 97% yield. ^{1}H NMR (DMSO-d_6) δ 9.45 (ddd, *J* = 47.6, 8.1, 1.8 Hz, 2H), 9.14 (ddd, *J* = 36.2, 4.3, 1.8 Hz, 2H), 8.05 (d, *J* = 9.1 Hz, 1H), 7.88 (ddd, *J* = 12.7, 8.1, 4.3 Hz, 2H), 7.49 (dd, *J* = 9.1, 2.5 Hz, 1H), 7.14 (d, *J* = 2.4 Hz, 1H), 6.56 (s, 2H).

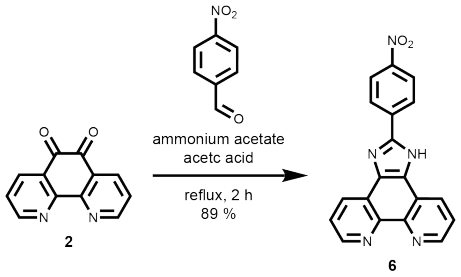
2.2.2.3 Synthesis of N_3-DPPZ



Amino-DPPZ (900.0 mg, 3.03 mmol, 1 eq.) was suspended in an aqueous solution of HCl (6 M, 35 mL) and heated at 70 °C for 20 min. The mixture was then cooled to 0 °C and $NaNO_2$ (627.2 mg, 9.09 mmol, 3 eq.) in H_2O (3 mL) was added dropwise. The mixture was stirred at 0 °C for 30 min before an aqueous solution of NaN_3 (3 mL, 590.1 mg, 9.08 mmol, 3 eq.) was added dropwise at 0 °C. The reaction was stirred at room temperature for 2 h before being neutralised using ammonia and filtered. The brown filtrate was washed with H_2O (2 x 10 mL) and diethyl ether (3 x 10 mL), yielding azido-DPPZ (837.2 mg, 2.59 mmol) with an 86% yield. ^{1}H NMR (DMSO-d_6) δ 9.46 (ddd, *J* = 8.3, 7.1, 1.7 Hz, 2H), 9.20 (ddd, *J* = 9.2, 4.3, 1.8 Hz, 2H), 8.34 (d, *J* = 9.0 Hz, 1H), 7.93 (quint, *J* = 4.3 Hz, 3H), 7.74 (dd, *J* = 9.0, 2.5 Hz, 1H).

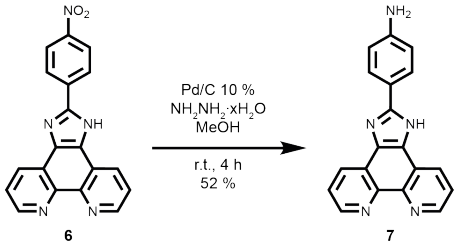
2.2.3 Synthesis of azido-ImPhen

2.2.3.1 Synthesis of 2-(4-nitrophenyl)-1H-imidazo[4,5-*f*]-1,10-phenanthroline (nitro-ImPhen)



4-nitrobenzaldehyde (540.3 mg, 3.57 mmol, 1.5 eq.) and ammonium acetate (5.403 g, 70.09 mmol, 30 eq.) were added using 11 mL acetic acid to a solution of 1,10-phenanthroline-5,6-dione (500.0 mg, 2.38 mmol, 1 eq.) in 10 mL acetic acid. The mixture was refluxed for 2 h and cooled down with an ice bath before the pH was adjusted to 7.0 using ammonia. The precipitate was isolated by vacuum filtration and washed with H_2O (3 x 20 mL), affording nitro-ImPhen (721.5 mg, 2.11 mmol) as an orange powder with an 89% yield. ^{1}H NMR (DMSO-d_6) δ 9.02 (dd, *J* = 4.2, 1.8 Hz, 2H), 8.91 (dd, *J* = 8.1, 1.8 Hz, 2H), 8.56 - 8.52 (m, 2H), 8.45 (d, *J* = 9.0 Hz, 2H), 7.82 (dd, *J* = 8.1, 4.3 Hz, 2H).

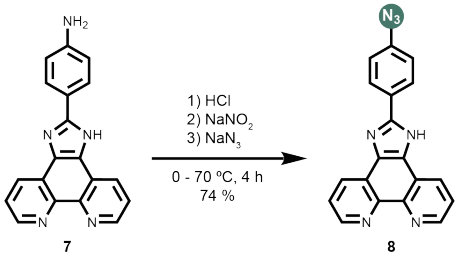
2.2.3.2 Synthesis of 2-(4-aminophenyl)-1H-imidazo[4,5-*f*]-1,10-phenanthroline (amino-ImPhen)



Nitro-ImPhen (500.0 mg, 1.46 mmol, 1 eq.) was dissolved in 110 mL methanol and hydrazine hydrate (5 mL, approx. 100 eq.) and palladium on carbon (50.2 mg, catalytic amounts) were added. The reaction was refluxed for 2 h and the cooled mixture was filtered over a celite pad. The filtrate was partially evaporated under reduced pressure, until a precipitate was obtained. The precipitate isolated by filtration and washed with H_2O (3 x 20 mL) and diethyl ether (3 x 20 mL), yielding amino-ImPhen (232.8 mg, 0.75 mmol) as an dark orange powder with a 51% yield. ^{1}H NMR (DMSO-d_6) δ 9.00 (dd, *J* = 4.2, 1.8

Hz, 2H), 8.90 (dd, *J* = 8.2, 1.8 Hz, 2H), 8.01 - 7.94 (m, 2H), 7.82 (dd, *J* = 8.1, 4.3 Hz, 2H), 6.73 (d, *J* = 8.6 Hz, 2H), 5.65 (s, 2H).

2.2.3.3 Synthesis of N_3-ImPhen



Amino-ImPhen (200.1 mg, 0.64 mmol, 1 eq.) was suspended in HCl (6 M, 10 mL) and stirred at 0 °C for 20 min. An aqueous solution of $NaNO_2$ (1 mL, 66.1 mg, 0.96 mmol, 1.5 eq.) was added dropwise and stirred for 30 min at 0 °C. NaN_3 (125.2 mg, 1.92 mmol, 3 eq.) in H_2O (1 mL) was added dropwise at 0 °C and the mixture was further stirred for 2 h at 0 °C. The pH was neutralised with ammonia, and the resulting precipitate was isolated by vacuum filtration and washed with H_2O (3 x 20 mL) and diethyl ether (3 x 20 mL). Azido-ImPhen (160.0 mg, 0.47 mmol) was obtained as a brown powder with a 74% yield. ^{1}H NMR (DMSO-d_6) δ 13.83 (s, 1H), 9.07 - 9.04 (m, 2H), 8.98 - 8.94 (m, 2H), 8.34 (d, *J* = 8.7 Hz, 2H), 7.91 - 7.85 (m, 2H), 7.41 (d, *J* = 8.8 Hz, 2H).

2.3 Screening of the cleavage activity of AMN-TFO hybrids

All samples were prepared in a total volume of 10 µL phosphate buffer (10 mM PO_4^{3-}, 150 mM NaCl and 10 mM $MgCl_2$, pH 6.0) with the target (0.5 pmol, 1 eq.) and *off*-target (0.5 pmol, 1 eq.) duplexes. The tested DBCO-TFO (50 pmol, 100 eq.) was added, followed by the tested N_3-ligand (50 pmol, 100 eq.) and metal salt (250 pmol, 500 eq.). Where appropriate, Na-*L*-asc (1 mM) was added. The resulting mixture was incubated for the specified duration and loading dye was added. PAGE analysis was carried out as described in general methods.

2.3.1 Cleavage activity of self-assembled PD-2 and PD-3 hybrids in the presence of copper

The samples were prepared as detailed above using either DBCO-TFO-2 or DBCO-TFO-3 in the presence of N_3-PD and $Cu(NO_3)_2$. Samples were incubated for 18 h.

2.3.2 Screening of ligands for AMN activity with TFO-2

The samples were prepared as mentioned above using DBCO-TFO-2 in the presence of N_3-PD. Next, $Cu(NO_3)_2$, $FeCl_3$, $Zn(OAc)_2$ or $Mn(OAc)_2$ were added, and Na-*L*-asc was added to one of the $Cu(NO_3)_2$ samples, and one of the $FeCl_3$ samples. Finally, samples were incubated for 18 h.

2.3.3 Screening of metals for the cleavage activity of PD-2

The samples were prepared as mentioned above using DBCO-TFO-2 in the presence of N_3-PD, N_3-DPPZ, N_3-ImPhen, N_3-Phen or N_3-benzyl-DPA, and $Cu(NO_3)_2$. Na-*L*-asc was added to all samples except for the N_3-PD samples. Samples were incubated for 3, 6, 18 or 24 h.

3 Results and discussion

3.1 Synthesis of N_3-ligands

N_3-DPPZ and N_3-ImPhen were synthesised as previously reported by Lauria *et al*.[21] (Figure VI.1) Briefly, starting from 1,10-phenanthroline-5,6-dione, nitro-DPPZ was prepared *via* Schiff base condensation with 4-nitrobenzene-1,2-diamine, with an 83% yield. The nitro functional group was then reduced to an amino group using hydrazine hydrate as a H_2 source and palladium on carbon as a catalyst, which was removed easily using a celite pad, yielding the amino-DPPZ with a 97% yield. The amino group was converted to an azide through intermediate conversion to the diazonium salt before reacting with NaN_3, yielding N_3-DPPZ with an 86% yield. N_3-ImPhen was prepared similarly, starting from 1,10-phenanthroline-5,6-dione and 4-nitrobenzaldehyde, yielding nitro-ImPhen with an 89% yield. Nitro-ImPhen was reduced to amino-ImPhen with a 51% yield and converted to N_3-ImPhen with a 74% yield similarly to the conversion of nitro-DPPZ to N_3-DPPZ.

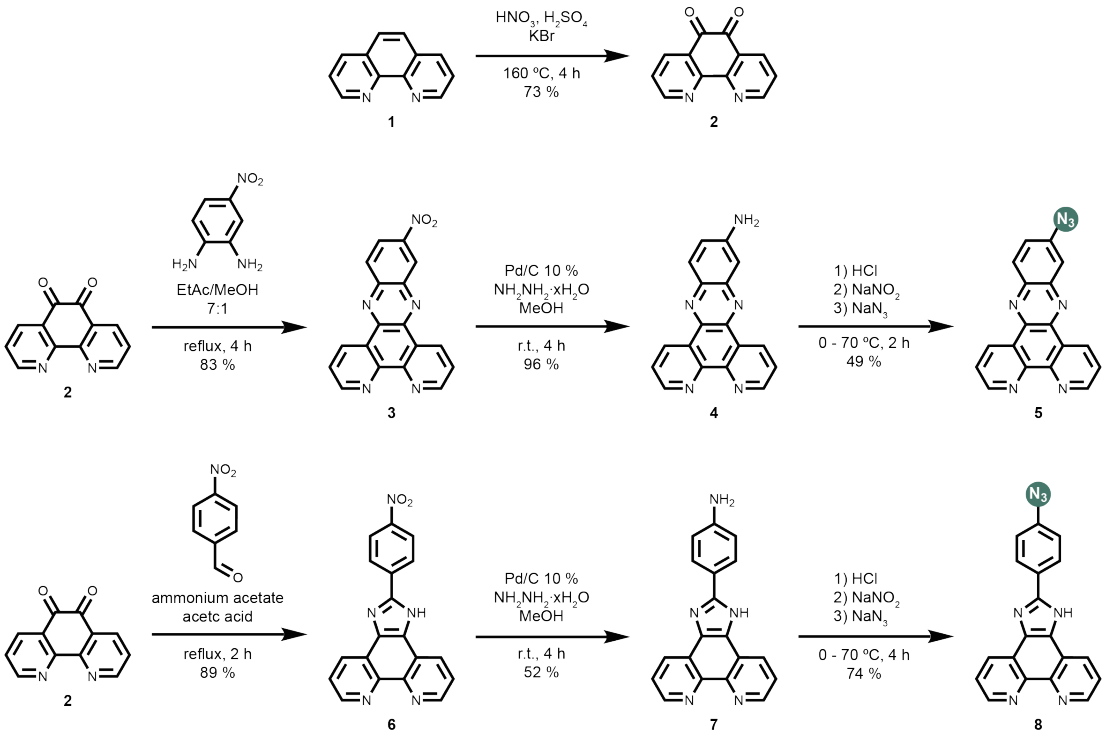


Figure VI.1: Synthesis of N_3-DPPZ and N_3-ImPhen according to the procedure reported by Lauria et al.[21]

N_3-benzyl-DPA was prepared by a coworker as reported in literature.[23] N_3-PD and N_3-Phen were synthesised as mentioned in Chapter V (Figure VI.2).

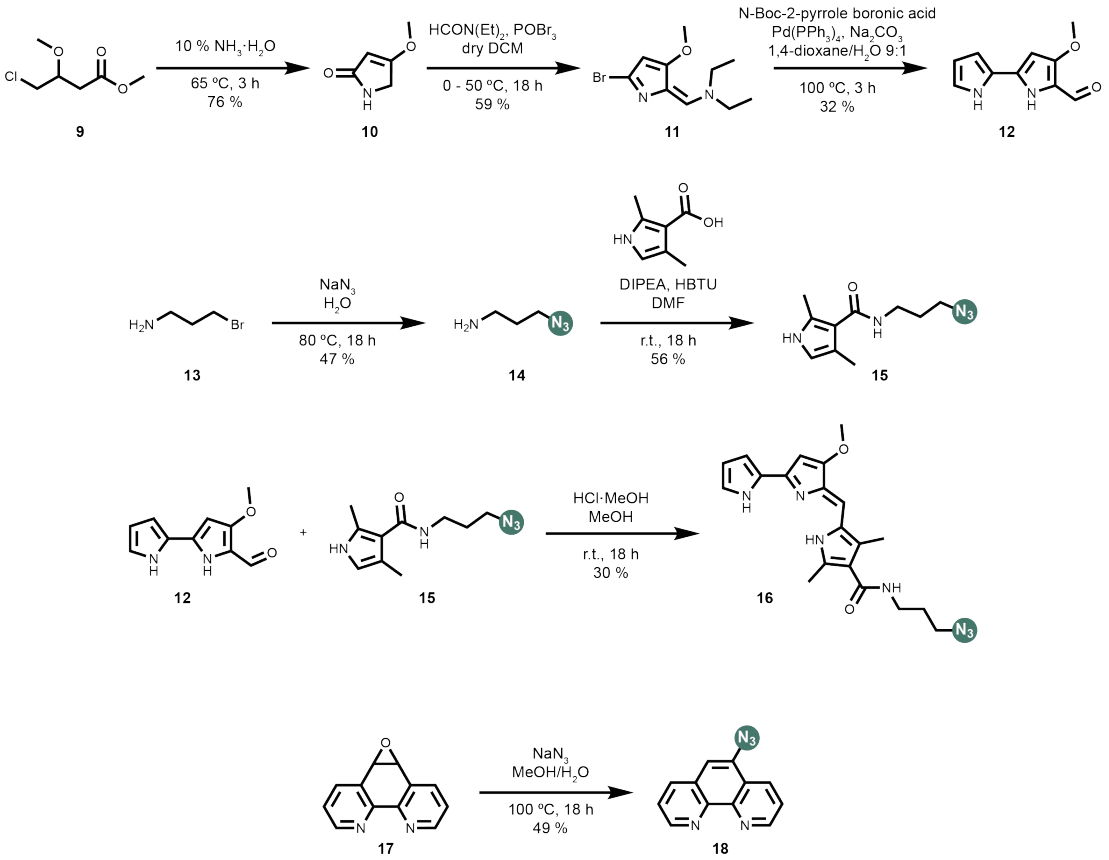


Figure VI.2: Synthesis of N_3-PD and N_3-Phen according to the procedure reported in Chapter V.

3.2 Self-assembly of AMN-TFO hybrids via *SPAAC*

3.2.1 Experimental design

SPAAC provided a fast method for labelling 5′-DBCO-modified TFOs that bypasses the need for HPLC purification. Therefore, a new assay was developed where the target duplex was used as a template for the self-assembly of the AMN-TFO hybrid *via* SPAAC, in the presence of an *off*-target duplex. The SPAAC labelling of the DBCO-TFO and the subsequent targeted cleavage activity upon addition of a metal centre were performed in a one-pot reaction, without isolation or purification steps (Figure VI.3). The experimental simplicity of this self-assembly process enabled facile screening of different ligands and metals for targeted cleavage activity of AMN-TFO hybrids. The potential of self-assembled PD-TFOs was easily compared in the presence of different metal centres and compared to different ligands that have been combined with TFO for Na-*L*-asc-mediated target specific cleavage activity.

To illustrate the scope of the self-assembly method and the potency of the newly developed PD analogue, N_3-PD was compared to different ligands reported for Cu-AMN applications that have been hybridised to TFOs including: N_3-Phen; N_3-DPPZ; N_3-ImPhen; and N_3-benzyl-DPA. DPPZ and ImPhen are derivatives of Phen, the standard ligand for Cu-AMN applications, with extended aromatic rings. Their azide derivatives were clicked onto TFOs by Lauria *et al.*[21] to evaluate the impact of increased aromaticity on intercalation and subsequently on target specific cleavage activity. The study revealed that the ImPhen-TFO hybrids achieved the highest triplex association—according to the intensity of the emergent band in PAGE analysis— surpassing both Phen- and DPPZ-TFO hybrids. They also displayed the highest activity during Na-*L*-asc-mediated cleavage of DNA in the presence of titrated copper(II). Compared to Phen and its increased aromatic congeners, the copper-caging ligand benzyl-DPA has increased denticity and more flexibility. McGorman *et al.*[23] studied its tethering to TFOs using CuAAC, resulting in high-specificty cleavage activity.

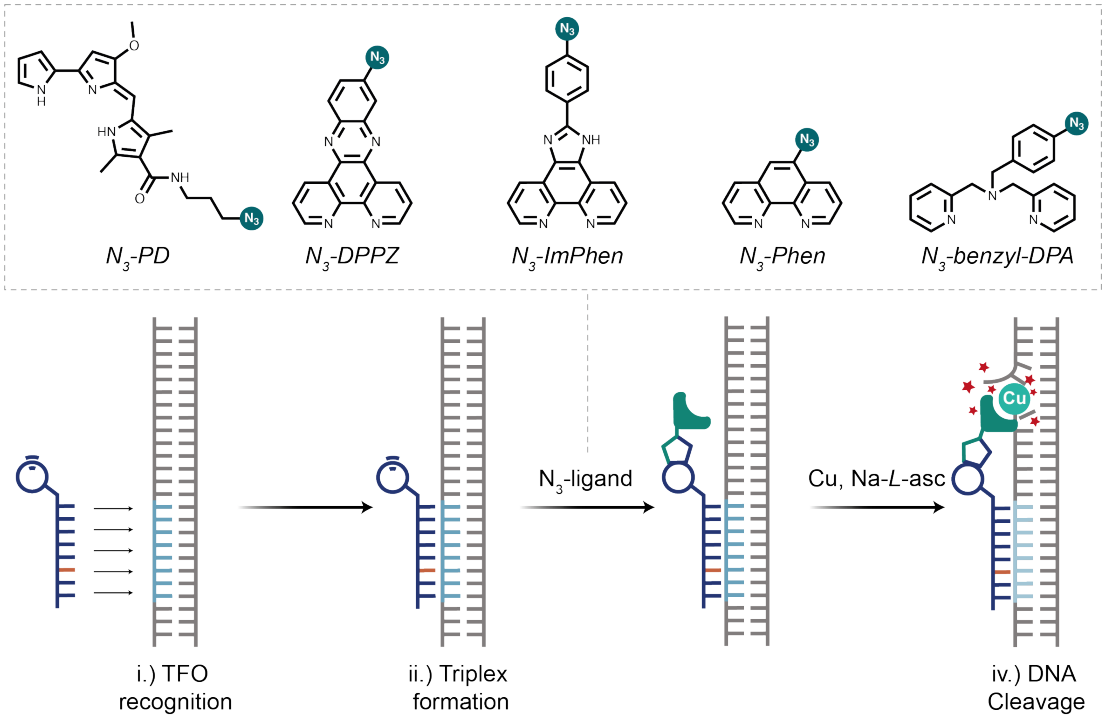


Figure VI.3: Schematic representation of the self-assembly assay. The first step is the addition of the DBCO-TFO to the duplex for triplex formation, then N_3-ligand is added (N_3-PD, N_3-DPPZ, N_3-ImPhen, N_3-Phen or N_3-benzyl-DPA) and the SPAAC is performed using the duplex as a template. The final step is the addition of a metal centre to initiate cleavage of the target duplex. All steps are performed in the same sample, without intermediate incubation time.

The DBCO-TFOs used in this study are as described in Chapters III, IV and V. TFO-2 and TFO-3 (Figure VI.4) were selected as PD-TFO-2 and PD-TFO-3 resulted in the most stable triplexes. These TFOs were modified with 5-methylcytosine (5mC) replacing all cytosines, and with the incorporation of one or two (TFO-2 and TFO-3 respectively) thiazole orange (TO) modification. TFO-2 has 1 TO at position (X_2), and TFO-3 has two TO modifications, one at (X_1) and the second at (X_2). A dibenzocyclooctone (DBCO) group was incorporated on the 5′-end to enable SPAAC functionalisation. The target and *off*-target duplexes are 40-mer and 29-mer duplex strands as described in previous chapter. The target duplex contains the triplex recognition domain, while the *off*-target does not.

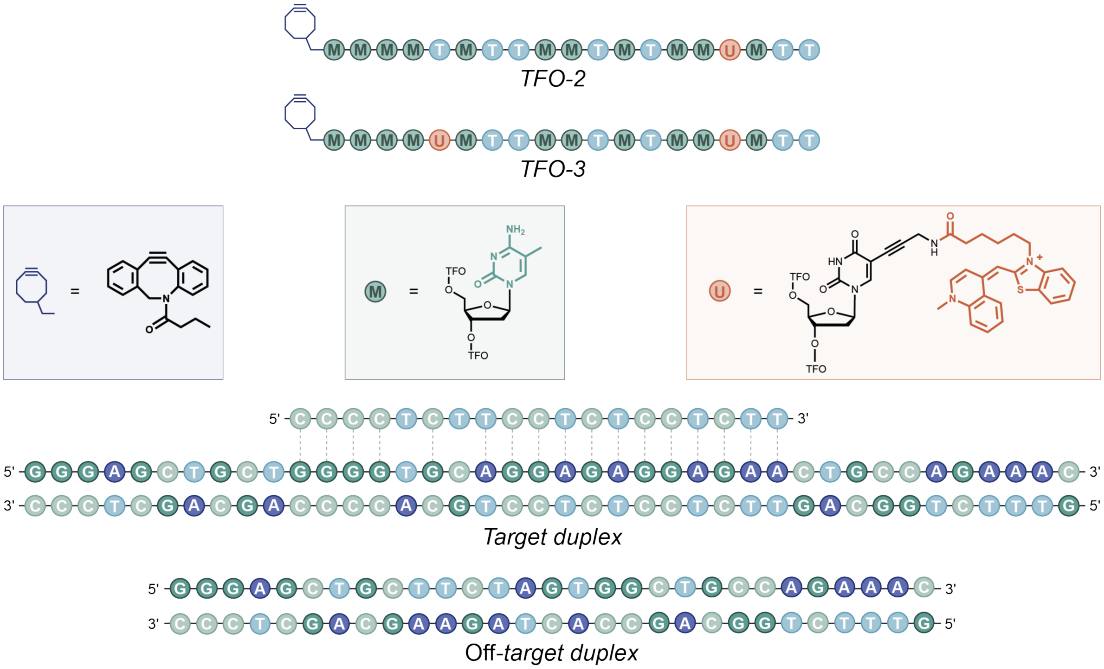


Figure VI.4: Structure of TFO-2 and TFO-3, 5mC, TO-modified dU and 5′-DBCO modifications, and target and *off*-target duplexes. TFO-2 has 1 TO modification away from the DBCO group and TFO-3 has 2 TO units, one away and one close to DBCO.

3.2.2 Comparison of TFO-2 and TFO-3 for self-assembly application

The self-assembly of PD-TFO-2 and PD-TFO-3 (Figure VI.5) resulted in hybrids that generated a clear depletion of the target duplex in the presence of copper. For both PD-TFO-2 and 3, the *off*-target band was not depleted, confirming that the cleavage remained target-specific during the self-assembly process. In the case of PD-TFO-3, the activity was limited by poor triplex formation. In contrast, self-assembled PD-TFO-2 resulted in a clear triplex

band, even though the non-modified DBCO-TFO-2 did not form a stable triplex. It can be hypothesised that through intercalation, PD helps to enhance triplex association, in a similar manner as TO, which is consistent with the reported intercalating property of the natural PD. However, when TO and PD are in proximity, as with TFO-3, the intercalation of two molecules could instead disrupt the triplex. Additionally, PD-TFO-2 visibly depleted the triplex band as well as the duplex band, proving the target-specific cleavage activity of self-assembled PD-TFO-2 in the presence of copper. Therefore, DBCO-TFO-2 was selected for further self-assembly experiments. Overall, this confirms the self-assembly method can produce PD-TFO hybrids *in situ* that retained target specific cleavage activity in the presence of copper, and without the need for exogenous reductant.

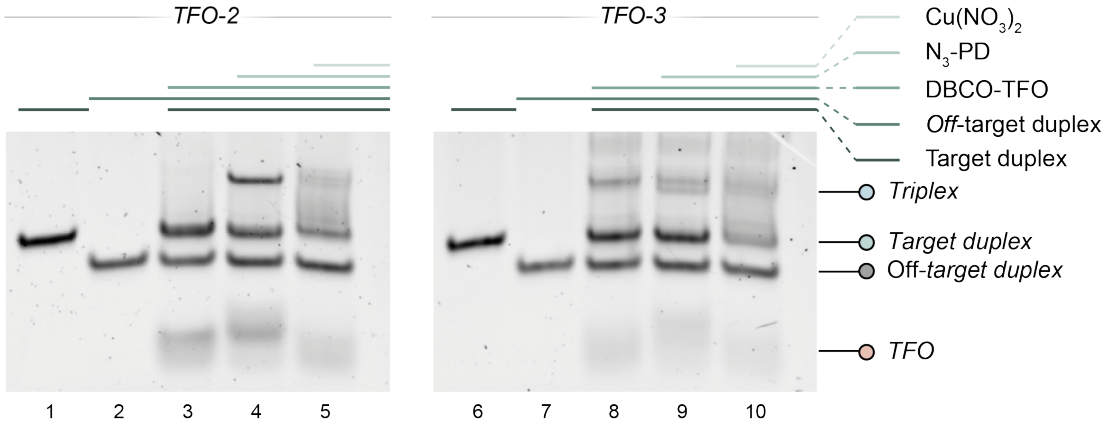


Figure VI.5: PAGE analysis showing the self-activated target specific cleavage activity of self-assembled PD-TFO-2 (left) and PD-TFO-3 (right) in the presence of copper. Lanes 1 and 6: target duplex, lanes 2 and 7: *off*-target duplex, lane 3: both duplexes + DBCO-TFO-2, lane 4: lane 3 + N_3-PD, lane 5: lane 4 + $Cu(NO_3)_2$, lane 8: both duplexes + DBCO-TFO-3, lane 9: lane 8 + N_3-PD and lane 10: lane 9 + $Cu(NO_3)_2$.

3.2.3 Screening of metal centre for the target-specific cleavage activity of self-assembled PD-TFO-2

The second parameter that was investigated for the self-assembly assay design was the choice of the metal centre. Therefore, the self-assembly experiment was repeated with DBCO-TFO-2 and N_3-PD, in the presence of either $Cu(NO_3)_2$, $FeCl_3$, $Zn(OAc)_2$ or $Mn(OAc)_2$ (Figure VI.6). Copper and iron were tested both in the presence and in the absence of Na-*L*-asc, as prodigiosin scaffolds are known to exchange electrons with redox-active metal centres, thereby triggering the production of ROS. Although PD is not reported

to cleave DNA in the presence of iron, zinc or manganese, these metal centres were selected to broaden the scope of the study. These metal centres are also reported to bind to porphyrins,[24-26] a well-studied class of compounds that have multiple pyrrole motifs, similarly to prodiginine scaffolds.

Results show that in the presence of zinc, the triplex band was faint, while the duplex band was very intense, suggesting that zinc inhibits triplex formation. In contrast, the addition of iron and manganese both resulted in an increase in intensity of the triplex band compared to the control lacking a coordinated metal ion. Upon the addition of Na-*L*-asc, in the case of iron, the triplex band intensity decreased somewhat, without an increase in the duplex band intensity, characteristic of cleavage of the triplex. The most active cleavage was observed with copper, in the absence of Na-*L*-asc, where both the triplex and target duplex band were significantly depleted. However, the PD-TFO band was also depleted, suggesting autocatalysis of the hybrid. However, this did not prevent the desired cleavage of the target duplex and triplex but presents a drawback for the use of copper instead of iron for PD-TFO hybrids. Overall, this provides the first demonstration of multi-metal screening in prodigiosin-based scaffolds and establishes self-assembly as a powerful and adaptable strategy for the development and optimisation of AMN-TFO hybrids.

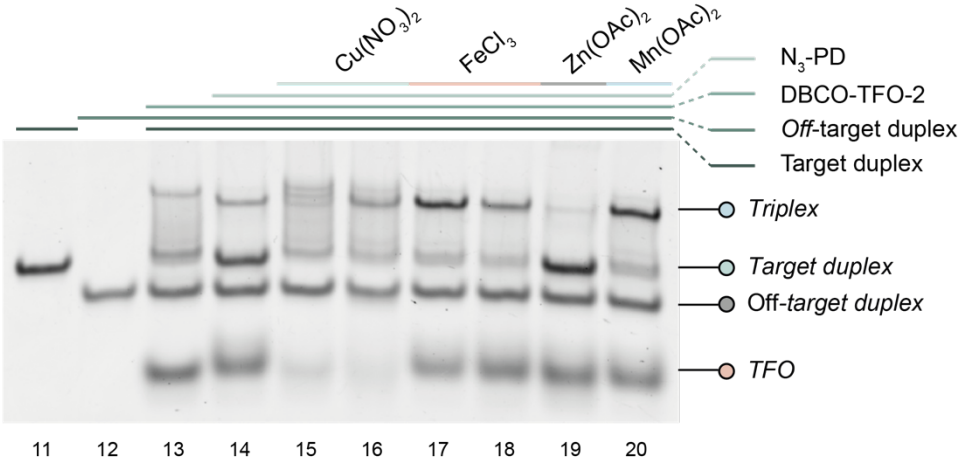


Figure VI.6: PAGE analysis showing the self-activated target specific cleavage activity of self-assembled PD-TFO-2 in the presence of different metals. Lane 11: target duplex, lane 12: *off*-target duplex, lane 13: both duplexes + DBCO-TFO-2, lane 14: lane 13 + N_3-PD, lane 15: lane 14 + $Cu(NO_3)_2$, lane 16: lane 15 + Na-*L*-asc, lane 17: lane 14 + $FeCl_3$, lane 18: lane 17 + Na-*L*-asc, lane 19: lane 14 + $Zn(OAc)_2$ and lane 20: lane 14 + $Mn(OAc)_2$.

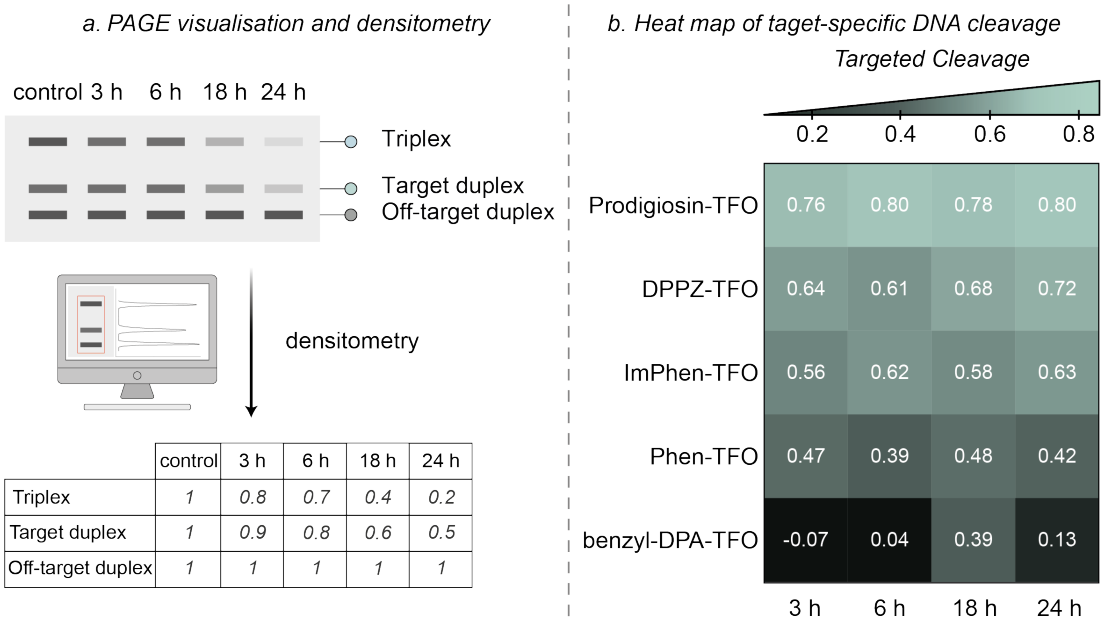
3.2.4 Screening of different ligands for copper-mediated cleavage activity of self-assembled AMN-TFO hybrids

Having established that TFO-2 and copper(II) ions were required for the cleavage activity of self-assembled PD-TFO hybrids, a range of alternative ligands: N_3-DPPZ, N_3-ImPhen, N_3-Phen and N_3-benzyl-DPA, were screened and compared directly to the observed activity of N_3-PD. Na-*L*-asc was added to all samples except N_3-PD samples. PAGE analysis was then performed to visualise the damage potential of the self-assembled AMN-TFO hybrids (Figure D.2). Band densitometry was employed to quantify the potential of target-specific AMN-TFO hybrids across ligands (Figure VI.7.a). Experiments were performed in triplicate, and a score was calculated using Formula 1 for each replicate of each ligand, at each time point.

$$score_x = \frac{1 - \frac{T_x}{T_0} + 1 - \frac{D_x}{D_0} + \frac{O_x}{O_0}}{3}$$

Formula 1: Calculation of the score for each ligand at each time point (x h) with T_x: intensity of the triplex band at t = x h, T_0 = intensity of the triplex band at t = 0 h, D_x = intensity of the target duplex band at t = x h, D_0 = intensity of the target duplex band at t = 0 h, O_x = intensity of the *off*-target duplex band at t = x h and O_0 = intensity of the target duplex band at t = 0 h.

A higher score was obtained when duplex and triplex band were depleted compared to the control, and a lower score when the intensity of the *off*-target band decreased. The score for each ligand was averaged at each time point and visualised in a heat map (Figure VI.7.b).



	control	3 h	6 h	18 h	24 h
Triplex	*1*	*0.8*	*0.7*	*0.4*	*0.2*
Target duplex	*1*	*0.9*	*0.8*	*0.6*	*0.5*
Off-target duplex	*1*	*1*	*1*	*1*	*1*

Figure VI.7: **a**. Cartoon representation of the concept of the experiment where PAGE gels are run with cleavage samples at different time points. Densitometry is then used to measure a ratio of intensity for each ligand at each exposure interval. The table in this figure does not reflect any specific result. **b**. Heat map representation of the score for targeted cleavage activity of self-assembled AMN-TFO hybrids in the presence of copper(II) ions. The score was calculated using Formula 1 for each ligand (PD, DPPZ, ImPhen, Phen and benzyl-DPA) at each time point (3, 6, 18 and 24 h). The targeted cleavage activity of DPPZ-, ImPhen-, Phen- and benzyl-DPA-TFO hybrids was measured in the presence of Na-*L*-asc.

Targeted cleavage increased slightly over time for all ligands but N_3-benzyl-DPA, which did not display any significant targeted cleavage activity. This does not reflect on the potential of benzyl-DPA as a Cu-AMN ligand but on the potential of N_3-benzyl-DPA in the self-assembly of *EGFR*-targeted AMN-TFOs *via* SPAAC. This could be explained by poor triplex formation or low yield of the SPAAC labelling with the *EGFR*-targeted TFOs. Further experiments would be necessary to test the triplex formation and SPAAC efficiency for these hybrids. N_3-PD displayed the most efficient targeted cleavage activity, despite the absence of Na-*L*-asc, followed by N_3-DPPZ. However, although N_3-DPPZ displayed strong cleavage activity in the self-assembly assay, the cleavage was not target-specific and required exogenous reductant. It can be hypothesised that the SPAAC efficiency for N_3-DPPZ is lower than for N_3-PD, which would result in non-specific DNA damage, as the unclicked N_3-DPPZ may introduce random DNA cleavage events. Indeed, the score of the ligand was impacted by the depletion of the *off*-target duplex, hindering the potential

of N_3-DPPZ in the self-assembly method for target-specific cleavage activity. N_3-ImPhen and N_3-Phen generated less *off*-target activity than N_3-DPPZ but, in contrast, did not display great cleavage activity in this self-assembly method.

Not only does the PD-TFO show significant damage potential in the self-assembly assay, it also did not generate significant *off*-target degradation. This study represents the first demonstration of a self-assembled strategy for rapid ligand screening in AMN-TFO hybrids, establishing a versatile approach to evaluate diverse scaffolds efficiently and to accelerate the identification of promising candidates for *EGFR*-targeted DNA cleavage.

4 Conclusion

This chapter demonstrated the feasibility of self-assembling AMN-TFO hybrids through SPAAC-mediated conjugation of azide-modified ligands to DBCO-functionalised TFOs *in situ*. By combining all components—TFO, ligand, metal and DNA duplexes—in a single reaction, conjugates capable of inducing target-specific cleavage were generated *in situ*. Furthermore, the screening of metal ions for the target specific cleavage activity of the PD-TFO hybrid showed that this hybrid is most active in the presence of copper, and without Na-*L*-asc. While manganese had no significant effect, the presence of zinc appeared to prevent triplex formation, and iron enabled partial Na-*L*-asc-mediated targeted cleavage. These results suggest that copper remains the most robust metal for PD-TFO-mediated target specific metallo-nuclease applications.

Among the ligands tested, PD showed the most promising activity, even when compared to other AMN-TFO in the presence of Na-*L*-asc. Notably, in the self-assembly assay, the generated PD-TFO was more active for self-activated target specific cleavage than the Phen-TFO analogue even in the presence of Na-*L*-asc. While DPPZ showed significant DNA damage, the self-assembled AMN-TFO also generated *off*-target damage. This could be due to a reduced efficiency of the SPAAC coupling, leading to unclicked N_3-DPPZ damaging both the target and *off*-target duplex. Further experiments, such as PAGE visualisation of the SPAAC or mass spectrometry, would be necessary to confirm this hypothesis. The hypothetical difference in SPAAC-efficiency between N_3-PD and N_3-DPPZ could be explained by reduced steric hindrance in the case of the aliphatic azide handle on N_3-PD, as opposed to the aromatic azide on N_3-DPPZ. A wider scope of ligand screening could be optimal to identify a possible link between the environment of the azide handle and the efficiency of the self-assembly.

Collectively, these findings highlight the potential of self-assembly as a rapid and flexible strategy for screening AMN-TFO hybrids. This approach eliminates the need for pre-synthesised conjugates and enables systematic screening of ligand-metal combinations directly in a DNA context, focused on target specific damage.

5 References

[1] Sigman, D. S.; Graham, D. R.; D'Aurora, V.; Stern, A. M. *J Biol Chem.* **1979**, *254,* (24), 12269-12272.

[2] McCord, J. M.; Day, E. D. *FEBS Letters.* **1978**, *86,* (1).

[3] Jiang, Q.; Xiao, N.; Shi, P.; Zhu, Y.; Guo, Z. *Coordination Chemistry Reviews.* **2007**, *251,* (15-16).

[4] Coleman, J. E. *Curr Opin Chem Biol.* **1998**, *2,* (2), 222-234.

[5] Wende, C.; Lüdtke, C.; Kulak, N. *Eur J Inorg Chem.* **2014**, *2014,* (16).

[6] Thomas, A. M.; Nethaji, M.; Mahadevan, S.; Chakravarty, A. R. *J Inorg Biochem.* **2003**, *94,* (1-2).

[7] Rajebhosale, B. S.; Dongre, S. N.; Deshpande, S. S.; Kate, A. N.; Kumbhar, A. A. *J Inorg Biochem.* **2017**, *175*.

[8] Sivanesan, D.; Youn, M. H.; Park, K. T.; Kim, H. J.; Grace, A. N.; Jeong, S. K. *Acta Crystallogr C Struct Chem.* **2017**, *73,* (Pt 11), 1024-1029.

[9] Andrew Kellett; Mark O'Connor; Malachy McCann; Mary McNamara; Patrick Lynch; Georgina Rosair; Vickie McKee; Bernie Creaven; Maureen Walsh; Siobhan McClean; et al. *Dalton Transactions.* **2011**, *40,* (5).

[10] Kumar, A.; Kumar, A.; Chinta, J. P.; Chinta, J. P.; Ajay, A. K.; Ajay, A. K.; Bhat, M. K.; Bhat, M. K.; Rao, C. P.; Rao, C. P. *Dalton Transactions.* **2011**, *40,* (41).

[11] Melvin, M. S.; Tomlinson, J. T.; Saluta, G. R.; Kucera, G. L.; Lindquist, N.; Manderville, R. A. *J Am Chem Soc.* **2000**, *122,* (26), 6333-6334.

[12] Montaner, B.; Perez-Tomas, R. *Curr Cancer Drug Targets.* **2003**, *3,* (1), 57-65.

[13] Arivizhivendhan, K. V.; Mahesh, M.; Murali, R.; Mary, R. R.; Thanikaivelan, P.; Sekaran, G. *ACS Sustainable Chemistry & Engineering.* **2019**, *7,* (3).

[14] Chang, T. M.; Sinharay, S.; Astashkin, A. V.; Tomat, E. *Inorg Chem.* **2014**, *53,* (14), 7518-7526.

[15] Park, G.; Tomlinson, J. T.; Melvin, M. S.; Wright, M. W.; Day, C. S.; Manderville, R. A. *Org Lett.* **2003**, *5,* (2), 113-116.

[16] Gibney, A.; Kellett, A. *Chemistry.* **2024**, *30,* (57), e202401621.

[17] Chen, C. H.; Sigman, D. S. *Proc Natl Acad Sci U S A.* **1986**, *83,* (19), 7147-7151.

[18] Dreyer, G. B.; Dervan, P. B. *Proc Natl Acad Sci U S A.* **1985**, *82,* (4), 968-972.

[19] Fox, K., R. ; Brown, T.; Rusling, D. A. *Chemical Biology.* **2018**, *Chapter 1*, 1-32.

[20] Fantoni, N. Z.; McGorman, B.; Molphy, Z.; Singleton, D.; Walsh, S.; El-Sagheer, A. H.; McKee, V.; Brown, T.; Kellett, A. *Chembiochem.* **2020**, *21,* (24), 3563-3574.

[21] Lauria, T.; Slator, C.; McKee, V.; Müller, M.; Stazzoni, S.; Crisp, A. L.; Carell, T.; Kellett, A. *Chem-Eur J.* **2020**, *26,* (70), 16782-16792.

[22] Panattoni, A.; El-Sagheer, A. H.; Brown, T.; Kellett, A.; Hocek, M. *Chembiochem.* **2020**, *21,* (7), 991-1000.

[23] McGorman, B.; Fantoni, N. Z.; O'Carroll, S.; Ziemele, A.; El-Sagheer, A. H.; Brown, T.; Kellett, A. *Nucleic Acids Res.* **2022**, *50,* (10), 5467-5481.

[24] Boucher, L. J. *Coordination Chemistry Reviews.* **1972**, *7,* (3).

[25] Chino, M.; Leone, L.; Zambrano, G.; Pirro, F.; D'Alonzo, D.; Firpo, V.; Aref, D.; Lista, L.; Maglio, O.; Nastri, F.; et al. *Biopolymers.* **2018**, *109,* (10).
[26] Weiss, J. *Journal of inclusion phenomena and macrocyclic chemistry 2001 40:1.* **2001**, *40,* (1).

Chapter VII

Conclusion and future work

April 2026

This project explored the rational design and evaluation of hybrids combining metal complexes with triplex-forming oligonucleotides (TFOs) for sequence-specific gene silencing, targeting the epidermal growth factor receptor (*EGFR*) oncogene. The work participated to the effort on targeted metal therapies through the combination of redox- and Pt-coordination-active metal complexes with TFOs. The research was developed along three main axes: (i) the design of *EGFR*-targeting TFOs and optimisation of biorthogonal coupling methods for platinum(II)-TFO conjugation, (ii) the development of new monofunctional platinum(II) capable of covalent adduct formation with DNA and of a prodigiosin-derivative ligand for self-activated artificial metallo-nuclease (AMN) application, and (iii) the establishment of a self-assembly method for ligand screening for target-specific DNA cleavage activity. Together, these studies demonstrated the versatility of strain-promoted azide-alkyne cycloaddition (SPAAC) for TFO functionalisation, and the potential of monofunctional Pt(II) hybrids and self-activated Cu-PD-TFO conjugates as efficient gene-directed DNA cleavage agents.

To address the aims of the project, the initial step consisted of the rational design of a set of parallel TFOs targeting a polypurine tract within the exon 5 of the *EGFR* gene. The sequences were developed to maximise triplex association through the incorporation of 5-methylcytosine (5mC) and thiazole orange (TO), improving protonation at higher pH and enhanced base stacking through intercalation along with fluorescence-based monitoring for triplex formation. TFOs incorporated either an internal octadiynyl modification for copper-catalysed azide-alkyne cycloaddition (CuAAC) or a 5'-dibenzocyclooctyne (DBCO) modification for SPAAC labelling.

The two classes of TFO were compared for conjugation using an azide-derivative of oxaliplatin, Pt-N_3-Oxali. While both routes overall yielded the desired hybrids, SPAAC offered a copper-free alternative while maintaining the same reaction times as CuAAC and resulted in hybrids of higher purity without the need for purification. The SPAAC-generated hybrids also showed higher triplex-association kinetics. These results established SPAAC as the method of choice for subsequent hybrid generation with the developed *EGFR*-targeting TFOs.

Based on the promising activity of pyriplatin and phenanthriplatin and their alternative mode of action, two new monofunctional Pt(II) complexes were prepared bearing tridentate di-(2-picolyl)amine (DPA) ligands modified with benzyl or propyl azides. These were developed to promote controlled, site-specific adduct formation with DNA, using TFOs to enable sequence-specificity. The Pt-N_3-DPA complexes were successfully attached to DBCO-modified TFOs *via* SPAAC, forming the first example of click-derived monofunctional Pt-TFO hybrids, without need for additional purification steps.

The ability of the hybrids to form suitable triplexes was characterised using PAGE and fluorescence melting analyses, showing target-specific triplex formation, with melting temperatures exceeding 50°C. The hybrids exhibited efficient and sequence-specific adduct formation activity with the target strand of the *EGFR* duplex, consistent with the expected reactivity of monofunctional Pt(II) centres. Notably, the hybrids containing propyl-DPA displayed slightly improved triplex formation compared to the benzyl-DPA analogues, suggesting a beneficial balance between flexibility and intercalative interaction. Denaturing PAGE experiment with fluorescently trackable strands on the duplex confirmed irreversible, covalent adduct formation with the target strand specifically. Enzymatic assays were carried out and showed inhibition of polymerase activity, highlighting the potential of these conjugates as site-specific gene silencing agents.

The next stage of the project focused on developing TFO hybrids capable of target-specific reductant-independent, or self-activated, oxidative DNA cleavage. A novel azide-functionalised prodigiosin (PD) analogue was synthesised and conjugated to the *EGFR*-targeted TFOs *via* SPAAC. The resulting PD-TFO hybrids aimed to combine triplex-forming capability of TFO scaffolds with copper-mediated redox activity of PD derivatives. Cleavage experiments showed a remarkable self-activation behaviour. In contrast to previously reported, phenanthroline-based, Cu-AMN-TFO hybrids, the PD-TFO conjugates induced copper-mediated targeted DNA cleavage in the absence of exogenous reducing agents such as sodium-*L*-ascorbate (Na-*L*-asc). The conjugates displayed target selectivity, with no observable *off*-target cleavage, and maintained efficient triplex formation at physiological temperature, with melting temperature above 50 °C. Collectively, these

findings establish the PD-TFO hybrids as a new class of self-activated AMNs, combining sequence-specific recognition with oxidative cleavage activity.

The final part of this work explored the use of SPAAC for rapidly screening azide-modified ligands for sequence-specific DNA cleavage once tethered to TFOs. The method exploited the rapidity, efficiency and orthogonality of the SPAAC reaction to generate AMN-TFOs, using the target DNA as a template. Upon introduction of copper and Na-*L*-asc, the hybrids were examined for their target-specific cleavage activity without isolation of the generated hybrids. Proof-of-concept experiment demonstrated that this method could reproduce and extend the results obtained for the PD-TFO hybrids, while enabling rapid comparison with other reported AMN ligands. Simple PAGE analysis of the samples enabled the quantification of targeted and random cleavage, enabling ranking of ligands. The self-assembly strategy therefore represents a powerful and flexible framework for the future design and optimisation of gene-targeted metal therapies.

The work presented in this thesis establishes a robust foundation for the rational development of gene-targeted metal therapeutics through modular TFO conjugation. Several directions emerge for future exploration, including the use of different DNA backbones on the TFO for enhanced cellular uptake and resistance to nucleases and to self-degradation. Together with the self-activation property of PD-TFO hybrids, and enzymatic inhibition of the monofunctional Pt(II)-TFO conjugates, it would offer a unique opportunity to achieve gene-silencing in the intracellular environment, without external stimuli. The PD-TFO hybrids would also benefit from being characterised further, using optimised qPCR quantification or sequencing of damaged duplexes to identify the precise mechanisms involved.

Overall, this thesis demonstrated the potential of biorthogonal chemistry for the labelling of TFOs with diverse metal complexes. Through the successful combination of precise nucleic acid recognition, efficient SPAAC conjugation and controlled metal reactivity, it advances the field of targeted metal-based therapies toward sequence-specific DNA modification for gene silencing. The methodologies and design principles established here can serve as a versatile foundation for future development in triplex-mediated targeted therapeutic design.

Chapter VIII

Appendices

Appendix A Development and Optimisation of TFO Probes Compatible with Click Chemistry for *EGFR*-targeted Interactions (Chapter III)

Appendix B Development of Monofunctional Azide-modified Platinum(II) Complexes and SPAAC-labelling of TFO Probes for *EGFR*-specific Coordination Activity (Chapter IV)

Appendix C Prodigiosin Modified Triplex-Forming Oligonucleotide Hybrids Enable Self-Activated DNA Cleavage (Chapter V)

Appendix D Self-assembly of AMN-TFO Hybrids Enables Facile Target-specific DNA Damage Screening (Chapter VI)

April 2026

Appendix A

A.1 Spectroscopic characterisation

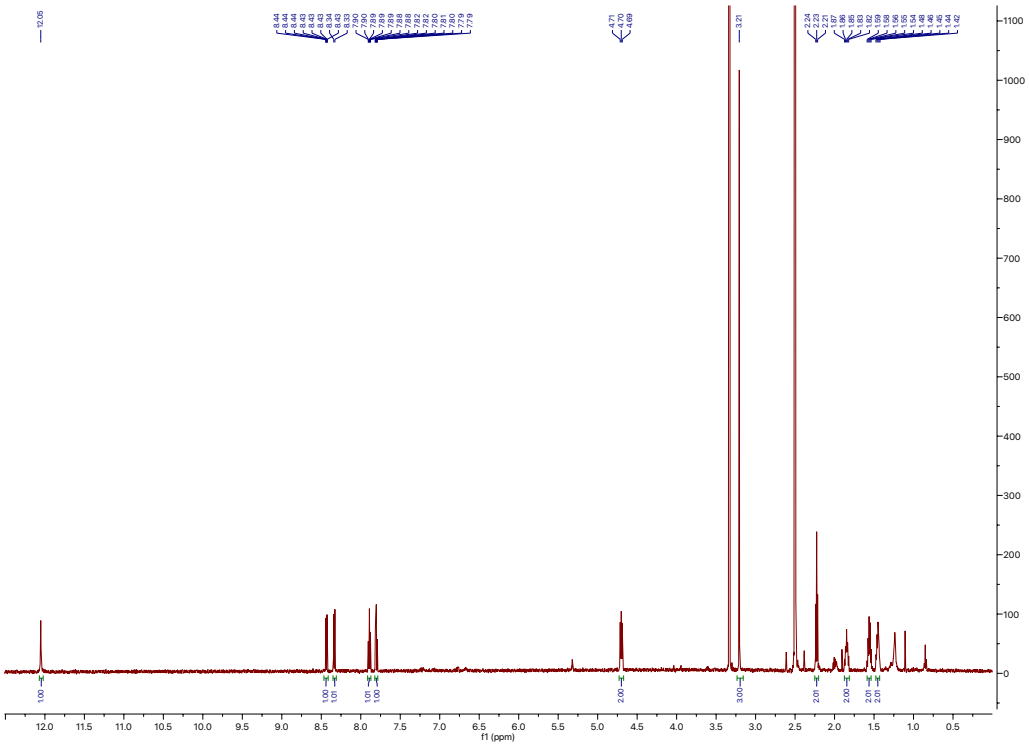


Figure A.1.1 ^{1}H-NMR of 3-(5-carboxypentyl)-2-methylbenzo[d]thiazol-3-ium bromide.

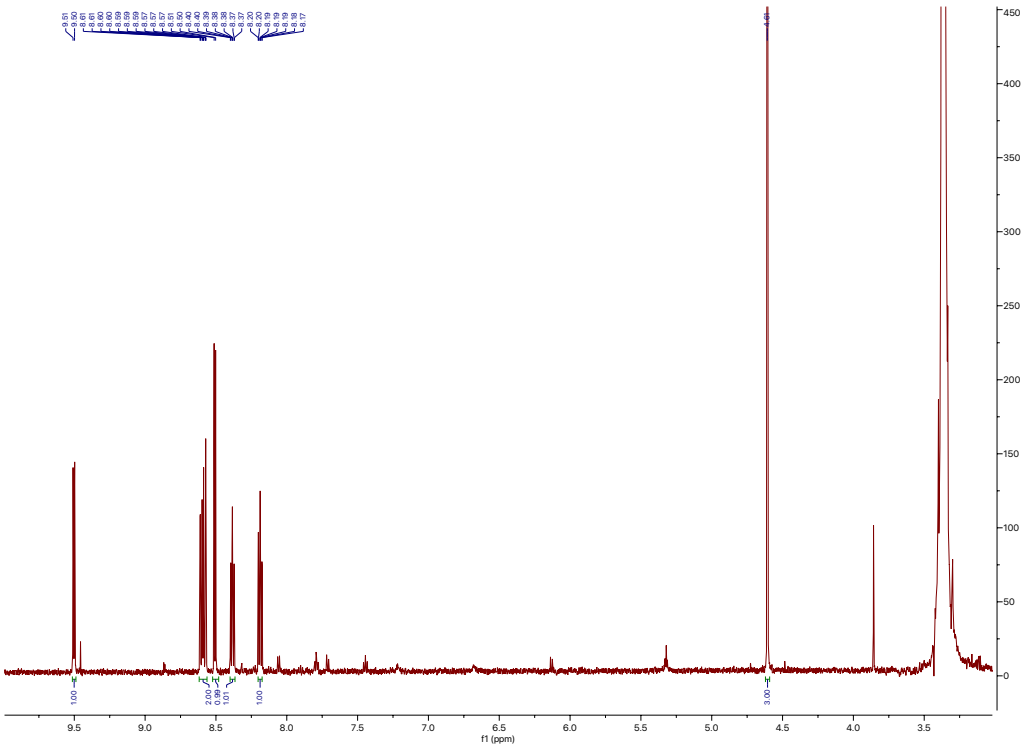


Figure A.1.2 ^{1}H-NMR of 4-chloro-1-methylquinolin-1-ium trifluoromethanesulfonate.

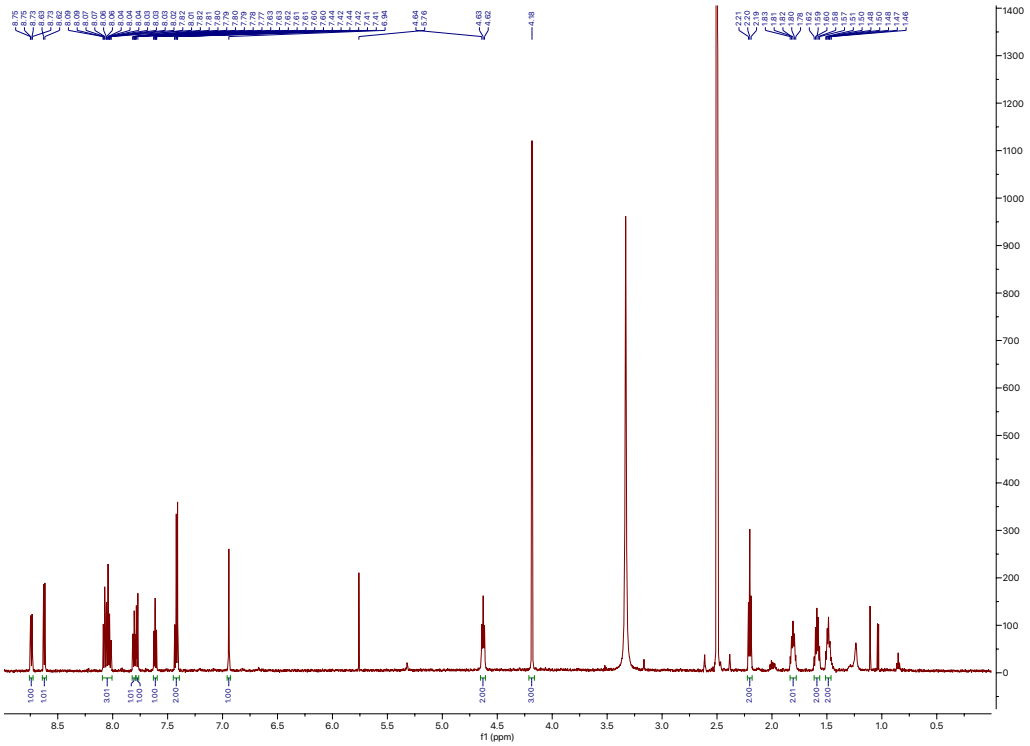


Figure A.1.3 ^{1}H-NMR of (E)-3-(5-carboxypentyl)-2-((1-methylquinolin-4(1H)-ylidene)methyl)benzo[d]thiazol-3-ium hexafluorophosphate (TO_{B6}).

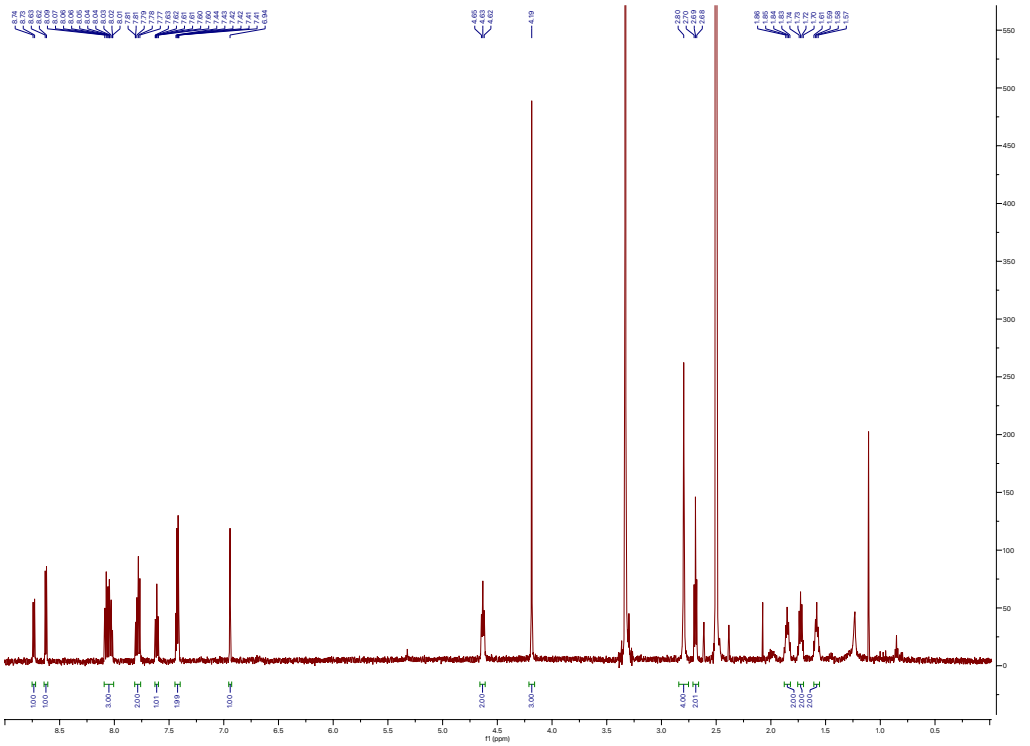


Figure A.1.4.1 ^{1}H-NMR of (E)-3-(6-((2,5-dioxopyrrolidin-1-yl)oxy)-6-oxohexyl)-2-((1-methylquinolin-4(1H)-ylidene)methyl)benzo[d]thiazol-3-ium hexafluorophosphate (NHS ester TO_{B6}).

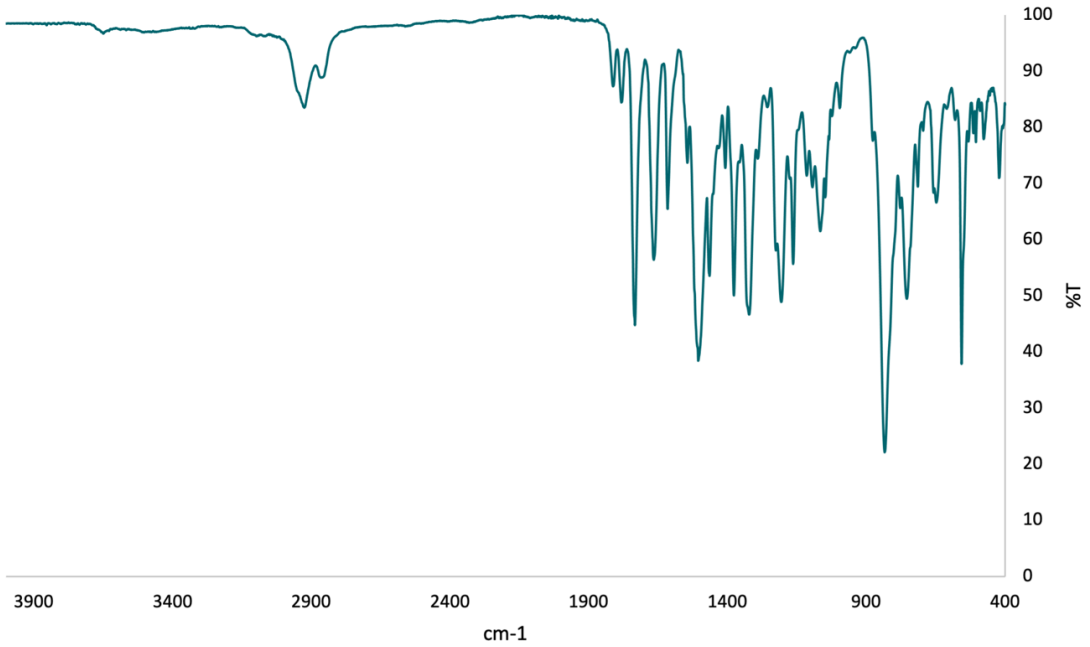


Figure A.1.4.2 IR spectrum of (E)-3-(6-((2,5-dioxopyrrolidin-1-yl)oxy)-6-oxohexyl)-2-((1-methylquinolin-4(1H)-ylidene)methyl)benzo[d]thiazol-3-ium hexafluorophosphate (NHS ester TO_{B6}).

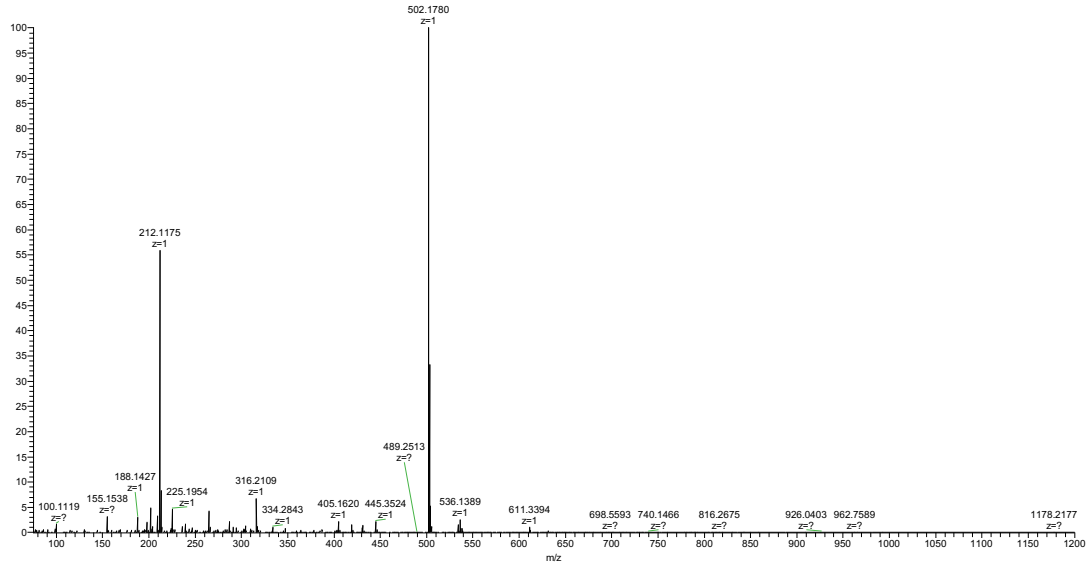


Figure A.1.4.3 ESI-MS of (E)-3-(6-((2,5-dioxopyrrolidin-1-yl)oxy)-6-oxohexyl)-2-((1-methylquinolin-4(1H)-ylidene)methyl)benzo[d]thiazol-3-ium hexafluorophosphate (NHS ester TO_{B6}).

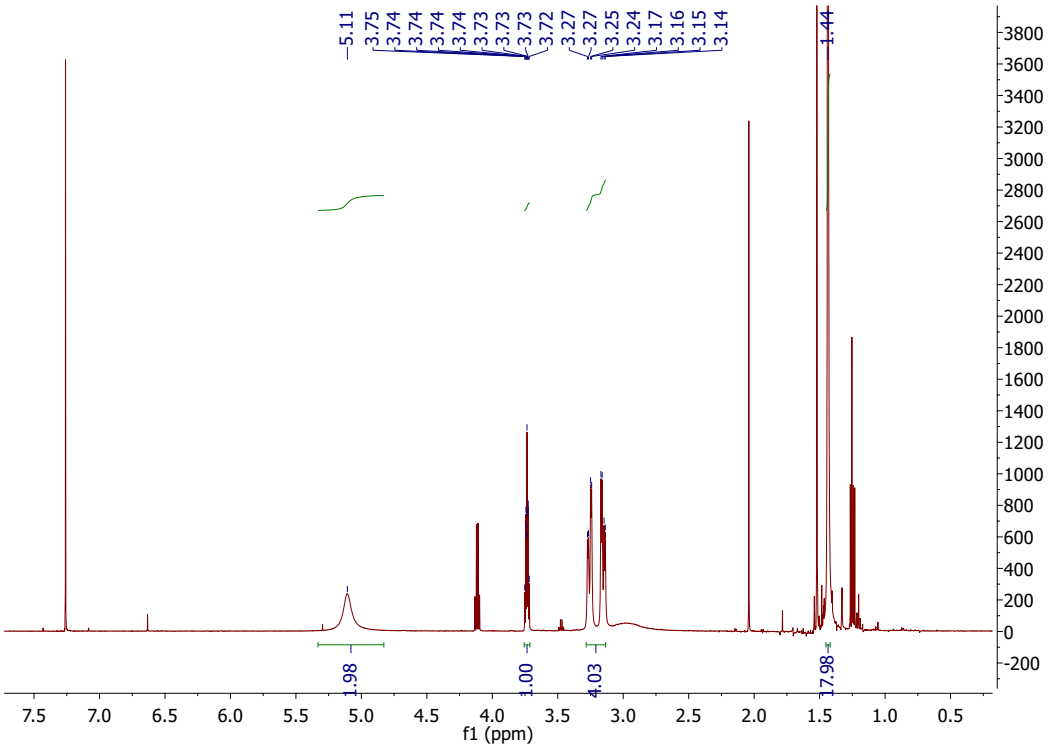


Figure A.1.5 ^{1}H-NMR of Di-tert-boc-2-hydroxy-1,3-diaminopropane.

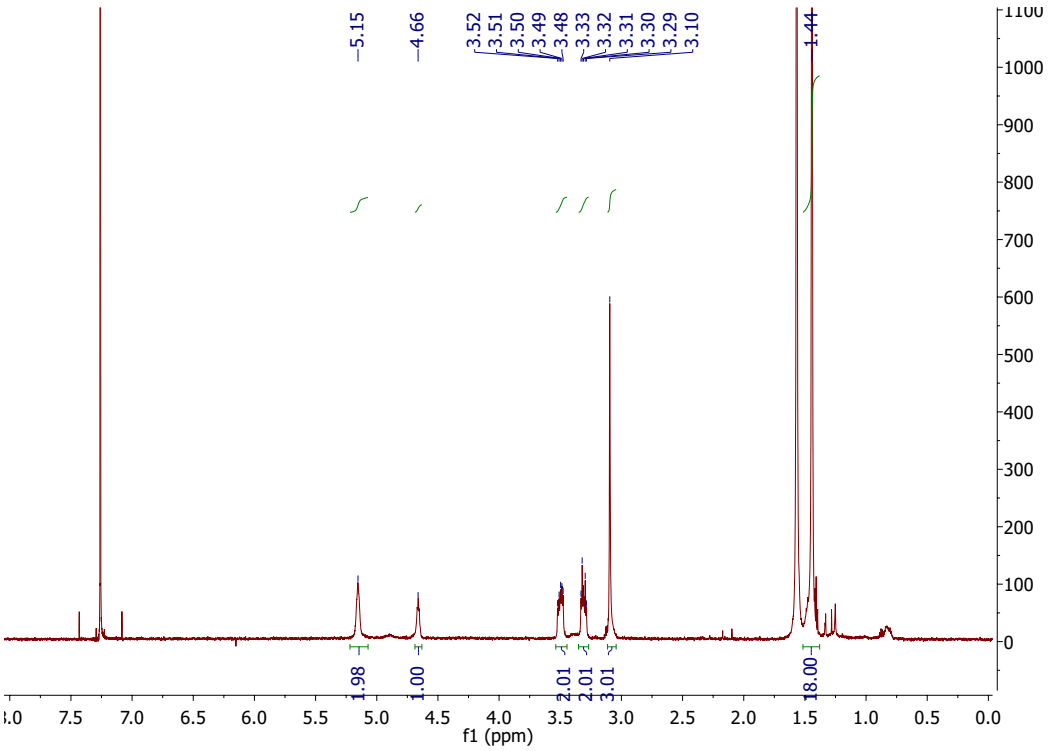


Figure A.1.6 ^{1}H-NMR of Di-tert-boc-2-methanesulfonyl-1,3-diaminopropane.

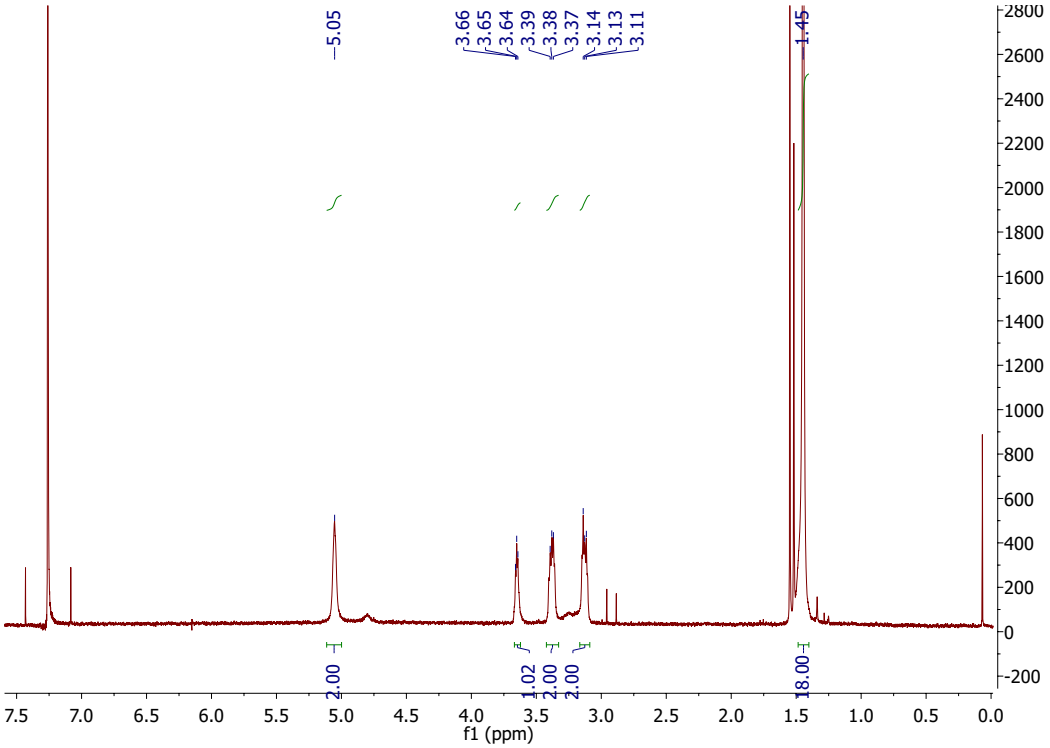


Figure A.1.7 [1]H-NMR of Di-tert-boc-2-azido-1,3-diaminopropane.

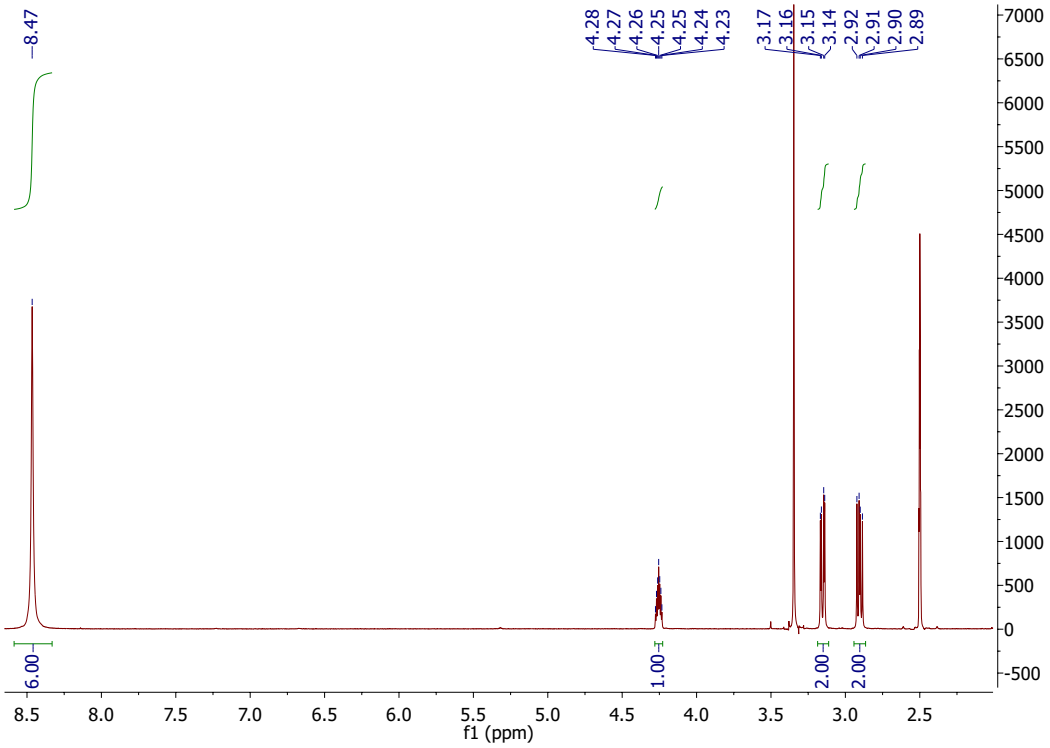


Figure A.1.8.1 [1]H-NMR of 2-azidopropane-1,3-diamine dihydrochloride.

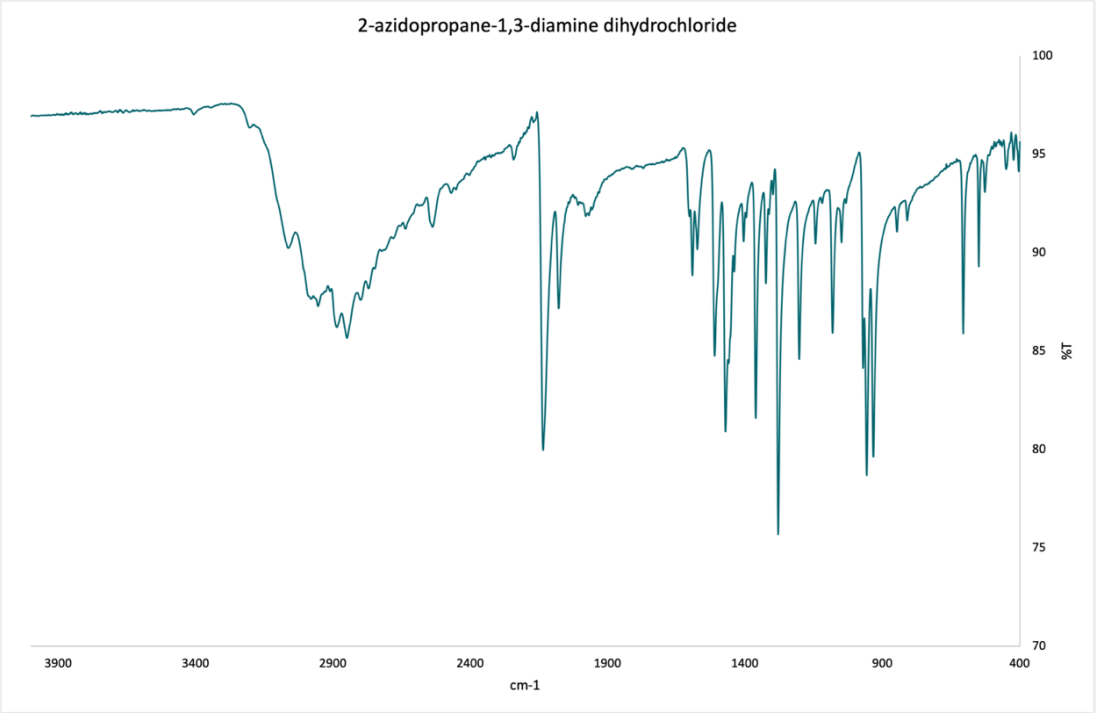


Figure A.1.8.2 IR spectrum of 2-azidopropane-1,3-diamine dihydrochloride.

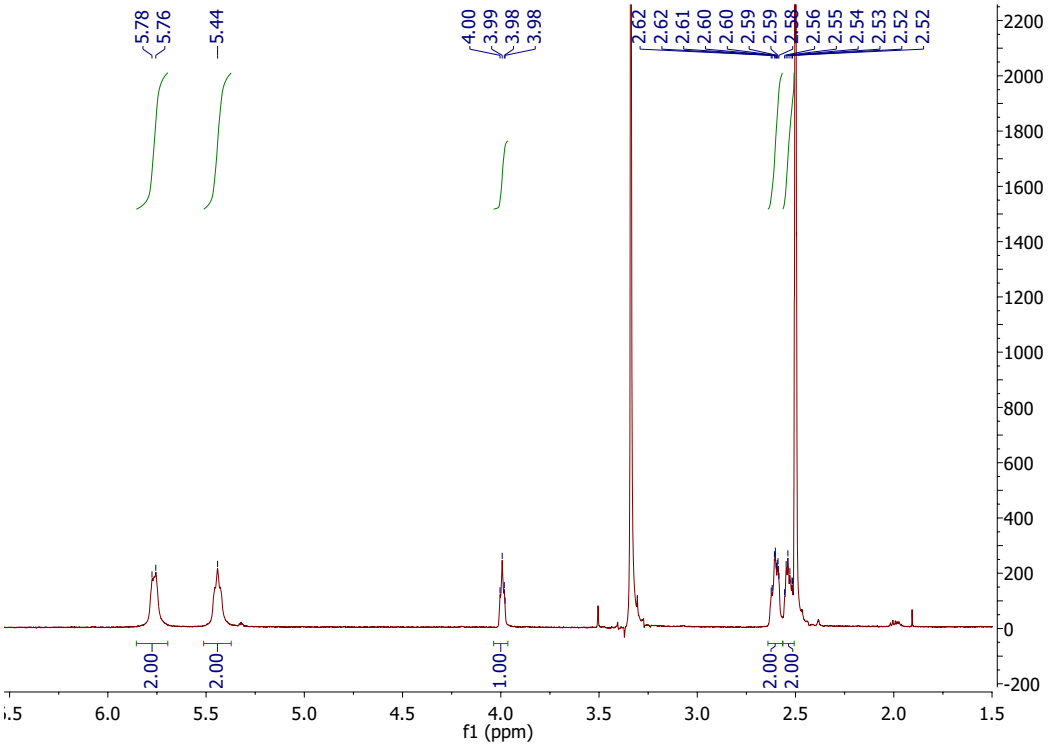


Figure A.1.9.1 ^{1}H-NMR of *cis*-[Pt(2-azidopropane-1,3-diamine)(Oxalate)] (Pt-N_3-Oxali).

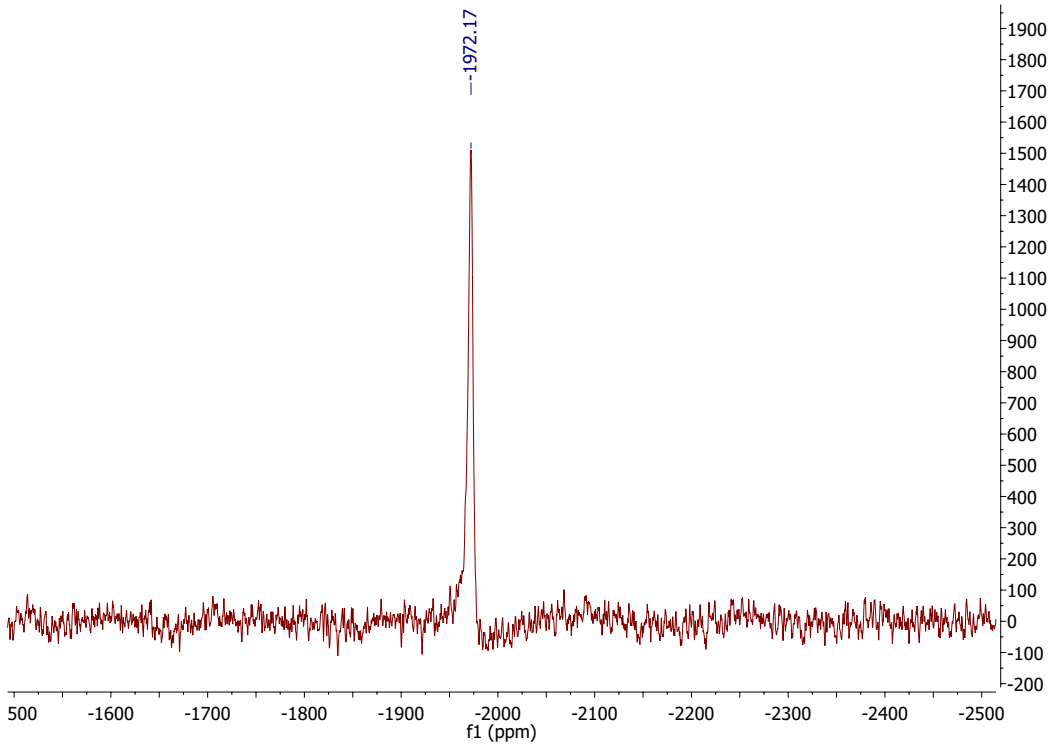


Figure A.1.9.2 ^{195}Pt-NMR of *cis*-[Pt(2-azidopropane-1,3-diamine)(Oxalate)] (Pt-N_3-Oxali) with polynomial baseline correction.

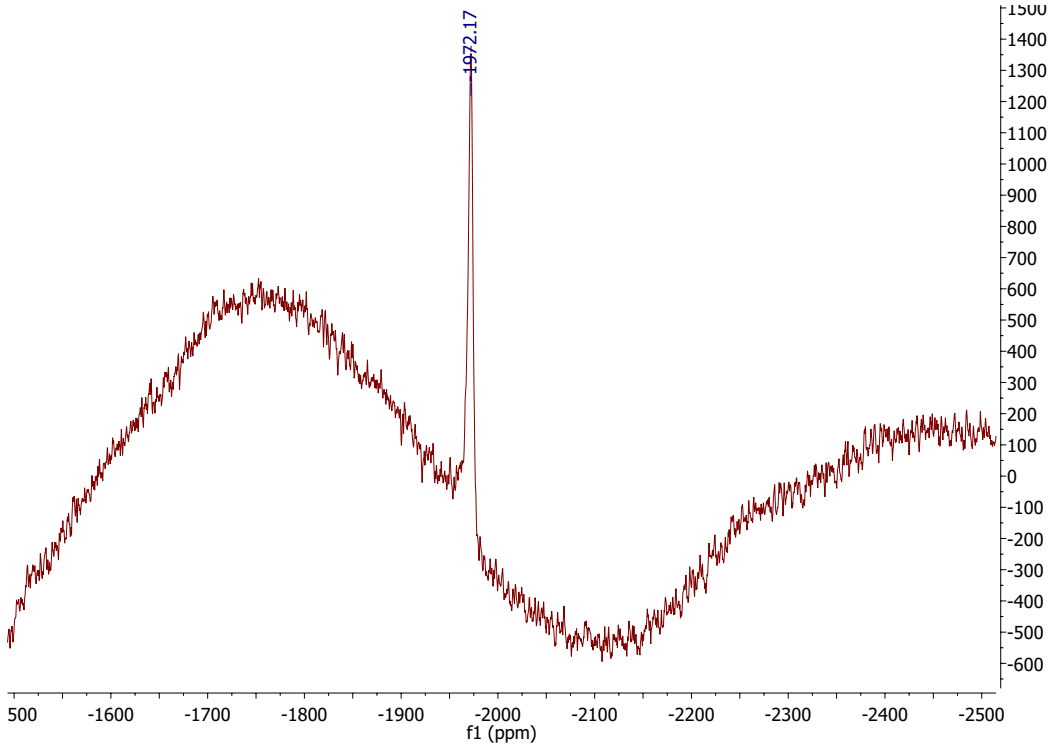


Figure A.1.9.3 ^{195}Pt-NMR of *cis*-[Pt(2-azidopropane-1,3-diamine)(Oxalate)] (Pt-N_3-Oxali).

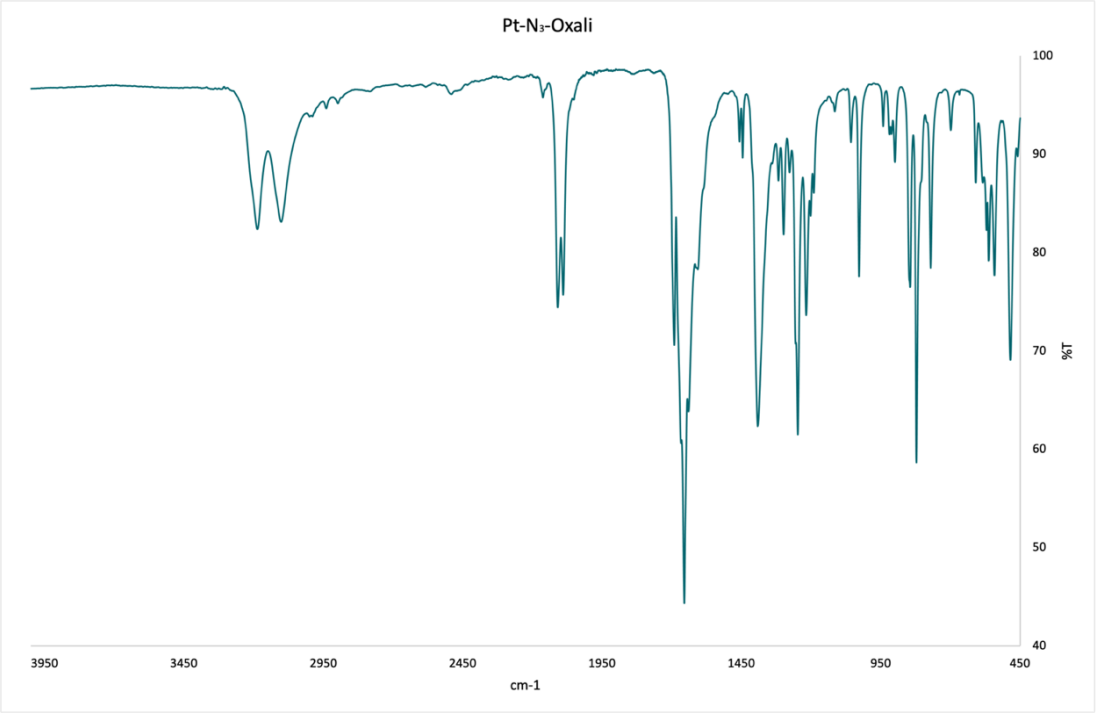


Figure A.1.9.4 IR spectrum of *cis*-[Pt(2-azidopropane-1,3-diamine)(Oxalate)] (Pt-N_3-Oxali).

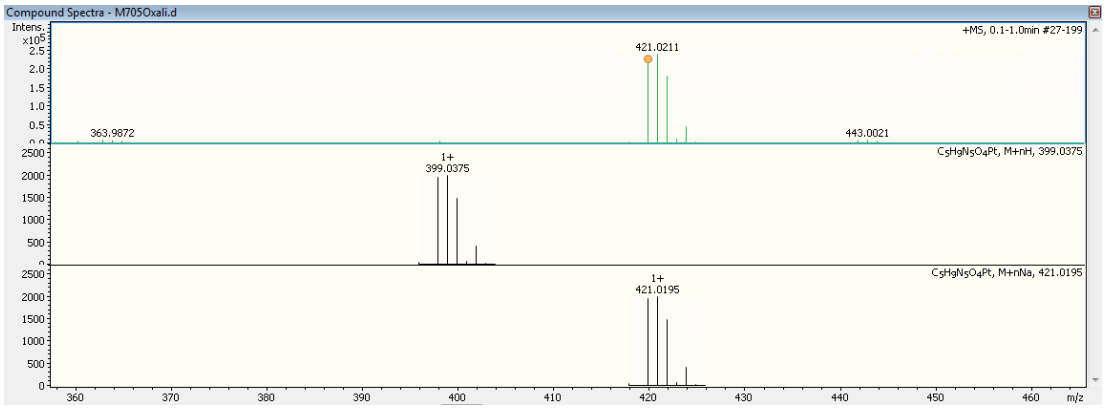


Figure A.1.9.5 ESI-MS of *cis*-[Pt(2-azidopropane-1,3-diamine)(Oxalate)] (Pt-N_3-Oxali).

A.2 HPLC trace and MS chromatogram of Pt-Oxali-TFO hybrids

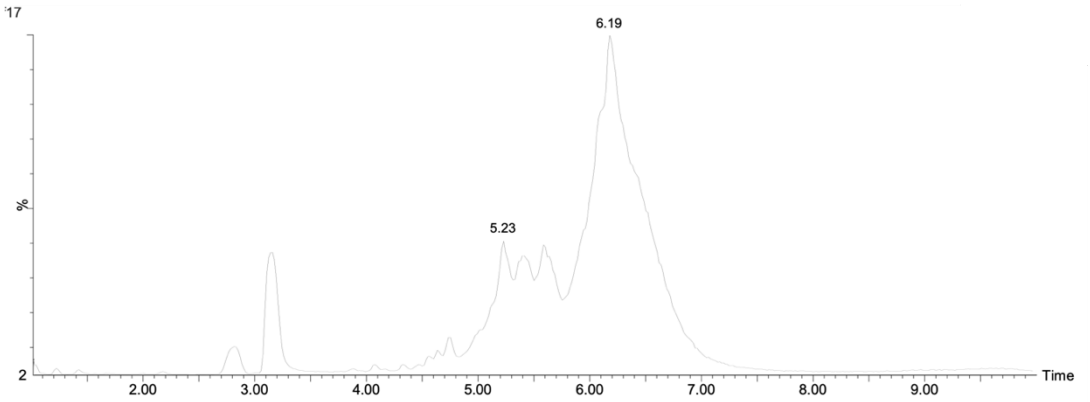


Figure A.2.1 HPLC trace of C1-O.

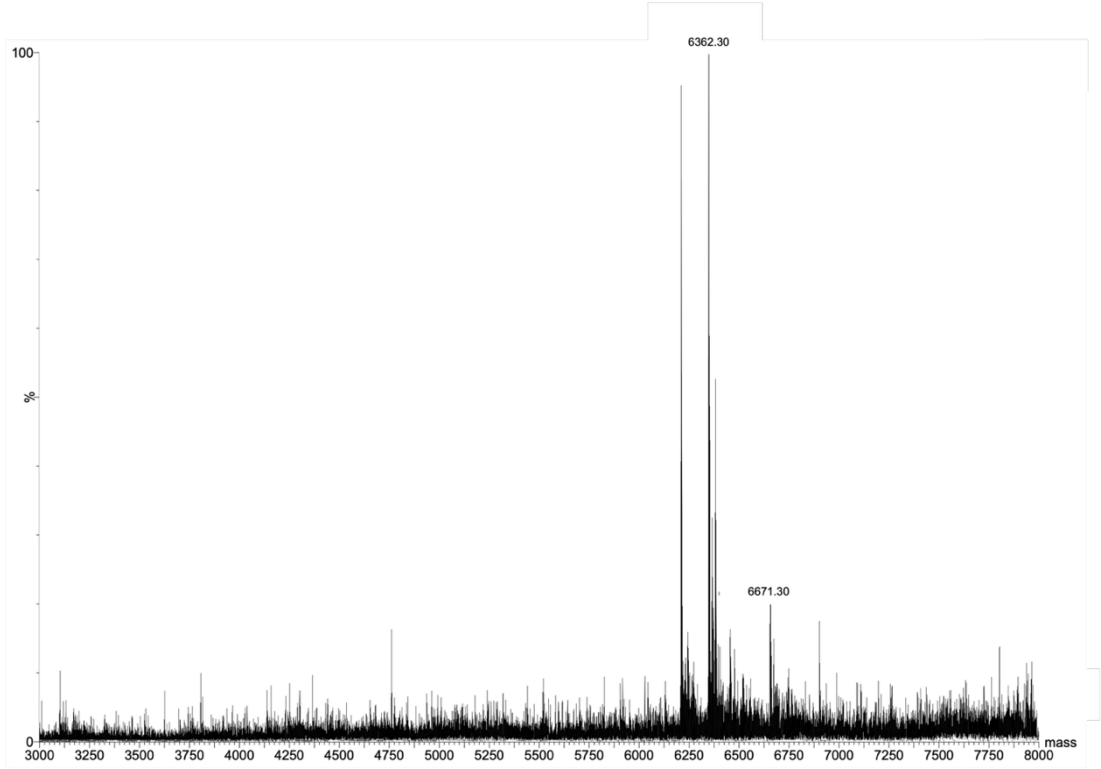


Figure A.2.2 MS chromatogram of C1-O.

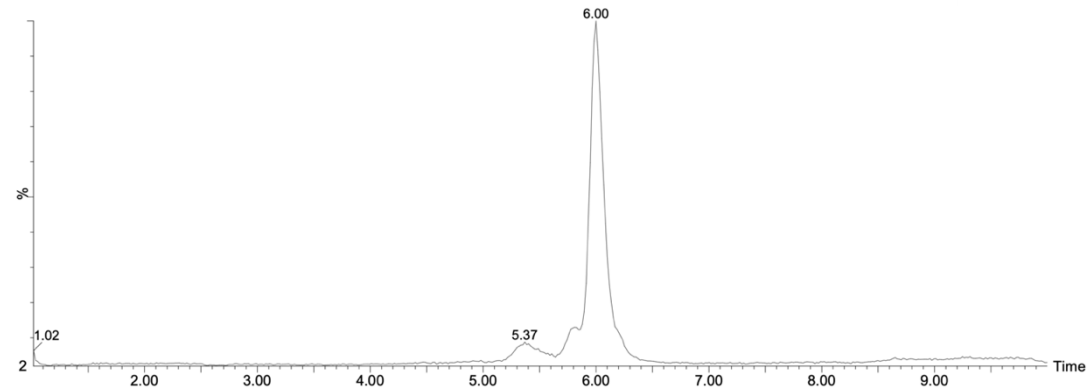


Figure A.2.3 HPLC trace of C2-O.

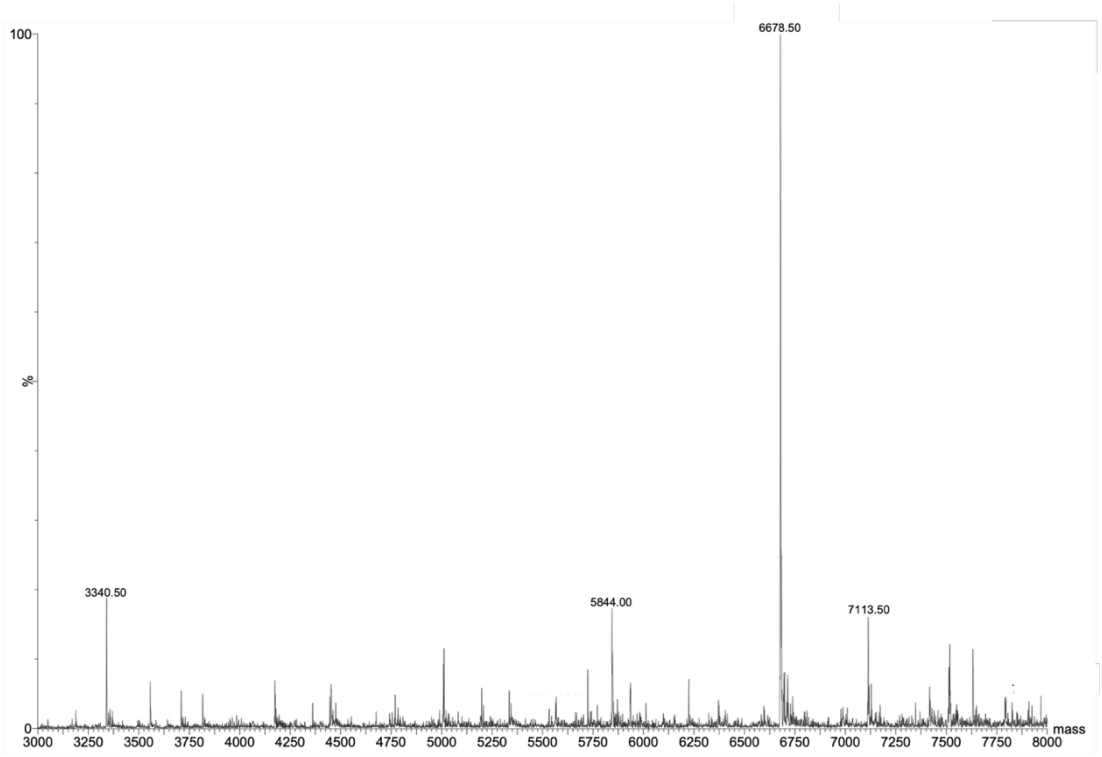


Figure A.2.4 MS chromatogram of C2-O.

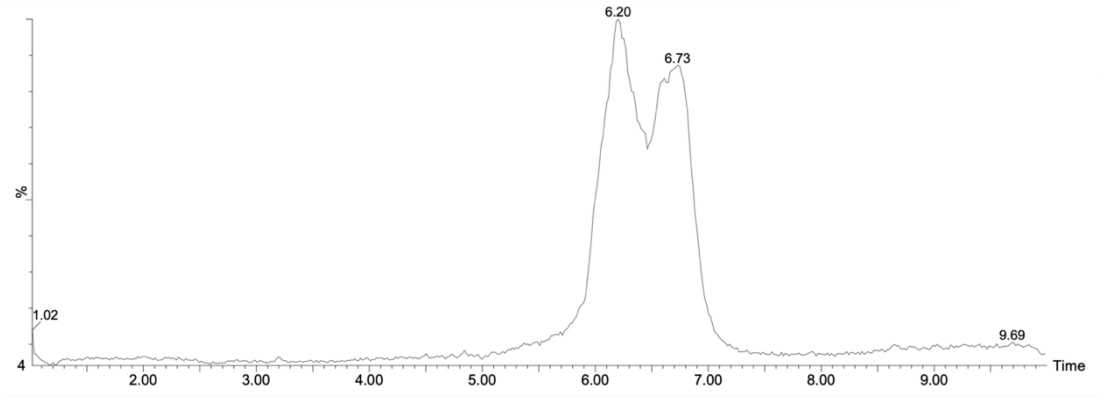


Figure A.2.5 HPLC trace of C3-O.

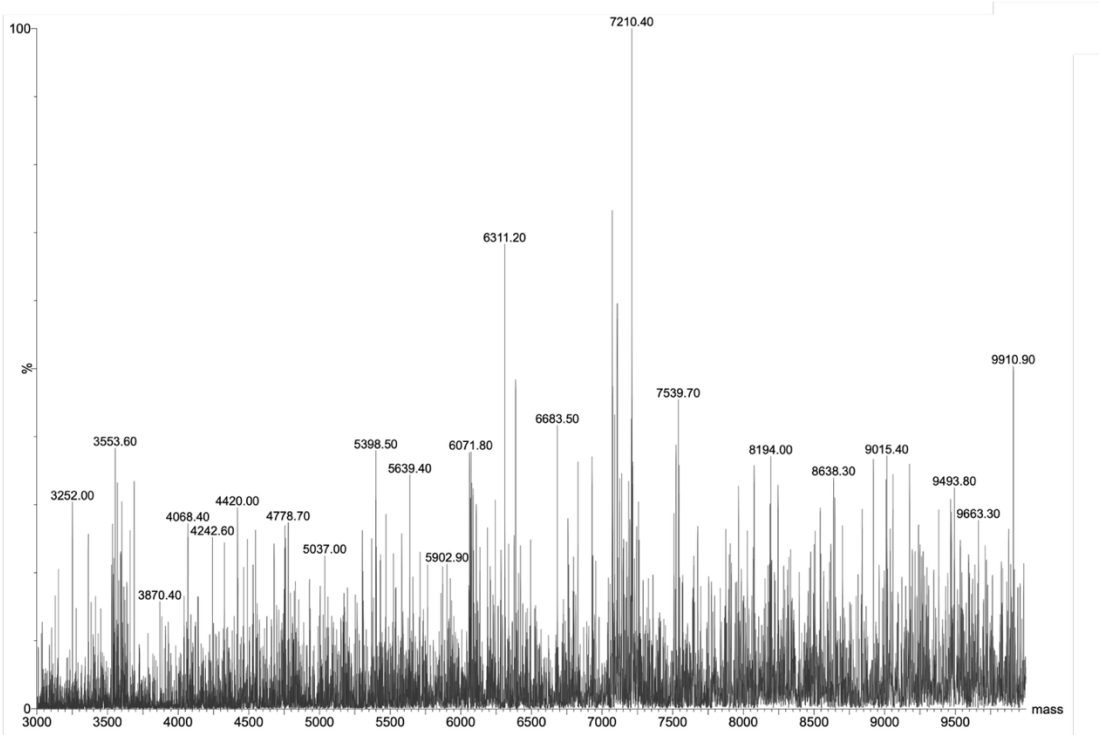


Figure A.2.6 MS chromatogram of C3-O.

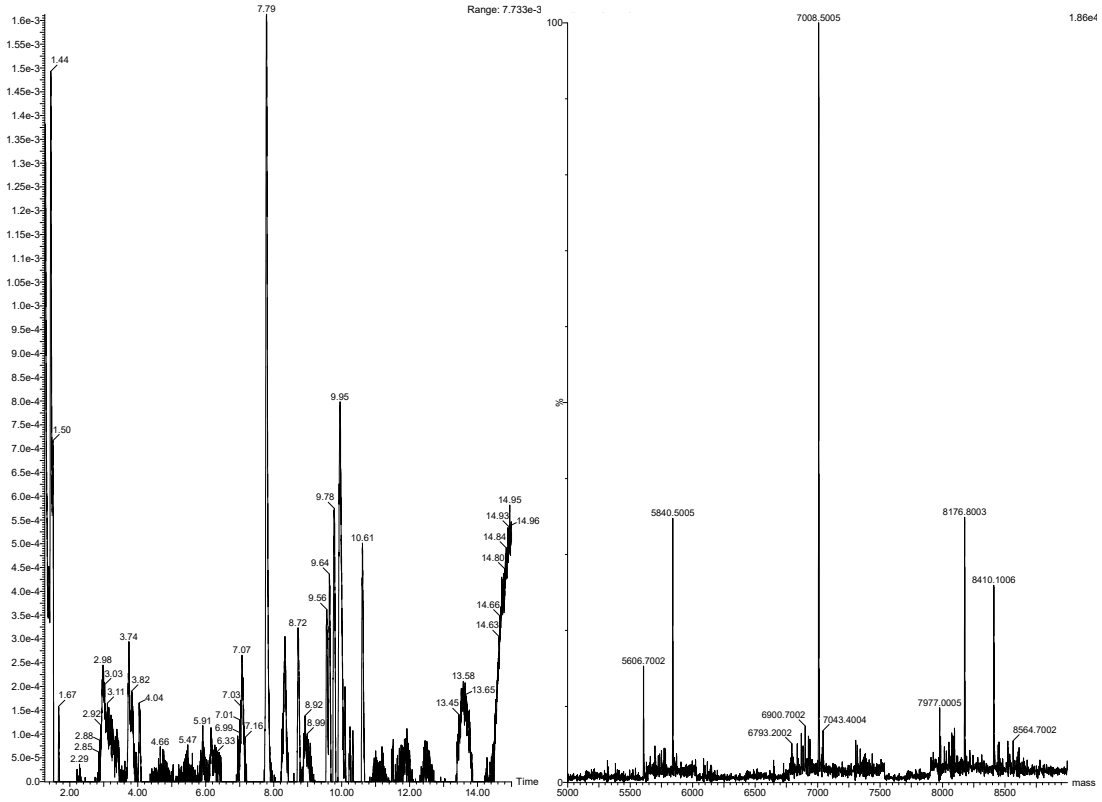


Figure A.2.7 HPLC trace and MS chromatogram of S1-O.

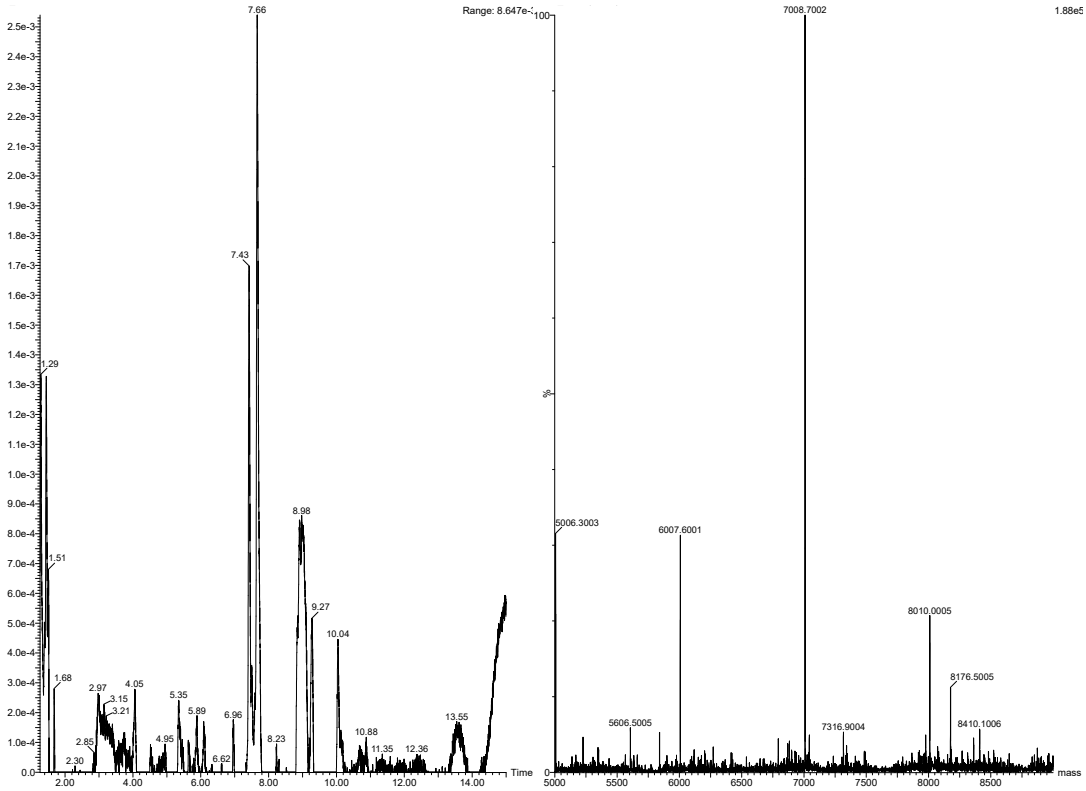


Figure A.2.8 HPLC trace and MS chromatogram of S2-O.

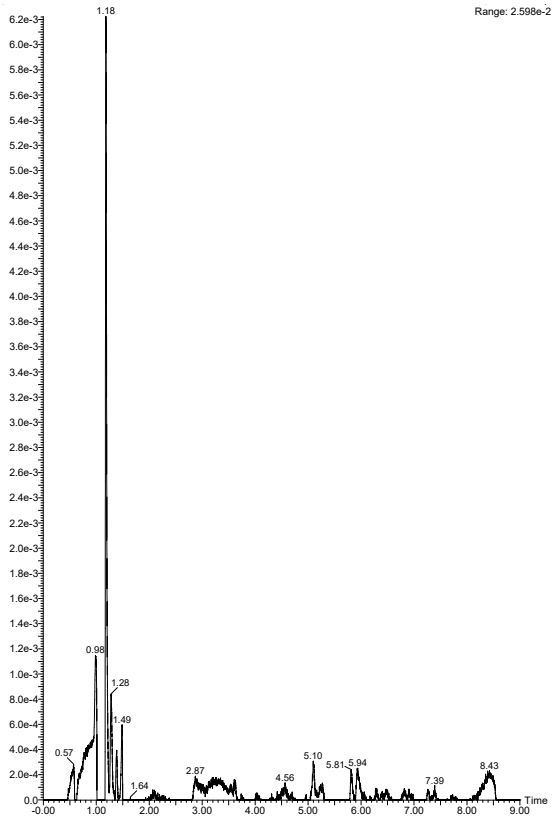


Figure A.2.9 HPLC trace of S3-O.

Appendix B

B.1 Spectroscopic characterisation

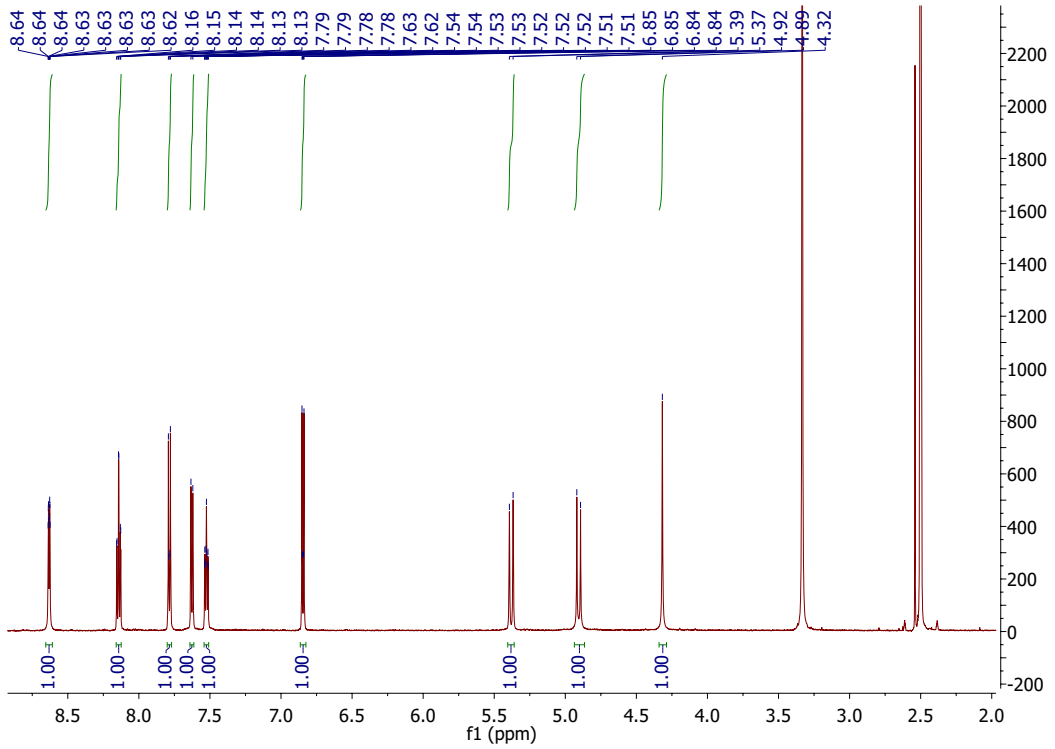


Figure B.1.1: ^{1}H-NMR of platinum (II) (N-(4-azidobenzyl)-1-(pyridin-2-yl)-N-(pyridin-2-ylmethyl)methanamine) chloride (Pt-N_3-benzyl-DPA) in DMSO-d_6.

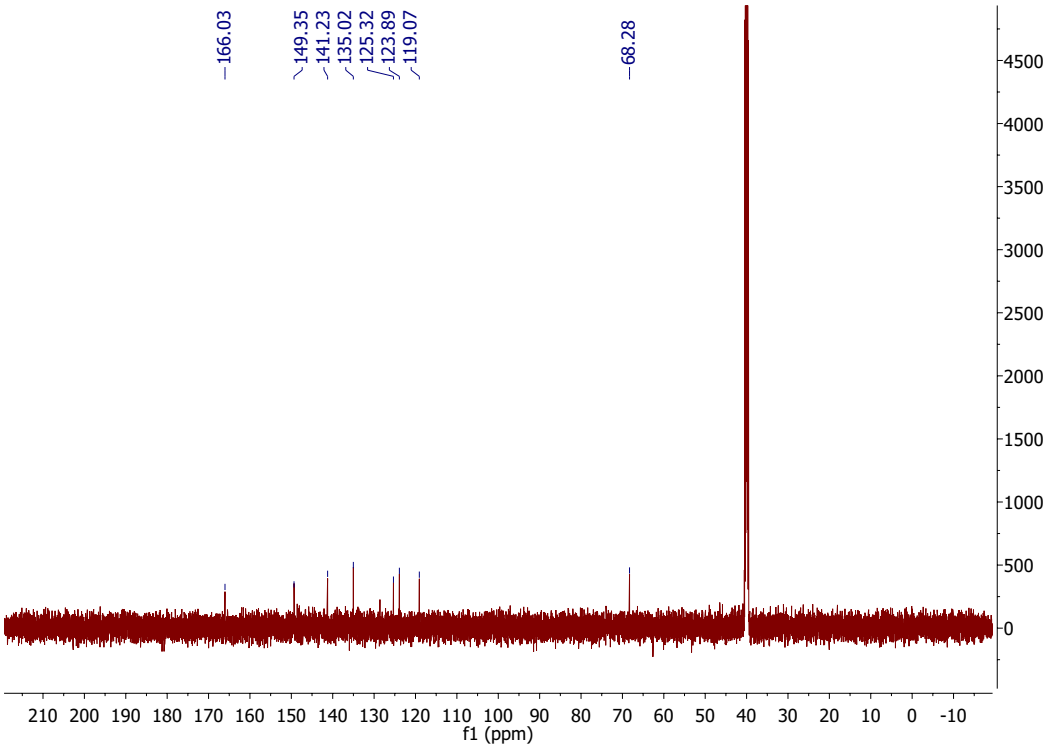


Figure B.1.2: ^{13}C-NMR of platinum(II) (N-(4-azidobenzyl)-1-(pyridin-2-yl)-N-(pyridin-2-ylmethyl)methanamine) chloride (Pt-N_3-benzyl) in DMSO-d_6.

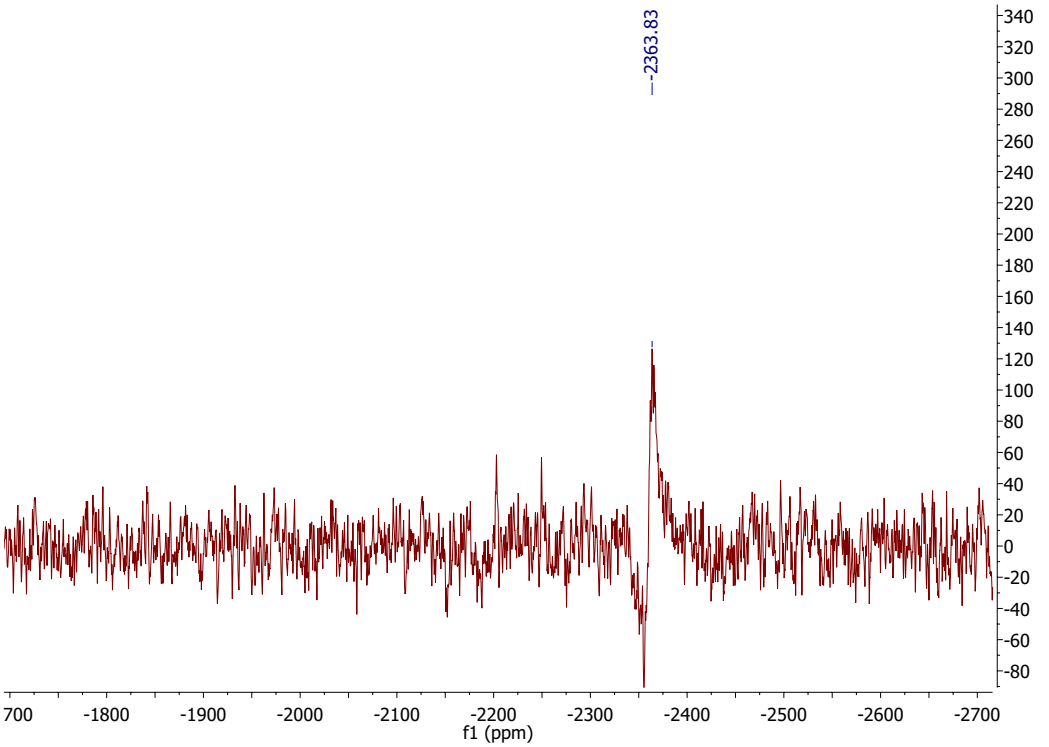


Figure B.1.3: ^{195}Pt-NMR of platinum(II) (N-(4-azidobenzyl)-1-(pyridin-2-yl)-N-(pyridin-2-ylmethyl)methanamine) chloride (Pt-N_3-benzyl) in DMSO-d_6.

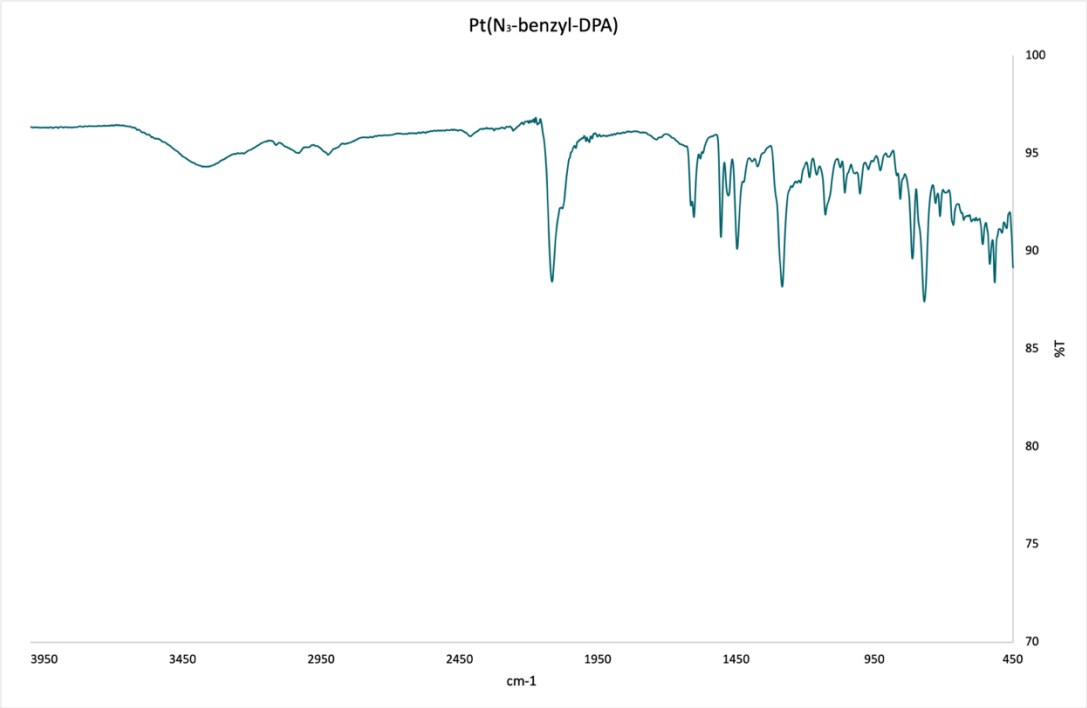


Figure B.1.4: IR spectrum of platinum(II) (N-(4-azidobenzyl)-1-(pyridin-2-yl)-N-(pyridin-2-ylmethyl)methanamine) chloride (Pt-N_3-benzyl).

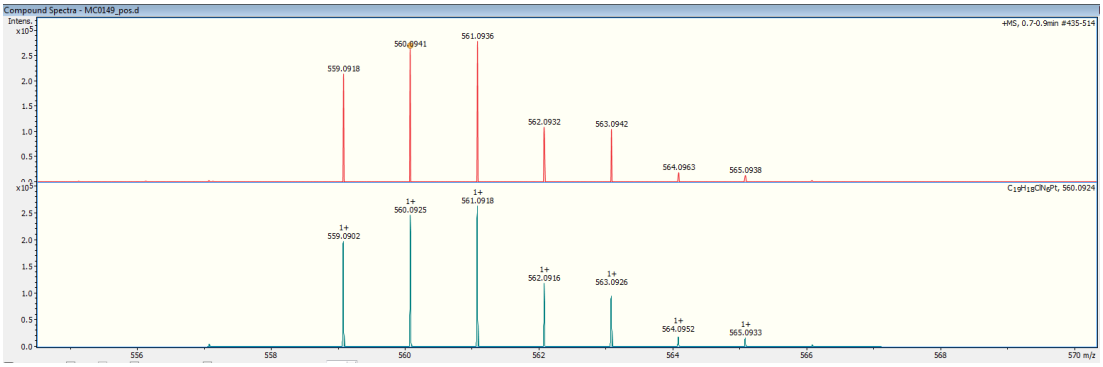


Figure B.1.5: ESI-MS of platinum(II) (N-(4-azidobenzyl)-1-(pyridin-2-yl)-N-(pyridin-2-ylmethyl)methanamine) chloride (Pt-N_3-benzyl).

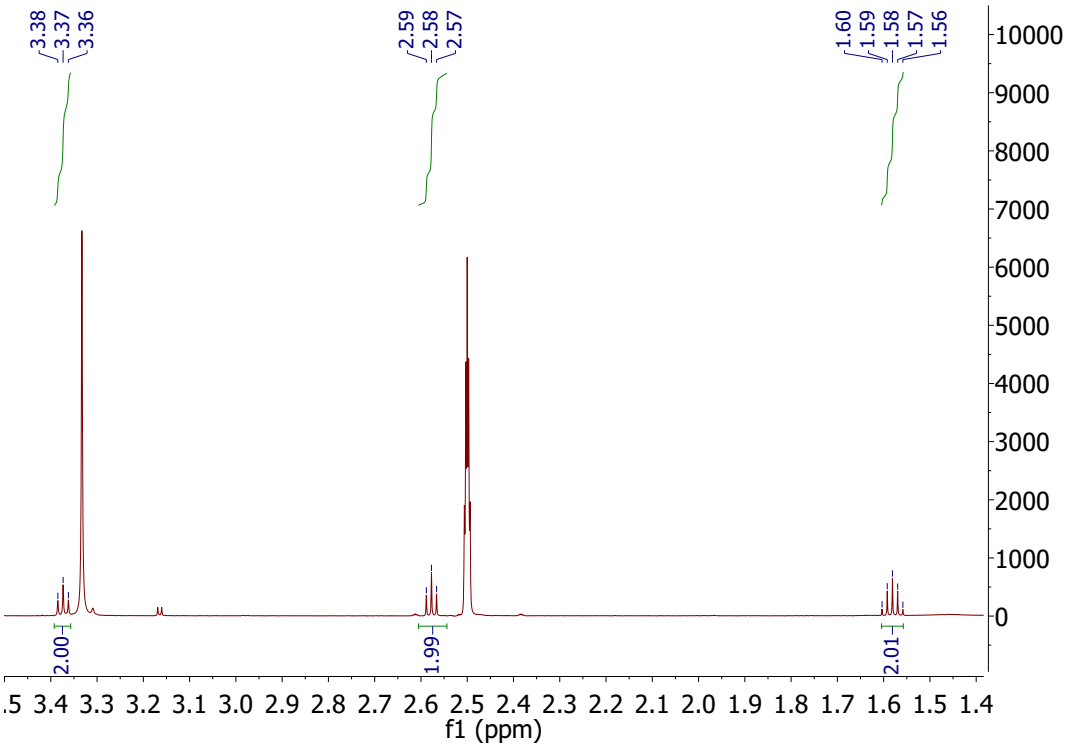


Figure B.1.6: ^{1}H-NMR of 3-azidopropyl-1-amine in DMSO-d_6.

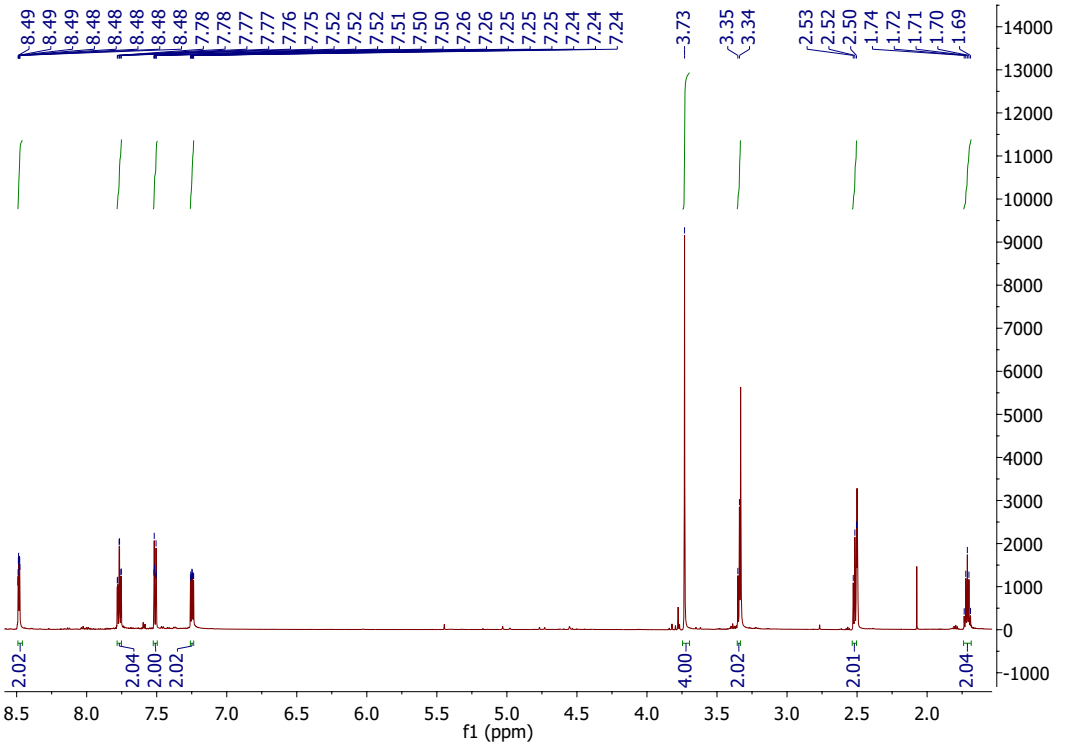


Figure B.1.7: ^{1}H-NMR of 3-azido-N,N-bis(pyridin-2-ylmethyl)propan-1-amine (N_3-propyl-DPA) in DMSO-d_6.

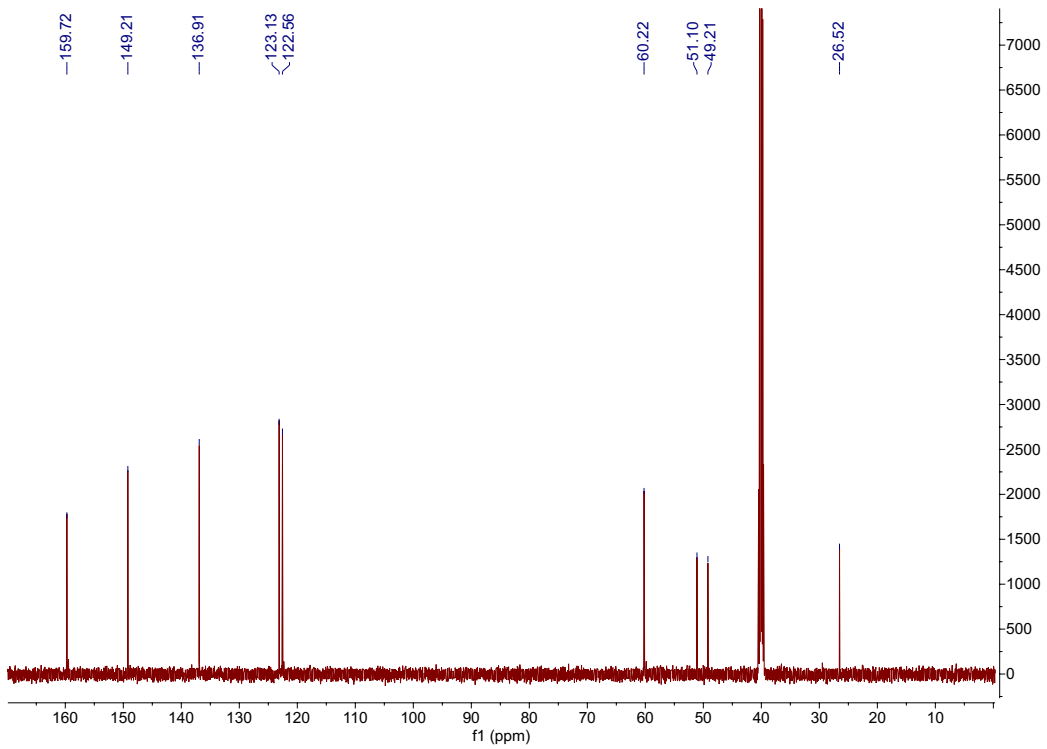


Figure B.1.8: ^{13}C-NMR of 3-azido-N,N-bis(pyridin-2-ylmethyl)propan-1-amine (N_3-propyl-DPA) in DMSO-d_6.

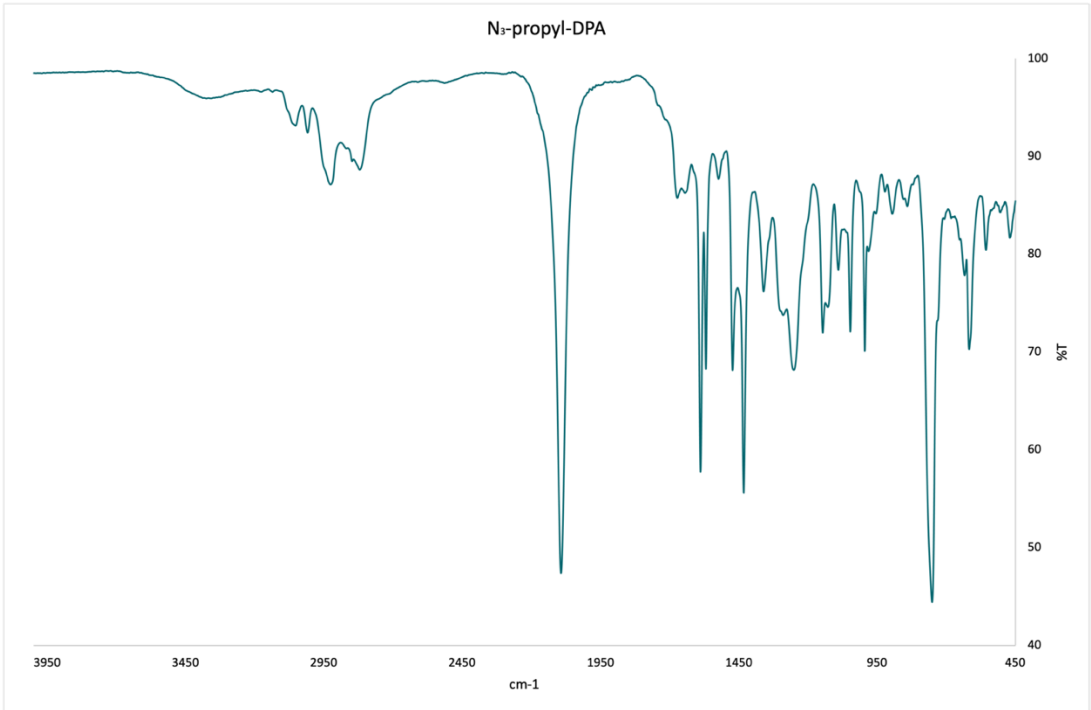


Figure B.1.9: IR spectrum of 3-azido-N,N-bis(pyridin-2-ylmethyl)propan-1-amine (N_3-propyl-DPA).

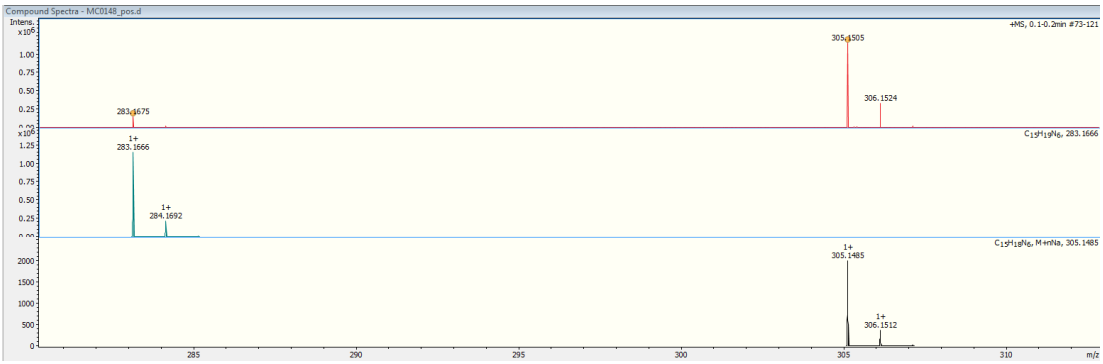


Figure B.1.10: ESI-MS of 3-azido-N,N-bis(pyridin-2-ylmethyl)propan-1-amine (N_3-propyl-DPA).

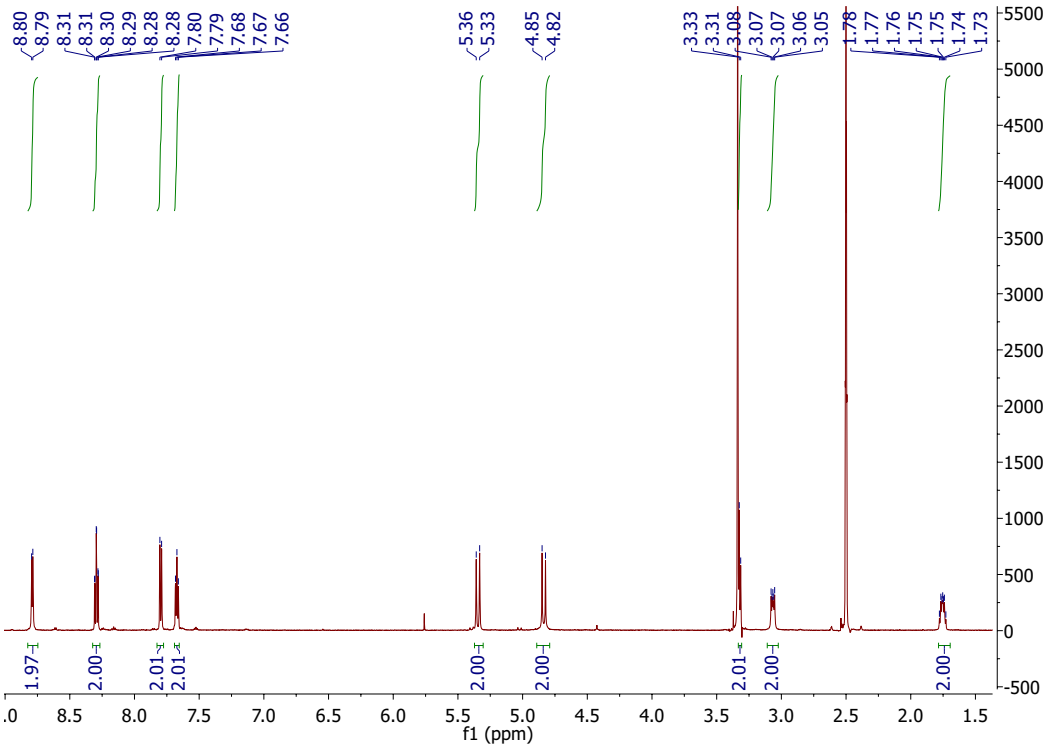


Figure B.1.11: ^{1}H-NMR of platinum (II) (3-azido-N,N-bis(pyridin-2-ylmethyl)propan-1-amine) chloride (Pt-N_3-propyl) in DMSO-d_6.

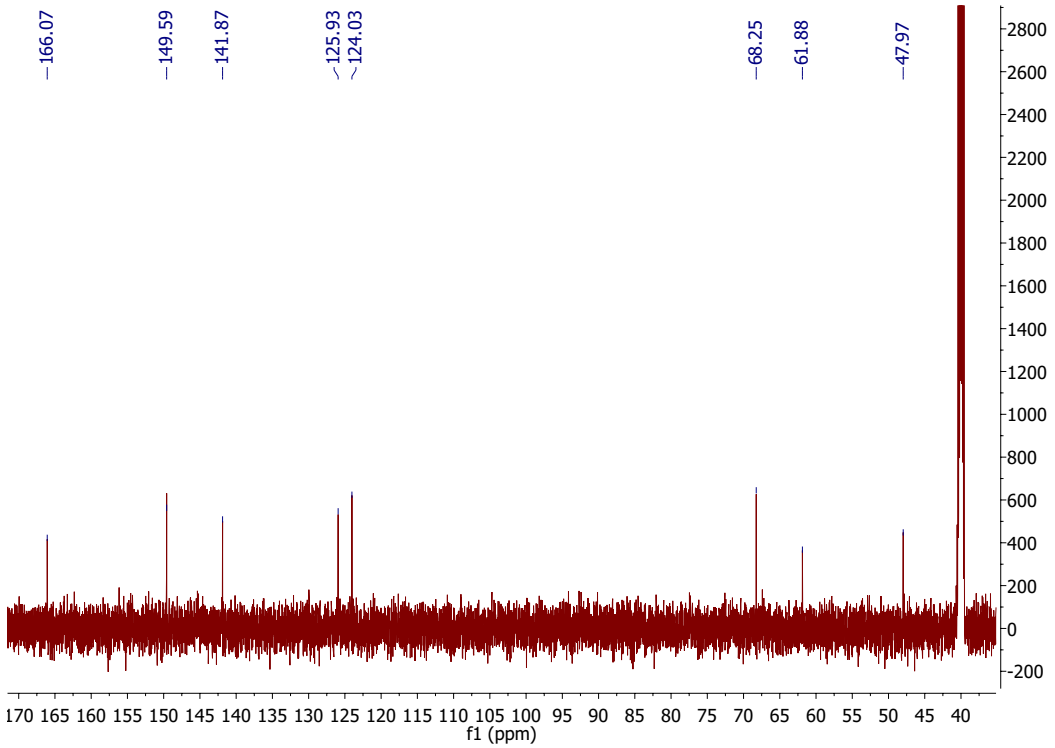


Figure B.1.12: ^{13}C-NMR of platinum(II) (3-azido-N,N-bis(pyridin-2-ylmethyl)propan-1-amine) chloride (Pt-N_3-propyl) in DMSO-d_6.

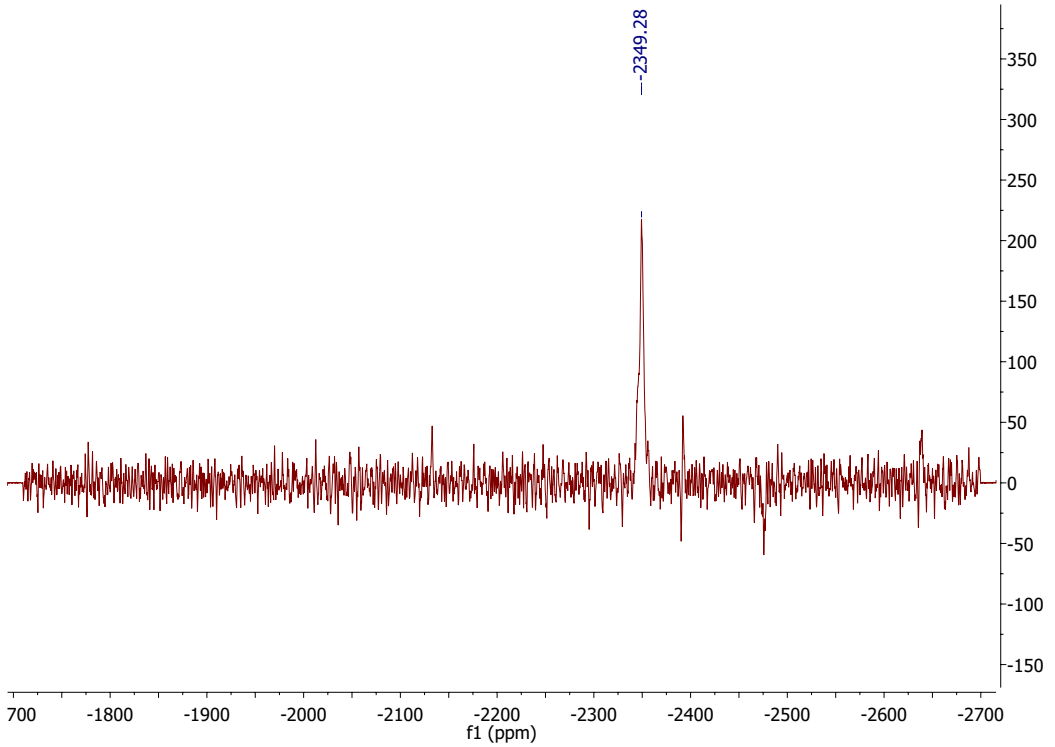


Figure B.1.13: ^{195}Pt-NMR of platinum(II) (3-azido-N,N-bis(pyridin-2-ylmethyl)propan-1-amine) chloride (Pt-N_3-propyl) in DMSO-d_6.

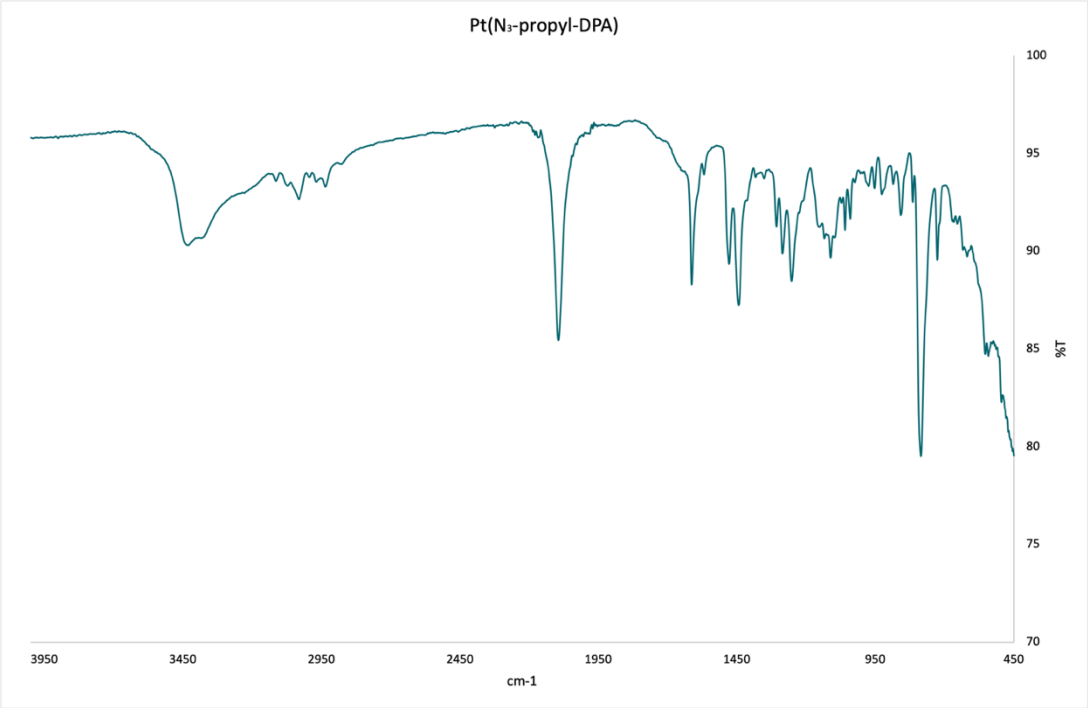


Figure B.1.14: IR spectrum of platinum(II) (3-azido-N,N-bis(pyridin-2-ylmethyl)propan-1-amine) chloride (Pt-N_3-propyl).

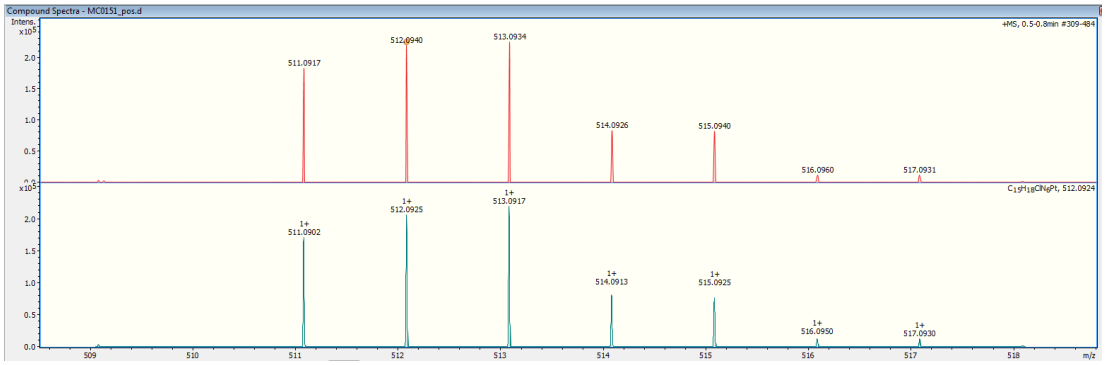


Figure B.1.15: ESI-MS of platinum(II) (3-azido-N,N-bis(pyridin-2-ylmethyl)propan-1-amine) chloride (Pt-N_3-propyl).

B.2 HPLC trace and MS chromatogram of Pt-TFO hybrids

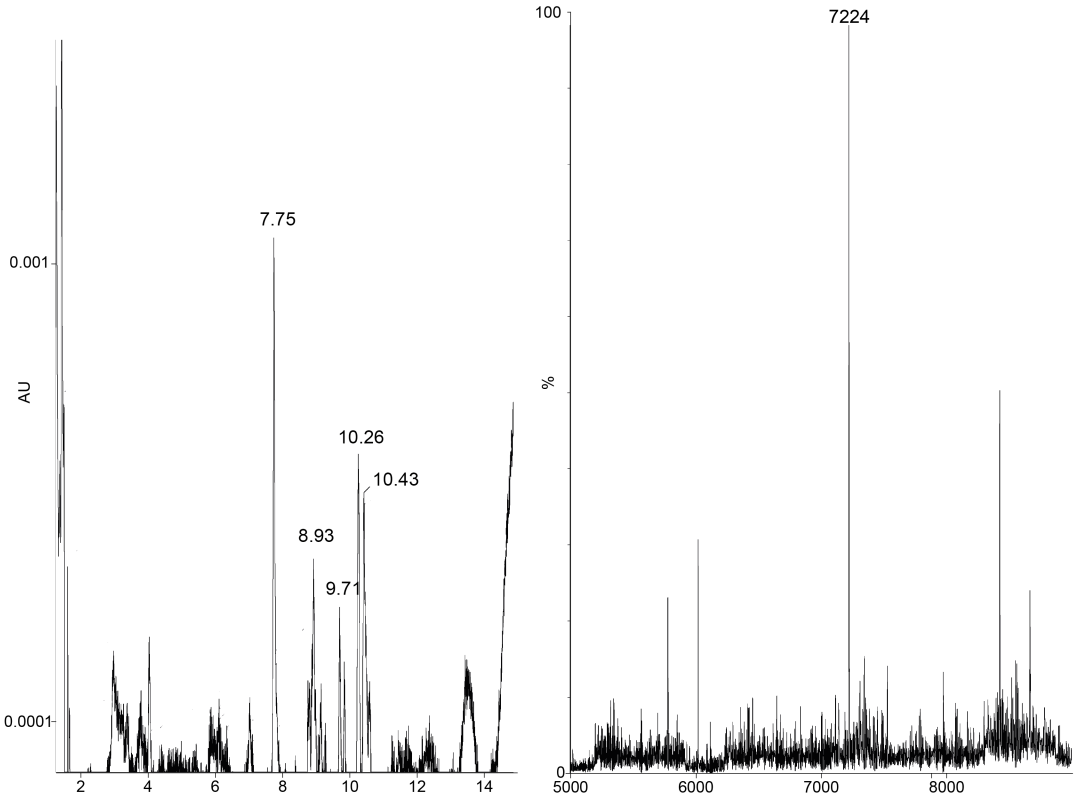


Figure B.2.1: HPLC trace and MS chromatogram of B-1.

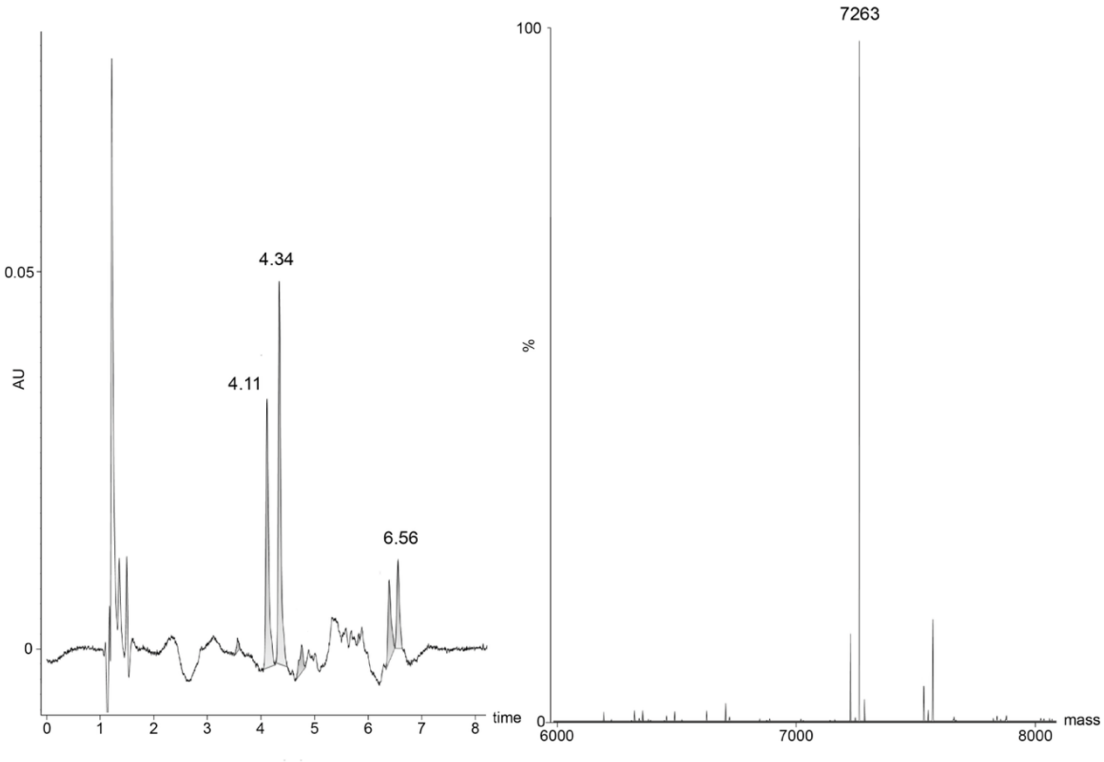


Figure B.2.2: HPLC trace and MS chromatogram of B-2.

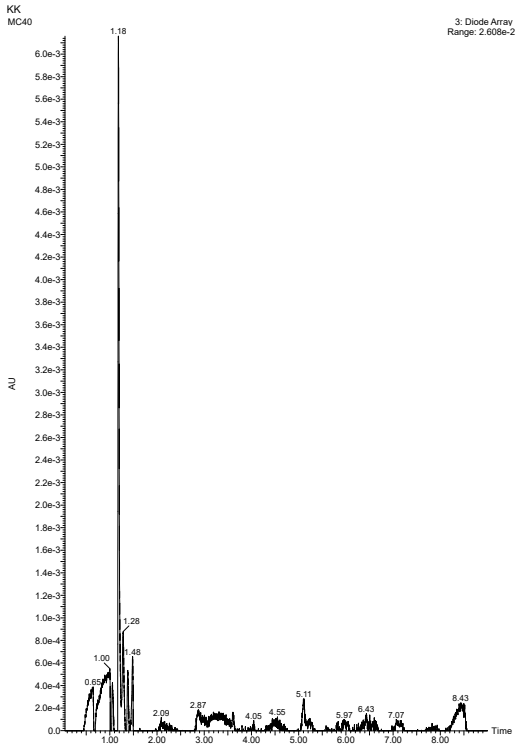


Figure B.2.3: HPLC trace of B-3.

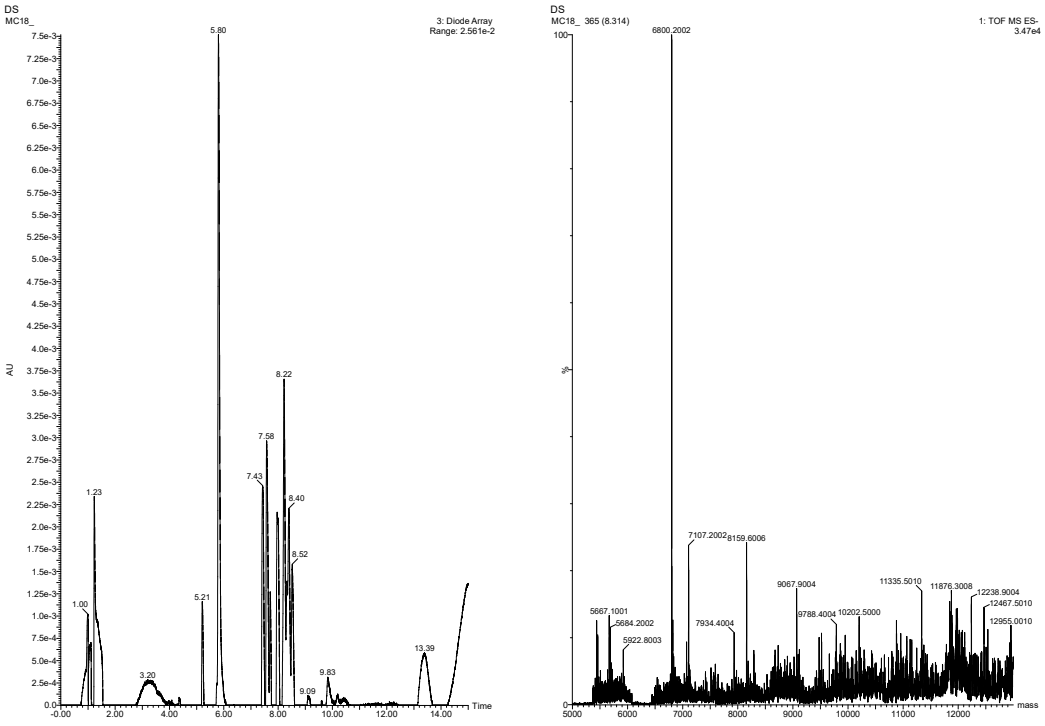


Figure B.2.4: HPLC trace and MS chromatogram of B-4.

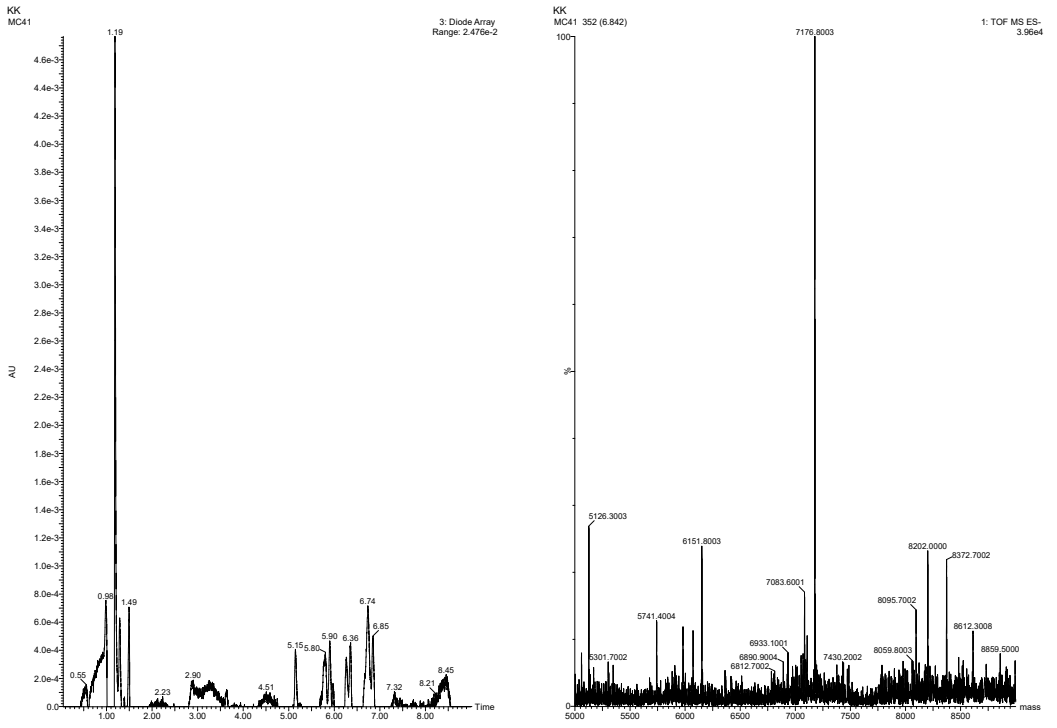


Figure B.2.5: HPLC trace and MS chromatogram of P-1.

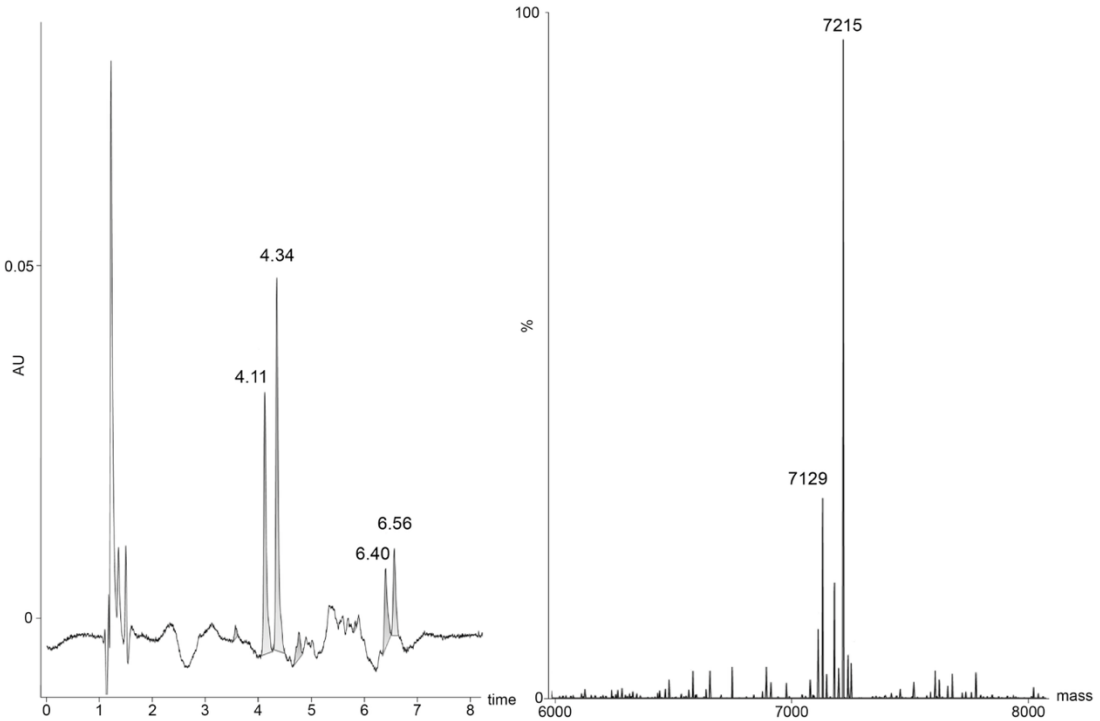


Figure B.2.6: HPLC trace and MS chromatogram of P-2.

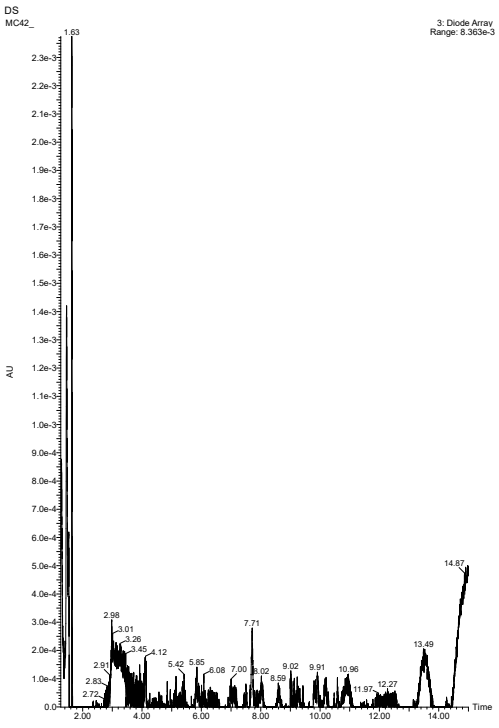


Figure B.2.7: HPLC trace of P-3.



Figure B.2.8: MS chromatogram of P-4.

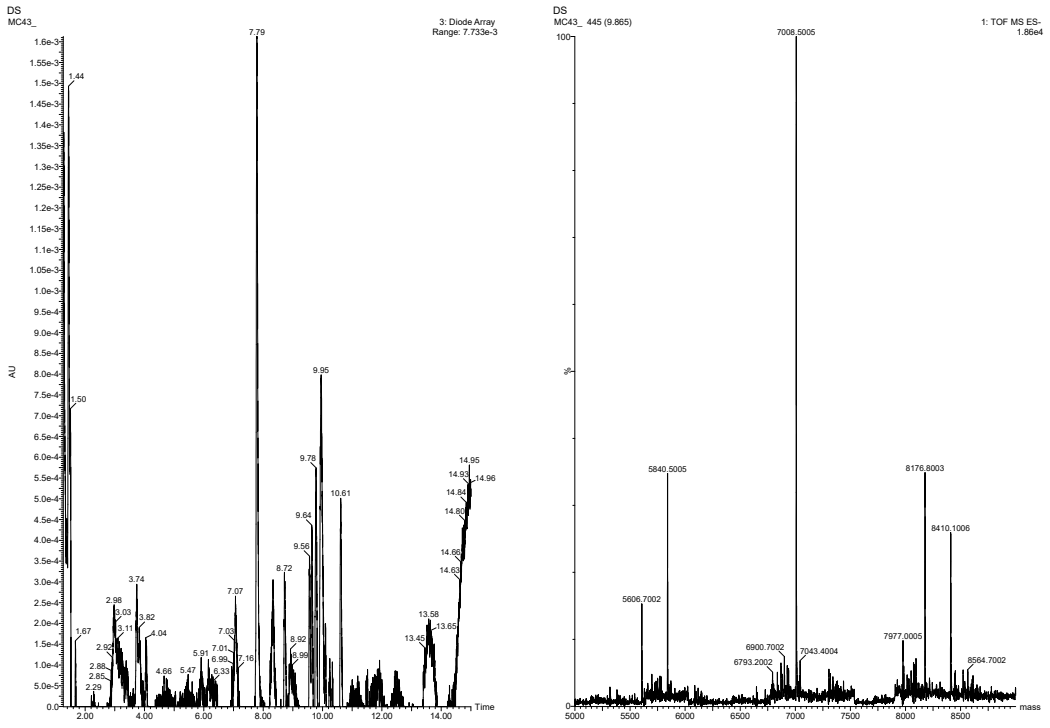


Figure B.2.9: HPLC trace and MS chromatogram of O-1.

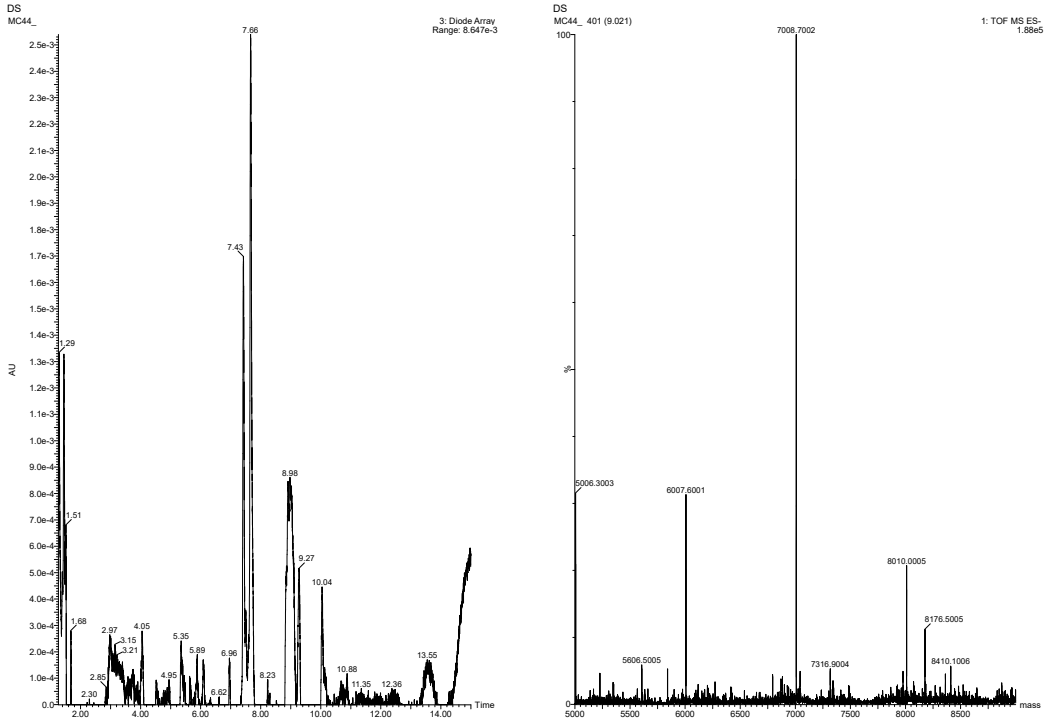


Figure B.2.10: HPLC trace and MS chromatogram of O-2.

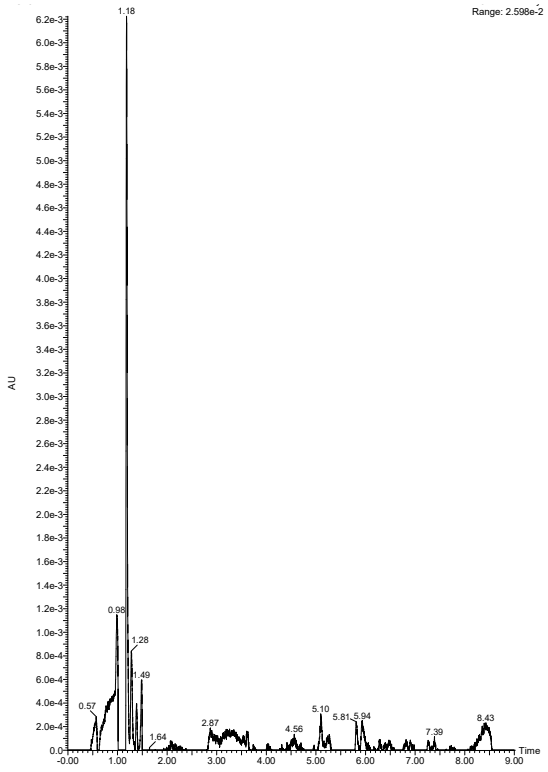


Figure B.2.11: HPLC trace and MS chromatogram of O-3.

B.3 PAGE gels

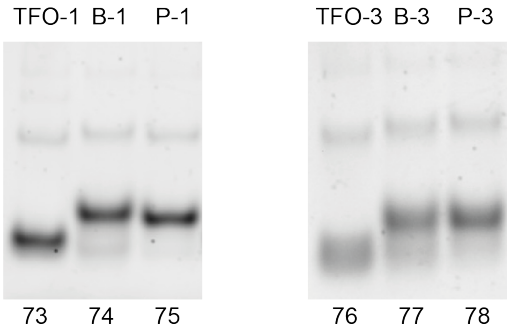


Figure B.3.1: PAGE analysis of SPAAC-generated hybrids.

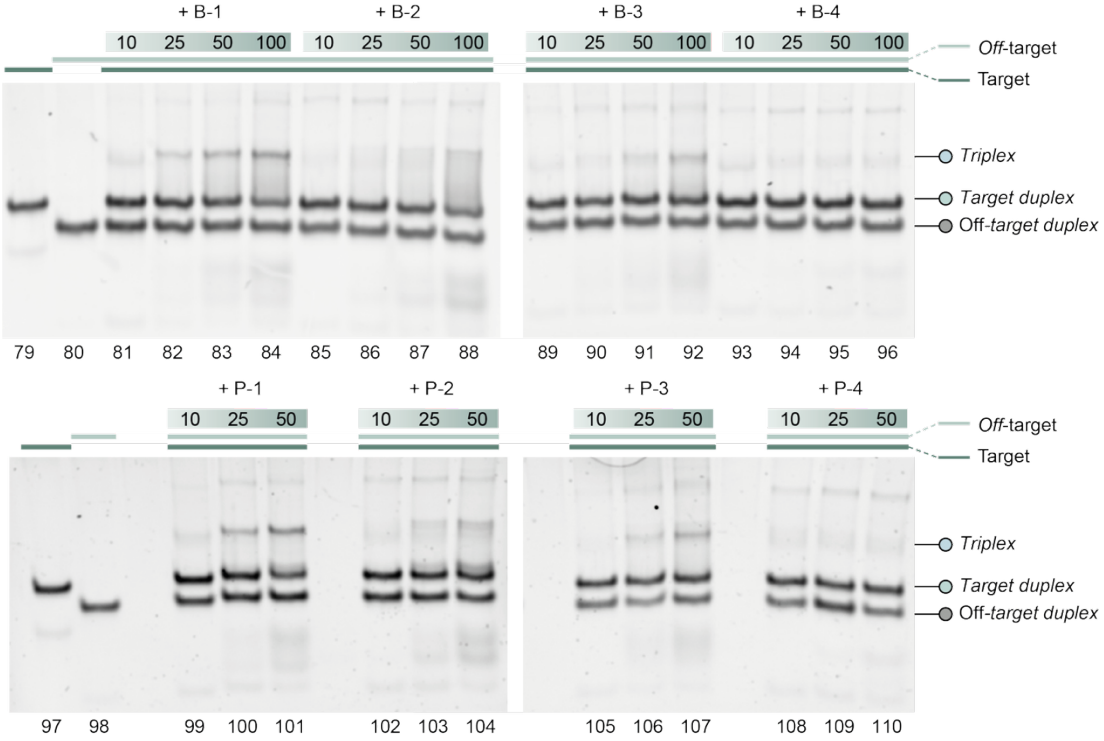


Figure B.3.2: PAGE analysis of the triplex formation activity of B-2, B-4, P-2 and P-4.

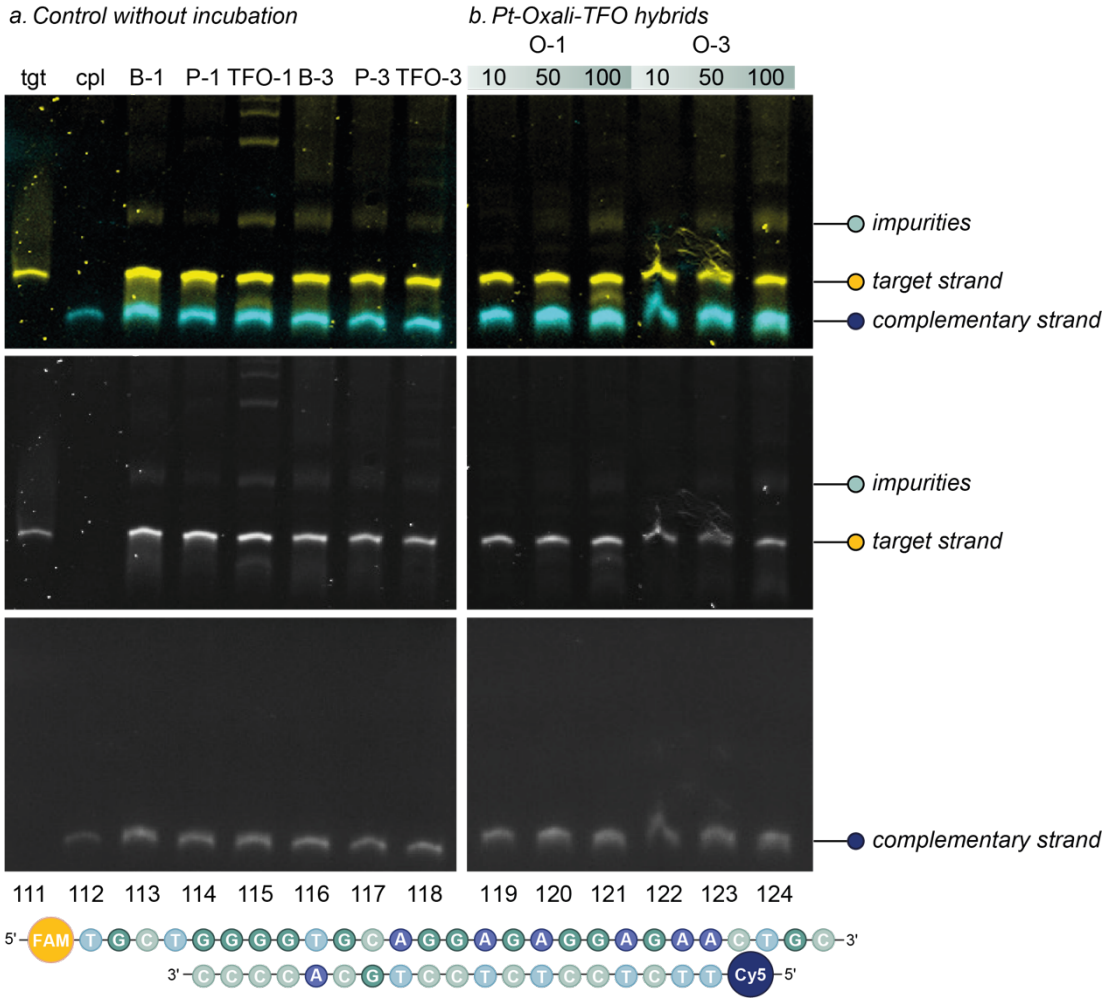


Figure B.3.3: Denaturing PAGE control experiments **a**. showing higher bands presents in TFO-1, TFO-3, B-1, B-3, P-1 and P-3 (100 eq.) with no prior incubation and **b**. showing the adduct formation from Oxali-TFO hybrids O-1 and O-3 in the presence of the labelled short target duplex across a gradient of Pt-TFO concentration (10, 50 and 100 equivalents) in phosphate buffer.

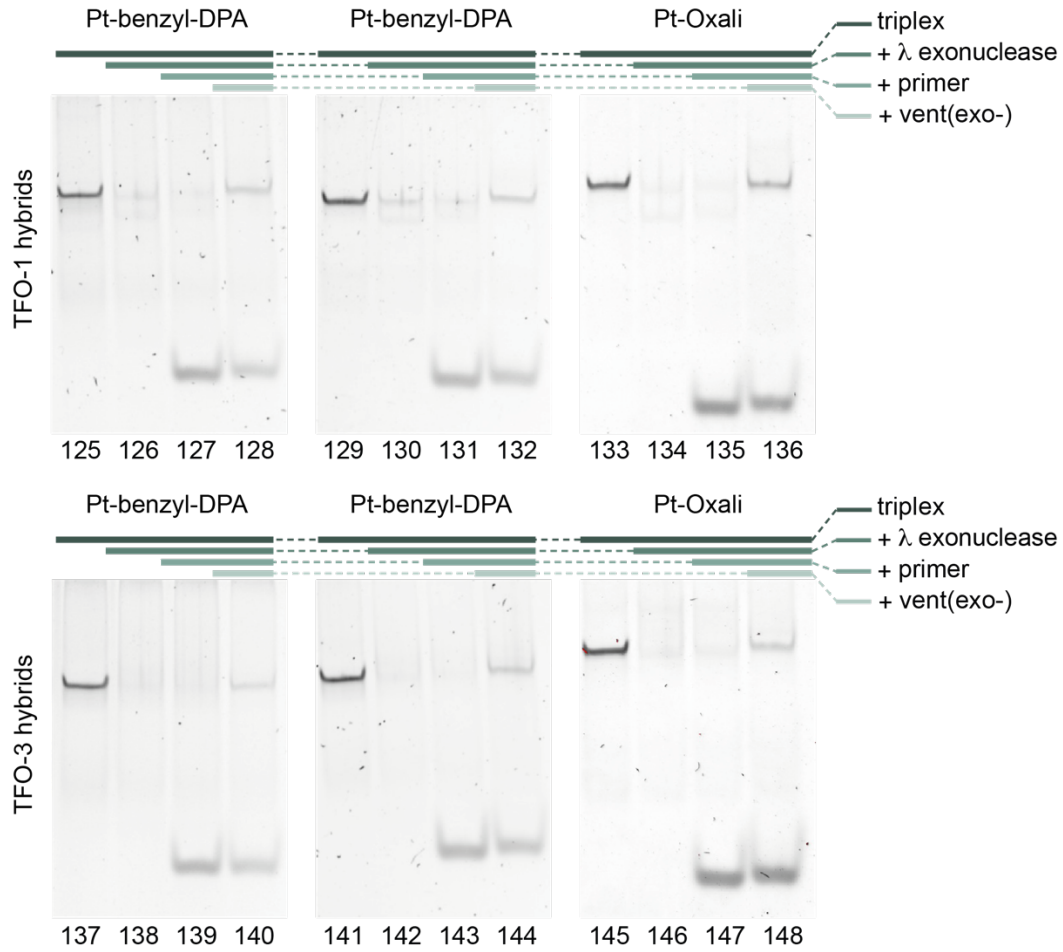


Figure B.3.4: PAGE gels showing the stepwise PEX inhibition experiment for each Pt-TFO hybrid, B-1, P-1, O-1, B-3, P-3 and O-3.

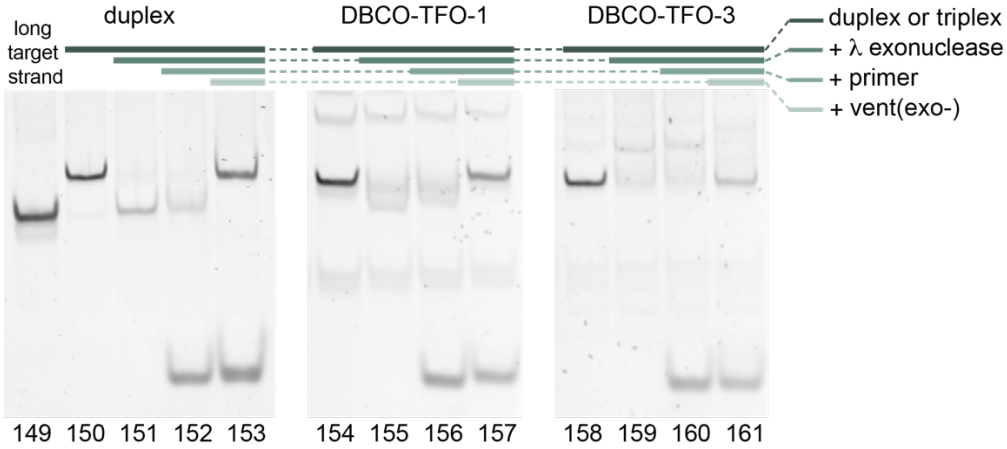


Figure B.3.5: PAGE gel showing the negative control for he PEX inhibition experiment, in the absence of TFO (left), in the presence of DBCO-TFO-1 (middle) or DBCO-TFO-3 (right). The migration of the long target strand is shown in lane 149. 5′-phosphate modified duplex (lane 150) is exposed to lambda exonuclease (lane 151) before addition of the primer (lane 152) and finally vent(exo-) (lane 153, showing recovery of the duplex lane. The same is repeated in the presence of DBCO-TFO-1 (lanes 154-157) and DBCO-TFO-3 (lanes 158-161) showing less duplex recovery.

Appendix C

C.1 Spectroscopic characterisation

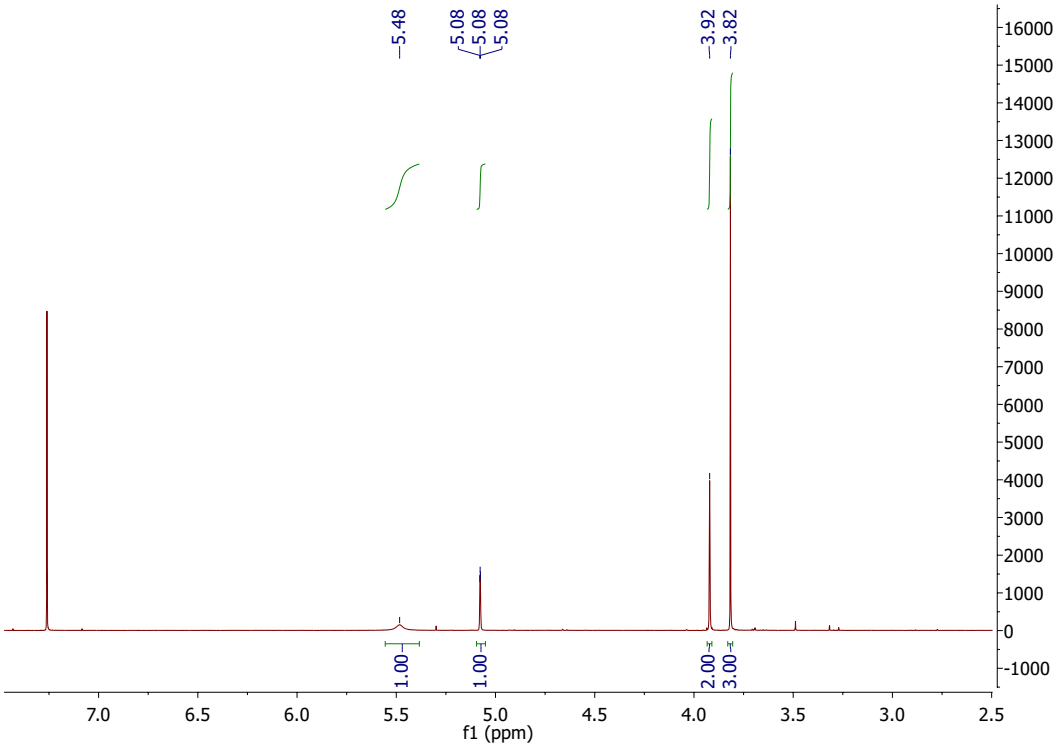


Figure C.1.1: ^{1}H NMR of 4-methoxy-3-pyrrolin-2-one in $CDCl_3$.

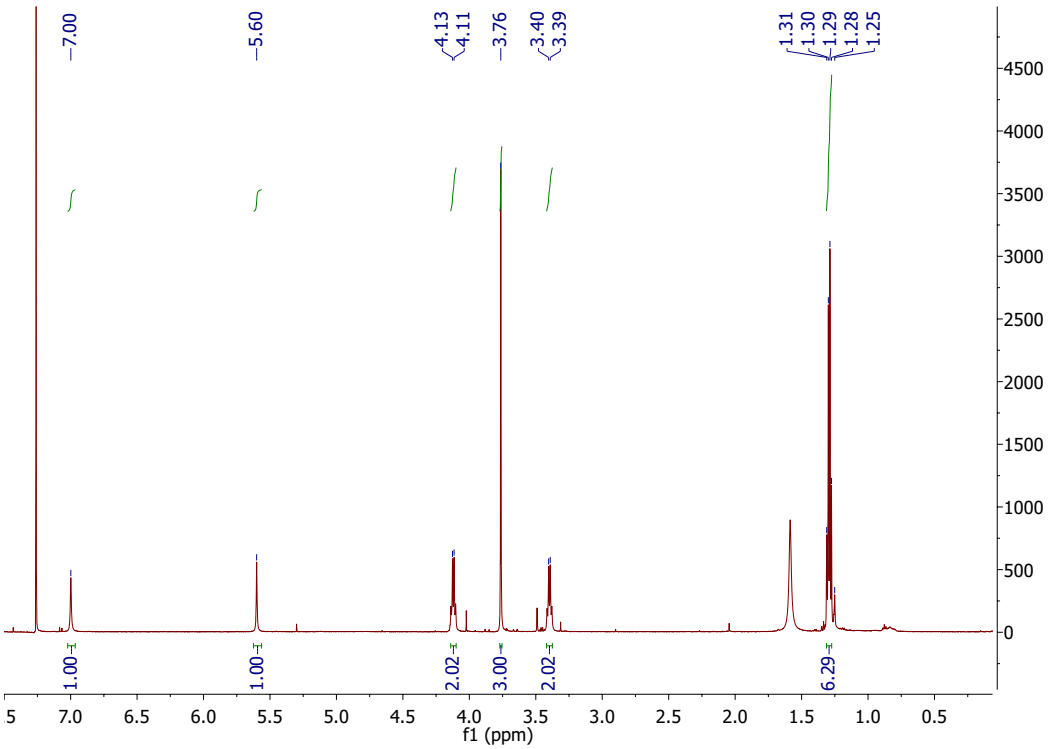


Figure C.1.2: ^{1}H NMR of N-((5-bromo-3-methoxy-2H-pyrrol-2-ylidene)methyl)-N-ethylethanamine in $CDCl_3$.

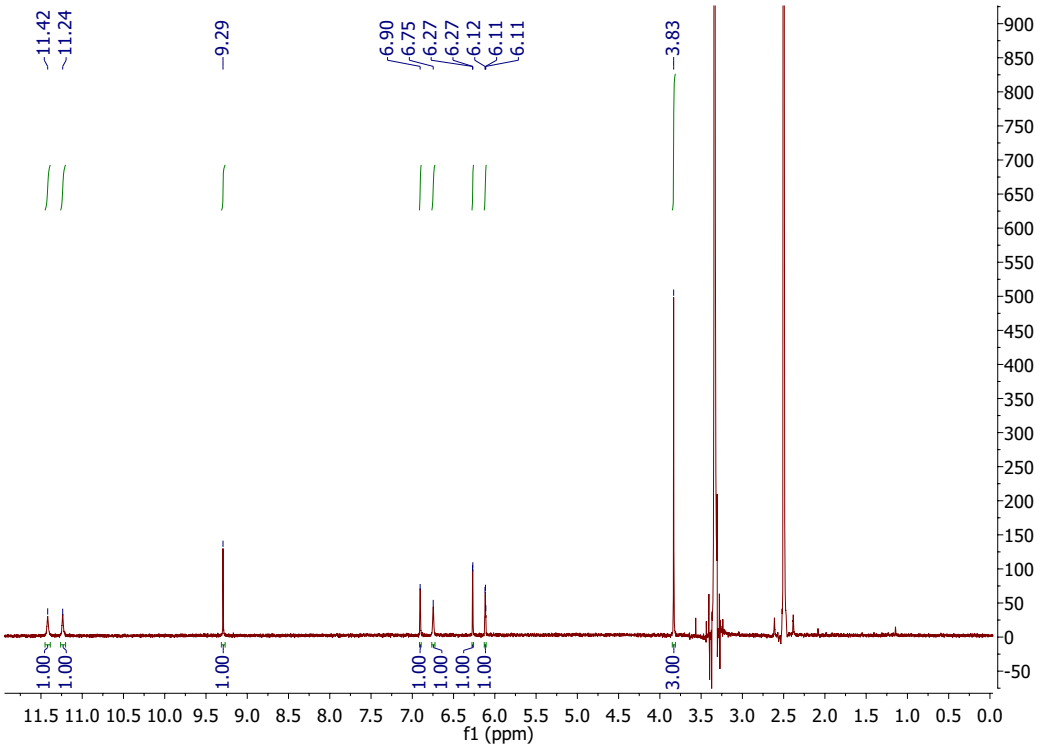


Figure C.1.3: ^{1}H NMR of 4-methoxy-1H,1'H-[2,2'-bipyrrole]-5-carbaldehyde in DMSO-d_6.

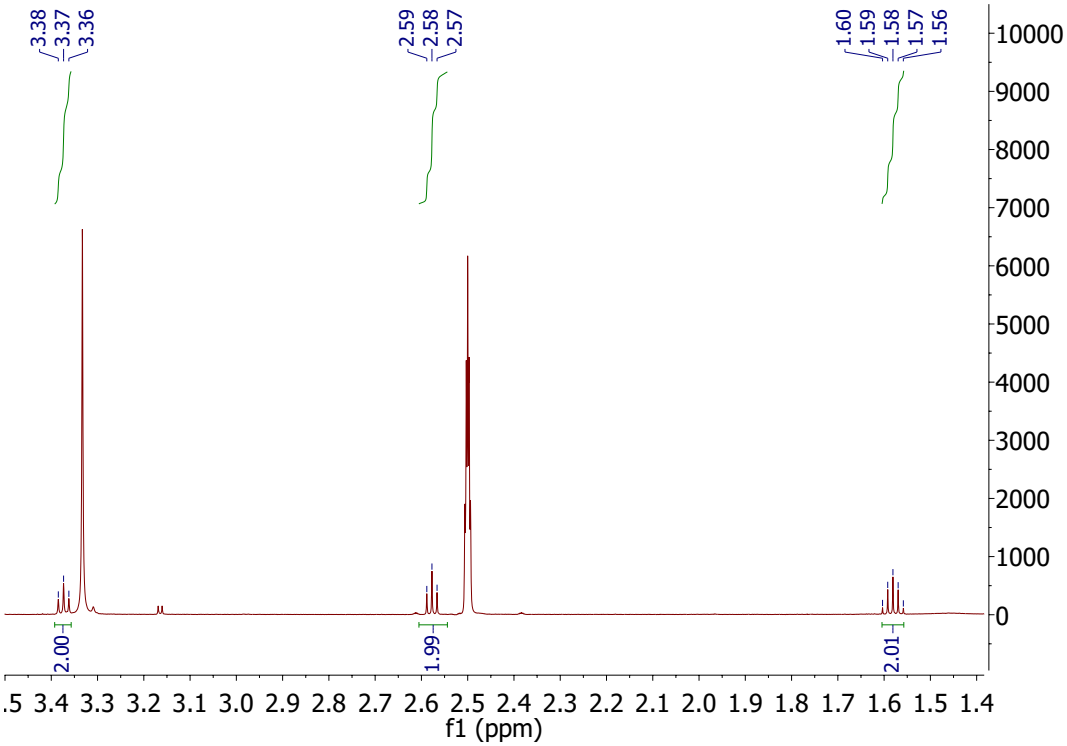


Figure C.1.4: ^{1}H NMR of 3-azidopropyl-1-amine in DMSO-d_6.

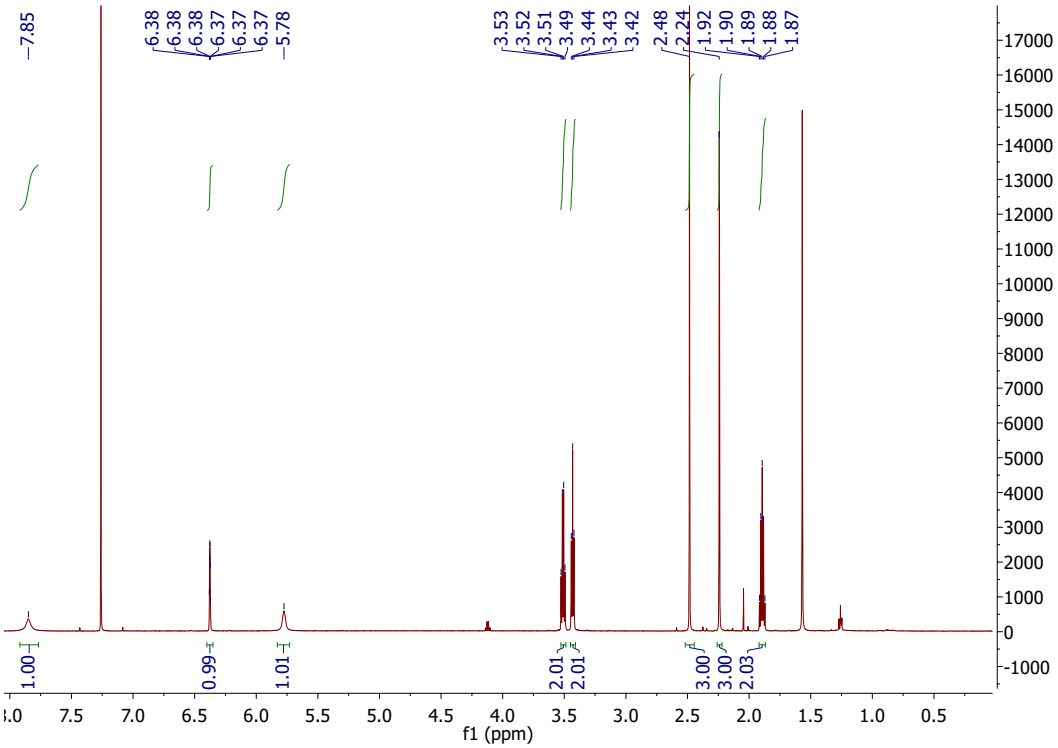


Figure C.1.5.1: ^{1}H NMR of N-(3-azidopropyl)-2,4-dimethyl-1H-pyrrole-3-carboxamide in $CDCl_3$.

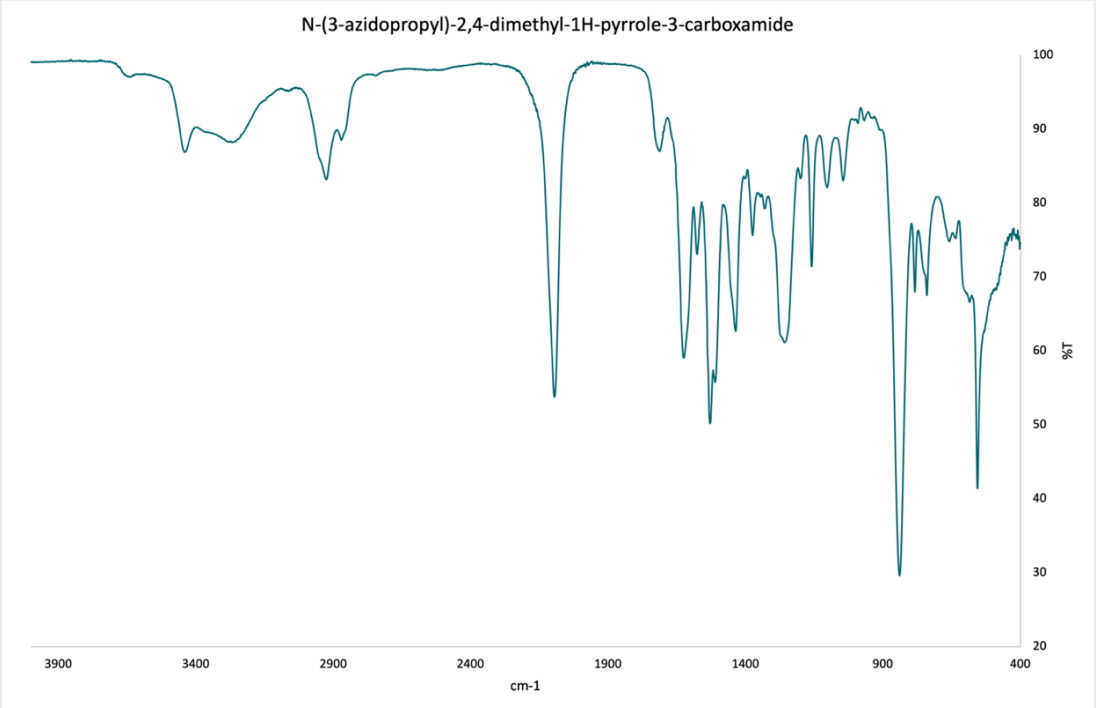


Figure C.1.5.2: IR spectrum of N-(3-azidopropyl)-2,4-dimethyl-1H-pyrrole-3-carboxamide.

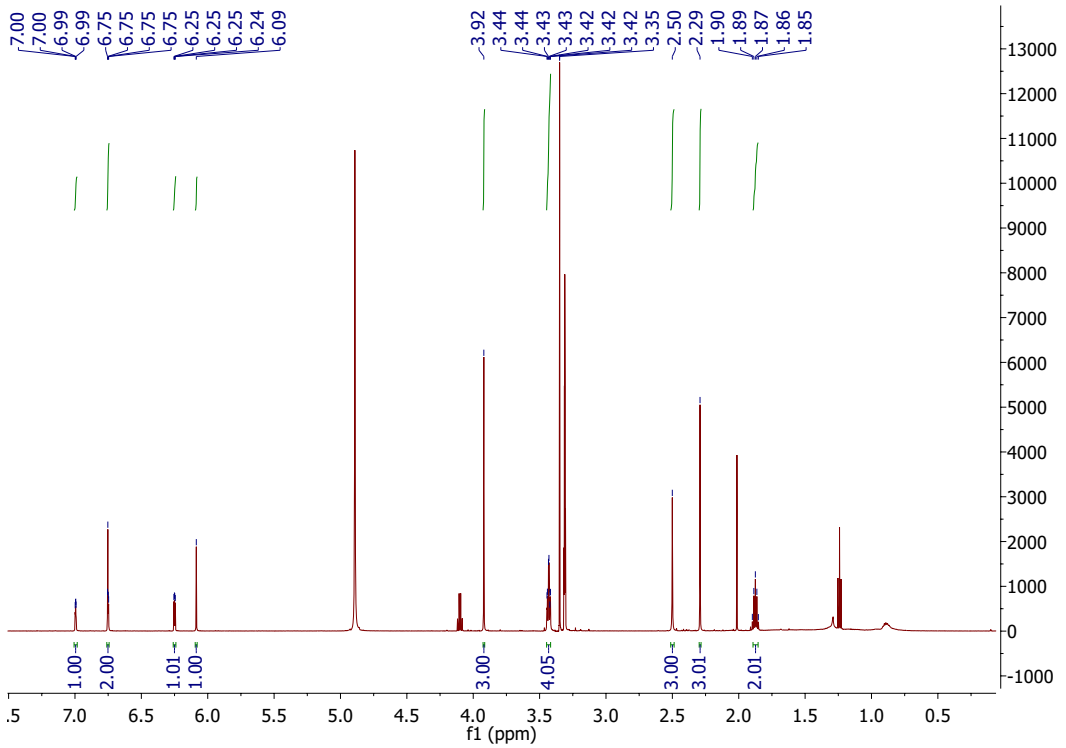


Figure C.1.6.1: ^{1}H NMR of N-(3-azidopropyl)-5-((4'-methoxy-1H,5'H-[2,2'-bipyrrol]-5'-ylidene)methyl)-2,4-dimethyl-1H-pyrrole-3-carboxamide (N_3-PD) in MeOD.

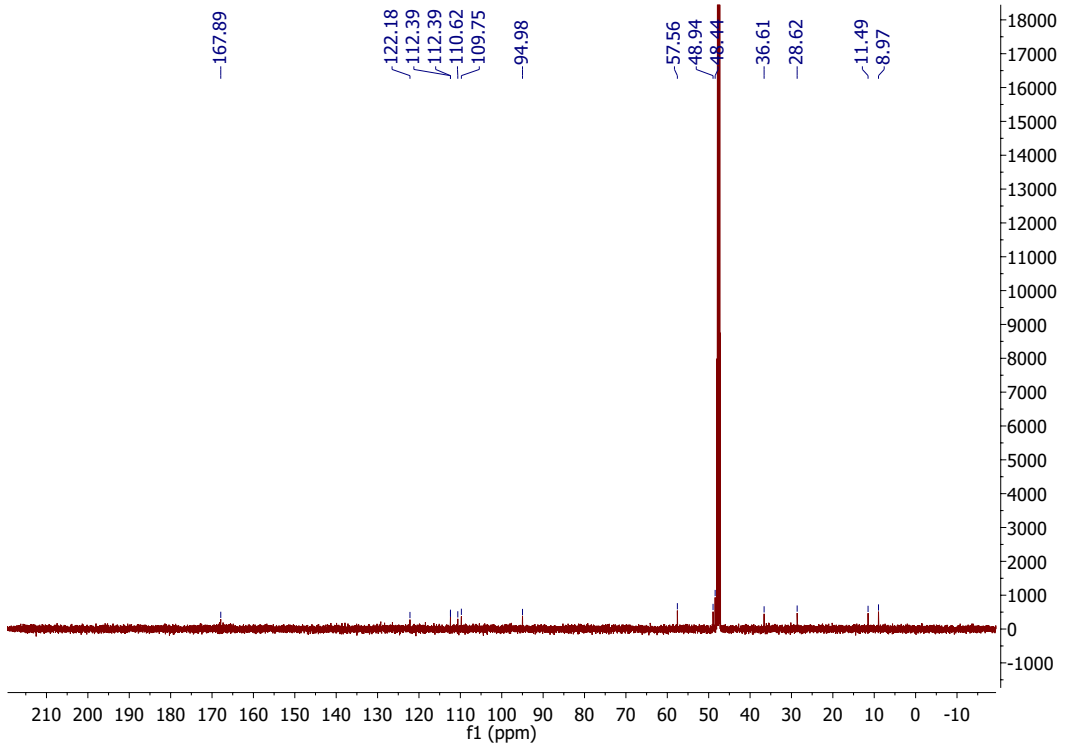


Figure C.1.6.2: ^{13}C NMR of N-(3-azidopropyl)-5-((4'-methoxy-1H,5'H-[2,2'-bipyrrol]-5'-ylidene)methyl)-2,4-dimethyl-1H-pyrrole-3-carboxamide (N_3-PD) in MeOD.

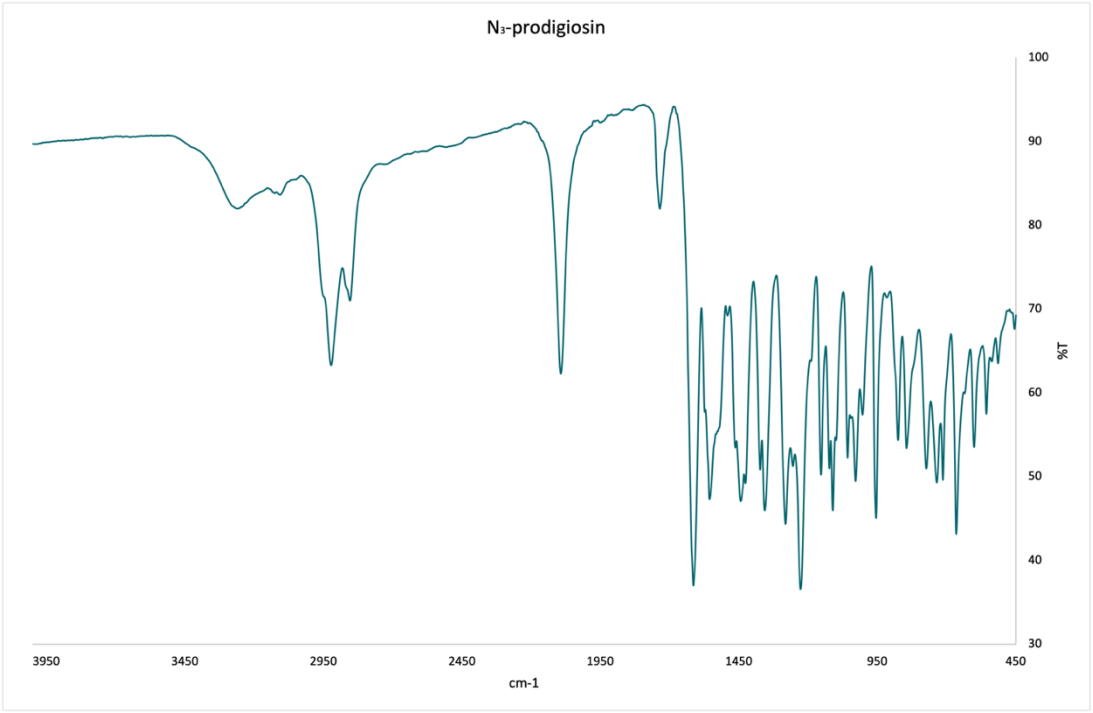


Figure C.1.6.3: IR spectrum of N-(3-azidopropyl)-5-((4'-methoxy-1H,5'H-[2,2'-bipyrrol]-5'-ylidene)methyl)-2,4-dimethyl-1H-pyrrole-3-carboxamide (N_3-PD).

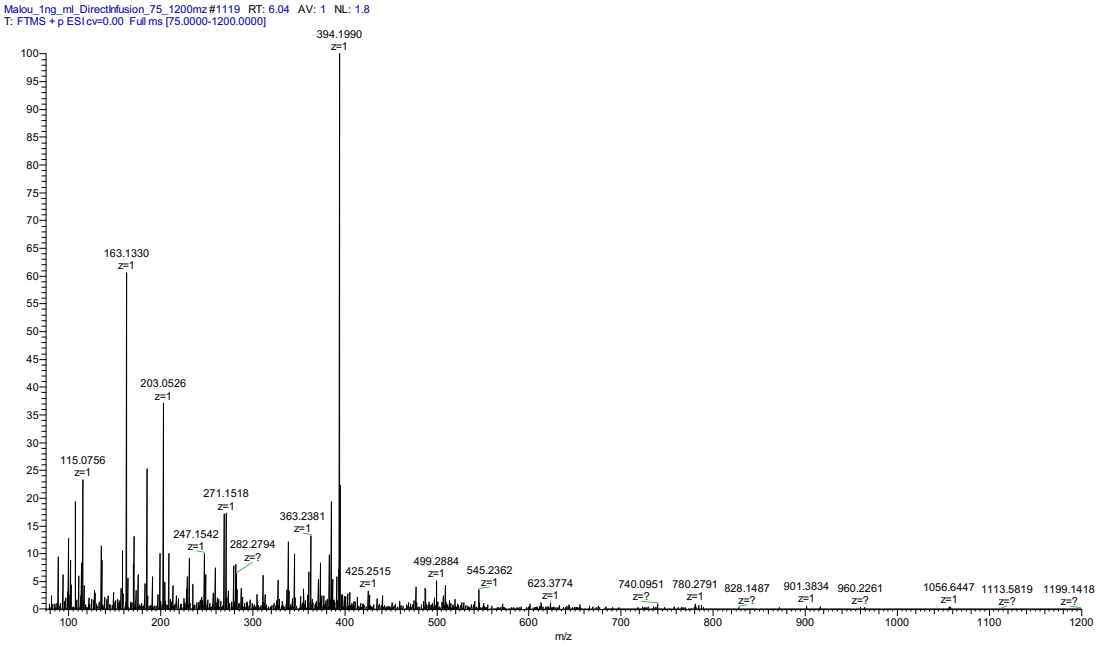


Figure C.1.6.4: MS chromatogram of N-(3-azidopropyl)-5-((4'-methoxy-1H,5'H-[2,2'-bipyrrol]-5'-ylidene)methyl)-2,4-dimethyl-1H-pyrrole-3-carboxamide (N_3-PD).

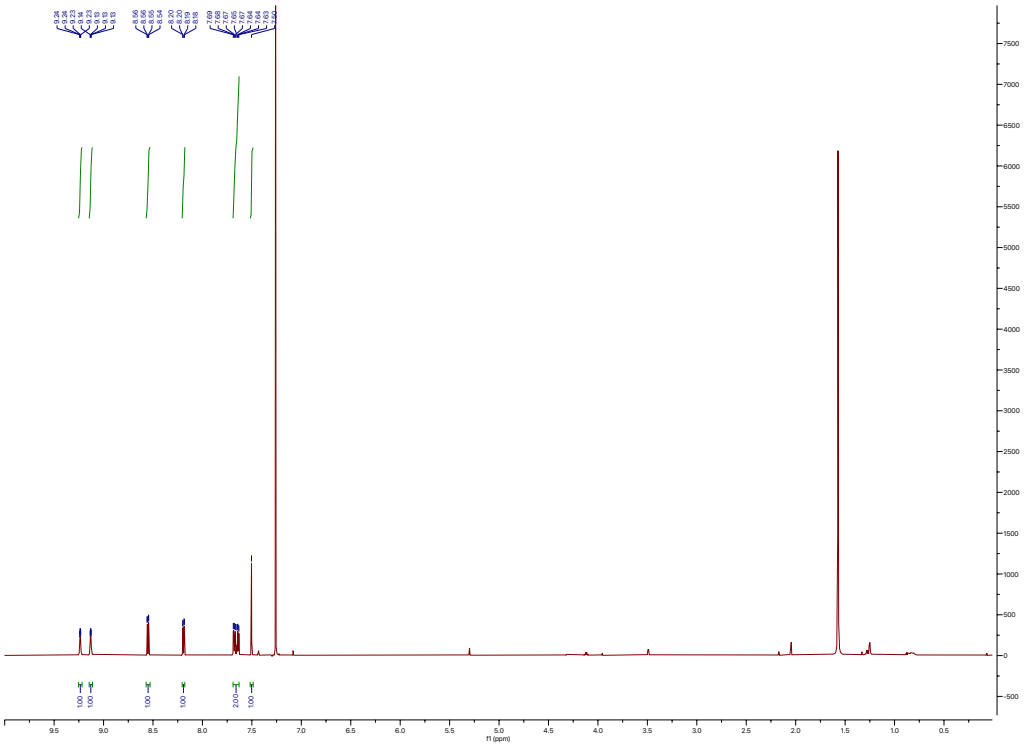


Figure C.1.7.1: ^{1}H NMR of 5-azido-1,10-phenanthroline in $CDCl_3$.

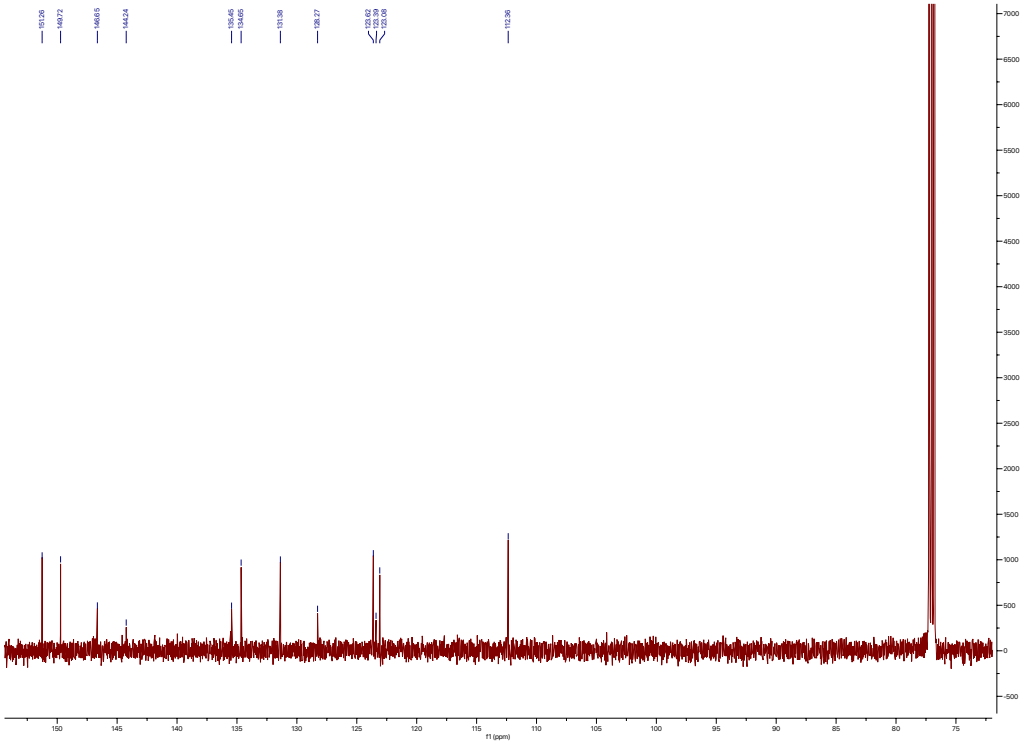


Figure C.1.7.2: ^{13}C NMR of 5-azido-1,10-phenanthroline in $CDCl_3$.

C.2 HPLC trace and MS chromatogram of the PD- and Phen-TFO hybrids

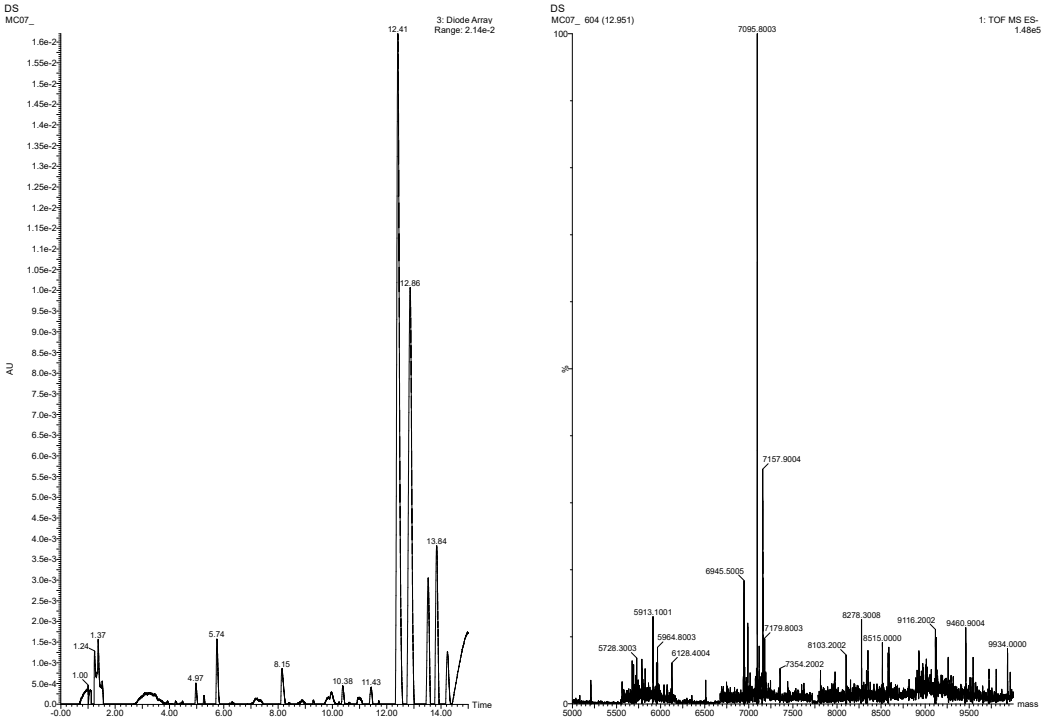


Figure C.2.1: HPLC trace and MS chromatogram of PD-1.

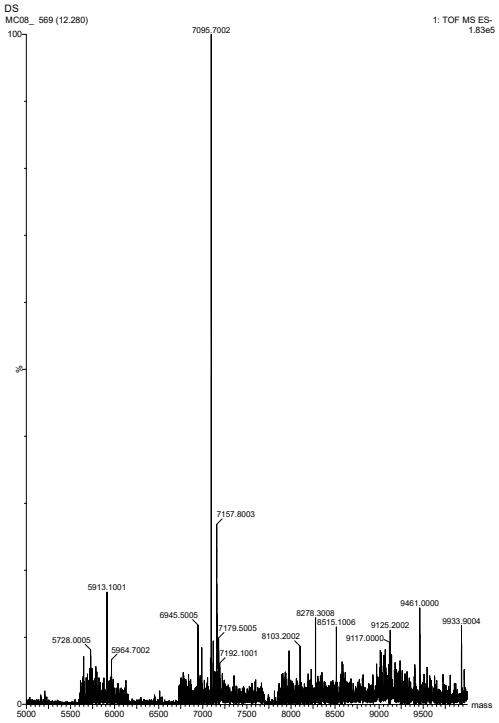


Figure C.2.2: MS chromatogram of PD-2.

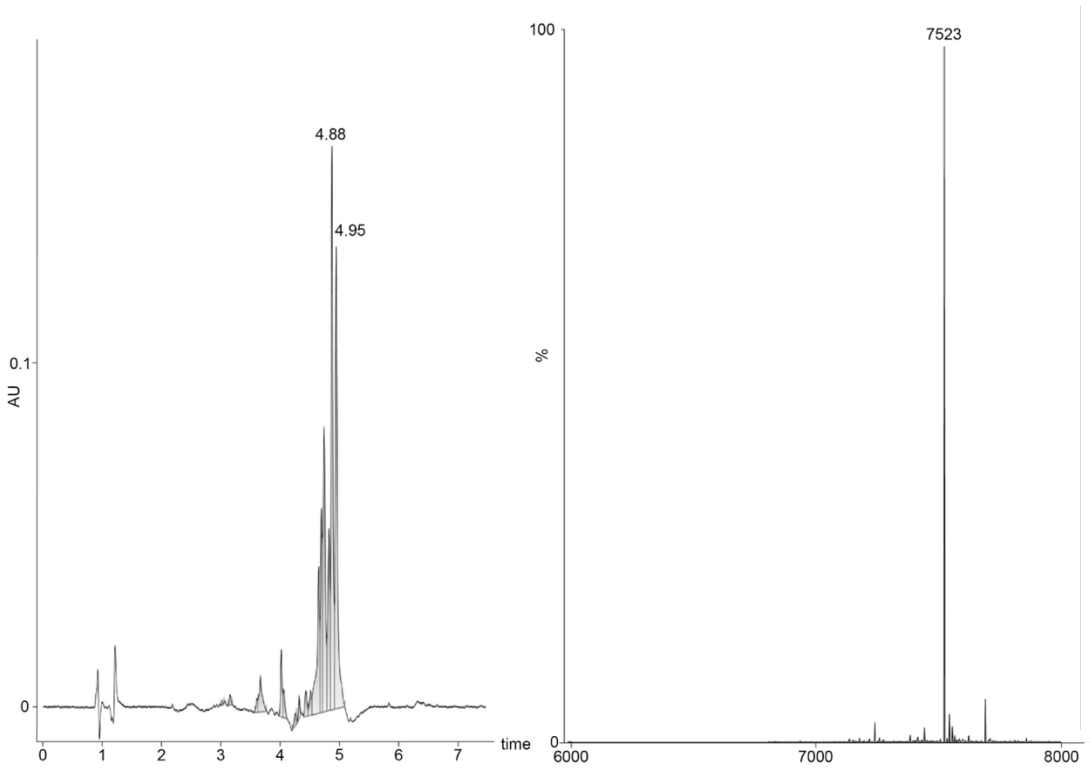


Figure C.2.3: HPLC trace and MS chromatogram of PD-3.

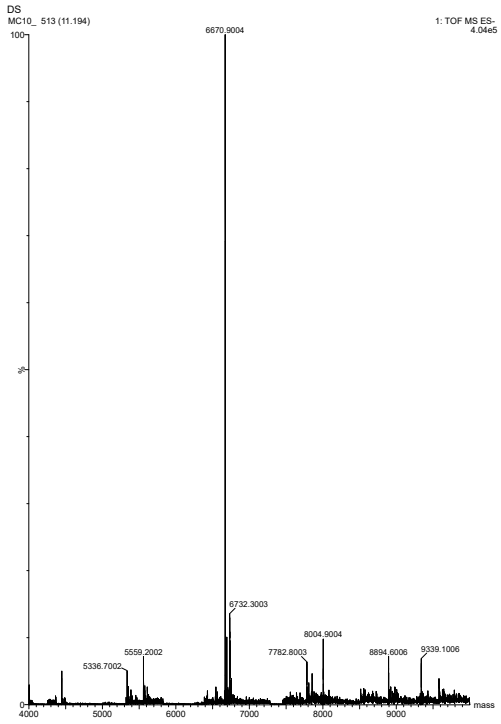


Figure C.2.4: MS chromatogram of PD-4.

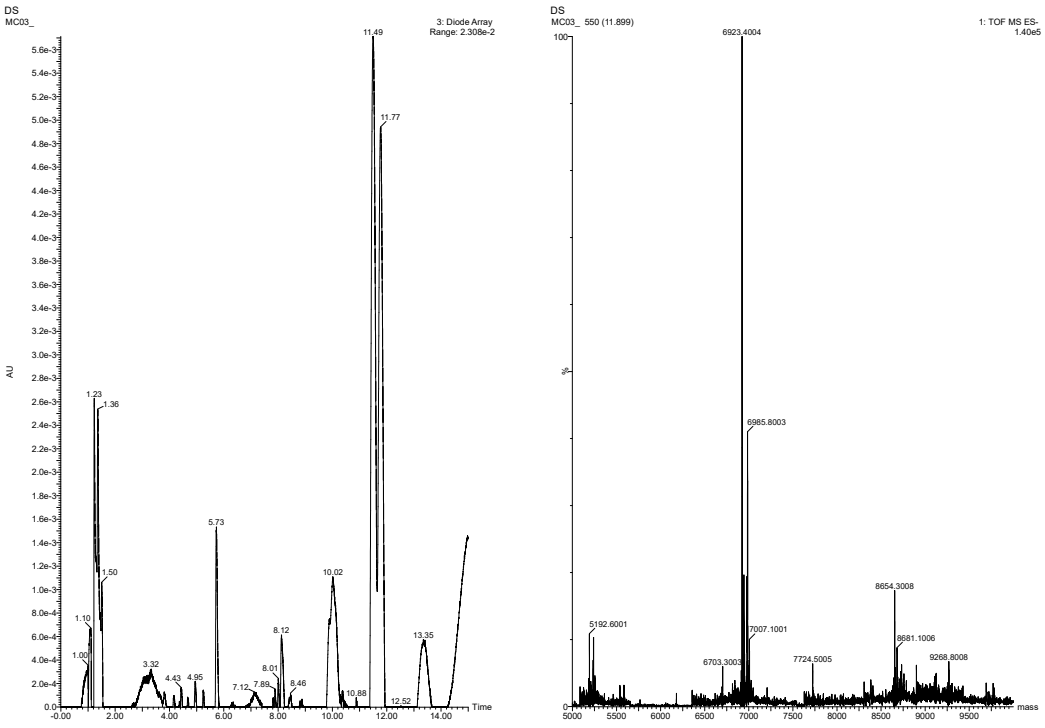


Figure C.2.5: HPLC trace and MS chromatogram of Phen-1.

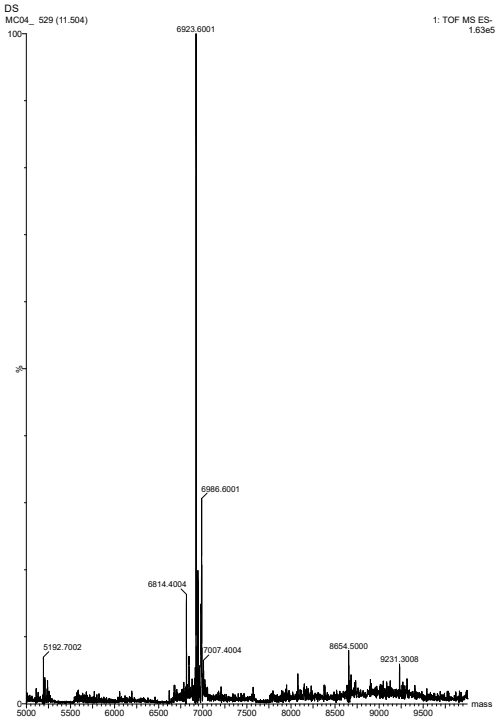


Figure C.2.6: MS chromatogram of Phen-2.

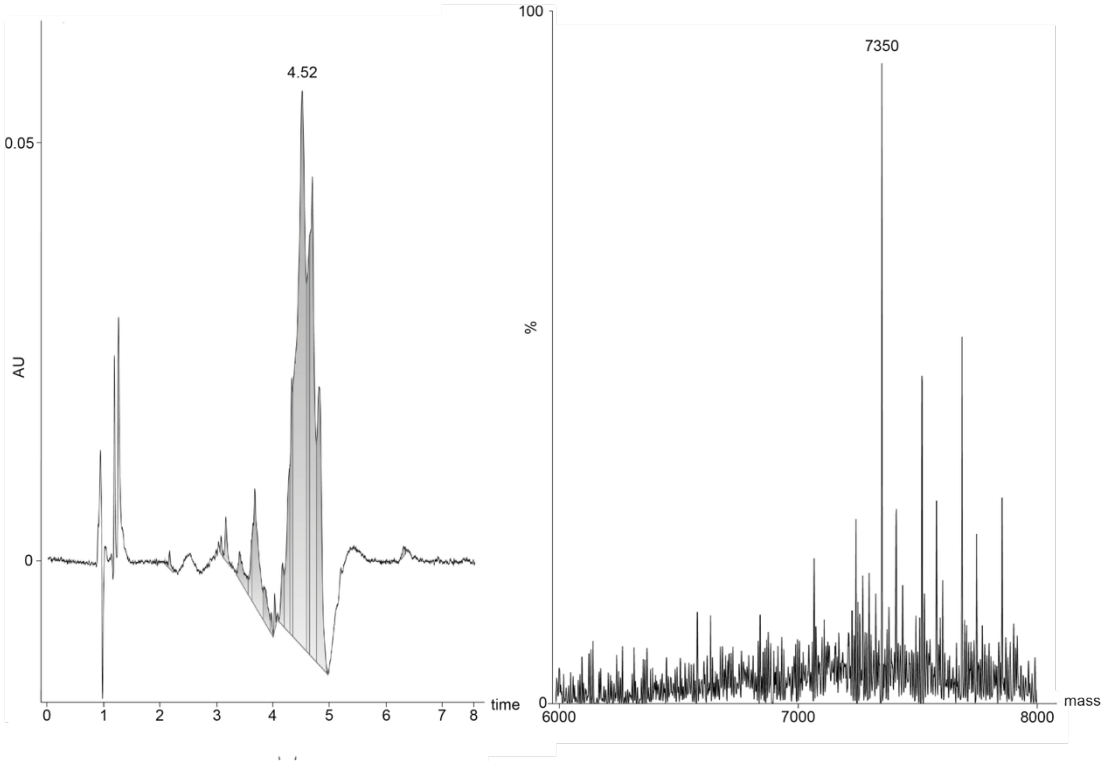


Figure C.2.7: HPLC trace and MS chromatogram of Phen-3.

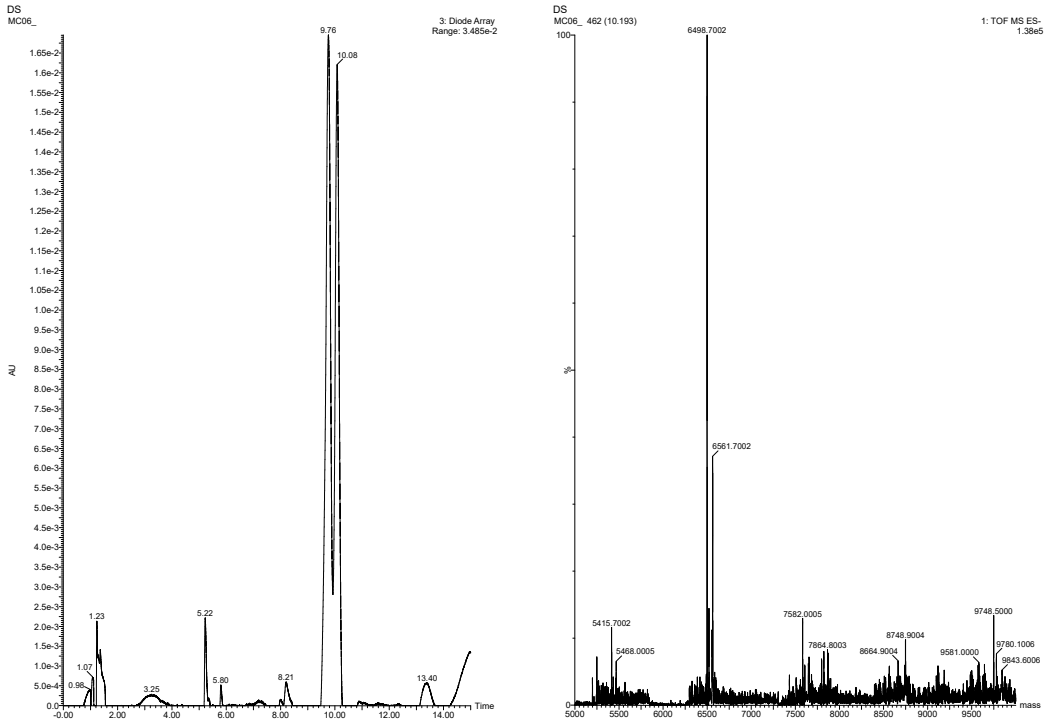
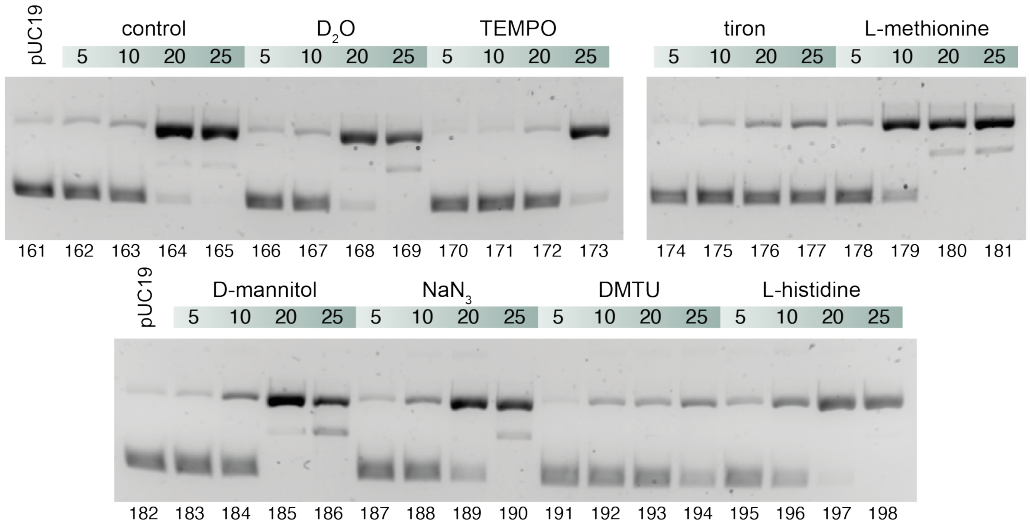


Figure C.2.8: HPLC trace and MS chromatogram of Phen-4.

C.3 Characterisation of the cleavage activity of [Cu(N$_3$-PD)(NO$_3$)$_2$].

a. *Na*-L-*asc-activated cleavage activity*



b. *Self-activated cleavage activity*

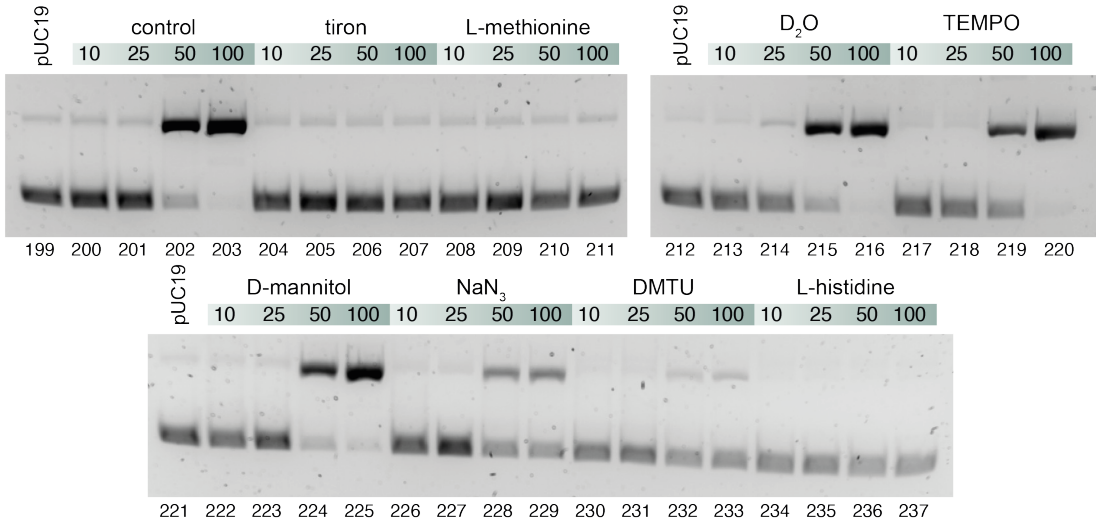


Figure C.3.1: Agarose gels showing the impact of ROS scavengers on the cleavage activity of [Cu(N$_3$-PD)(NO$_3$)$_2$] a. in the presence of Na-*L*-asc (lanes 161 to 198, concentration of 5, 10, 20 or 25 µM) and b. without Na-*L*-asc (lanes 199 to 237, concentrations of 10, 25, 50 or 100 µM).

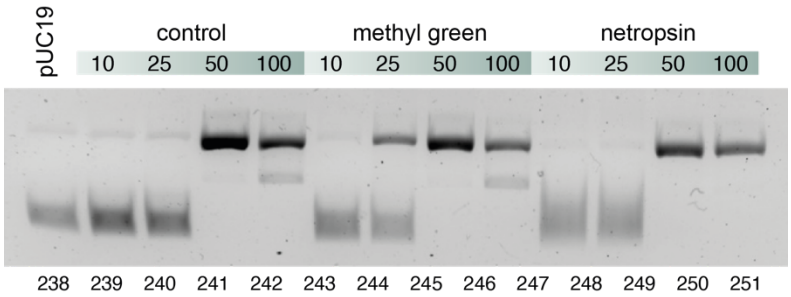


Figure C.3.2: Agarose gel showing the impact of major and minor groove binders on the self-activated cleavage activity of [Cu(N_3-PD)(NO_3)$_2$]. Lanes 243 – 246: in the presence of methyl green, lanes 247 – 251: in the presence of netropsin.

Appendix D

D.1 Spectroscopic characterisation

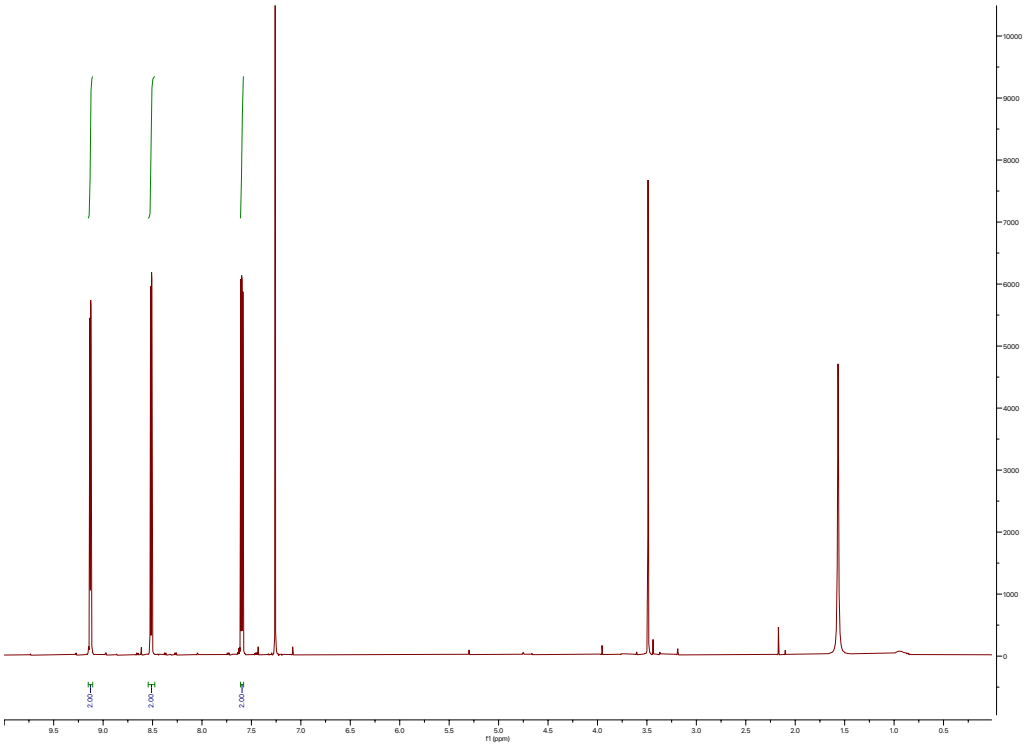


Figure D.1.1: ^{1}H NMR spectrum of 1,10-phenanthroline-5,6-dione.

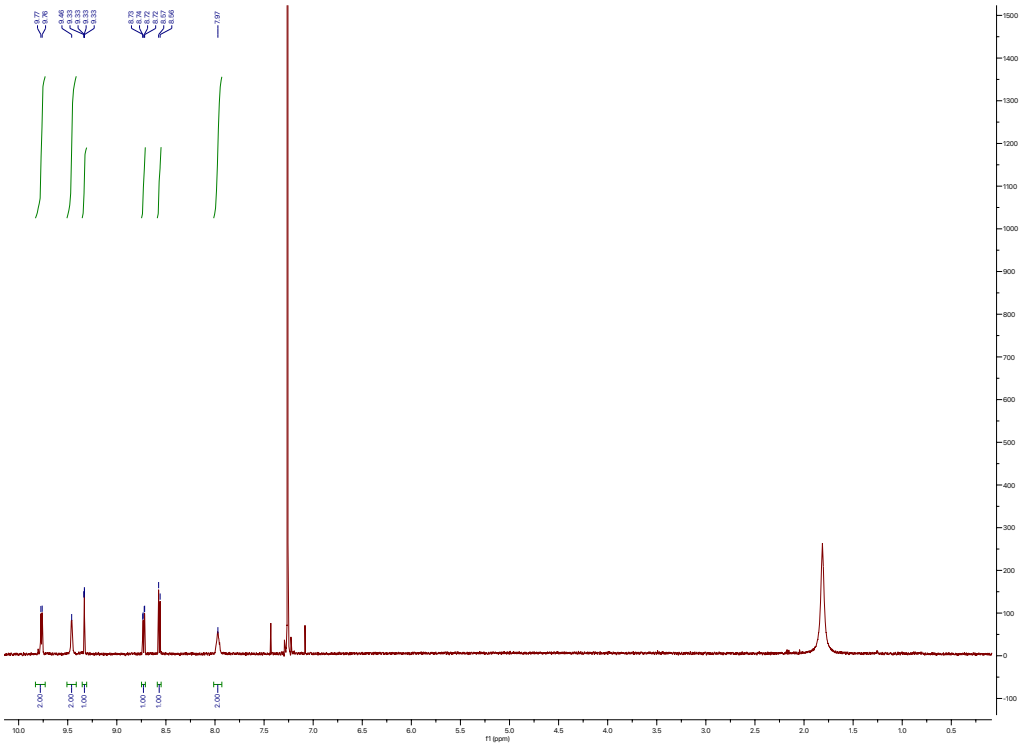


Figure D.1.2: ^{1}H NMR spectrum of nitro DPPZ.

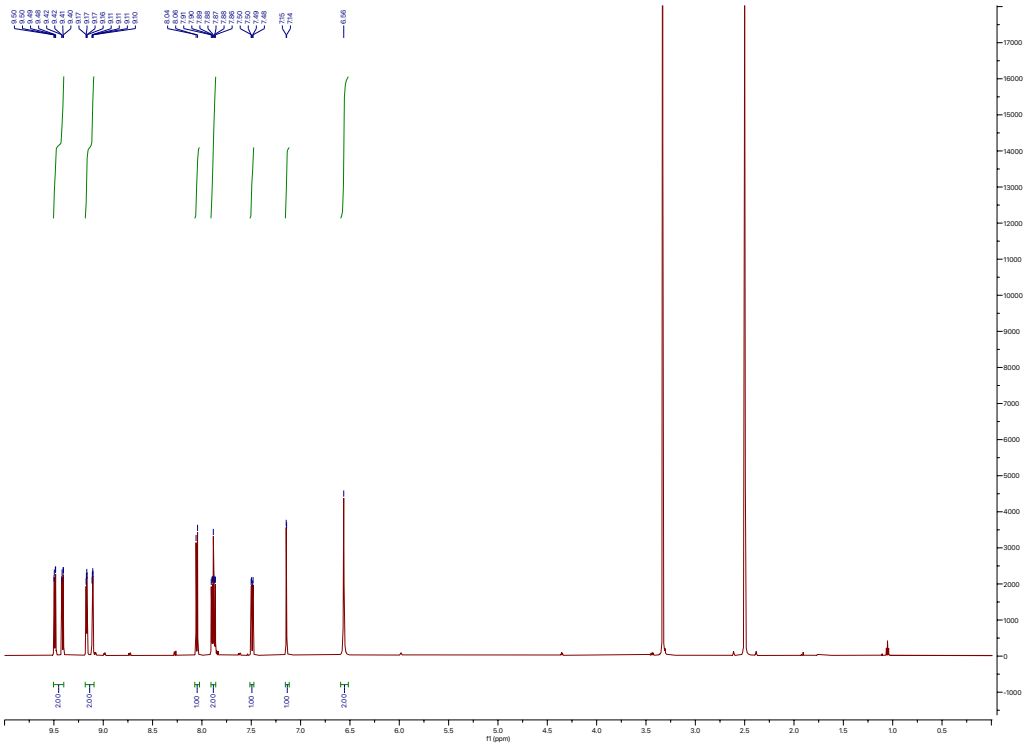


Figure D.1.3: ^{1}H NMR spectrum of amino DPPZ.

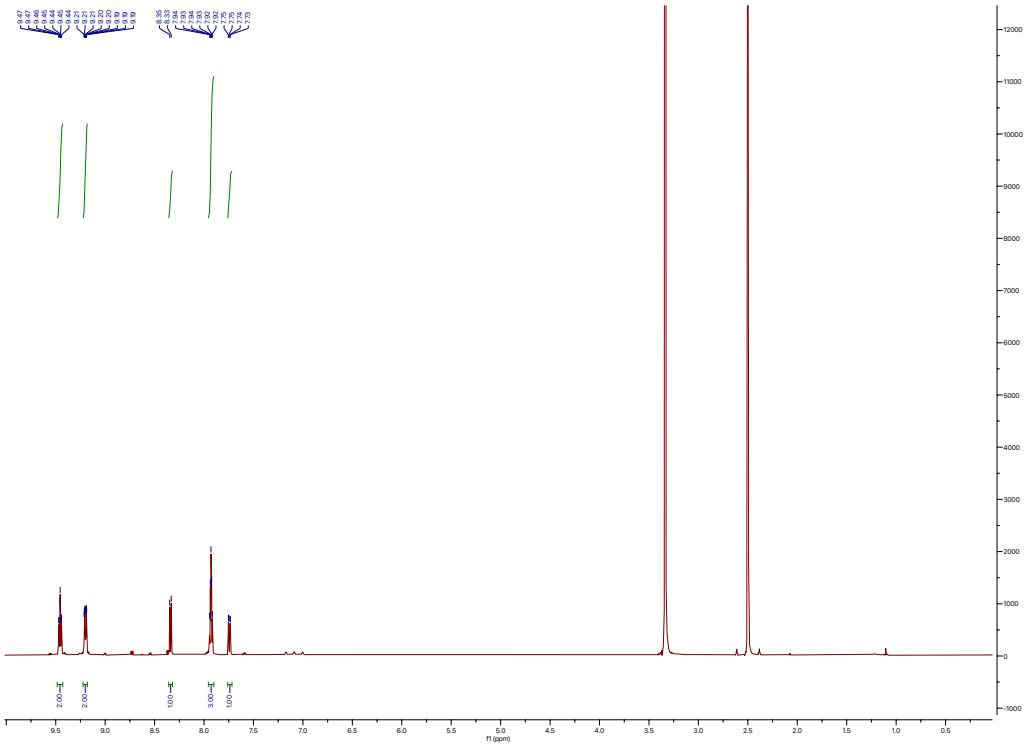


Figure D.1.4: ^{1}H NMR spectrum of azido DPPZ.

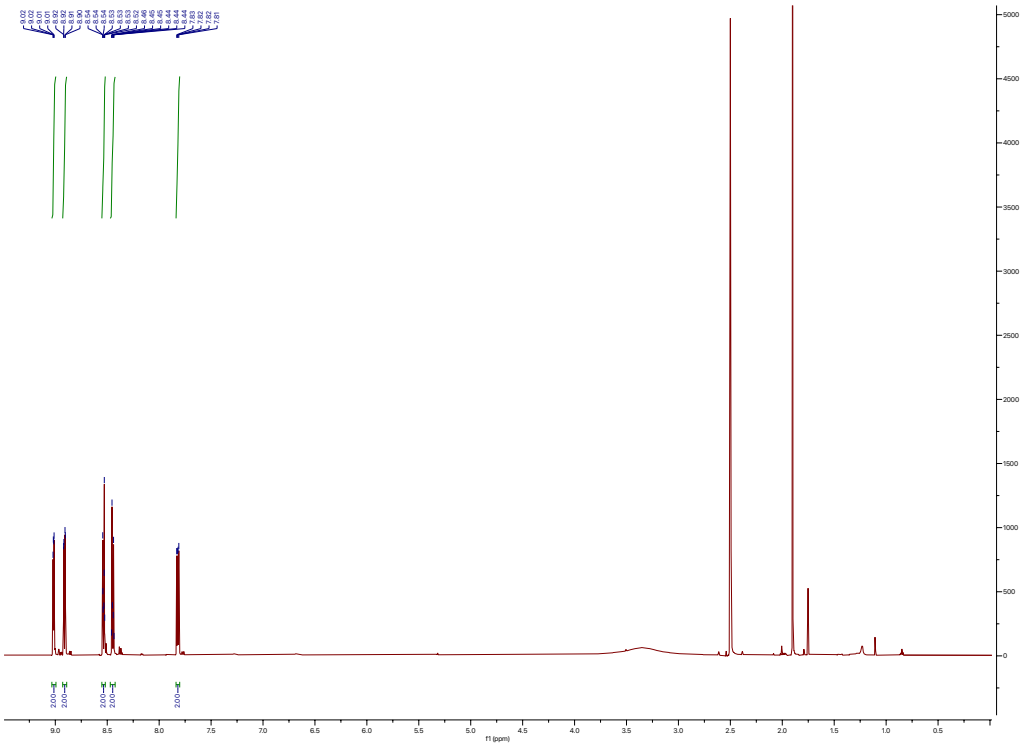


Figure D.1.5: ^{1}H NMR spectrum of nitro ImPhen.

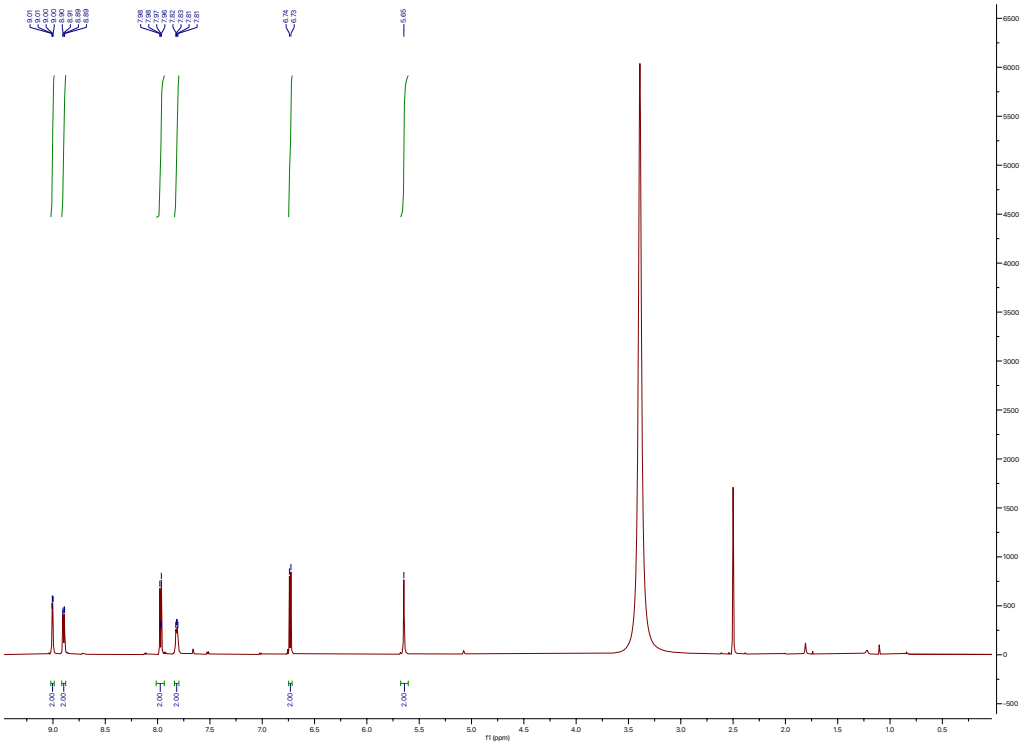


Figure D.1.6: ^{1}H NMR spectrum of amino ImPhen.

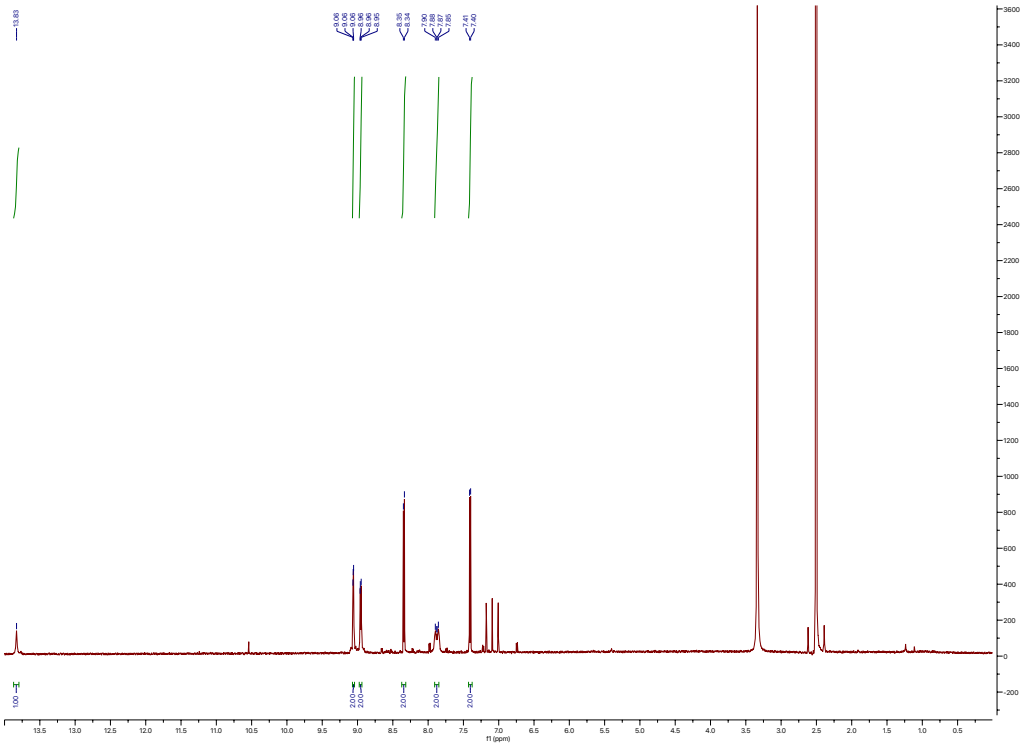


Figure D.1.7: ^{1}H NMR spectrum of azido ImPhen.

D.2 PAGE analysis of the self-assembly assay

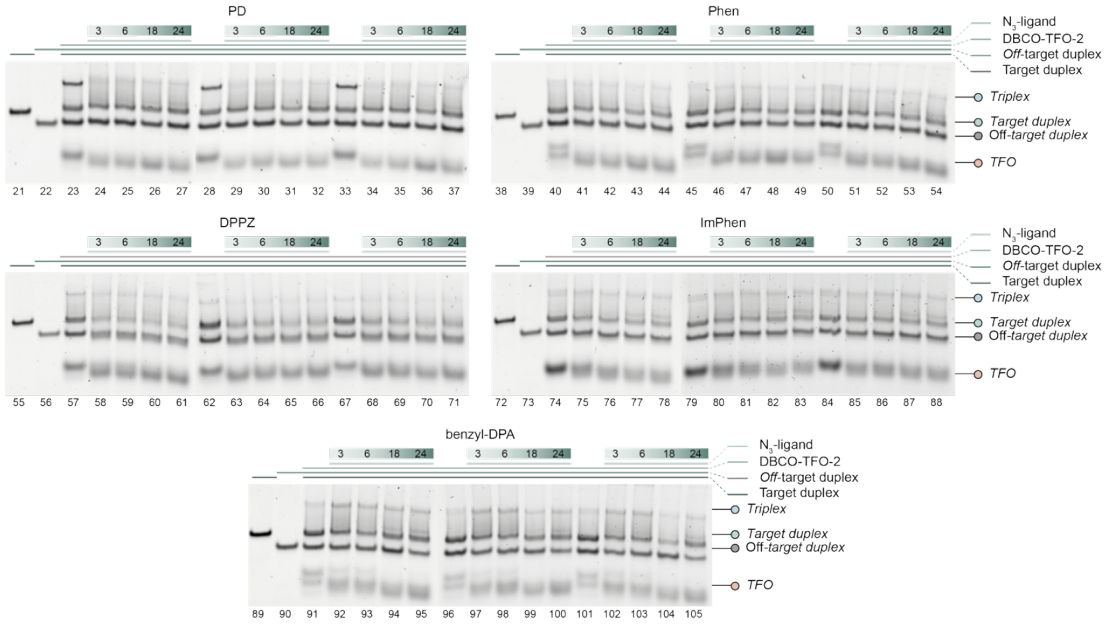


Figure D.2.: PAGE analysis showing the target-specific cleavage activity of self-assembled TFO-2 hybrids in the presence of copper, using N_3-PD, N_3-Phen, N_3-DPPZ, N_3-ImPhen or N_3-benzyl-DPA. Except for PD hybrids (lanes 21 - 37), all lanes contain 1 mM Na-*L*-asc. Lane 21: target duplex. Lane 22 *off*-target duplex. Lanes 23, 28, 33: target + *off*-target duplex + TFO-2 + N_3-PD. Lanes 24 - 27, 29 - 32, 34 - 37: lanes 23, 28, 33 + $Cu(NO_3)_2$ with 3, 6, 18 or 24 h incubation. Lanes 38, 55, 72 and 89 : target duplex + Na-*L*-asc. Lanes 39, 56, 73 and 90: *off*-target duplex + Na-*L*-asc. Lanes 40, 45 and 50: target + *off*-target duplex + TFO-2 + N_3-Phen + Na-*L*-asc. Lanes 41 - 44, 46 - 49, 51 - 54: lanes 40, 45 and 50 + $Cu(NO_3)_2$ with 3, 6, 18 or 24 h incubation. Lanes 57, 62 and 67: target + *off*-target duplex + TFO-2 + N_3-DPPZ + Na-*L*-asc. Lanes 58 - 61, 63 - 66, 68 - 71: lanes 57, 62 and 67 + $Cu(NO_3)_2$ with 3, 6, 18 or 24 h incubation. Lanes 74, 79 and 84: target + *off*-target duplex + TFO-2 + N_3-ImPhen + Na-*L*-asc. Lanes 75 - 78, 80 - 83, 85 - 88: lanes 74, 79 and 84 + $Cu(NO_3)_2$ with 3, 6, 18 or 24 h incubation. Lanes 91, 96 and 101: target + *off*-target duplex + TFO-2 + N_3-benzyl-DPA + Na-*L*-asc, lanes 92 - 95, 97 - 100, 102 - 105: lanes 91, 96 and 101 + $Cu(NO_3)_2$ with 3, 6, 18 or 24 h incubation.